Magnetic and Transport measurements on dilute PdGd Alloys

by

Mukul Saran

A thesis
presented to the University of Manitoba
in partial fulfillment of the
requirements for the degree of
Doctor of Philosophy
in
Physics

Winnipeg, Manitoba

ISBN 0-315-33921-7

MAGNETIC AND TRANSPORT MEASUREMENTS ON DILUTE PdGd ALLOYS

BY

MUKUL SARAN

A thesis submitted to the Faculty of Graduate Studies of
the University of Manitoba in partial fulfillment of the requirements
of the degree of

DOCTOR OF PHILOSOPHY

I hereby declare that I am the sole author of this thesis.

I authorize the University of Manitoba to lend this thesis to other institutions or individuals for the purpose of scholarly research.

Mukul Saran

I further authorize the University of Manitoba to reproduce this thesis by photocopying or by other means, in total or in part, at the request of other institutions or individuals for the purpose of scholarly research.

Mukul Saran

The University of Manitoba requires the signatures of all persons using or photocopying this thesis. Please sign below, and give address and date.

ABSTRACT

The low-field (0-700 Oe), low-frequency (2400 Hz) a.c. susceptibility in a driving field of about 0.12 Oe RMS, the zero-field d.c. and a.c. resistivities and the high-field magnetoresistance of a series of random PdGd alloys, ranging in concentration from 2 to 10 at.% Gd have been measured in a temperature-interval between 1.5 K and 10 K using a variety of electric and magnetic response techniques in order to investigate co-operative magnetic transitions in these alloys.

A phase-locked magnetometer was used to measure a.c susceptibility. The resistivity measurements employed a conventional four-probe method. For measurement of the high-field resistivity, a superconducting magnet capable of producing fields up to about 85 kOe, was used.

Down to the lowest achievable temperatures with the present equipment the least concentrated alloy with 2 at.% Gd appears to remain in a paramagnetic state. The 3 and 4 at.% alloys show characterstics of a para- to ferromagnetic transition below a critical temperature. The higher concentration alloys appear to exhibit more complex ordering; for the latter it is conjectured that below an ordering temperature, a helical magnetic structure

(presumably with a non-vanishing ferromagnetic component) in the d-band of Palladium may be energetically favoured due to interactions of the band electrons with the local impurity-moments.

ACKNOWLEDGEMENTS

Credit for guiding the initiation, execution and completion of this research project is due to my thesis supervisor, Dr. Gwyn Williams. In addition to his command of the subject, his cheerful and friendly disposition made the research more pleasant to conduct. Others who contributed to the success of this work through theoretical or technical assistance are Dr. P. Gaunt, Dr. R.M. Roshko, Dr. H.P. Kunkel and Mr. Gilles Roy. I would like to thank all of them for their invaluable help. Thanks are also due to Mr. Bradley Ingham and Mr. Boris Lamontagne for their several hours of assistance with plotting graphs. In addition, I wish to thank Mr. E.Z. Zastre for numerous beneficial discussions on questions related to this project.

Through the duration of this work, I benefitted greatly from the inspiration and motivation received from my parents. It is to them that I wish to dedicate my thesis. Finally, I acknowledge the useful help in typing, preparing diagrams, proof-reading and related chores from my supportive wife, Anshu.

CONTENTS

Chapter I

THEORIES OF DILUTE ALLOYS

1.1 INTRODUCTION

Dilute alloys formed through the substitution of small amounts (a few atomic %) of a Hund's rule magnetic impurity (e.g. a transition or a rare-earth element) into a host--- metallic or non-metallic--- have long been studied in an effort to understand the microscopic interactions which exist between any pair of the dissolved impurity moments. Magnetic ordering at low-temperatures in such alloys is inextricably linked with the presence of these interactions. The first question to be answered is, however, what happens to the impurity state as it is embedded in the host? Non-metallic hosts usually do not disturb the ionic state; the impurities exhibit the Hund's rule magnetic moment (crystal field effects may need to be accounted for). The presence of a broad conduction band in metallic hosts, however, tends to delocalise the magnetic electrons (the d-electrons in transition metals and the f-electrons in the rare-earths) and thereby destroy the localised moment. Further, for certain hosts the existence of localised moments may depend upon the temperature as well. A local moment at high temperature may dissipate completely as the temperature is lowered.

Two slightly different approaches to the problem of localised moments in metallic hosts have been in existence for some time. One due to Friedel [1,2] and refined by Anderson [3], attempts to find out the conditions for moment formation at an impurity site. It uses the Hartree-Fock single-electron formulation adding as weak perturbations the Coulomb and other intra-ionic interactions responsible for the Hund's rule in the atomic d- and f-shells. It then describes the electronic states of the impurity's magnetic shell in terms of virtual bound states. A virtual bound state is an electronic state which is strongly admixed with the free-electron conduction states and has a finite energy width. Critics of this approach disagree with the strong emphasis it places on the itinerant aspects of the local moment problem.

The other approach typified by the Hirst model (configuration-based approach) [4] is a moments-survival approach. It predicts the conditions under which an impurity loses it's original Hund's rule ionic configuration of electronic states and hence it's moment, when placed in a metallic environment. It concludes that the perturbation of the many-electron ionic configurations of the impurity by interaction with the conduction electrons can only rarely wipe out the localised moments. Explicit conditions on the relative strengths of various kinds of electronic interactions for survival of moments are predicted by the

model. In the present study the Hirst model seems to be more appropriate as we shall observe later. However, for comparison, both approaches merit a more detailed exposition.

1.2 PROBLEM OF MOMENT RETENTION

1.2.1 The Friedel-Anderson Model

(a) Anderson's Explanation:

When the 3d-shell of a first-row transition impurity atom is placed in a metal, it experiences a perturbation due to the conduction states that are degenerate with the impurity state corresponding to a given spin σ. The d-state, therefore, acquires a partial free character -- a process termed "mixing". In the vicinity of the impurity the state of an electron is described by a mixture of ionic and conduction states. In the Anderson picture, it results in the formation of a virtual bound state. The characterstic feature distinguishing it from a normal state is the following: the normal bound state has a single electron bound to the core. However, the mixing between the conduction electrons and the valence electrons of the impurity weakens the effect of the binding potential such that it is no longer able to support a normal bound state. The nuclear charge is then screened by a charge cloud contributed by a component of the total wave-function of the system in a time averaged sense. No single electron forms

this cloud. Whereas the unperturbed impurity state was well-defined in energy, the new state has a width in energy, and hence is spread out in space. Mixing thus results in a partial delocalisation of bound electrons.

If the virtual level width Δ is not too large, the usual intra-atomic Coulomb interactions that are responsible for the Hund's rules in isolated impurity must also be important. They cause a splitting in the energies of the opposite spin states. Both spin-up and spin-down states then acquire a width due to mixing with the conduction electrons. For potentially magnetic impurities these two states must be one on either side of the host Fermi level (fig 1.1). The one below the Fermi level will be occupied and the actual formation of moments at a site is determined by an interplay of three factors:

a) conduction electron density
b) admixing strength, measured by Δ
c) "energy step" U between opposite spin states in the band.

A higher conduction-band density favours delocalisation. The stronger the delocalisation effect, the more ineffective is the exchange U in maintaining the spin-imbalance in the d-band; local moment is thus weaker. A similar tendency is favoured by a mixing strength Δ which is larger than the intra-band spin splitting U. If one or more of these

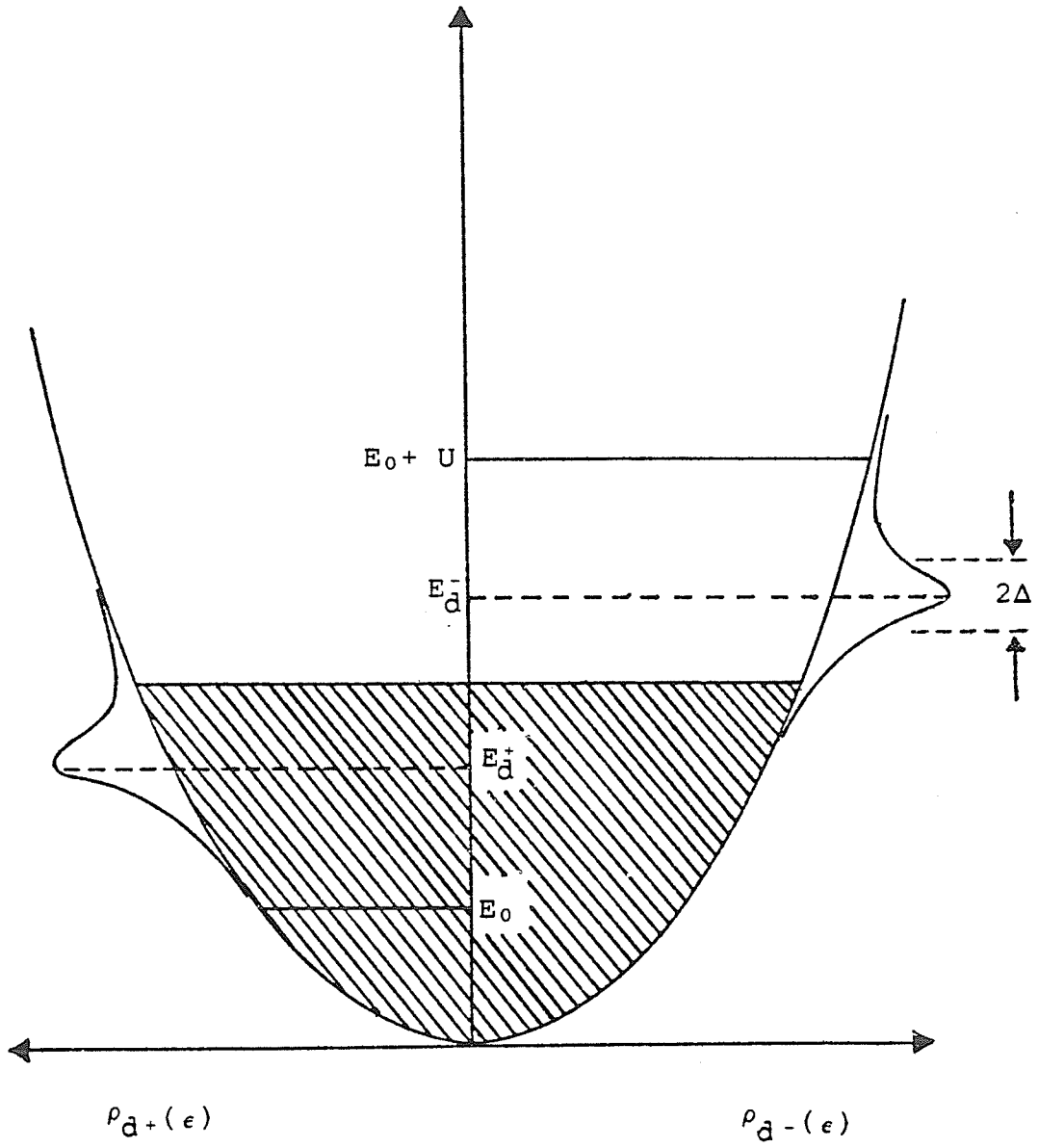

Fig.(1.1): Impurity sub-levels E_0 and $E_0 + U$ perturbed by s-d mixing interactions. The broadened sub-levels are marked E_{d+} and E_{d-}.

parameters are altered to favour spin-flips, ultimately the situation breaks down co-operatively and the impurity loses all its localised moment.

(b) Mathematical Outline of Anderson's Approach:

The impurity in Anderson model is represented essentially through its d-shell Hamiltonian, with an explicit inclusion of the spin-dependent, intra-d shell electron-electron Coulomb correlation energy, U. Thus,

$$H = E_0 (n_{d+} + n_{d-}) + U n_{d+} n_{d-} \tag{1.1}$$

E_0 is the energy of the unperturbed d-state of the impurity; $n_{d\sigma}$ is the occupation number for the spin state σ and U is the correlation energy that is responsible for localised magnetism.

The total alloy system is then represented as a sea of free electrons (conduction electrons of the host) containing in its midst a d-state impurity which senses its environment through a mixing Hamiltonian, H_{kd}. In such a picture, the alloy Hamiltonian is written as

$$\sum_{k\sigma} e_k C^*_{k\sigma} C_{k\sigma} + \{E_0(n_{d+} + n_{d-}) + U n_{d+} n_{d-}\} + \sum_{k\sigma} V_{kd} (C^*_{k\sigma} a_{d\sigma} + a^*_{d\sigma} C_{k\sigma}) \tag{1.2}$$

The first term is the free-electron energy in terms of the free electron creation and annihilation operators, $C^{*}_{k\sigma}$ and $C_{k\sigma}$ respectively. The introduction of the d-state creation and annihilation operators $a^{*}_{d\sigma}$ and $a_{d\sigma}$ in the third term, portrays mixing of the ionic and conduction states; V_{kd} represents the matrix element of the admixing interaction between these states.

The Anderson Hamiltonian describes an interacting multi-fermion assembly. The use of the Hartree-Fock approach simplifies it to a single-electron problem. This simplification is achieved on the premise that the interactions are weak enough to be renormalised. In that limit the pair interaction term $Un_{d+}n_{d-}$ in the impurity Hamiltonian must be replaced by

$$Un_{d+}\langle n_{d-}\rangle + U\langle n_{d-}\rangle n_{d+}$$

The one-particle energies in that approximation are

$$H^{\sigma} = H_{cond} + \sum_{\sigma} E_{d\sigma} n_{d\sigma} + H_{kd} \qquad (1.3)$$

where,

$$E_{d\sigma} = E_0 + U \langle n_{d-\sigma} \rangle \qquad (1.4)$$

are the spin-dependent energies for the d-state. If a spin-up state is occupied and has an energy E_0, a spin-down state will have the energy E_0+U in an unperturbed case.

Using the equations of motion approach to determine the evolution of the d-state and the conduction states under the influence of mixing, or following Anderson, using the Green's function technique, modified d-state energies are given by

$$E'_{d\sigma} = E'_0 + U \langle n_{d\,-\sigma} \rangle - i\Delta \tag{1.5}$$

where

$$E'_0 = E_0 + P \{ \sum_k |V_{kd}|^2 / (\epsilon - \epsilon_k) \} \tag{1.6}$$

is the d-state shifted in energy due to mixing, and

$$\Delta = \pi . |V_{kd}|^2 . \rho(\epsilon) \tag{1.7}$$

is the energy width that the d-state acquires, again, due to mixing. $\rho(\epsilon)$ is the conduction electron density of states. The density of states for the virtual level is a Lorentzian:

$$\rho_{d\sigma}(\epsilon) = \Delta/\pi . [(\epsilon - E'_{d\sigma})^2 + \Delta^2] \tag{1.8}$$

A self-consistency condition is obtained when integration is performed over the density of states (eqn 1.8) to calculate the d-state occupation number. When combined with eqn(1.5) it leads to a set of two self-consistent equations :

$$\langle n_{d\sigma} \rangle = 1/\pi . \cot^{-1}[E_0' - \epsilon_f + U.\langle n_{d-\sigma} \rangle]/\Delta \qquad (1.9)$$

For magnetism of the d-state, these must admit of a solution such that $\langle n_{d+} \rangle \neq \langle n_{d-} \rangle$ for given values of Δ/U and $(E_0 - \epsilon_f)/U$. Non-magnetic solutions correspond to an equality of $\langle n_{d+} \rangle$ and $\langle n_{d-} \rangle$. The transition curve demarcating the magnetic and non-magnetic regions follows an equation obtained from eqn(1.9) with the use of the fact that $\langle n_{d+} \rangle = \langle n_{d-} \rangle$:

$$U.\rho_{d\sigma}(\epsilon_f) = 1 \qquad (1.10)$$

In fig.(1.2), the transtion "phase diagram" is shown. The magnetic region corresponds to $U\rho_{d\sigma}(\epsilon_f) > 1$. It is clear that when the unperturbed d spin-states E_0 and E_0+U are symetrically disposed about the Fermi level, local moments can form for the largest values of Δ, limited by U/π.

(c) Critique of the Model:

A major objection to the model is that it places a rather strong emphasis on the itinerancy of d-electrons. It allows a free interchange of electrons between the d-states and the conduction states with no reference to the ionic energy conservation rquirements. The basis for these deficiencies is the starting assumption. The natural state for an

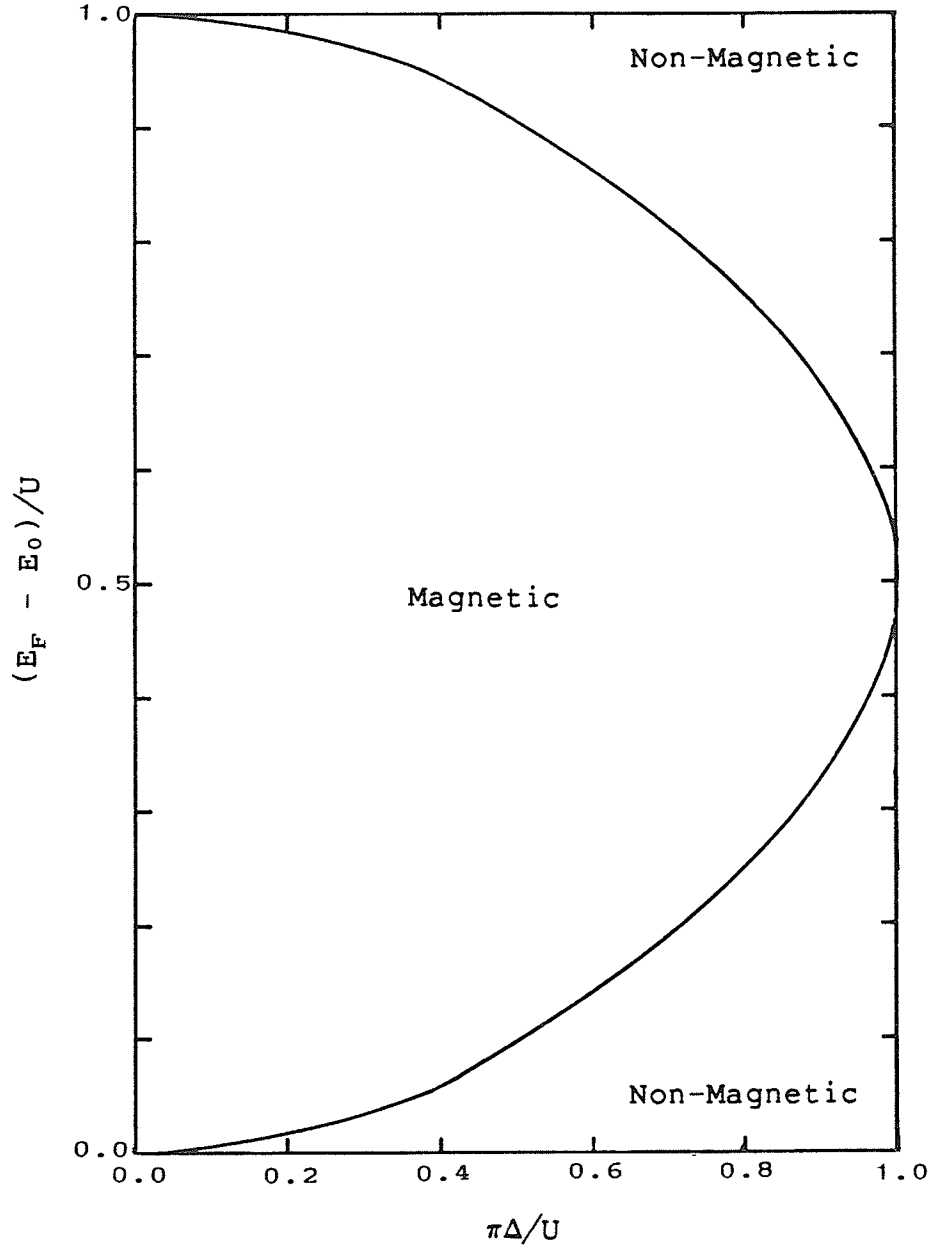

fig.(1.2): Magnetic phase diagram in Anderson's model.

impurity in a metal is assumed to be completely itinerant. The electron correlations, which are normally quite large in isolated ions, are only assigned a secondary role in moment formation.

A related feature is the use of Hartree-Fock approach. It sets a limit on the range of parameters U and Δ for which the model is valid when consistency with the uncertainty principle is required. An electron in the virtual bound state can only remain bound so long as to avoid communication about the occupation or otherwise of other spin-states or orbitals. Since the addition of an electron raises the energy by U approximately, the one-electron life-time is $\hbar/U$. This must be provided by the mixing interaction. This requires

$$\hbar/\Delta < \hbar/U$$

or, simply that

$$U/\Delta < 1 \qquad (1.11)$$

In the limit $U/\Delta >> 1$, the correlation effects are very important and the H-F approach is invalid. But, this also is the limit in which local moment is formed. Thus, the Anderson model does not seem to be equipped to treat the local-moment magnetism in the strongly magnetic limit.

1.2.2 The Hirst Model

(a) Hirst's Explanation:

The configuration-based approach of Hirst [4] pictures an impurity as preserving its bare-ion level structure with well-defined configurations $3d^n$ or $4f^n$ and with the usual intra-configurational splittings such as the L-S multiplets, crystalline electric field levels and spin-orbit levels etc. even when subject to interactions with the conduction electrons. These impurity states can only be perturbed; rarely can they be destroyed completely by such interactions. The intra-ionic Coulomb interactions represent a tendency towards the formation of ionic many-electron states belonging to definite configurations $3d^n$ or $4f^n$; mixing interactions tend to break the configurations with attendant itinerancy of the 3d or 4f electrons. A competition between the two tendencies is the crux of the local moment problem. In contrast to the Friedel-Anderson model this model does not treat the Coulomb and other intra-ionic interactions as weak perturbations; instead it treats the mixing interactions as perturbations on the ionic level structure. Hence integral occupancy of ionic levels is a central feature of this model. In this formulation the problem reduces to one of moment retention. The condition for moment retention is that "the stabilisation energy of the bare-impurity ground state, relative to levels belonging to higher configurations be large compared to the mixing width" [4].

(b) Mathematical Outline of Hirst's Approach:

First, the description of the d-state of the impurity in the Hirst model incorporates the ionic energy level scheme; the natural state of the impurity in the metal is assumed to have a largely ionic character. So,

$$H_i = -Vn + Un(n-1)/2 + H_{intra} \qquad (1.12)$$

The first term, proportional to the occupation number n of the 3d or 4f state, is the nuclear-electronic binding energy. The second represents the Coulomb pair-wise interactions between the electrons of the magnetic shell. H_{intra} takes account of the other intra-ionic splittings.

Secondly, the mixing Hamiltonian uses a partial-wave description for the conduction electrons, assuming that mixing conserves angular momentum. So,

$$H_{kd} = \sum_{k l \sigma} V_{kd} \left(C^*_{k l \sigma} a_{l \sigma} + a^*_{l \sigma} C_{k l \sigma}\right) \qquad (1.13)$$

The conduction electrons are described by a free-electron Hamiltonian, as before. The notation is similar to that of the Anderson model. The mixing strength is measured again by Δ, the rate at which mixing transitions occur when the configurational energetics allow. It is given as in eqn.(1.7). While Δ is taken as a measure of the

delocalisation tendency, U is taken to be indicative of the degree of localisation. A potentially magnetic impurity will have

$$U/\Delta \gg 1 \tag{1.14}$$

The condition above assumes a certain stable configuration for the impurity. What determines the stability? The impurity Hamiltonian H_i suggests an answer when expressed as

$$E(n) = U/2.\ [n - n_{min}]^2 + \text{const.} \tag{1.15}$$

where

$$n_{min} = V/U + 1/2 \tag{1.16}$$

For given values of V and U, the configuration with minimum energy occurs when the deviation from n_{min} is the least. Hence V/U controls the configuration stability. Eqn.(1.15) is pictured in fig.(1.3) and a case of configuration stability for $n = n_0$ is depicted. The intra-ionic splittings are depicted schematically.

A stable configuration n_0 is separated from the neighbouring ones, n_0+1 and n_0-1 by energies $E^{\pm}_{exc}$. E^{-}_{exc} is the energy needed to transfer an ionic electron to the conduction band, at least at the Fermi level. E^{+}_{exc} is the

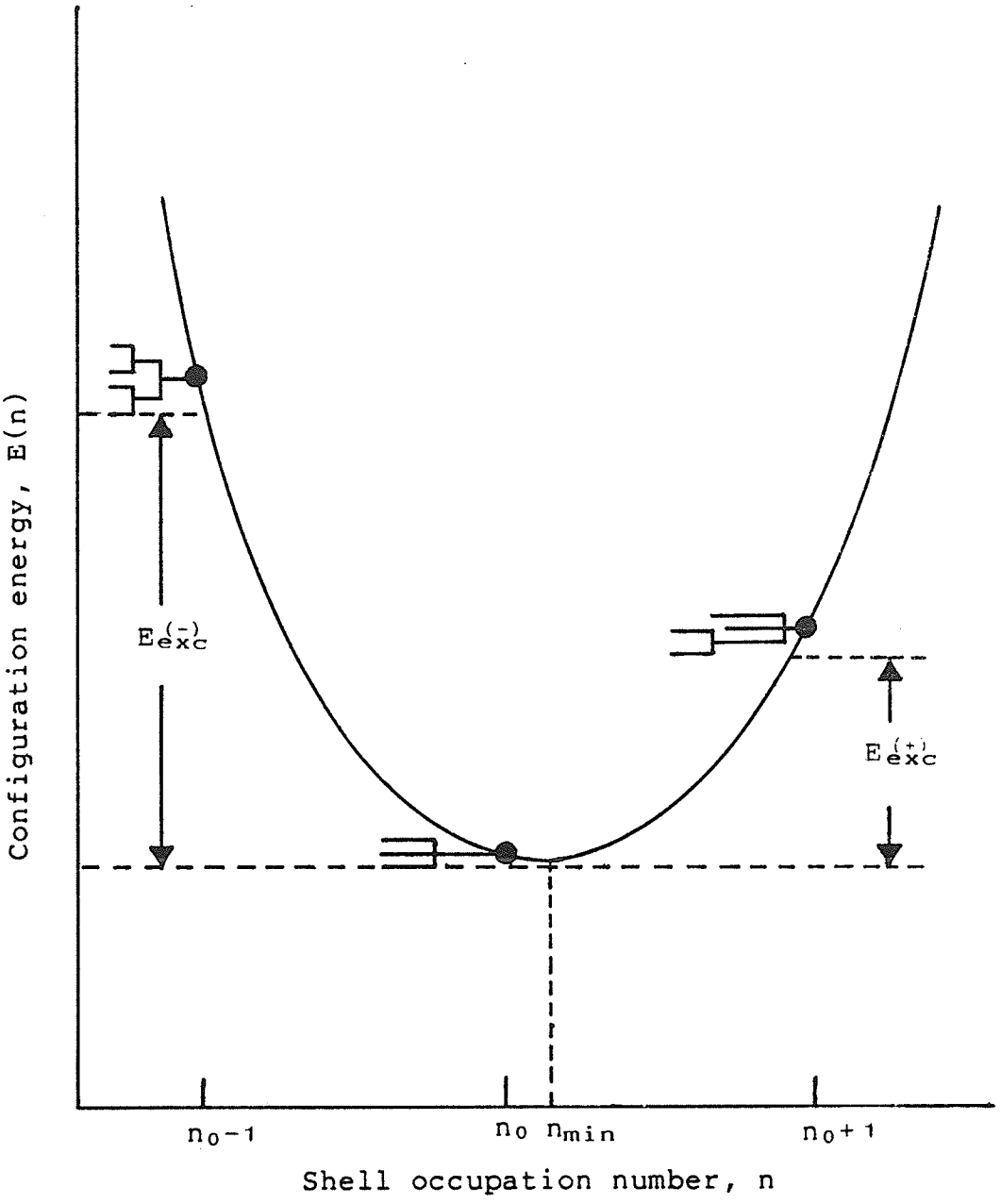

Fig.(1.3): Configuration energies in the Hirst model. Intra-configurational splittings are represented schematically.

corresponding requirement to add a conduction electron "sitting" at the Fermi level to the impurity configuration. The respective values are,

$$E^{-}_{exc} = V - (n_0 - 1)U + \epsilon_f \tag{1.17}$$

and

$$E^{+}_{exc} = -V + n_0U - \epsilon_f \tag{1.18}$$

In contrast to Anderson's model, the position of the impurity ground energy with respect to the Fermi level of the host is inconsequential. It is the difference between neighbouring configuration energies that is physically significant. A configuration in the absence of mixing is stable provided, simply, that

$$E^{\pm}_{exc} > 0 \tag{1.19}$$

Configuration stabilty conditions [eqns (1.19)] can be so manipulated by varying V that a stable configuration n_0 crosses over to another stable one, n_0-1 (say). At the point, called "configuration crossover", where the two are equally stable with respect to n_{min}

$$n_{min} = n_0 - 1/2$$

$$V/U = n_0 - 1 \qquad (1.20)$$

The presence of mixing tends to cause instability of ionic configurations. However, it can act only in accordance with the energy conservation requirements of the configurational scheme. To the lowest order the mixing processes within the lowest levels of a stable configuration are "frozen". Higher order processes lead to an effective mixing strength

$$I = |V_{kd}|^2 / E_{exc} \qquad (1.21)$$

where

$$E_{exc}^{-1} = [(E_{exc}^{+})^{-1} + (E_{exc}^{-})^{-1}] \qquad (1.22)$$

The condition for configuration stability in the presence of mixing requires more than just that

$$E_{exc}^{\pm} > 0$$

it needs the excitation energy E_{exc} to exceed the mixing strength

i.e. $E_{exc} > \Delta$

This prevents an impurity in its ground state, stable in the sense of the above inequality, from making a spontaneous

mixing transition. Thus only such impurity levels as are energetically unstable relative to levels belonging to other configurations may experience a life-time broadening due to mixing transitions.

A configuration stability diagram [fig.(1.4)] conveniently summarises the above observations. The locus of all points given by

$$E_{exc} = \Delta$$

or

$$\Delta/U = -V^2/U^2 + (2n-1)V/U - n(n-1) \qquad (1.23)$$

in the Δ-V plane gives the boundary between stable and unstable "phases" of the impurity moment. Above the locus $E_{exc} < \Delta$. An isolated impurity enjoys stability of a configuration n over a range of values of the binding potential V. For a V outside of that range another configuration becomes stable. The integers on the V-axis correspond to configuration cross-over. The range of stability of a configuration becomes progressively smaller as the mixing strength increases, until at the limiting value of Δ an almost bound state can be supported only by a single binding strength. For Δ larger than that, Anderson's description is more appropriate as the configurational structure suffers a complete breakdown. For Δ below the

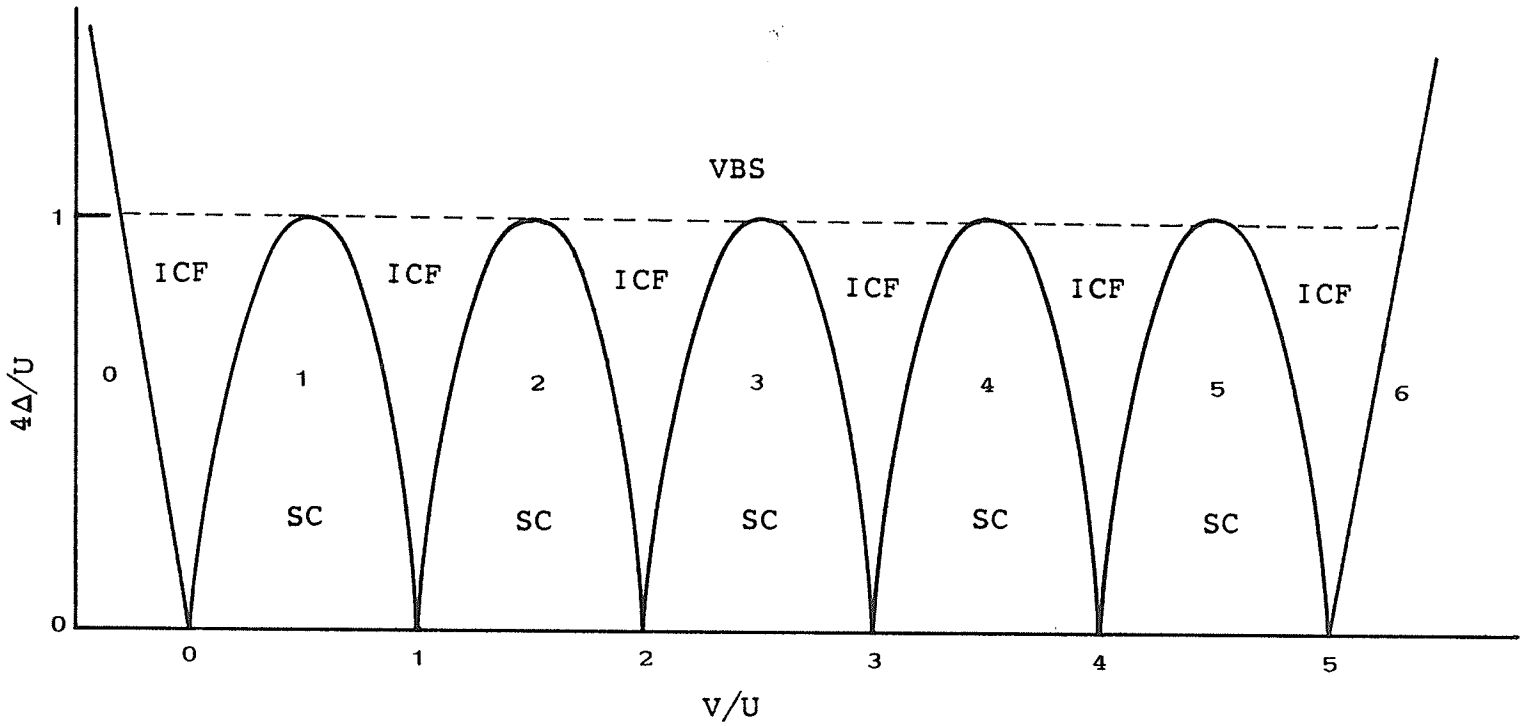

Fig.(1.4): Configuration Stability diagram for an impurity ion in the plane of the binding potential, V, and mixing strength, Δ. SC symbolises 'Stable Configuration'. ICF and VBS denote regions of interconfiguration fluctuations and virtual bound state spin fluctuations respectively.

limiting value U/4, the impurity shows inter-configuration fluctuations for an appropriate range of V because of the proximity of the cross-over point. Mixing drives these spontaneous fluctuations. In this region the configurations have a definition to within a value Δ.

Interestingly the 4f impurities lie very close to the V-axis in the stability diagram. For them, $\Delta/U \sim 10^{-3}$ chiefly because the 4f shell is deep within the atom, well-screened by electrons in the outer shells. Hence in a metallic environment, such impurities are most likely to demonstrate moment localisation with some possibility of crossover. In PdGd, even though one of the parameters favouring delocalisation of moment -- the Fermi density of states -- is high due to s-d hybridisation in pure Pd, localised Gd moments can still be observed. The Hirst model is particularly well-suited for a description of such impurities. For 3d impurities, Δ/U could assume a range of values, demonstrating a VBS type of behaviour for some hosts (e.g. Al) but a near-ideal local behaviour for others (such as Mn in noble-metals).

1.3 INTERACTION BETWEEN LOCALISED MOMENTS

The question to be answered next deals with the possible mechanisms of interaction between a pair of impurity atoms embedded in a metal, given that they have stabilised their moments in the sense of the Hirst or of the Anderson model ($U.\rho(\epsilon_f) > 1$).

1.3.1 The RKKY Mechanism

The roots of the RKKY interaction mechanism can be traced back to the early problem of contact hyperfine interactions between nuclear moments and the s-state electrons. Zener [5] proposed that electron-electron interactions of a form similar to that of the contact hyperfine interactions were the cause of ferromagnetism in metals. The so-called s-d model proposed that the conduction electron spins interact with a localised spin through

$$H = -J \sum_i \vec{S}.\vec{s}_i \; \delta(\vec{r}_i) \qquad (1.24)$$

where S is the local spin and J is the exchange parameter. Schrieffer and Wolff [6] have shown that indeed the Anderson Hamiltonian transforms to the s-d Hamiltonian for a well localised spin in the limit of weak mixing ($U/\Delta >> 1$).

Rudermann and Kittel [7] treated the problem of contact interactions mathematically. Their results supported well the early suggestion of Frohlich and Nabarro [8] that such interactions could lead to a polarisation of nuclear moments. Once the form of the polarisation was obtained by Rudermann and Kittel, the original suggestion of Zener was applied in greater detail to ferromagnetism in metals by Kasuya [9] and by Yosida [10a].

Thus there was a new possible mechanism of interaction, named the RKKY interaction after those credited for its

development, between two well separated local spins. The exchange interaction $-J\vec{S}.\vec{s}$ causes a polarisation of conduction electron spins around the spin $\vec{S}$. Two distant spins then interact through the associated polarisation clouds. The nature and strength of the effective interaction depend on the inter-spin separation and the range of the electron spin polarisation around a given local spin. The extension to the problem of impurity spins in a non-magnetic host is rather direct.

To investigate the character of spin polarisation induced in the conduction band of a linear, stationary, and translationally invariant host due to a single localised impurity, it is assumed that the interaction is through an effective magnetic field the magnitude of which is obtainable from the s-d model.

$$\vec{H}_{eff} = J/g\mu_B \vec{S} \delta(\vec{r}_i) \qquad (1.25)$$

The effective field is then decomposed into its Fourier components. The spin polarisation $\vec{s}(\vec{r})$ of the conduction electron gas in response to the effective field is calculated through the linear response theory:

$$\vec{s}(\vec{r}) = 1/g\mu_B \sum_{q} \vec{H}(\vec{q}) \chi(q) \exp(i\vec{q}.\vec{r}) \qquad (1.26)$$

where $\chi(q)$ is the wave-vector dependent susceptibility. The Fourier transform of the effective exchange field H_{eff} is

$$\vec{H}_{eff}(q) = J/g\mu_B \vec{S} \tag{1.27}$$

Substitution leads to

$$\vec{s}(\vec{r}) = J \vec{S}/g^2\mu_B^2 \sum_{q} \chi(q) \exp(i\vec{q}.\vec{r}) \tag{1.28}$$

The response is proportional to the Fourier transform of $\chi(q)$. The latter is calculated in the second-order perturbation limit for a non-interacting electron gas.

$$\chi(q) = 2\mu_B^2 \rho(\epsilon_f) F(q/2k_f) \tag{1.29}$$

where

$$F(x) = 1/2 [1 + \{(1-x^2)/2x\} \ln |(1+x)/(1-x)|] \tag{1.30}$$

is the usual Lindhard function. Combining eqn.(1.29) with eqn.(1.28), the nature of the spin polarisation is given by

$$\vec{s}(\vec{r}) = -CJ [\text{Cos } 2k_f r/(2k_f r)^3 - \text{Sin } 2k_f r/(2k_f r)^4] \vec{S} \tag{1.31}$$

The constant C is related to the Fermi energy ϵ_f, the Fermi momentum and the lattice point density in the crystal. The polarisation $\vec{s}(\vec{r})$ [fig.(1.5)] is the RKKY polarisation.

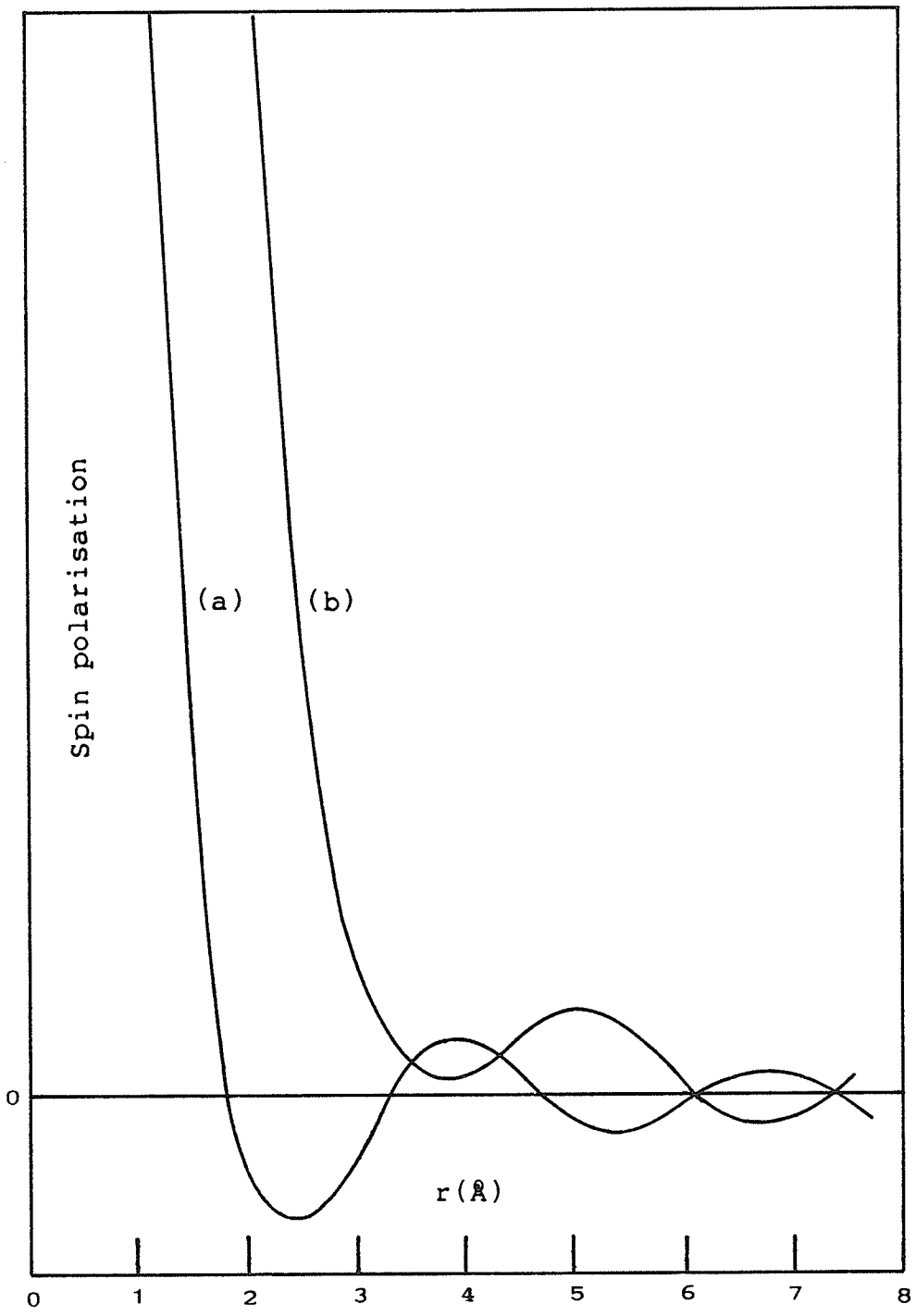

Fig.(1.5): Unenhanced, (a), and enhanced, (b), RKKY polarisations around an impurity.

At large distances ($k_f r >> 1$) from the impurity the polarisation shows r^{-3}-damped oscillations with a period π/k_f. Most of it is confined to a small region around the impurity. The sense of the polarisation (whether parallel or anti-parallel to the impurity spin) is determined by the sign of the exchange coupling J (whether +ve or -ve). These characteristics can give rise to several interesting ordering phenomena in dilute magnetic alloys because the polarisation provides a long-distance indirect mechanism for interaction between moments. Thus, for example, an impurity spin $\vec{S}_j$ localised at site j may interact with the polarisation cloud associated with that at site i according to an interaction of the form $-J\vec{s}(\vec{r}_{ij}).\vec{S}_j$. Hence the RKKY coupling energy is (replacing $\vec{r}_{ij}$ by $\vec{r}$, for convenience)

$$H_{RKKY} = -J(\vec{r})\ \vec{S}_i.\vec{S}_j$$

$$J(r) = -CJ^2\ [\text{Cos}\ 2k_f r/(2k_f r)^3 - \text{Sin}2k_f r/(2k_f r)^4] \qquad (1.32)$$

In real metals and alloys, the approximation of independent electrons is seldom valid. For example, in Pd which has a narrow d-bands, the inter-electron Coulomb effects assume significance. The free-electron susceptiblity that enters eqn.(1.28) must then be replaced by a more appropriate expression.

Wolff [11], using the random phase approximation (RPA) calculated the spin-density induced by an external magnetic field in a degenerate, interacting electron gas to be

$$\vec{s}(q) = \{g\mu_B^2 F(q) / [1-\bar{v}F(q)]\} \vec{B}(q)$$

where $\vec{B}(q)$ is the Fourier transform of a weak, externally applied magnetic field in the z-direction, and

$$F(q) = -\sum_{k} [n_{k+q} - n_k] / [\epsilon(k+q) - \epsilon(k)] >> 0 \qquad (1.33)$$

gives the wave-vector dependent susceptibility function. In the RPA, the presence of Coulomb interactions renormalises the electronic energies to

$$\epsilon(k) = \hbar^2 k^2/2m - 1/(2\pi)^3 \int_{k<k_f} v(k-k')dk' \qquad (1.34)$$

Secondly, it induces exchange scatterings between the virtual particles created by the applied field. Through the denominator $[1 - \bar{v}F(q)]$, this leads to an enhancement of the normal RKKY polarisation. The effect is most pronounced for small q due to the monotonically decreasing nature of F(q). The function $\vec{s}(q)$ is sharpened in q-space and that means a larger width in real space for its Fourier transform, $\vec{s}(\vec{r})$. The effective range of polarisation is pushed out and the magnitude is enhanced [fig.(1.5)]. The screening of Coulomb interactions causes the range to be further enhanced by giving $\bar{v}$ a wave-vector dependence that tends to sharpen the low-q region in $\vec{s}(q)$.

The true range of RKKY polarisation in actual alloys depends on the shape details of the Fermi surface. The r^{-3} drop in oscillation amplitude is a consequence of a spherical Fermi surface assumed for calculation. Pd metal has a complex Fermi surface [12,13]. The structure has flat and cylindrical sections to it. The amplitude attenuation for flat geometry is r^{-1} and is r^{-2} for a cylindrical one [14].

Finally a comment about the divergence of s(q) as $\bar{\nu}F(q)$ approaches unity: the infinity is related to the approach towards electron-gas ferromagnetism which involves interactions strong enough to invalidate Wolff's treatment, based as it is, on a perturbation expansion about an unpolarised ground state of the electron-gas.

1.3.2 Covalent Admixture Mechanism

Between two localised impurity moments, the admixture interaction occurs through a mixing of the localised orbital of one with that of another. The inter-impurity distance determines the process through which such a mixing of states is brought about. In dilute alloys, for example, where large inter-impurity separations are involved, the conduction electrons are the "carriers" of the interaction. It occurs through a process known as 'Double Resonance Coupling'. B.Caroli [15a] and A.Blandin [16] have treated this problem in the Green's function formalism. In more

concentrated alloys or in pure metals a direct admixture process, treated formally by T.Moriya [17], is effective. A description of the above processes follows.

(a) Double Resonance Coupling:

Consider two isolated, non-degenerate, localised, moment-bearing states. The coupling between them, when they are brought to a distance R can be qualitatively understood in terms of the Anderson's model. A free-electron with spin σ and wave-vector k gets scattered from the first impurity. For a 3d impurity the l=2 component of the plane wave suffers a resonance scattering. Hence the phase-shift δ of that component is the most dominant of all. The asymptotic form of the scattered wave-function is, therefore, represented as

$$\psi_{\sigma}(k) = \exp(ik.r) + \exp(i\delta_{\sigma}) \text{ Sin } \delta_{\sigma} .\exp(ikr)/kr \qquad (1.35)$$

At the second impurity, this electron suffers another resonance scattering which depends upon the phase-shifts produced by the first impurity through the modified wave-function $\psi_{\sigma}(k)$. The Anderson's approach remains valid for the second impurity provided the mixing elements V_{kd} are now evaluated with $\psi_{\sigma}(k)$ instead of the plane-wave states. Thus in the Anderson Hamiltonian $\langle k|V|d_2\rangle$ are replaced by

$$\langle\psi_{\sigma}(k)|V|d_2\rangle = V_{kd}[\exp(ikR) + \text{Sin}\ \delta_{\sigma}.\ \exp\{i(kR + \delta_{\sigma})\}/kR] \tag{1.36}$$

This expression is easily obtained if $\psi_{\sigma}(k)$ is referred to an origin at impurity 2 for evaluating the matrix element. The effective energy shift Γ_2' and the level-width Δ_2' of the virtual d-state on the second impurity are obtained by replacement of $\langle\psi_{\sigma}(k)|V|d_2\rangle$ into the Anderson's expression:

$$\Gamma - i\Delta = \sum_{k} |V_{kd}|^2/(e + is - e_k) \tag{1.37}$$

The result is

$$\Gamma_2' - i\Delta_2' = \Gamma_2 - i\Delta_2 - \Delta_2\ \text{Sin}\ \delta_{\sigma}.\exp\{i(2k_0R + \delta_{\sigma})\}/k_0^2R^2 \tag{1.38}$$

where electrons are assumed to be free with energy $\hbar^2k^2/2m$. Γ_2 and Δ_2 are the displacement and the level-width respectively for the second impurity considered in isolation. The presence of the first impurity modifies these parameters to their new, energy-dependent values Γ_2' and Δ_2'. This, in turn, causes the population n^{σ} of the localised d-electrons on the second impurity to become variable and, consequently, an indirect coupling exists between the two impurities. For distant impurities, only the electrons in the vicinity of the Fermi level are relevant for coupling.

The coupling energy between two non-degenerate d-states in the Hartree-Fock approximation at low-temperatures ($k_BT << \Delta$) is given as [15b,16]:

$$E_i(R) = E_f/\pi \sum_{\sigma} \text{Sin } \delta_1^{\sigma}.\text{Sin } \delta_2^{\sigma}.\text{Cos}(2k_fR+\delta_1^{\sigma}+\delta_2^{\sigma})/(k_fR)^3 \qquad (1.39)$$

δ_1^{σ} and δ_2^{σ} are the phase-shifts produced by two isolated impurities. The expression assumes collinear moments. In case of an arbitrary angle θ between moments m_1 and m_2, the interaction energy contains a magnetic coupling term besides a non-magnetic term that represents the energy obtained in bringing the two impurities to a distance R from their initial infinite separation. The effective magnetic coupling energy is

$$E_i = E_f/2\pi \sum_{\sigma,\sigma'} \text{Sin } \delta_1^{\sigma}.\text{Sin } \delta_2^{\sigma'}.\text{Cos}(2k_fR+\delta_1^{\sigma}+\delta_2^{\sigma'})/(k_fR)^3 \; m_1.m_2$$

where $m = 2\mu_B S_i$. $E_i(R)$ can be written with an effective exchange interaction J(R),

$$E_i(R) = J(R)\, S_1.S_2$$

$$J(R) = A \,\text{Cos}(2k_fR + \delta)/(k_fR)^3 \qquad (1.40)$$

A and δ depend upon ϵ_f and the phase-shifts δ^{σ}. In dilute random alloys, it is extremely difficult to say anything about the sign of the double-resonance coupling. The radial dependence of the inter-impurity double-resonance

interaction closely resembles that of the RKKY interaction. Furthermore, because the asymptotic limit ($k_f R >> 1$) for which the form of the admixture coupling is valid, is usually approached even at near-neighbour separation this type of coupling is effective at close range. For larger separations it is much weaker. Hence making the distinction between the direct and indirect admixing mechanisms depending upon the range over which they are effective is only an artifice. Finally, a necessary aspect to note is that the resonance coupling has been treated in the Anderson picture which is really only applicable in cases where localisation is, at best, weak.

(b) Direct d-d Admixture Process:

The problem of the sign of interaction between two neighbouring, magnetic virtual d-levels ($U/\Delta >> 1$ in the Anderson picture of localised moments) immersed in a sea of conduction electrons and interacting with each other through direct d-d admixture has been treated by Alexander and Anderson [18] and by Moriya [17] using the Hartree-Fock approach.

The sign of the direct interaction between these levels is found to depend upon the location of the (single-impurity) spin-up and spin-down virtual sub-levels relative to the Fermi energy (assumed to be a fixed parameter). If one of the sub-levels (either E_0 or E_0+U) falls much closer

to the Fermi energy than the other, the interaction between the neighbouring d-levels is expected to be ferromagnetic. In this case, economy in energy is achieved by an actual to and fro transfer of an electron with a given spin between the two virtual levels. When one sub-level at each of the neighbouring sites has a higher density of states near the Fermi energy, such transitions are favoured. If, on the other hand, the spin-up and spin-down virtual sub-levels at each of the two impurity sites are symmetrically disposed about the Fermi energy, the neighbouring virtual d-levels prefer an antiferromagnetic exchange. In this case, the total energy of the system is reduced by a virtual transfer of electrons from a full spin-up level on one atom to the empty spin-up level on the other and vice-versa. This process does not require a high level-density at the Fermi surface.

Alexander and Anderson [18] calculated the energy changes brought about by the presence of d-d mixing in the two situations described above. The starting Hamiltonian is written in the Anderson picture for two single-impurity virtual d-levels. A d-d mixing term is added to it. The form of the mixing is

$$H_{dd} = \sum_{\sigma} [V_{12} a^{*}_{1\sigma} a_{2\sigma} + V_{21} a^{*}_{2\sigma} a_{1\sigma}] \qquad (1.41)$$

where V_{12} represents the transfer integral between the d-states and $a^{*}_{i\sigma}$, $a_{i\sigma}$ are the creation and annihilation operators for electrons with spin σ at site i. The energy change is calculated both for the parallel and for the antiparallel interactions.

a) For the parallel case,

$$\delta E = -V^2 [\rho^{+} + \rho^{-}] \qquad (1.42)$$

where

$$\rho^{\sigma} = \Delta/[\pi.\{(\epsilon_f - E_0 - Un^{-\sigma})^2 + \Delta^2\}] \qquad (1.43)$$

is the density of states for the single-impurity, virtual sub-level corresponding to spin σ and n^{σ} is the corresponding occupation number. As before, Δ is the level-width.

b) For antiparallel interactions,

$$\delta E = -2V^2/U \qquad (1.44)$$

Which orientation is preferred in the presence of direct d-d interactions depends upon the relative magnitudes of the energy gain. Hence for parallel alignment,

$$U/2\ [\ \rho^{+} + \rho^{-}\ ]\ >\ 1 \qquad (1.45)$$

This condition determining the orientation of the two moments is independent of the mixing strength, V, so long as it remains weaker than the intra-band exchange U (i.e. $V/U << 1$). The following simple rules governing the relative orientations of the neighbouring d-shells emerge:

Atoms with nearly half-filled d-shells (such as Mn) have a tendency for antiferromagnetic coupling.

With a rise in the number of d-electrons there is an increasing trend towards ferromagnetic d-d interaction.

1.4 ORDERING OF MOMENTS

The RKKY interaction mechanism leads to some interesting ordering effects in dilute magnetic systems. When two distant local moments interact through the first zeros of the associated long range oscillatory conduction electron polarisations ferromagnetism results. Phenomenologically, the situation is described quite well by the Weiss mean-field theory which takes account of such long range interactions in terms of an effective field at the site of each local spin.

An interesting possibility occurs when the long-range oscillating character of the RKKY polarisation favours the formation of long-period magnetic structures.

Turov [19] presents the example of simple spiral structures to illustrate the conditions under which those structures may be favoured. A spiral structure with its axis in the z-direction has spin components descibed by

$$S_n^x = S \cos(Q.R_n)$$

$$S_n^y = S \sin(Q.R_n)$$

$$S_n^z = 0 \qquad (1.46)$$

where S is the mean value of the ionic spin. The coupling between any spin pairs is described through the effective Hamiltonian

$$H_{eff} = - \sum_{ij} J(R_{ij}) \, S_i . S_j$$

where the effective coupling constant can be written as

$$J(R_{ij}) = \text{const.} \sum_{q} F(q/2k_f).\exp(iq.R_{ij}) \qquad (1.47)$$

in linear response theory (section 1.3.1), where $F(q/2k_f)$ or $F(q)$ in short, is the Lindhard function giving the wave-vector dependent susceptibility for a free conduction electron gas [eqn.(1.30)].

With the use of eqns(1.46) the energy of a simple spiral with wave-vector Q could be found from the effective Hamiltonian to be given as

$$E(Q) = -NS^2J(Q) \tag{1.48}$$

where $J(Q)$ is the Fourier "cousin" of $J(R_{ij})$, i.e.

$$J(Q) = \Sigma\, J(R_{ij})\, \exp(-iQ.R_{ij}) \tag{1.49}$$

The largest value of $J(Q)$ minimises the energy and, the value of Q that maximises $J(Q)$ gives the periodicity of the most stable spiral structure. The value $Q=0$ corresponds to ferromagnetism in the alloy. A maximum in $J(Q)$ at non-zero Q stabilises a spiral structure with periodicity $d=2\pi/Q$. To be sure that a maximum in $J(Q)$ exists, the energy difference between the spiral and ferromagnetic structures must be considered. If Umklapp processes are allowed so that the scattered wave-vector q may differ from its "resonant" value Q by a reciprocal lattice vector K, i.e. if

$$1/N.\ \sum_i \exp(iq.R_i) = \delta(q - K) \tag{1.50}$$

then the energy difference can be expressed as [eqns(1.48) and (1.47)]

$$J(Q) - J(0) = \text{const.} \sum_K [F(K + Q) - F(K)] \tag{1.51}$$

The sum on the right contains pairs of terms with vectors K and -K. Assuming Q to be small, any such pair can be expanded as

$$F(K + Q) + F(K - Q) - 2F(K) \approx F''(K).Q^2 \qquad (1.52)$$

The function F(q) is singular at $q=2k_f$; its second derivative changes sign.

$$F''(q) < 0 \quad \text{for} \quad q < 2k_f$$

$$F''(q) > 0 \quad \text{for} \quad q > 2k_f \qquad (1.53)$$

The terms in the sum [eqn(1.51)] for which $K < 2k_f$ (i.e. K/2 penetrates the Fermi surface) make a contribution that decreases with increasing Q. On the other hand, terms with $K > 2k_f$ (those with K/2 lying outside the Fermi surface) have an opposite effect; the contribution increases with increasing Q. The sum must therefore, possess a maximum at an intermediate non-zero Q value. This fact is directly related to the existence of Kohn anomaly in the Lindhard function {or equivalently in the wave-vector dependent susceptibility $\chi(q)$} at $q=2k_f$. Further, if Umklapp processes were disallowed in this simple picture, the energy difference J(Q) - J(0) would contain only one term, corresponding to K=0, and hence, the Kohn anomaly would be unable to ensure maximisation of J(Q). Then, spiral

structure stabilisation would not follow as a normal consequence of a singularity in the function F(q). Yosida and Watabe [20] made a numerical calculation of the curve J(Q) - J(0) for a heavy rare-earth hexagonal crystal with c/a = 1.57 on the basis of the simple theory outlined above. It provided support for the essential arguments of the theory when its predictions were compared with the known inter-layer turn angles for the spins on hexagonal lattice planes of the h.c.p. heavy rare-earths Tm and Er. More complex ordering patterns may result when lattice anisotropies are accounted for. The various possibilities are depicted in fig.(1.6). These magnetic structures have been known to exist in pure rare-earth metals and, as described above, the essential mechanism is the long-range oscillatory interaction amongst atoms. The concept of helical spin arrangement in a dilute alloy with randomly distributed magnetic impurities is not immediately obvious until it is realised that static spin modulations (with wave-vector q) in the conduction band may be stabilised by the intra-band exchange interactions once they are excited by the s-f exchange interaction between the conduction electron spins, s_i, and the impurity spins, S_j:

$$H_{sf} = -j \sum_{ij} s_i . S_j \; \delta(r_i - R_j)$$

The form of the spin-density wave is

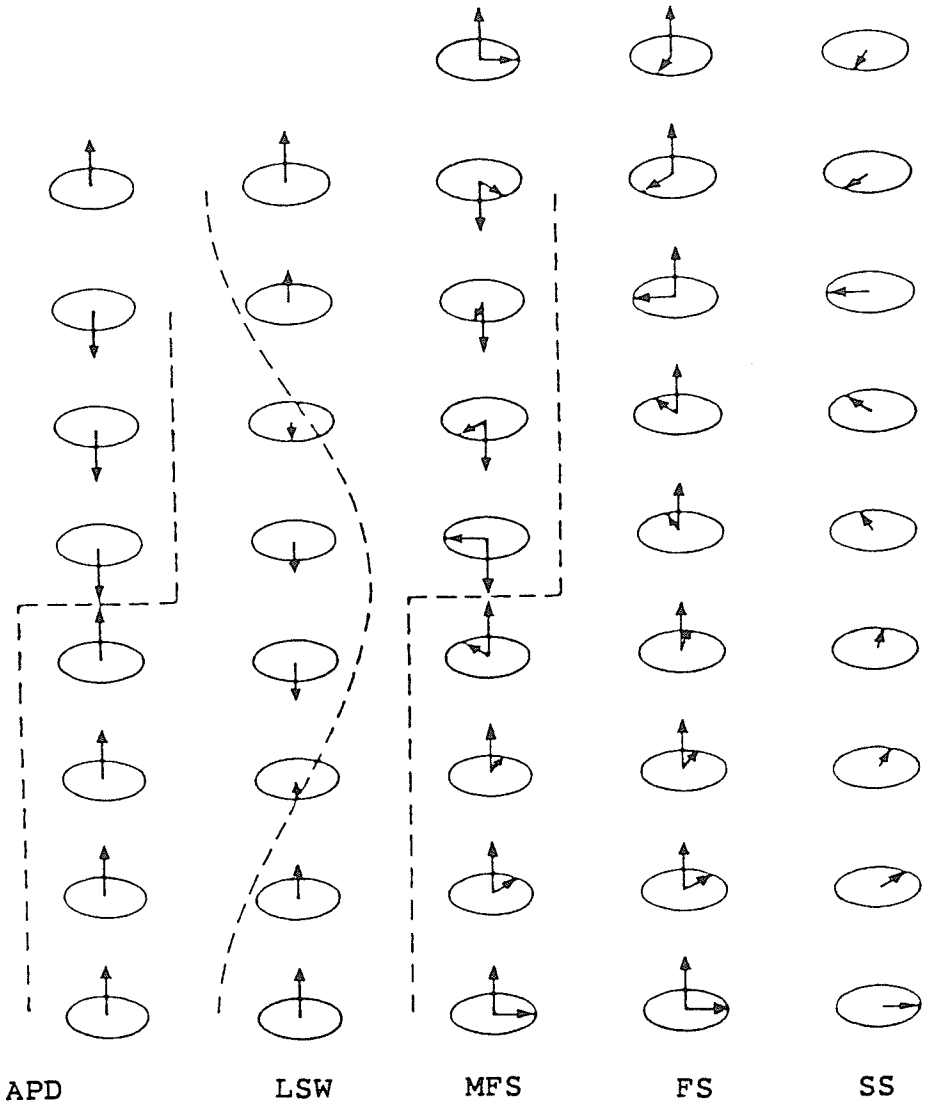

Fig.(1.6): Patterns of magnetic order [19].

SS: Simple Spiral

FS: Ferromagnetic Spiral

MFS: Modulated Ferromagnetic spiral

LSW: Longitudinal Spin Wave

APD: Anti-Phase Domain Structure

$$s(R) = \langle -j \sum_i s_i \, \delta(r_i - R_j) \rangle = bN \, \mathrm{Cos}(q.R) \, \hat{e} \qquad (1.54)$$

so that it has a spin polarisation described by a wave-vector q. This wave simply has an aligning effect on the impurity spin through the s-f interaction. The vector q for spin-density wave (SDW) stabilisation is not necessarily commensurate with the lattice periodicity, being determined, in the Hartree-Fock approximation, solely by the self-consistency condition [22a]. The effect of such a wave on the properties of alloys is similar to that of helical ordering of local moments in the pure rare-earths. Data on dilute YGd and ScGd alloys has been interpreted in terms of the Overhauser-type SDW stabilisation by Sarkissian and Coles [23] and by Southern and Sherrington [24].

Palladium metal, which is the host for Gd in the present study, has holes in its d-band, which bear a small moment. A coupling between Gd moments and the d-holes exists through exchange interaction. A strong exchange interaction exists amongst the d-holes. Could it not be that the moment-bearing impurity, Gd, induces an SDW in the d-band which is subsequently stabilised by the strong intra-band exchange?

Chapter II

THEORIES OF ELECTRIC AND MAGNETIC BEHAVIOUR OF DILUTE ALLOYS

2.1 INTRODUCTION

The preceding chapter outlines the framework for describing the state of a magnetic impurity embedded in a metallic host and the modes in which it can interact with another impurity placed in the same host. The attempt now is to set up a framework for understanding the results of any measurements on electrical resistivity and magnetic susceptibility designed to derive information on the local-moment phenomena in the alloys of interest, namely PdGd.

2.2 ELECTRICAL PROPERTIES

The electric properties of dilute alloys containing magnetic impurities are frequently understood in terms of the s-d model. The model was suggested originally by Zener. The anomalous resistivity of CuMn alloys reported by Gerritsen and Linde [25] led other researchers [9a,26,27] to investigate the other magnetic properties of this system and, subsequently, to interpret the results qualitatively on the basis of s-d exchange. Yosida [28] is credited with quantifying the s-d model for the specific case of resistivity of CuMn alloys (which are now known to be spin

glasses for c ≤ 5 at.%). Yosida simulated the system in terms of two oppositely ordered groups of spins. He also mentioned an appropriate modification for the case of ferromagnetic alloys. Long and Turner [29] did a similar calculation for a Palladium-based system, PdFe, taking into account the special electronic structure of this host. All these resistivity calculations are limited to first order perturbation. The s-d model which forms the basis of these calculations may lead in the second order to a low-temperature logarithmic divergence in the resistivity -- the so-called Kondo effect -- provided that the effective s-d interaction is negative in sign (i.e. $J < 0$). This effect was first obseved by De Haas and Van den Berg (1933) at Leiden in impure samples of Gold. As already observed in section (1.3.1), the same s-d Hamiltonian is responsible for an effective, long-range coupling between two distant magnetic impurities in the second order. The following discussion is limited to first order calculations of resistivity only.

2.2.1 The s-d Model

Yosida's calculation assumes that while the impurity loses its s-electrons to the host conduction band, it retains its d-electrons and its level structure. The d-moment dynamics are explicitly neglected except via the exchange interaction. The n-body Hamiltonian for this system is perturbed by

$$H' = \sum_{in} V(r_i - R_n) - 2 \sum_{in} J(r_i - R_n)\ s_i.S_n \qquad (2.1)$$

where r_i refers to the electronic coordinates and R_n to the ionic ones. V is the translation symmetry-breaking potential which arises due to the valence difference between the impurity and the host. It usually has a screened Coulomb form. J is the exchange parameter, with s_i and S_n representing the conduction-electron and impurity spins respectively. The exchange term is simple in form because an orbital moment on the impurity is assumed to be either non-existent (as in case of S-state ions such as Mn, Gd etc.) or quenched due to crystalline electric fields in the host matrix [30].

The Hamiltonian [eqn.(2.1)] is transformed to a field representation:

$$\begin{aligned} H' = {} & 1/N \sum_{k k'} V(k,k').\exp[i(k-k').R_n].(a^*_{k+}a_{k+} + a^*_{k'-}a_{k'-}) \\ & -1/N \sum_{k k'} J(k-k').\exp[i(k-k').R_n].\{(a^*_{k'+}a_{k+} - a^*_{k'-}a_{k-}).S^{\zeta}_n \\ & + a^*_{k'+}a_{k-}S^+_n + a^*_{k'-}a_{k+}S^-_n\} \end{aligned} \qquad (2.2)$$

V(k,k') and J(k,k') are related to the matrix elements of V and J between the conduction electron states |k> and |k'> which are plane waves only in the lowest order of approximation because the periodic symmetry is broken. Both

are assumed to depend only on the magnitude of the difference $(k - k')$. S_n^{ζ}, $S_n^{\pm}$ are the three components of the localised spin S_n in the field-operator formalism, whereas $a^*_{k\sigma}$ and $a_{k\sigma}$ are the field operators for the conduction electron assembly.

The response of the conduction electrons to the applied electric field is calculated next. At any impurity site the interaction with the conduction electron would depend upon the relative orientation of their spins. Thus the distribution functions $f^{\pm}$ for the spin-up and spin-down conduction electrons would, in general, be different from each other and also from the equilibrium distribution f_0 in the absence of an electric field. The assumption is that, to first order

$$f^{\pm}(E_k) \approx f_0(E_k) - k_x E \, \Phi^{\pm}(E_k) \, df_0/dE_k \tag{2.3}$$

where k_x is the wave-vector component in the direction of the applied electric field E and $\Phi^{\pm}$ are functions to be determined through the use of the transport equation. The current densities due to spin-up and spin-down electrons are then given by

$$j^{\pm} = -e/V \sum_k [f^{\pm}(E_k) - f_0(E_k)] . \, hk_x/m \tag{2.4}$$

where V is the total volume. Upon substitution for $f^{\pm}(E_k)$ and subsequent evaluation of the sum as an integral over k-space upto the Fermi limit, the current densities are given in terms of $\Phi^{\pm}$:

$$j^{\pm} = cE\epsilon_f^{3/2}\ \Phi^{\pm}(\epsilon_f) \tag{2.5}$$

From the elementary relation $j = E/\rho$, the resistivity is calculated as

$$\rho = [\Phi^{+}(\epsilon_f) + \Phi^{-}(\epsilon_f)]^{-1}/c\epsilon_f^{3/2} \tag{2.6}$$

The functions $\Phi^{\pm}$ are calculated using the transport equation.

$$(\delta f/\delta t)_f + (\delta f\ /\delta t)_c = 0 \tag{2.7}$$

where,

$$(\delta f/\delta t)_f = (\delta f_0/\delta E_k).eE.hk_x/m \tag{2.8}$$

is the rate of change of the electronic distribution due to the applied electric field. The corresponding quantity due to the collisions is calculated using the Golden Rule for transition probabilities, taking appropriate account of the probabilities of occupation or non-occupation of the initial and final states k and k' related by scattering. Separate

calculations are made for elastic and inelastic processes. The latter involve flips of the scattered conduction electron spins and of the impurity spin whereas the former do not. This results in a rather large expression for the resistivity. However, the essential result is that in the paramagnetic phase the contribution to the electrical resistivity due to exchange scattering is temperature independent, and is given as [28],

$$\begin{aligned}\Delta\rho &= ac J^2\{\langle S_x^2\rangle + \langle S_y^2\rangle + \langle S_z^2\rangle\} \\ &= ac J^2 S(S+1)\end{aligned} \tag{2.9}$$

where,

$$a = 3\pi m^* \Omega / 2e^2 \hbar \epsilon_f^2 \tag{2.10}$$

Ω denotes the volume per palladium atom and ϵ_f, the Fermi energy.

Yosida's calculation adapted to the case of systems ordering ferromagnetically yields for the s-d resistivity [31]:

$$\begin{aligned}\Delta\rho(T) = ac\ \{&[\ V^2 + J^2\langle S_z^2\rangle + J^2\Gamma] \\ &- 4J^2V^2\langle S_z\rangle^2/[\ V^2 + J^2\langle S_z^2\rangle + J^2\Gamma]\}\end{aligned} \tag{2.11}$$

where, in these equations

$$\Gamma(S,S_z,H/T) = [S(S+1)- \langle S_z^2\rangle - \langle S_z\rangle].[1 + \tanh(g\mu_B H/2kT)] \quad (2.12)$$

The magnetic resistivities in the absence of external fields can be calculated for two temperature extremes -- T=0 and $T=T_c$ -- assuming strong potential scattering due to impurities.

$$\Delta\rho(0) = ac\ V^2 \quad (2.13)$$

and

$$\Delta\rho(T) = ac[V^2 + J^2S(1+4S)] \quad (2.14)$$

Then the difference furnishes an estimate for J; the former can be estimated from the measured resistivity. Subsequently, V can also be estimated using eqn.(2.13).

2.2.2 Long and Turner Model

For alloys with an exchange-enhanced host such as Palladium, a modification to Yosida's result for ferromagnetic resistivity was formulated by Long and Turner [29].

The presence of 0.36 holes/atom in the Pd d-band [32] causes additional terms to appear in the Hamiltonian. They represent exchange interactions of the d-holes with the localised impurity moments S_n and with the conduction

electrons. The state of the d-band and its coupling to the impurity is described by the following terms:

$$H_d = \sum_{k\sigma} \epsilon_d(k)\, C^*_{dk\sigma} C_{dk\sigma} + I \sum_i n_{i+} \cdot n_{i-} \tag{2.15}$$

This represents the d-hole Hamiltonian which takes into account a strong localisation of the d-holes through the inclusion of an exchange energy I between the holes with opposite spin orientations located on the same site. $\epsilon_d(k)$ are single-particle d-hole energies. C^* and C represent the creation and annihilation operators for the d-holes in the specific momentum (k) and spin (σ) states.

$$H_{ld} = J_{ld} \sum_n p_n S_n \cdot \sigma_d(R_n) \tag{2.16}$$

This Hamiltonian represents the d-hole coupling to the localised moment. The numerical parameter p_n allows this exchange to proceed only if R_n is a localised-impurity site. $\sigma_d(R_n)$ is the d-hole spin-density at the impurity site, represented in terms of Pauli matrices σ, as

$$\sigma_d(R_n) = 1/N. \sum_{kq} \sum_{\alpha\beta} C^*_{d\,k+q\,\alpha} \cdot C_{dk\beta} \sigma_{\alpha\beta} \exp(iq.R_n) \tag{2.17}$$

The terms related to resistive processes include the symmetry-breaking impurity potential and the usual conduction electron-impurity exchange. In addition, the s-electrons now interact with the d-holes in the Pd matrix. A brief description follows:

$$H_{sd} = U \sum_{n} \sigma_d(R_n).\sigma_s(R_n) \tag{2.18}$$

where $\sigma_s(R_n)$ has a representation and an interpretation similar to that for $\sigma_d(R_n)$. The operators involved, however now refer to the conduction electrons. The Hamiltonian represents the conduction-electron - d-hole exchange.

$$H_{ls} = J_{ls} \sum_{n} p_n S_n.\sigma_s(R_n) \tag{2.19}$$

This is the usual exchange between local impurity spin and the conduction electrons.

$$H_{HF} = V \sum_{\substack{kq \\ a}} \sum_{n} p_n C_{s\,k+q\,a}.C_{s\,k\,a} \exp(iq.R_n) \tag{2.20}$$

In second-quantised notation, this is the Hartree-Fock potential due to the presence of the impurity.

The total Hamiltonian then consists of these above-listed terms in addition to the conduction electron kinetic energy.

The model treats the scattering problem in two separate temperature domains -- a low-temperature domain where the dynamical states of the impurity spins are described in terms of spin-waves excited in the coupled impurity-host d-band system and, a high-temperature domain ($T \rightarrow T_c$) where the dynamics of the spin are better described in terms of an

effective-field picture. Expectation values $\langle S_z \rangle$ and $\langle S_z^2 \rangle$ for the impurity are obtained for the two temperature ranges, to be used later in the Yosida's result appropriately modified for a ferromagnetic system. The essential features of the result are the following:

a) At low temperatures the expectation values of S_z and S_z^2 vary as $T^{3/2}$.

b) In the mean-field limit, both expectation values show direct proportionality to $(T_c-T)/T_c$. However, while $\langle S_z \rangle$ vanishes at T_c, as expected, $\langle S_z^2 \rangle$ reduces to a constant value of $S(S+1)/3$.

The model then concerns itself with the problem of including the additional resistive mechanisms that arise due to the presence of the d-holes into the Yosida's result. For example, a negligible contribution to resistivity arises due to scattering of s-electrons from the polarisation of the Pd d-band by the impurity spin. Additionally, an s-electron can now scatter indirectly from an impurity spin through a preliminary scattering from an electron-hole pair which propogates in the matrix and subsequently scatters at an impurity site through the interaction H_{id}. Use of the conventional many-body techniques allows an 'effective exchange interaction', J_{eff}, to be defined between the conduction electrons and the impurity.

$$J_{eff} = J_{ls} + U\bar{\chi}_{pd} \cdot J_{ld} \tag{2.21}$$

Use of the effective exchange parameter in place of the usual J_{ls}, and substitution of the values for $\langle S_z \rangle$, $\langle S_z^2 \rangle$ in the Yosida's result, appropriately modified for a ferromagnetic system lead to the conclusion of the model.

At low-temperatures ($T \rightarrow 0$), the resistivity has the form given by,

$$\Delta\rho(T) = Ac + Bc^{-1/2} \cdot T^{3/2} \tag{2.22}$$

where

$$A = a\,(V^2 - J_{eff}^2)^2/(V^2 + J_{eff}^2) \tag{2.23}$$

and B has a more cumbersome expression though it depends basically on the same parameters as A. The interesting feature is that the $T^{3/2}$ dependence results from electron-magnon scattering. The random nature of the alloy modifies the spin-wave resistivity from T^2 to $T^{3/2}$.

At temperatures approaching the transition point, the magnetic resistivity should, according to this model, show a linear dependence on the fractional "distance" away from the Curie point, $(T_c - T)/T_c$.

$$\Delta\rho(T) = ac\,[A' - B'(T_c - T)/T_c] \tag{2.24}$$

where

$$A' = V^2 + J_{eff}^2 S(S+1) \tag{2.25}$$

and B' has a more complex form but it depends on the same quantities V, S and J_{eff}. Above the Curie point, the spin disorder is complete; the resistivity contribution remains unaltered above that point. The linear decrease in magnetic resistivity below the ordering temperature reflects an increasing degree of magnetic order in the alloy. The resistivity "knee" observed in ferromagnetic systems in a temperature range around the ordering temperature has a rather simple explanation in the Long and Turner model. The linear dependence of $\Delta\rho(0)$ on concentration agrees well with the experiments. Yet, the suggested linear dependence of the spin-disorder resistivity $\Delta\rho(T_c) - \Delta\rho(0)$ on concentration and, a $c^{-1/2}$-dependence of the coefficient of $T^{3/2}$ term in eqn.(2.22) is not supported experimentally. Long and Turner trace this failure to the mean-field assumption that the polarising field has a linear dependence on c.

The effect of an externally applied magnetic field H on the resistivity can be easily derived from Yosida's result [33]. The longitudinal magnetoresistance, defined as

$$\Delta\rho_m(H,T) = \rho_m(0,T) - \rho_m(H,T) \tag{2.26}$$

is predicted to be dependent upon the ratio H/T:

$$\Delta\rho_m(H,T) = ac\ \{J^2\langle S_z\rangle \tanh\ \delta/2 + 4V^2J^2\langle S_z\rangle^2/\{V^2+\ J^2[S(S+1)-\langle S_z\rangle \tanh\ \delta/2]\} \tag{2.27}$$

where, for convenience the ratio $g\mu_B H/kT$ has been abbreviated as δ.

2.2.3 The Magnetic Structures and Electrical Resistivity

A possible consequence of s-f exchange in rare-earth metals and some dilute alloys is the occurrence of periodically modulated magnetic structures. The incongruence, in general, of the modulation wave-vector Q with the reciprocal lattice vector K has interesting consequences. The periodic magnetic structure has its own "magnetic" reciprocal lattice superimposed on the "structural" reciprocal lattice. The former has its own Brillouin zone planes located half-way between the length Q of the "magnetic structure cell" prependicular to the direction of the wave-vector Q. At these boundaries, sometimes referred to as antiferromagnetic superzone boundaries, the electronic energies become discontinuous as a function of k. The Bragg reflection condition is then modified to

$$k - k' = K \pm Q \qquad (2.28)$$

in the reciprocal space. The condition simply reaffirms that additional points are present in the reciprocal space at $(K \pm Q)$. Due to the presence of additional Brillouin zones at $\pm Q/2$ {and at $(K \pm Q)/2$, in general}, the conduction electron spectrum is modified in the vicinity of those zones if a mechanism through which the conduction electrons can "see" the magnetic structure exists. Quite obviously, a spin-dependent electronic exchange is such a mechanism. An energy gap of the order of the exchange strength appears in the conduction spectrum. Fig.(2.1) represents a case where $Q \parallel c$, so that along the k_z-axis in reciprocal space, the length of a magnetic cell is Q, with Brillouin zone boundaries at $\pm Q/2$. The energy spectrum $E(k_z)$ then has the periodicity Q. The dashed curve represents a repeat of $E(k_z)$ curve but centered at Q. The intersection with the original $E(k_z)$ curve appears at $Q/2$. The exchange interaction causes the intersection to be replaced by an energy gap at wave-vectors $k_z = \pm Q/2$ due to the fulfilment of the Bragg conditions at those values. The size of the gap is determined mainly by the exchange strength, and is temperature-dependent, vanishing gradually as the temperature is raised towards the Néel point.

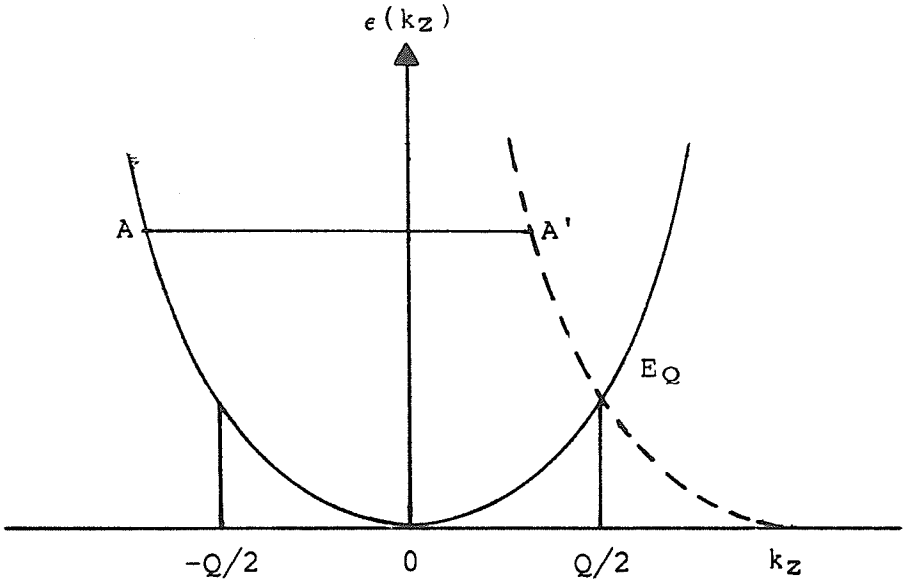

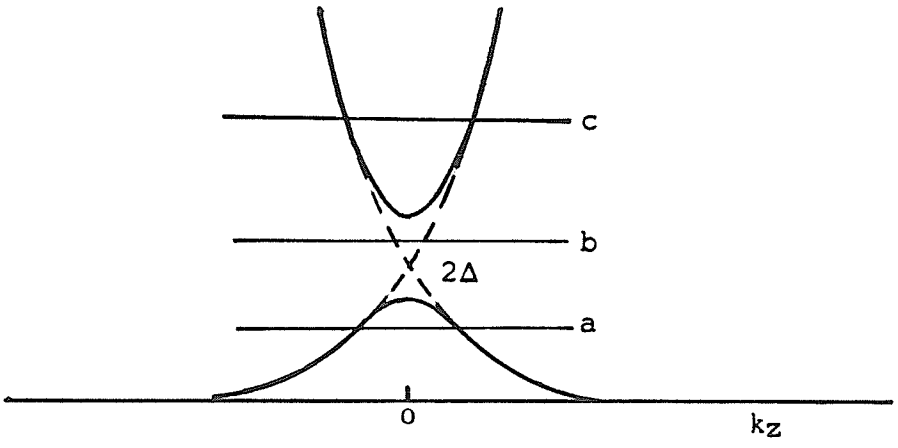

Fig.(2.1): (a) Modification of conduction electron spectrum due to magnetic zone boundaries at ±Q/2.

(b) Energy gaps (width 2Δ) appear at ±Q/2. [19]

During the transition through the Néel point, boundaries of the zones related to the newly established periodic magnetic structure appear in the Fermi neighbourhood. The associated energy gaps, of the order of the s-f exchange constant, in the spectrum of the conduction electrons make large areas of the previous Fermi surface unavailable to them. So long as the thermal energy is adequate to raise the electrons across the energy gap to available states the resistivity does not rise. With falling temperature, however, a temperature-dependent rise occurs. As the temperature declines further, the initial magnetic order gets more and more firmly established; the collective fluctuations in it diminish and consequently, the resistivity component due to scattering of electrons from such fluctuations also decreases. The two processes together lead to a maximum in the resistivity. Maxima below the respective ordering temperatures in the resistivity of the higher concentration ($c \geq 6$ at.% Gd) PdGd samples are noted in the present study.

2.3 MAGNETIC PROPERTIES

Magnetic phase transitions form part of a class of phenomena observed in a variety of physical systems, which can be characterised by singularities or divergences in the second-order derivatives of an appropriate thermodynamic potential near the transition point. These are variously termed as 'continuous transitions' or 'second-order' critical

phenomena. These phenomena are cooperative processes because they involve a multitude of mutually interacting particles. A macroscopic approach to the description of the state of magnetic systems is embodied in the mean-field theories where the magnetic milieu of an elementary spin is described in terms of an average effective field due to the rest. Although such theories do allow for the existence of phase transtions and critical phenomena, their quantitative description of the divergence of the susceptibility (a second-order derivative of the Gibb's free energy with respect to H) or of the convergence of magnetisation (<u>not</u> a second-order derivative of G) to zero in the critical region is at variance with experimental evidence. Following Guggenheim, power laws may be more suited to deal with the processes in the critical region. Critical phenomena are characterised by an increase of microscopic fluctuations of the order parameter (magnetisation) and the correlation lengths in the neighbourhood of the critical point; the mean-field theories completely neglect such fluctuations and hence are inadequate to deal with them. Thus, for T close to T_c in a ferromagnet, several critical exponents can be defined:

$$\chi(t) \sim (-t)^{-\gamma'} \qquad T < T_c$$

$$\chi(t) \sim t^{-\gamma} \qquad T > T_c$$

$$M(t) \sim t^{\beta} \qquad T < T_c$$

$$= 0 \qquad T \geq T_c$$

$$M(H) \sim H^{1/\delta} \qquad T = T_c$$

where $t=(T-T_c)/T_c$ is the reduced temperature; H is the internal field in the specimen (taking account of the demagnetising effects), χ and M are the susceptibility and magnetisation of the sample, respectively and γ, β and δ are the critical indices. Statistical models have been developed in an attempt to simulate the critical behaviour. The most studied models are the Ising and the Heisenberg models. They attempt to simulate the magnetic behaviour in terms of a regular lattice of magnetic atoms with pair-wise, short-ranged exchange interactions. Whereas the former model simplifies the problem by assuming a high degree of uniaxial anisotropy, the latter assumes a completely isotropic exchange. The forms of the exchange terms in the two cases are

$$H = \sum_i \sum_j J_{ij} S_i^z . S_j^z \qquad \text{(Ising)}$$

$$H = \sum_i \sum_j J_{ij} \vec{S}_i . \vec{S}_j \qquad \text{(Heisenberg)} \qquad (2.29)$$

With these interactions as the starting point, each model obtains a set of critical exponent values. The two sets thus obtained differ from each other [Table 2.1]. As indicated by the table, the critical exponents are sensitive to the dimensionality of the lattice. In the present work, PdGd may be considered a three-dimensional system of randomly

distributed spins. Also listed in the table are the common experimentally determined values of the critical indices for ferromagnetic systems. Agreement of these with the Ising and Heisenberg calculations is much better than with the classical theories (i.e. those based upon well-established thermodynamic principles).

TABLE (2.1)

Theoretical values of some critical exponents [34-37]

Model	Exponent			
	α	β	γ	δ
Classical	0	0.5	1	3
2D- Ising	0	0.125	1.75	15
3D- Ising	0.125	0.312	1.25	5
3D- Heisenberg	-0.13	0.38	1.37	4.45
3D- Disordered	-1	0.5	2	5
Ferromagnetic systems	< 0.16	0.33	1.33	4.1

An extensive list of critical exponents, defined for each thermodynamic function can be found in the book by Stanley [37]. Using thermodynamics, several inequalities amongst them have been established. Efforts have been directed at verifying them both theoretically (using the values for

critical indices calculated in various models) and experimentally. Many of the inequalities seem to be satisfied as equalities provided experimental errors in the determination of the indices are accounted for. No theoretical proofs for the equalities exist. In the absence of these, it cannot be said as to how many indices are needed for a complete description of the critical phenomena.

To justify the equalities relating the various critical exponents a useful idea is that of scaling although it is based on a theoretically unproven hypothesis. It yields an equation of state for the magnetic system which can be compared against experiment. It defines power-law indices for all quantities of interest in a magnetic system and yields relations amongst these exponents similar to the inequalities mentioned earlier but with the difference that the latter are validated as equalities. Widom's equality [38]

$$\gamma' = \beta (\delta - 1) \tag{2.30}$$

is the most relevant in the present study because at least two of the indices in the equality are obtainable through the susceptibility measurements alone.

2.3.1 Scaling Hypothesis

To introduce the scaling ideas, Gibb's free energy G(t,H) near a critical point serves as a useful thermodynamic potential. An unproven assumption that G(t,H) is a generalised, homogeneous function is made. Mathematically, it means that

$$G(\lambda^a t, \lambda^b H) = \lambda\, G(t,H) \tag{2.31}$$

Immediately, an equation of state follows from the fact that magnetisation M is given by

$$M = -(\partial G/\partial H)_t$$

and can be expressed as

$$M(t,H) = \lambda^{b-1}\, M(\lambda^a t, \lambda^b H) \tag{2.32}$$

This equation furnishes the various magnetic critical exponents in terms of the unknown constants 'a' and 'b'.

$$\beta = (1-b)/a$$

$$\gamma' = \gamma = (2b-1)/a$$

$$\delta = b/(1-b) \tag{2.33}$$

Widom's equality [eqn.(2.30)] follows as a corollary. A consequence of the scaling theory is the symmetry of the

critical indices about T_c. For this reason γ' and γ are not differentiated above.

A calculation of δ on the basis of measurements on magnetisation in field require a prior knowledge of T_c according to the power law $M(0,H) \sim h^{1/\delta}$. The estimates are therefore, dependent on the accuracy of T_c. This is an uncomfortable situation. In the scaling theory it is possible to define δ in a way independent of Curie temperature estimate. Such a definition is more suited to the experimental conditions. First, by choosing the parameter λ such that $\lambda = t^{-1/a}$ the equation of state [eqn.(2.32)] can be re-written with the help of eqns.(2.33) as

$$M(t,H) = t^{\beta} M(H/t^{\gamma+\beta}) \qquad (2.34)$$

Since the measurements in this work have been on susceptibility rather than on magnetisation, a more appropriate form of the equation of state is

$$\chi(t,H) = H^{-\gamma/\gamma+\beta} F(H/t^{\gamma+\beta}) \qquad (2.35)$$

In the critical region, $\chi(t,0)$ must diverge. Physically, of course, the divergence is limited and manifests itself as a critical peak. The peak is seen even in an applied magnetic field, although it is suppressed and shifted to a higher

temperature. The peak position at any field H can be obtained from eqn.(2.35) by requiring that

$$(\delta\chi(t,H)/\delta t)_{t_p} = 0 \qquad (2.36)$$

The result is

$$t_p \sim H^{1/\gamma+\beta} \qquad (2.37)$$

This provides an additional means to check the scaling theory against the experiment. The value of the peak susceptibility is then obtained from the equation of state [eqn.(2.35)].

$$\chi(t_p,H) \sim H^{(1/\delta - 1)} \qquad (2.38)$$

The scaling hypothesis is thus adapted to the experimental situation.

Kadanoff et al [39] provide a microscopic plausibility argument which justifies intuitively the scaling ideas introduced through the generalised, homogeneous Gibb's function approach earlier. It proceeds as follows:

A system of spins, considered as an Ising lattice, has two alternate ways of description. One [fig.(2.2)] is to treat the lattice (with spacing a_0) as being composed of individual spins σ arranged on the lattice sites assuming

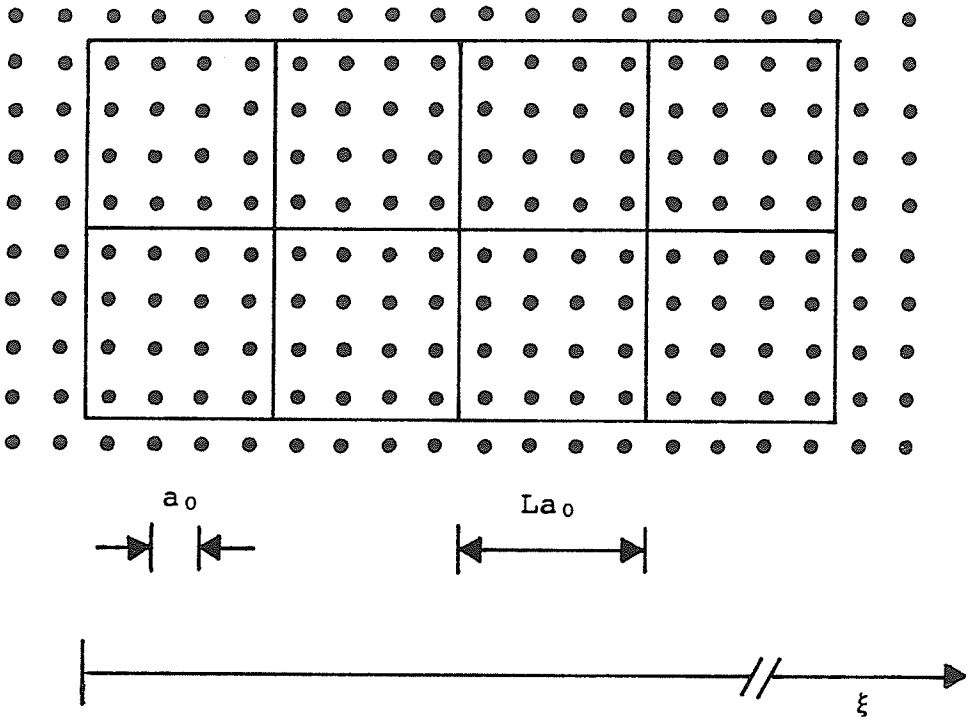

Fig.(2.2): Kadanoff site- and cell-pictures.
ξ is the correlation length.

that only the nearest-neighbours interact through the z-components of the spins. The Gibb's free energy per spin G(t,H) is written as a function of parameters t and H which describe the crucial effects of spin-spin interactions and the spin-external field interactions respectively. The second way [fig.(2.2)] is to divide the lattice into cells of side L, associate a moment μ with each cell, and then to consider it as a collection of mutually interacting cells. The difference between the two is merely one of scales. The Gibb's free-energy may now need to be written in terms of new parameters $\tilde{t}$, $\tilde{h}$. Because they describe the inter-cell interactions and cell-external field interactions respectively, they may depend upon the size L of the cell.

In the critical region, the pairwise interactions between spins (or cells) remain short-ranged whereas fluctuations in the order parameter grow in range, indicating large correlation lengths. When the magnetic spin-spin (or cell-cell) correlations span a large region of the lattice the details of the spin-spin (or cell-cell) interactions are rendered unimportant. Hence, the cell description and the site description must be completely equivalent under those conditions. This indicates that $\tilde{h}$ and $\tilde{t}$ must be proportional to H and t respectively. As mentioned before, $\tilde{h}$ and $\tilde{t}$ may depend upon the cell size. The assumption is that

$$\tilde{h} = L^{x}H$$

$$\tilde{t} = L^{y}t$$

where x and y are two new parameters.

By calculating the variation of the Gibb's free energy for an infintesimal variation of the magnetic field by using either the site or the cell description, Kadanoff relates the cell moment μ to the spin moment σ as

$$\sigma = L^{x-d}\mu \tag{2.39}$$

where d accounts for the dimensionality of the system. If H is independent of the position r of the spin (or the cell) the average $<\sigma>$ and $<\mu>$ for the same physical problem must be identical functions of the respective variables. Thus,

$$<\sigma> = F(t,H) = L^{x-d}\, F(L^{y}t, L^{x}H) \tag{2.40}$$

This leads immediately upon integration with respect to $\tilde{h}$ to the result which forms the basis of the scaling theory -- a homogeneous, generalised form for the Gibb's function.

$$G(L^{y}t,\ L^{x}H) = L^{d}\, G(t,H)$$

provided the restriction $1 << L << \xi/a_0$ is relaxed to allow all values of L. ξ measures the correlation length.

The reasonable assumption that at the critical point the fluctuations in the order parameter become so long-ranged

that they lose sensitivity to the details of the interatomic interactions and that the nature of these fluctuations depends only on the symmetries of the order parameter and the dimensionality of the problem also forms the basis for the 'universality hypothesis'. According to the latter all phase transitions of a given order occuring in physically different systems are identical; only, the variables describing the transition need to be renamed. Kadanoff has demonstrated that scaling follows from the hypothesis of universality in his formulation. It is possible to verify the scaling hypothesis in the current system PdGd from the susceptibility measurements performed. As discussed in Chapter V, scaling hypothesis appears to hold for the present PdGd system for, at least, the lower concentrations considered.

2.4 DISORDERED SYSTEMS AND MAGNETIC SUSCEPTIBILITY

Dilute random alloys such as the PdGd alloys currently under study possess a compositional disorder. The magnetic impurities are distributed statistically on the lattice (perhaps, with some short-range magnetic order, which subtracts from perfect randomness). The earlier treatments [40-42] of disordered magnetic alloys have used the molecular field approximation for an Ising model in which the spins interact through the RKKY interaction. The indirect coupling between randomly distributed spins leads to a distribution $P(h_i)$ of internal fields. Depending upon

the approach followed and the temperature range considered, $P(h_i)$ could be a Lorentzian or a Gaussian. Incorporating this distribution of internal fields into the Weiss mean-field theory produces a broad maximum in susceptibilty $\chi(T)$, the temperature at the peak being directly proportional to the impurity concentration. The approach obviously fails to account for a rather sharp cusp in the low-field a.c. susceptibility at a "freezing" temperature T_f observed experimentally [43] in some alloy systems. These are now known as "spin-glasses" , a term first coined by B.R. Coles with reference to the strange magnetic behaviour of AuCo system. The term often refers to a magnetic state where a spin-disorder has been "frozen" into the alloy such that there is no net magnetisation in the alloy, yet there are long time-correlations between spins on various lattice sites. Edwards and Anderson [44] proposed a novel mean-field theory based on the Heisenberg interaction Hamiltonian for a spin pair, in order to explain the spin-glass susceptibility cusp. Soon afterwards followed an Ising model based calculation of susceptibility, incorporating the long-range RKKY interactions. It adopted essentially the same approach as that of Edwards and Anderson. This model due to Sherrington and Kirkpatrick [45], found a magnetic phase diagram which predicts three possible types of magnetic state for the random spin system -- spin-glass, ferromagnetic and paramagnetic -- depending upon the detailed characterstics of the interaction. It predicts

phase transitions between these ground states as the interaction characterstics were changed, through a change of impurity concentration, for example. The SK model calculations in the ferromagnetic regime of concentration have been applied recently to a study of the systematics of the experimentally observed susceptibility peaks in the vicinity of a phase transition in PdMn by Roshko and Williams [46]. The calculations reproduce the behaviour with changing applied fields in fair detail. A comparison of the model calculations with scaling predictions leads to the conclusion that as the internal field distribution broadens, the region of validity of the scaling predictions diminishes. Deviations from ideal scaling are observable in PdGd alloys at higher concentrations.

In the following sections a review of the Edwards-Anderson and Sherrington-Kirkpatrick approaches to the problem of susceptibility peaks in disordered Heisenberg or Ising systems is presented.

2.4.1 The Edwards-Anderson Model

An actual RKKY spin-glass system is modelled in terms of randomly distributed, classically described magnetic dipoles which, nevertheless, interact in a Heisenberg-like manner. The interaction Hamiltonian is

$$H = - \sum_{ij} J_{ij} S_i . S_j \qquad (2.41)$$

where J_{ij} is a pair-wise interaction parameter. Standard statistical-mechanical procedure is applied to write down the free-energy, and hence the magnetic response of the system. However, the random site distribution of magnetic atoms on the lattice is simulated by conceiving of a lattice of magnetic atoms with randomly distributed "exchange" bonds J_{ij}. Thus with each J_{ij} there is a probability factor ϵ_{ij} associated. This probability of having a particular interaction J_{ij} operative is included in the definition of J_{ij} itself. The true free-energy must therefore be averaged over all possible distributions $\{J_{ij}\}$ that occur with a probability $P\{J_{ij}\}$. If $F(J_{ij})$ is the free-energy for a given distribution the ensemble free-energy is

$$F(T,H) = \int F(J_{ij}) . P(J_{ij}) \, dJ_{ij} \qquad (2.42)$$

where

$$F(J_{ij}) = -kT \log \{Tr \exp(-\beta H)\} \qquad (2.43)$$

$P(J_{ij})$ is assumed to be a Gaussian for simplicity.

$$P(J_{ij}) = \exp[-J_{ij}^2/2J^2\rho_0^2] \tag{2.44}$$

where ρ_0 is the density of occupation and $J^2 = \sum_{ij} J_{ij}^2$. The configuration average of $F(J_{ij})$ as indicated in eqn.(2.42) involves an average of the logarithm of the partition function (this averaging procedure is valid only for quenched random systems where the position of a spin is not free to change as the temperature is allowed to vary). A replica-technique is invoked here to perform the average most easily. It is based on the following limit:

$$\log z = \lim_{n \to o} (z^n - 1)/n \tag{2.45}$$

where

$$z^n = \Pi\, z_\alpha = \mathrm{Tr.}\, \exp\, [-\beta \sum_{\alpha=1}^{n} H^\alpha) \tag{2.46}$$

The averaging thus needs to be done on the n th power of z. The index α may be interpreted as refering to the α th "replica" which is identical to the given disordered system. On substituting the Hamiltonian [eqn.(2.41)] into eqn.(2.46) and on performing the configuration average over the distribution $P(J_{ij})$, the following expression is obtained:

$$\langle z^n \rangle = \mathrm{Tr} \quad \exp \left[3\rho/2\rho_0 \sum_{ij} \sum_{\alpha\beta} S_i^{\alpha}.S_j^{\alpha} \; S_i^{\beta}.S_j^{\beta} \right] \tag{2.47}$$

where

$$\rho/\rho_0 = 2J^2/3(kT)^2 \tag{2.48}$$

The configuration average above, therefore, allows the argument of the exponential to be interpreted as a fictitious effective Hamiltonian with interacting replicas of a homogeneous system. The trace in eqn.(2.47) involves an integration over spin variables and is evaluated using a variational procedure. Once evaluated, the free energy can also be calculated. A replica correlation factor $q_{\alpha\beta} = \langle S_i^{\alpha}.S_j^{\beta} \rangle$ appears in the expression for free energy. It is assumed that a single correlation factor $q_{\alpha\beta} = q_n$ describes the disordered state, such that

$$\lim_{n \to o} q_n = q$$

The parameter q, which symbolises the spin-correlation between Gibb's-like replicas of the disordered system, plays the role of an order parameter. Through its relation to the free energy, it also appears in the thermodynamics of the system. In particular, its relation to the magnetic susceptibility is

$$\chi = \chi_o(1 - q)$$

$$\chi_0 = a/T \tag{2.49}$$

Above the spin-glass temperature, T_{sg}, the "frozen" correlations are broken; hence q = 0 and the susceptibility behaves as that for a paramagnet. Just below the "freezing" temperature the order parameter q, as obtained by Edwards and Anderson, is

$$q(T) = -1/2 \; [\; 1 - (T_{sg}/T)^2] \tag{2.50}$$

Therefore, from equations (2.49) and (2.50)

$$\chi = \chi_0 - O(T_{sg}-T)^2 \tag{2.51}$$

Eqn.(2.51) together with the fact that $\chi = \chi_0$ for $T > T_{sg}$ represents an asymmetric cusp in the susceptibility at the "freezing" temperature

$$T_{sg}^2 = 2J^2/9k_B^2 \tag{2.52}$$

The asymmetry is considered to be the effect of a simple mean-field approximation and may be removed in better approximations. Experimentally, the cusps are observed to be symmetric about the "freezing" temperature.

Although the EA solution turned out to possess certain unphysical instabilities (such as a negative entropy at low temperatures), the new replica technique to deal with disordered systems and with the order parameter q useful for their description, were two extremely valuable outcomes of the EA attempt. More advanced replica techniques have since been used [47,48].

2.4.2 The Sherrington-Kirkpatrick Model

Sherrington and Kirkpatrick (referred to as SK) solved a disordered Ising model with long-range interactions [45] of the RKKY type. In this model the interactions of a given spin are not limited to the nearest neighbours only. The spin interacts with all other spins but with a Gaussian distribution of interaction strengths J_{ij}, similar to that assumed in the EA model.

$$P(J_{ij}) = [2\pi J^2]^{-1/2} \exp [-(J_{ij} - J_0)^2/2J^2] \tag{2.53}$$

J_0 and J are scaled

$$J_0 = \tilde{J}_0/N \quad , \quad J = \tilde{J}/N^{1/2} \tag{2.54}$$

so that $\tilde{J}_0$ and $\tilde{J}$ are intensive variables. This is a useful procedure because the model works in the thermo-dynamic limit, $N \to \infty$. The configuration averaging over J_{ij}'s leads to

$$\langle z^n \rangle = \mathrm{Tr}_a \exp \{ \sum_{i \neq j} [\beta J_0/2 \sum_{a=1}^{n} S_i^a S_j^a + (\beta \tilde{J})^2/4 \sum_{a\beta} S_i^a S_j^a S_i^\beta S_j^\beta] \} \tag{2.55}$$

The trace here is evaluated by the method of steepest descents. The thermodynamic limit is taken before the $n \to 0$ limit in the replica solution. An expression for the free energy, along with the self-consistency equations for the magnetisation $m(T) = \langle\langle S_i \rangle_T \rangle_J$ and the spin-glass parameter $q(T) = \langle\langle S_i \rangle_T^2 \rangle_J$ are obtained.

$$q = (2\pi)^{-1/2} \int dz \exp(-z^2/2) \tanh^2 \nu(z)$$

$$m = (2\pi)^{-1/2} \int dz \exp(-z^2/2) \tanh \nu(z) \tag{2.56}$$

where,

$$\nu(z) = \beta [\tilde{J} q^{1/2} z + J_0 m] \tag{2.57}$$

The nature of the magnetic state of the disordered alloy is determined by the values of q and m. A non-vanishing magnetisation m and the spin-glass parameter q indicate ferromagnetism. With a non-zero q and m = 0, the state is a spin-glass one. Depending upon the ratio $\tilde{J}_0/\tilde{J}$ one or the other type of magnetic state sets in as the temperature is reduced below the greater of $\tilde{J}_0$ or $\tilde{J}$. A magnetic phase diagram is obtained using eqns.(2.56) and (2.57) in terms of the dimensionless parameters $kT/\tilde{J}$ and $\tilde{J}_0/\tilde{J}$ [as shown in

fig.(2.3)]. The SK model exhibits magnetic phase transitions. A ferromagnet to spin-glass phase transition is predicted by the model. The SG phase boundary is defined either by eqns.(2.56) and (2.57) with $q \neq 0$, $m \to 0$ or by a divergence of the calculated susceptibility. To calculate $\chi(T)$, the Hamitonian contains an added field term which appears subsequently in the arguments of the tanh functions in eqns.(2.56). The result is

$$\chi(T) = [1 - q(T)] \,/\, [kT - \tilde{J}_0\{1 - q(T)\}]$$

$$= \chi^{(0)}/(1 - \tilde{J}_0\chi^{(0)}) \qquad (2.58)$$

where $\chi^{(0)}$ is the result for $\tilde{J}_0 = 0$. However, once again this simplest solution due to SK is similar to the mean-field solution of the EA model and shares its instabilities when applied in the spin-glass region. These deficiencies have been removed to some extent by the improved replica techniques. However, one important conclusion relates to non-ergodicity of the SK model. The spin-glass order parameter has unequal time and ensemble averages. Further, the model overlooks the short-range spin-correlations which exist in critical systems, and hence cannot be expected to describe phase transtions accurately.

The effect of fluctuations in disordered magnets can be quite simply considered within the framework of an effective field theory under various approximation schemes. Southern

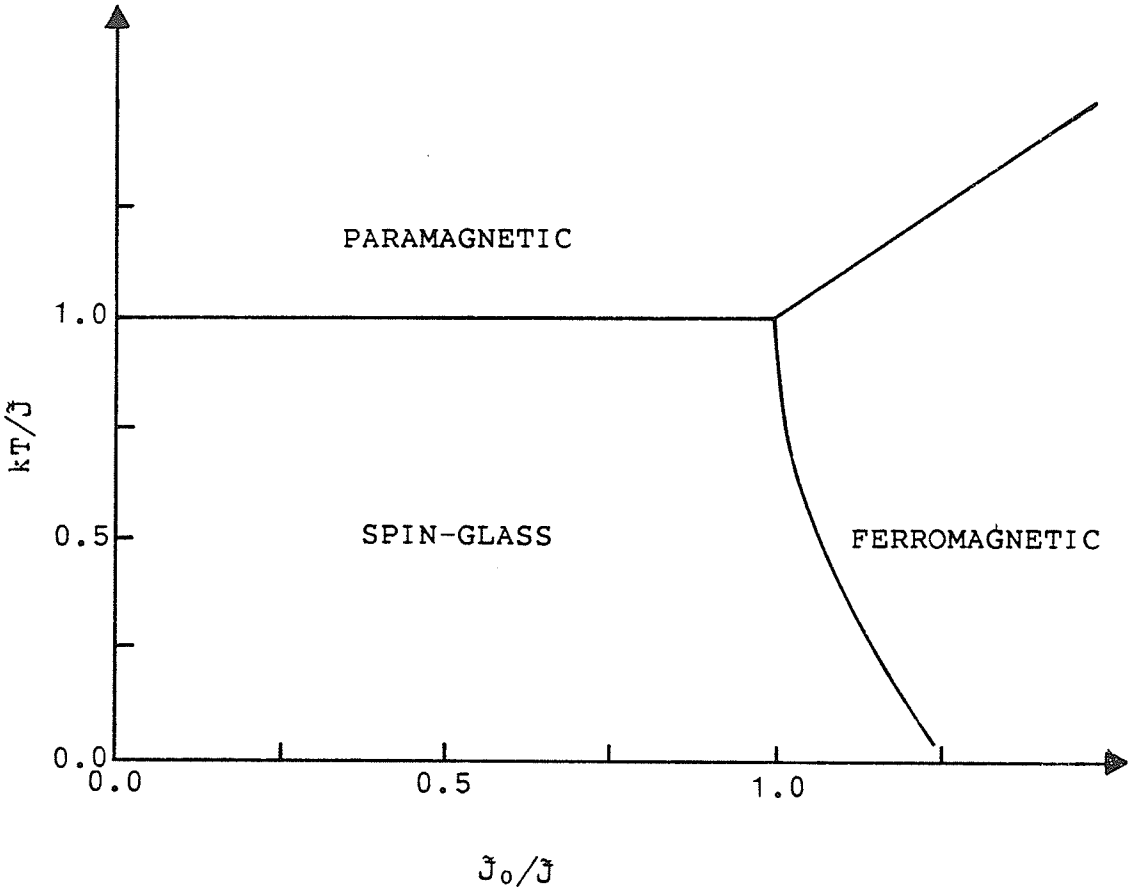

Fig.(2.3): Phase diagram in the Sherrington-Kirkpatrick model [ ].

[49] has summarised the approximation techniques used for the purpose. He also demonstrates that it is possible within an effective-field picture to arrive at the SK order parameter equations for m and q. He uses an Ising model with a random distribution of exchange bonds between spins to simulate the spatial disorder. A Gaussian distribution of bonds needs to be assumed. This effective-field approach has the advantage that the spurious low-temperature behaviour due to the use of replica techniques for the SK model may be avoided.

Roshko and Williams [46] applied a generalisation of this effective-field approach (with an arbitrary spin Ising model) to study numerically the results of an SK-like model in the ferromagnetic regime. A comparison with the experimental data on ferromagnetic PdMn alloys and with the scaling predictions was also made. They found the qualitative features of the data to be reproducible in considerable detail. The generalised equations for the order parameters $m = \langle\langle S_i\rangle_T\rangle_J$ and $q = \langle\langle S_i\rangle_T^2\rangle_J$ are

$$m = (2\pi)^{-1/2} \int dz \exp(-z^2/2)\, S.B_S[\beta S(\tilde{J}_0 m + \tilde{J} q^{1/2} z + h)]$$

$$q = (2\pi)^{-1/2} \int dz \exp(-z^2/2)\, S^2 B_S^2[\beta S(\tilde{J}_0 m + \tilde{J} q^{1/2} z + h)] \qquad (2.59)$$

For S = 1/2 these are identical to the corresponding SK equations. Numerical solution of these equations with a Gauss-Legendre quadrature in conjunction with Newton's method yields a ferromagnetic ground state for

$\tilde{J}_0/\tilde{J} \geq 1.25$

A comparison with the scaling theory was quite useful in that it substantiated its predictions that the ferro-paramagnetic transition peak decreases in height and moves up in temperature as the applied field increases, for pure ferromagnets ($\tilde{J}_0/\tilde{J} \rightarrow \infty$). The power-law predictions of the scaling theory are followed with uniquely defined critical indices. The values of these indices were, expectedly those predicted by the usual mean-field theory.

However, if the presence of competing interactions broadens the effective field distribution, the calculations showed that the "apparent" value of the critical index δ, obtained by fitting a single power law over the whole range of frequently used experimental field and temperature ranges decreases. A reduction in the range of fit brings back the indices to the values expected for the m.f. theory. Data on PdMn alloys show similar behaviour [50a b,51]. The effect of an increasing competition between ferromagnetic and anti-ferromagnetic spin interactions is thus found to lead to a reduction in the range of validity of scaling. Intuitively, such a result should be justifiable in the Kadanoff picture of scaling. He considered large correlated regions that exist near a phase transition due to the presence of critical fluctuations to be equivalently describable on different scales and showed how this concept led to scaling.

If two competing kinds of fluctuation are present this equivalence of the description of the system on any scale smaller than the correlated dimensions may not be valid. Scaling predictions would thus not be expected to hold. The present data on PdGd, appear to indicate no substantial competition between opposing interactions.

Chapter III

REVIEW

3.1 PURE PALLADIUM

Palladium metal is of specific interest among transition metals for its peculiar electronic structure. In metallic state, there is a hybridisation of the full 4d-states with the empty 5s-states; as a result 0.36 holes/atom are generated in the d-band and a compensating 5s-band is formed [fig.(3.1)]. The 5s electrons are "light" compared to the narrow d-band electrons. The former are thus largely responsible for conduction processes and the latter for the magnetic properties of Palladium. Because the conduction band is formed through an itinerancy of the d electrons, the Fermi level lies within the narrow d-band. The result is a high density of states at the Fermi surface. This has consequences both for the electrical and magnetic properties of the metal.

Palladium has been known to exhibit a T^2-dependence of resistivity at low temperatures. The specific heat and the resistivity data [52] point to a non-magnetic origin of this term. The s-band to d-band scattering induced by electron-electron interactions, which manifest themselves as either the charge-density oscillations of the Baber mechanism [53] or the spin-density fluctuations in the Palladium d-band

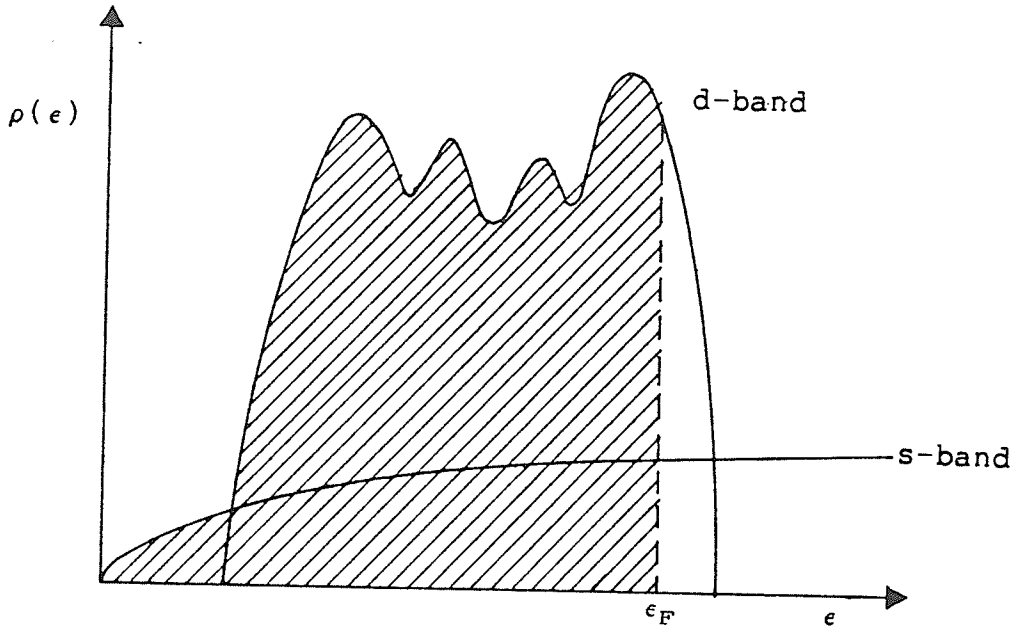

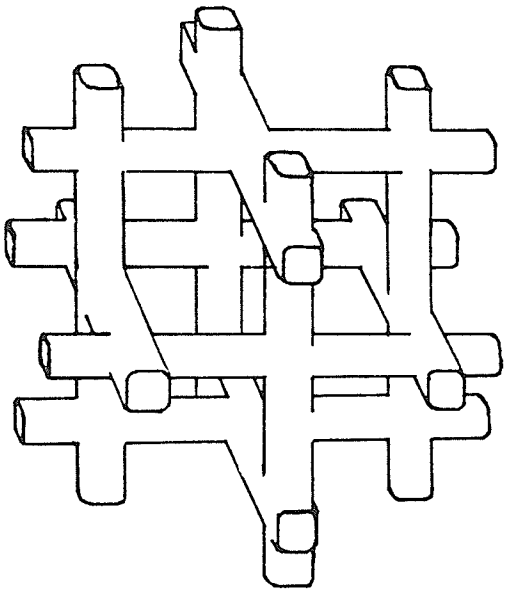

Fig.(3.1): Schematic representation of the band structure of pure Palladium and the associated Fermi surface.

[54-56] are believed to be the cause of this T^2-behaviour. A high d-band density of states at the Fermi surface favours a unidirectional interband scattering. The phonon-induced interband scattering also has its share in resistivity but it is much less effective than electron-electron scattering at low temperatures.

The high paramagnetic susceptibility and the specific heat are also manifestations of a large density of states at the Fermi level. Mueller et al [12] and Anderson [13] calculated the value for the latter to be 1.14 states per unit energy per spin direction per atom. The high susceptibility of Palladium qualifies it to be referred to as an incipient ferromagnet. The usual expression for Pauli susceptibility

$$\chi_0 = 2\mu_B^2 \rho(\epsilon_f) \qquad (3.1)$$

is not sufficient to describe the magnitude of χ_0 even with the large value of $\rho(\epsilon_f)$ for Pd. Stoner considered the intra d-band electron-electron Coulomb correlations. He showed that the Pauli susceptibility is enhanced by what is known as the "Stoner enhancement factor":

$$\chi = \chi_0/[1 - \rho(\epsilon_f).I] \qquad (3.2)$$

where I is the electron exchange parameter and $\rho(\epsilon_f)$ is the density of states at ϵ_f. The Stoner factor $[1 - I.\rho(\epsilon_f)]^{-1}$ may be as large as 15 in Palladium [57].

Besides a large value, the susceptibility shows a strong temperature dependence with a maximum at 85 K. Several possible causes have been proposed. Neutron diffraction and specific heat experiments [58-60] have however, demonstrated an absence of any ferromagnetic ordering. The most accurate band structure calculations of Mueller et al and Anderson referred to earlier have not been able to quantitatively match the temperature variation of susceptibilty.

Nevertheless, it is the high value of susceptibility that makes Palladium a magnetically interesting host. Alloying it with a few tenths of an atomic percent of Cobalt or Iron is sufficient to produce a spontaneous moment at low temperatures [61,62]. The indirect interaction of the separated impurity ions through the RKKY polarisation of the Pd d-band due to s-d exchange, is ascribed to be the cause of a spontaneous moment. A similar behaviour is noted with Manganese substituted in Pd instead of Fe or Co. However, larger Mn concentrations are required. The behaviour of Mn in Pd is rather well understood as a result of a large volume of work carried out on the system [33,50a b, 63,64]. The PdMn system provides a nice reference for the study of the less commonly studied PdGd system because both Mn and Gd are S-state ions and are known to exhibit local moment

behaviour down to very low temperatures in dilute alloys with Palladium. Hence it is instructive to review the generally accepted and known facts about both the systems.

3.2 MANGANESE IN PALLADIUM

Starting from the earliest resistivity measurements by Sarachik and Shaltiel [65] and Williams and Loram [31b], a consensus has emerged that the PdMn system exhibits a variety of ordering behaviour [66] ranging from the paramagnetism of pure Palladium to the anti-ferromagnetism of Manganese. For lowest concentrations ($27 \leq c \leq 575$ ppm) PdMn is a spin glass because distant Mn impurities interact via the tails of the long-ranged RKKY polarisation [fig.(3.2)]. Ferromagnetism is observed for $0.1 \leq c \leq 2.5$ at.% Mn. This is due to the Mn-Mn indirect interactions through the exchange enhanced ferromagnetic sections of the RKKY polarisation. For $2.5 \leq c \leq 5.0$ at.% Mn, the possibility of direct nearest-neighbour anti-ferromagnetic Mn-Mn interaction increases. Frustation effects are noticeable in the decreasing magnitudes of the ordering temperatures as c increases above 2.5 at.% Mn [fig.(3.3)]. Above 5 at.% Mn, the direct antiferromagnetic Mn-Mn interactions are in full competition with the long-ranged ferromagnetic, indirect RKKY interactions. This results in a spin-glass state for the system. Mn concentrations above 25 at.% result in the formation of intermediate compounds. The RKKY polarisation of the Pd matrix around a Mn impurity

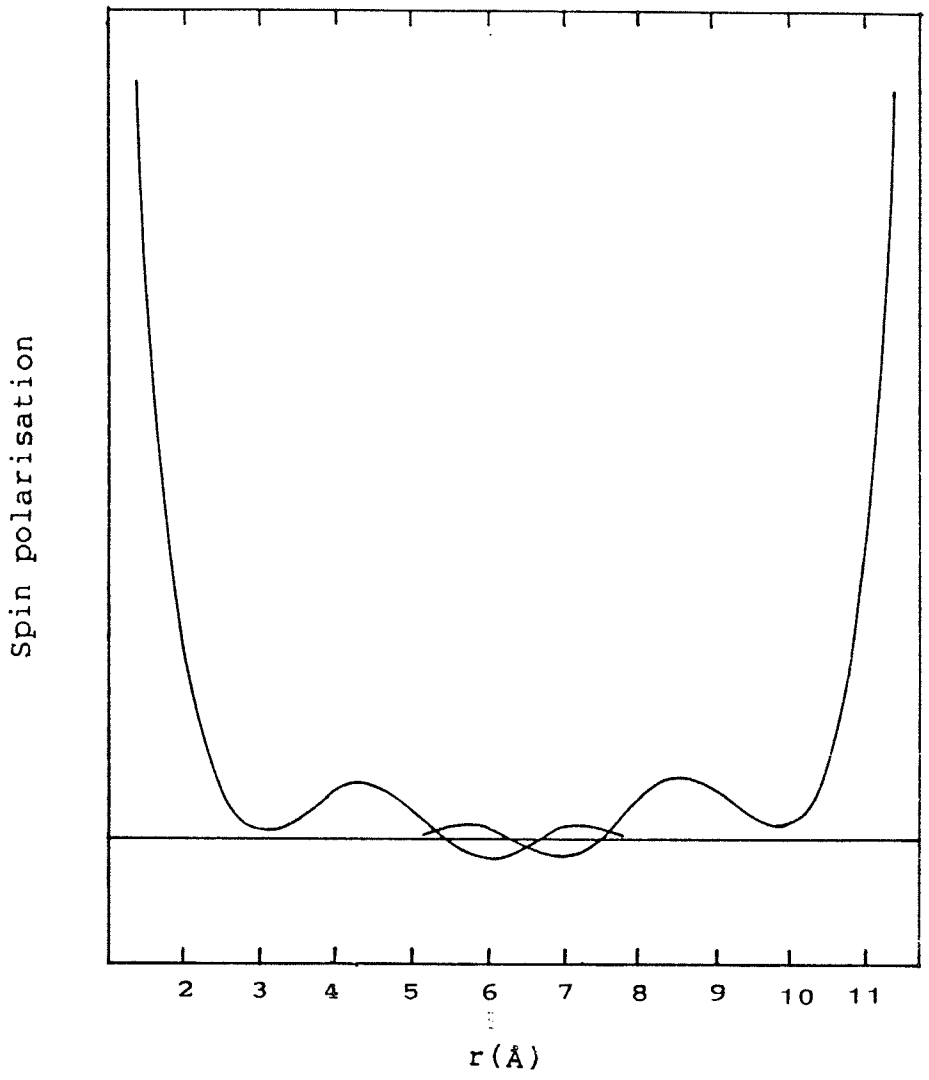

Fig.(3.2): Interaction between distant impurity moments through the tails of the associated RKKY polarisations; the situation depicted leads to a spin-glass state.

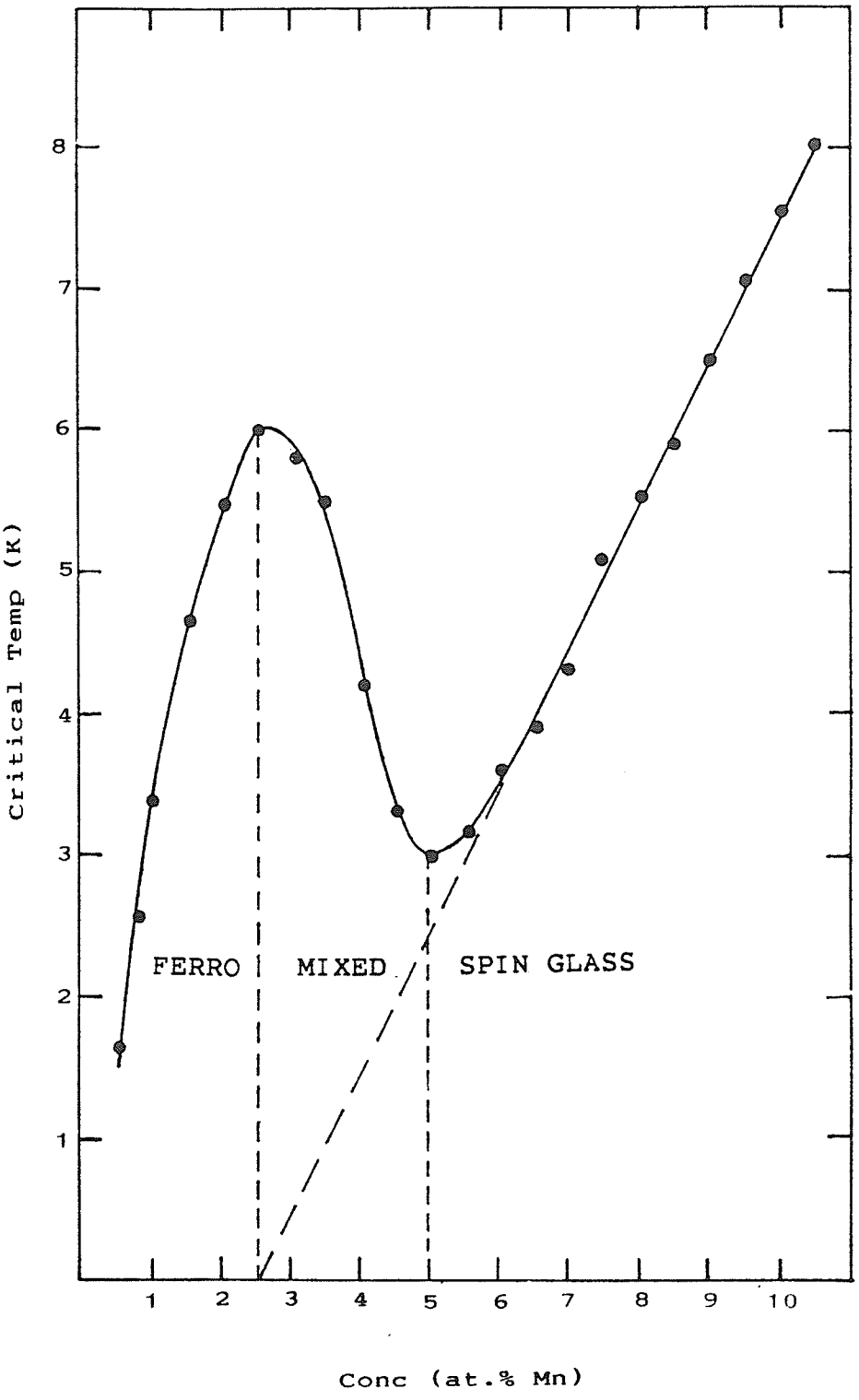

Fig.(3.3): Magnetic phase diagram for PdMn.

[66].

ion causes "giant" moments to be detected for the dissolved Mn ions. Star et al [67] measured a value $\mu = 7.5\mu_B$ in the ferromagnetic concentration regime. High field magnetisation measurements by Smit et al [68] indicated that "the giant moment of Mn in Pd gradually decreases from $7.7\mu_B$ for c = 0.48 % to $5.3\mu_B$ at c = 9.8 %". The latter is close to the free-ion value.

The conclusions about PdMn find support in measurements on specific heat [63,69], on magnetisation [70], on resistivity [31b] and on magnetoresistance [33]. The low-field a.c. susceptibility measurements [50a] further confirm the resistivity measurement results.

One question that has been debated is how best to represent a giant moment -- as a giant spin or as an enhanced g-factor. Two main approaches exist. Specific heat and magnetisation measurements are describable in terms of a normal ionic spin and an enhanced splitting factor for PdMn. The magnetoresistance measurements of Kleiman and Williams [33] indicate an enhancement of both the spin and the Landé factor. The latter approach has the advantage that it describes also the data for PdFe and PdCo more satisfactorily than the former, which needs to assume a distribution of g-values to obtain any good degree of fit to the observed data. The physical origin of such a distribution is unclear.

3.3 GADOLINIUM IN PALLADIUM

While ferro-magnetic behaviour has been noticed in PdGd alloys [71,72] no evidence of giant moments is found. On the contrary it has been debated whether Gd has a dwarf moment in Pd.

Crangle [73] reported the earliest observation of ferromagnetism in PdGd from his magnetisation measurements in fields upto 20 kOe for alloys upto 10 at.% Gd. The results indicated a lower than free-ion value of saturation magnetic moment per Gd-atom and a concentration dependence of that value. The moment per atom decreased with decreasing Gd concentration. The ferromagnetic transition temperatures were deduced using the Arrott plots of H/σ vs σ^2, and were found to be concentration-dependent as well. However, Sarachik and Shaltiel [65] found no evidence of a ferromagnetic transition through their resistivity measurements at temperatures about T_c deduced by Crangle. Bellarby and Crangle [71] found peaks in specific heat measurements on PdGd with c = 3, 5 and 7.7 at.% Gd which indicated magnetic phase transitions. The transition temperatures, however, were not in agreement with Crangle's first determination of T_c's. Later measurements by Cannella et al [72] on low-field a.c. susceptibility, $\chi(T)$ and on the electrical resistivity clearly indicated the presence of magnetic ordering below well-defined temperatures in alloys containing 2, 3 and 5 at.% Gd. The ordering temperature

estimates agreed with the specific heat peak temperatures of Bellarby and Crangle. The work of Zweers et al [74] on the specific heat of some well homogenised alloys between 1.2 K and 20 K also showed sharp-peaked magnetic contribution. The existence of ferro-magnetism in dilute PdGd alloys is, therefore, fairly well established.

The other question, that regarding the size of Gd moments in Pd, had first been addressed by Peter et al [75]. They detected a significant negative g-shift through EPR measurements. In a later publication [76] Shaltiel et al described more EPR measurements to study the coupling between valence electrons and magnetic impurity ions in metals of high paramagnetic susceptibility; the PdGd system is one of those studied. Again, a temperature-dependent negative g-shift is described. At the lowest temperatures the magnitude of shift is about 0.06. It increases gradually to about 0.12 at temperatures around 30 K and remains constant thereafter. Coles et al [77] advanced an explanation for the observations. They suggested a positive 5s-4f exchange but a negative 4d-5s hybridisation. Together, this would lead to a weak anti-ferromagnetic matrix polarisation around the Gd ion, explaining the weak negative g-shift. As mentioned previouly, Crangle's high-field (upto 20 kOe) magnetisation data had indicated a lower than free-ion value for the saturation moment of Gd in Pd. Guertin et al [78] extended the magnetisation measurements

to higher fields (upto 150 kOe) on alloys with $0.2 \leq c \leq 5$ at.% Gd. They concluded that the saturation moment was concentration independent and equal to the free-ion value within experimental error. Later high-field magnetisation (upto 210 kOe) and susceptibility experiments by Guertin et al [79] on 2 at.% Gd alloy again provided no conclusive evidence for dwarf moments. The magnetisation data in fields upto 215 kOe of Praddaude et al [80] placed a lower limit on the saturation Gd moments at the free-ion value. The upper bound is set by experimental uncertainties. It is currently believed, therefore, that no dwarf moments exist in PdGd. The moments are close to the free-ion value.

An attempt to empirically fit the slow trend to Gd-moment saturation even in high magnetic fields led Pradduade et al [80] to propose an interesting but ad hoc idea. The empirical formula designed to fit the observed data was

$$\sigma = aH/\sqrt{H(H + H_0)}.\ B\ \{\beta J\sqrt{H(H + H_0)}\} + \chi_{mat}H \qquad (3.3)$$

where

$$a = Ng\mu_B S$$

$$\beta = [g\mu_B(1 - \delta)/k\ ].1/(T - \theta)$$

The factor $(1 - \delta)$ accounts for s-f exchange interaction and θ is the paramagnetic Curie temperature that results from

Gd-Gd interactions. χ_{mat} has the interpretation of the Pd matrix susceptibility. The quantity $\sqrt{H.H_0}$ is related to the concept referred to above. It has the interpretation of a matrix polarisation dependent anisotropy field that acts perpendicular to the applied field. The suggested possible origins for the fields were either the direct Gd-Gd interactions and/or a negative s-f exchange interaction. The anisotorpy field is weakly concentration dependent. For 2 at.% Gd, the value estimated for the anisotropy field from the fit of the empirical relation [eqn.(3.3)] is about 17 kOe.

3.4 GADOLINIUM IN OTHER HOSTS

The literature has a substantial amount of data on the magnetic behaviour of alloys of Gd with other metals. A study of the alloys of Gd with Yttrium and with Scandium is particularly interesting insofar as it may help to clarify the observations on the PdGd alloys in the present work.

The resistivity data on YGd alloys ($c \leq 10$ at.% Gd) obtained by Sarkissian and Coles [23] has been interpreted in terms of an Overhauser type stabilisation of a spin-density wave in the d-band of the host through a localised exchange interaction with the impurity moment. The orientation of an impurity spin at a site then depends upon the position of the site relative to the phase of the spin-density wave. The YGd resistivity shown in fig.(3.4) first

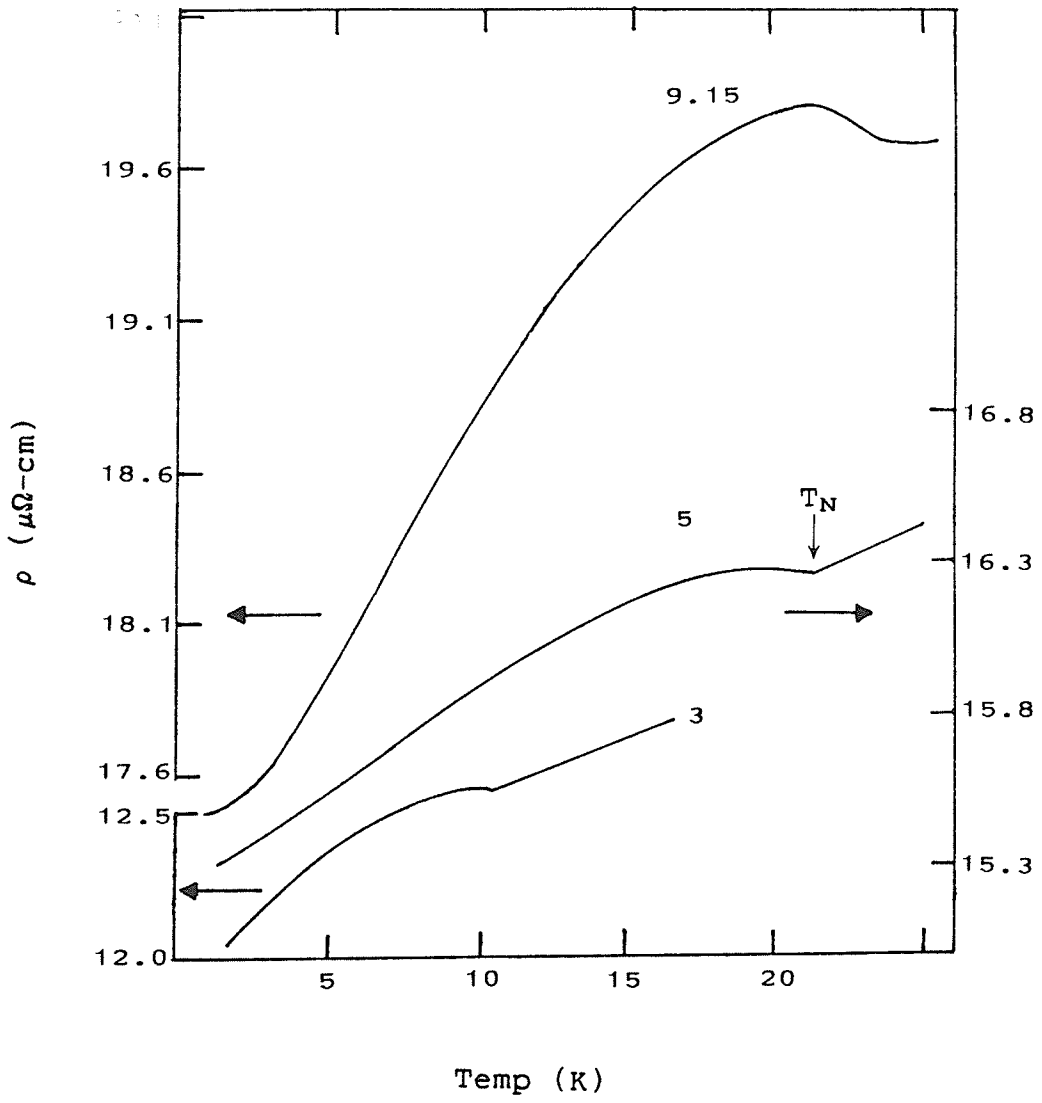

Fig.(3.4): Resistivity of YGd alloys with helically ordered states. [23]. The numbers marked represent the respective concentrations.

rises below the temperature marked T_N, passes through a maximum and then declines at lower temperatures. The same behaviour is also noted below the Néel temperature in Chromium and in some helically ordered rare-earths. The helically ordered YGd and ScGd alloys yield a susceptibility maximum at the ordering temperatures determined from the resistivity data. As the Gd concentration is reduced below a certain value (c = 2.6 at.% Gd) the characterstic behaviour of resistivity vanishes abruptly although the susceptibility maxima remain in the χ vs T curves. These more dilute alloys have a temperature dependence of resistivity characterstic of a spin-glass, i.e. have a $T^{3/2}$ variation at low-temperatures. This indicates that at 2.6 at.% Gd in Yttrium, there is magnetic transition from a helically ordered state to a spin-glass state. A much larger solute concentration is required to show any ordering at all in Scandium-based alloys but the results are similar. More recent single-crystal resistivity data on YGd system [81,82] has indicated that the helical order that sets in at 2.6 at.% Gd in Y is preserved in alloys with Gd concentrations as high as 68 at.% Gd. Beyond that a completely ferromagnetic order is seen. The transition alloy Y + 68 at.% Gd shows the presence of an antiferromagnetic state at an interval of 2 K below the temperature of ferromagnetic ordering. The resistivity curve therefore possesses an antiferromagnetic resistivity maximum preceding the ferromagnetic saturation of resistivity, as shown in fig.(3.5).

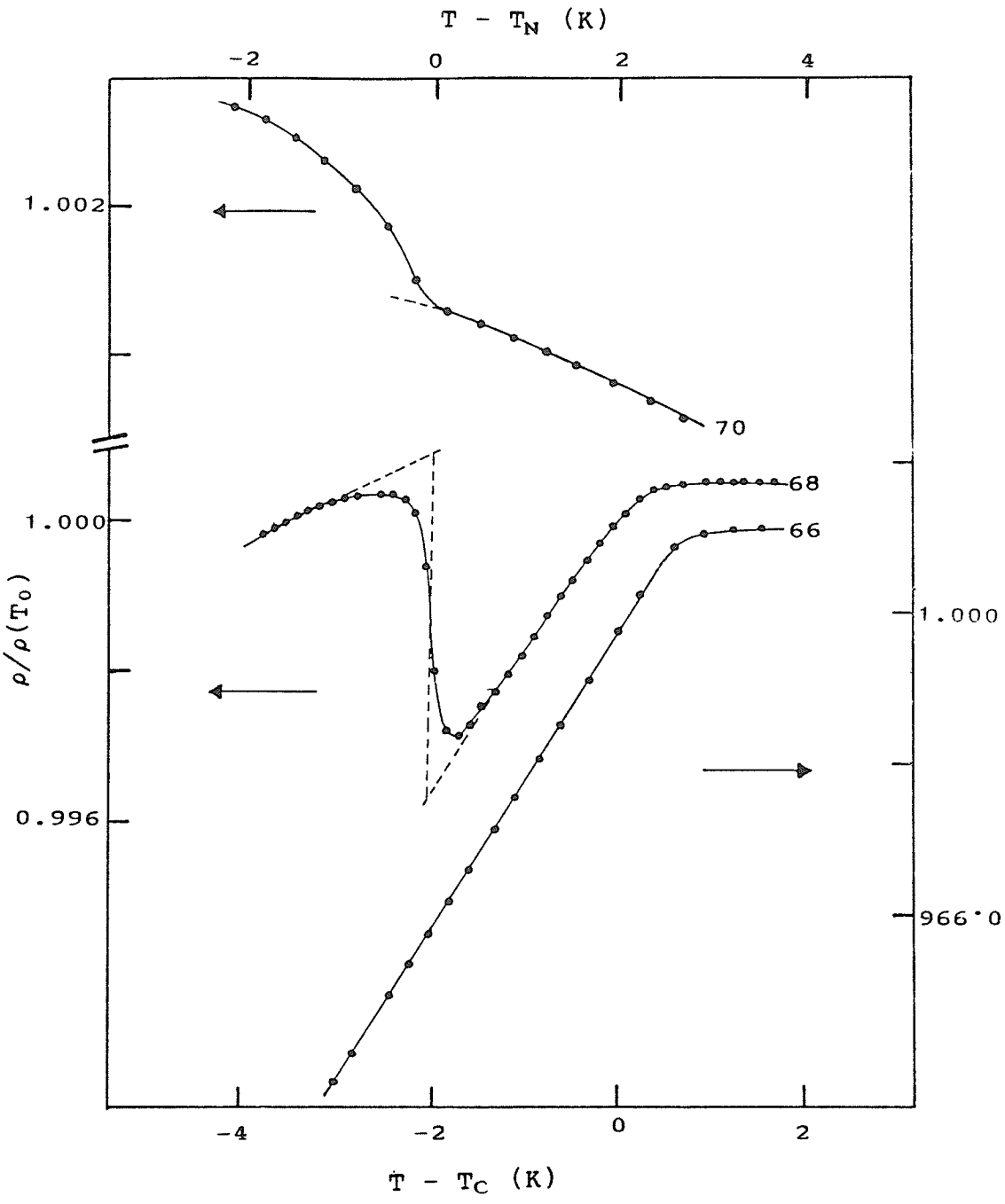

Fig.(3.5): Resistivity of YGd alloys with Gd-concentrations of 66, 68 and 70 at.%. The 68 at.% alloy shows a peak below the ferromagnetic ordering temperature. [81].

The existence of an antiferromagnetic component in the magnetic order in YGd and ScGd systems has an independent confirmation in the numerous neutron diffraction studies performed on these systems [83-85]. The rise in the resistivity of these alloys below the respective ordering temperatures is believed to be due to magnetic super-zone gap effect [86]. A similar rise in resistivity similar to that described in above systems has been noted in PdGd alloys (with $c \geq 7$) in the present study. If a similar mechanism is at work in this case, at least a qualitative explanation of the resistivity maxima is straightforward.

Chapter IV

EQUIPMENT AND EXPERIMENTAL PROCEDURES

4.1 SAMPLE PREPARATION

The PdGd alloy samples ranging in concentration from 2 at.% Gd to 10 at.% Gd (nominally) were prepared by dilution of a Pd + 10 at.% Gd master alloy. The latter was obtained by melting together appropriate quantities of pure specimens of Pd (99.999 % pure, supplied by Sigmund Cohn) and of Gadolinium (99.99 % pure, supplied by Rare Earth Products) in an inert Argon atmosphere on the water-cooled hearth of an arc-furnace. Gadolinium has a lower melting point (1356 C) compared to that of Palladium (1552 C). To minimise losses of Gd in the simultaneous melting process it was wrapped in a Pd foil and then melted. After the first melting the maximum possible uncertainty in the Gd concentration was estimated assuming that all losses could be attributed to evaporation of Gadolinium. If A_1 and A_2 are the atomic weights of Gd and Pd respectively and ω_1, ω_2 are the respective masses used in alloying, the uncertainty in the master alloy concentration is given by

$$\Delta x = x - \beta/(\alpha + \beta) \qquad (4.1)$$

where,

$$\alpha = A_1/A_2 = 1.478 \quad , \quad \beta = \omega_1/\omega_2$$

Here, x refers to fractional nominal concentration of the alloy. In the worst case scenario adopted above, the compositional uncertainty is expected not to exceed 0.1 at.% Gd. The importance of proper homogenisation, especially in PdGd alloys has been emphasised by other researchers [69]. The master alloy was therefore turned over and remelted 9 times in succession. The small weight losses were very likely a result of surface evaporation of Pd and hence should not affect the concentration significantly. The master alloy was cold-rolled, etched, wrapped in Tantalum foil and then annealed under vacuum (3×10^{-6} torr) for 48 hrs. at about 1000 C (as measured by a Pt + 13 at.% Rh vs Pt thermocouple) and then quenched under iced water. Dilution of the master alloy pieces with varying amounts of pure Pd was done to obtain lower concentration samples. The samples so obtained were cold-rolled, cut into pieces and annealed and quenched in a manner similar to that described above. The solubility limit of Gd in Pd is about 12 at.% at about 1100 C [87]. The higher concentration alloy samples -- 7 at.% to 10 at.% Gd -- were lowered into liquid Nitrogen for storage to retard the process of clustering and precipitation. The same samples were used to cut smaller pieces for both the a.c. susceptibility and the resistivity measurements.

The samples for susceptibility measurements were typically 1.250 x 0.105 x 0.010 cm^3 in dimensions. A single sample strip of this size was found inadequate to give sufficiently large susceptibility signals when external d.c. biasing fields were switched on. Hence a host of them stacked one on top of the other lengthwise, held together and separated by pieces of masking tape, were used.

The samples for the zero-field a.c. resistivity measurements were also thin rectangular strips about 10 cms long and approximately 0.1 cms wide.

Following completion of all measurements on the system of alloys, about two and a half years after the initial preparation a Pd + 8 at.% Gd sample was examined under a JEOL transmission electron microscope to check for the presence of ordered intermetallic Pd_3Gd compound phases. A circular disc of the sample was cut for this purpose from the resistivity specimen and polished with a solution of 50 % methanol, 33 % Nitric acid and 17 % Phosphoric acid in a twin-jet electro-polisher.

Another unpolished piece of the specimen was examined by an X-ray energy-dispersive technique to obtain rapid estimates of concentrations of Gd and other impurities in Pd using the EDAX hardware and software. The sample was cleaned on the surface with methanol and brushed with Freon. No other preparation was necessary.

4.2 MAGNETIC SUSCEPTIBILITY

A.c. susceptibility of PdGd samples was measured as a function of temperature in a number of externally applied d.c. fields. A description of the equipment and the measurement techniques follows.

4.2.1 The Cryostat Assembly

As shown in fig.(4.1) an inner double-walled glass dewar narrows down to a long tail at the bottom. It is meant to contain liquid Helium into which a sample probe could be lowered. An open liquid N_2 dewar surrounds the He dewar. Two sensing coils L_1 and L_2 whose purpose will be made clear later, are so arranged inside the liquid N_2 bath as to surround the tail section of the inner dewar. Two concentric external d.c field coils capable of producing fields up to 1 kG along the sample axis when connected in series, are also arranged within the liquid N_2 bath. Individually, the field coils could produce 215 Oe/amp and 186 Oe/amp respectively. Both are constructed with a 22 gauge enamelled Copper wire. The two sensing coils are constructed to be closely similar to each other. Each has 4000 turns of 35 gauge enamelled Copper wire wound on a nylon core-former. The measured inductances of the two coils are 205 mH and 202 mH respectively. The liquid N_2 bath serves two purposes -- it cools and maintains temperature uniformity in the field- and sensing coils, and, provides an extra thermal insulation for the liquid Helium

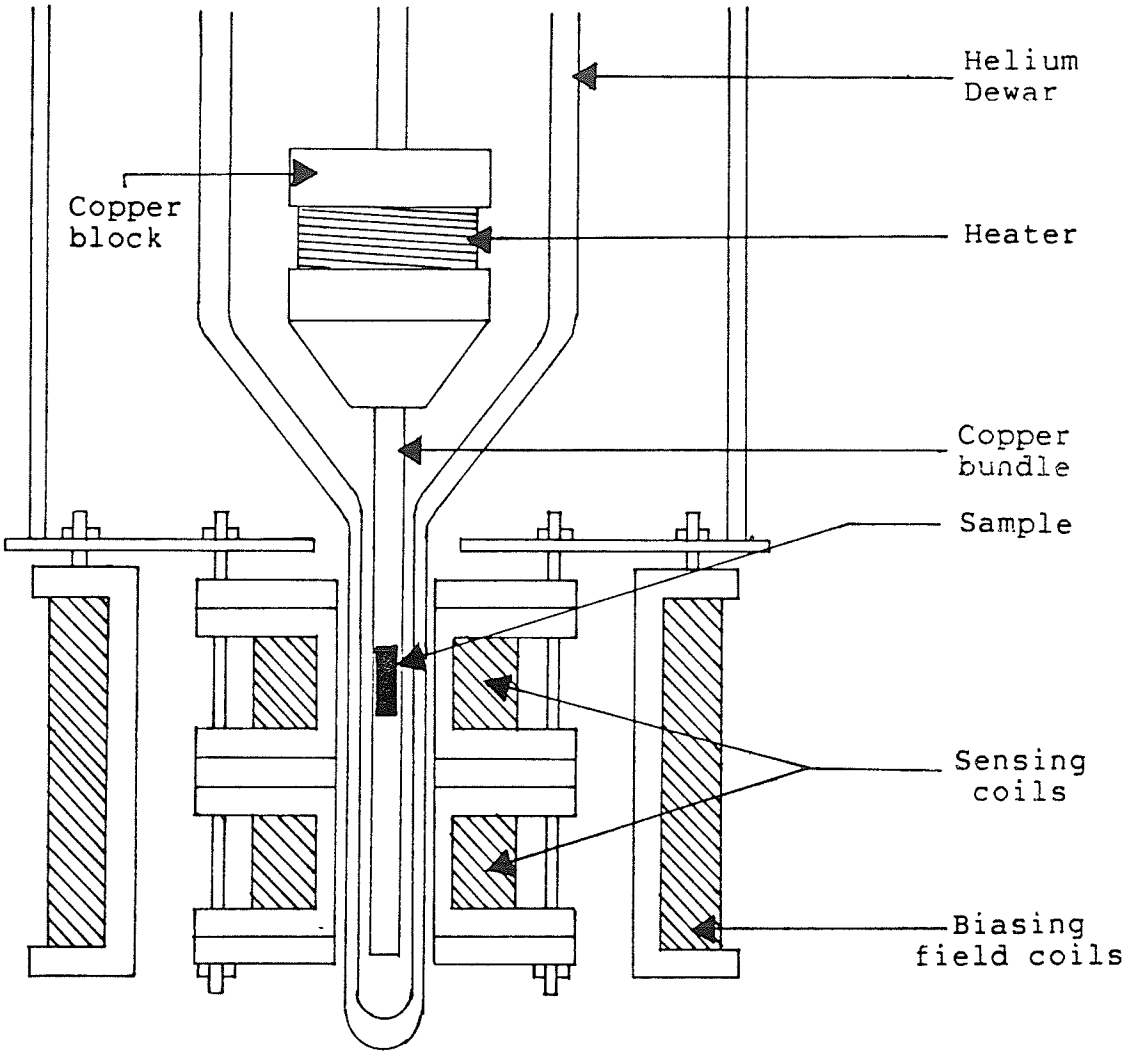

Fig.(4.1): Arrangement of sample-insert, sensing coils and d.c. biasing-field coils for measurement of a.c. susceptibility.

contained in the inner dewar. The degree of thermal contact between the inside of the He-dewar and the outer N_2 jacket can be varied by controlling the pressure in the vacuum space separating them.

The sample probe consists of a machined Cu-block wound with a nichrome heater wire (50 Ω) to which a long bundle of thin Copper wires is soft-soldered. The block-and-tail assembly is suspended at the end of a long, hollow stainless steel rod which, in turn, is anchored to a metal plate at the top of the cryostat assembly. The Cu-wire tail holds the sample in the narrow tail-section of the inner dewar. Provision is made so that the sample probe may be moved vertically to allow positioning of the sample at the centre of the sensing coil L_2. A Germanium resistance thermometer is embedded above the sample in the Cu-wire bundle, just outside the magnetic field region to avoid interference in temperature readings in the presence of externally applied magnetic fields. This constraint causes some difficulties in precise temperature measurements above 4.2 K (discussed later in Chapter V).

4.2.2 Temperature Control and Measurement

In the range of interest (i.e. between 2 K and 7 K approximately) two temperature control techniques were used. Below the boiling point of He, a continuous sweep of temperature was obtained by pumping on the Helium bath

surrounding the sample. A constant current back-off power supply was employed to compensate for the vertical component of the earth's field at the sample so as to always cool the sample in zero field. Data were taken as the system was allowed to gradually warm up at a controlled rate, both in zero and non-zero applied d.c. fields. The warm-up rate was controlled by a combination of pumping-speed regulation and use of the nichrome heater. Above the boiling point of He, the heat leak into the system was found to be sufficient to cause a gradual rise in temperature. The amount of heat leakage could be controlled by increasing or decreasing the thermal link beween the sample space and the N_2 bath around it. No heating currents through the nichrome heater were needed. The usual warm-up rates were approximately 1.5 K/hr.

The Ge-resistor, calibrated from 4.2 K to 100 K by Cryocal (city, Florida) and, from 1.4 K to 4.2 K in our laboratory against Helium vapour pressure, was the only thermometer needed for temperature measurement in the working range. The resistor was unaffected by thermal and magnetic cycling.

The temperature-measuring Ge-resistor output was fed into the X-channel of a Phillips PM8120 X-Y recorder. A back-off circuit had to be employed in the Ge-resistor output circuit (which fed the X-channel input) to bring the signal on scale. However, to measure the temperature the Ge-output

was monitored directly on a DANA 5330 (module 700) DVM capable of measuring voltages accurately to ± 1 μV. A current of 10 μA was supplied to the Ge-resistor by a constant current source and was periodically monitored through a DVM by measuring the voltage this current produced across a standard 1 kΩ resistor. The Germanium resistor circuit and the back-off control circuit are depicted in fig.(4.2).

4.2.3 Measurement of Susceptibility

Fig.(4.3) shows the essentials of a phase-locked magnetometer designed by I. Maartense [88] for the measurement of susceptibility. Two sensing coils L_1 and L_2 are arranged in two different resonant LC circuits which are set initially to have equal resonant frequencies

$$\omega = (L_1C_1)^{-1/2} = (L_2C_2)^{-1/2}$$

Circuit 2 is driven by the first resonator circuit. The measurement of susceptibility is based on the fact that if a magnetic sample is inserted into the coil L_2, the coil reactance and hence also the frequency of the second resonator circuit is altered , leading to a phase difference between the responses of the two LC-circuits. The phases may be compared in a phase detector which produces a correction voltage to restore the frequency ω_2 of the second LC-circuit to its initial value through a voltage-controlled reactance in that circuit. The control voltage required to

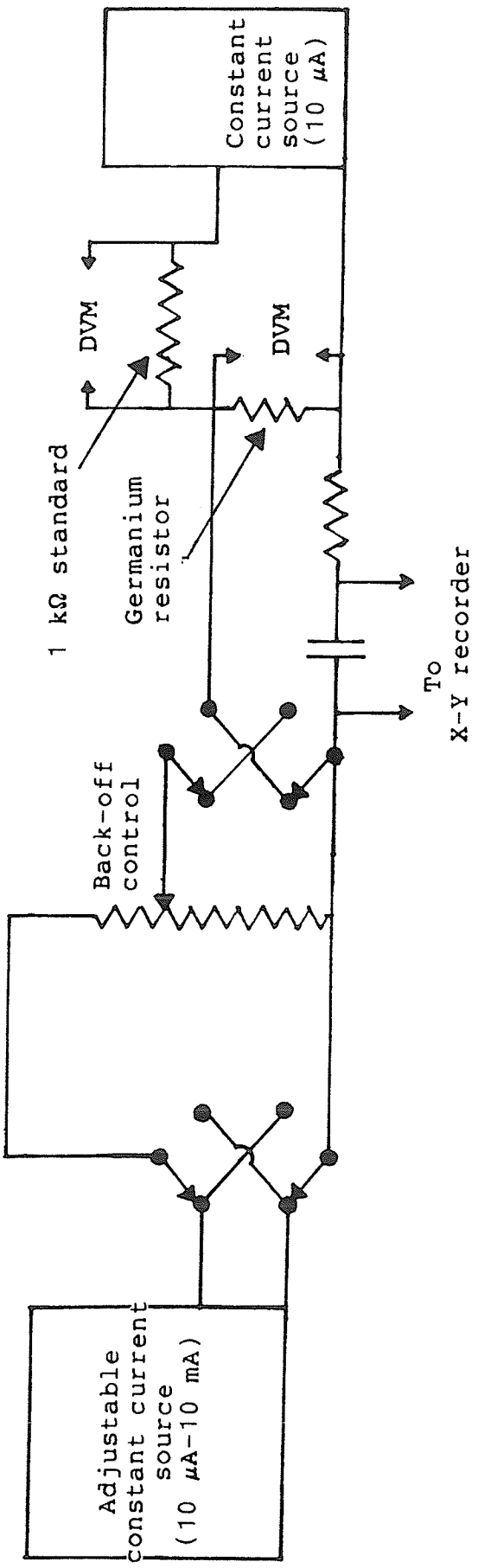

Fig.(4.2): Signal back-off and sample-temperature monitor circuit.

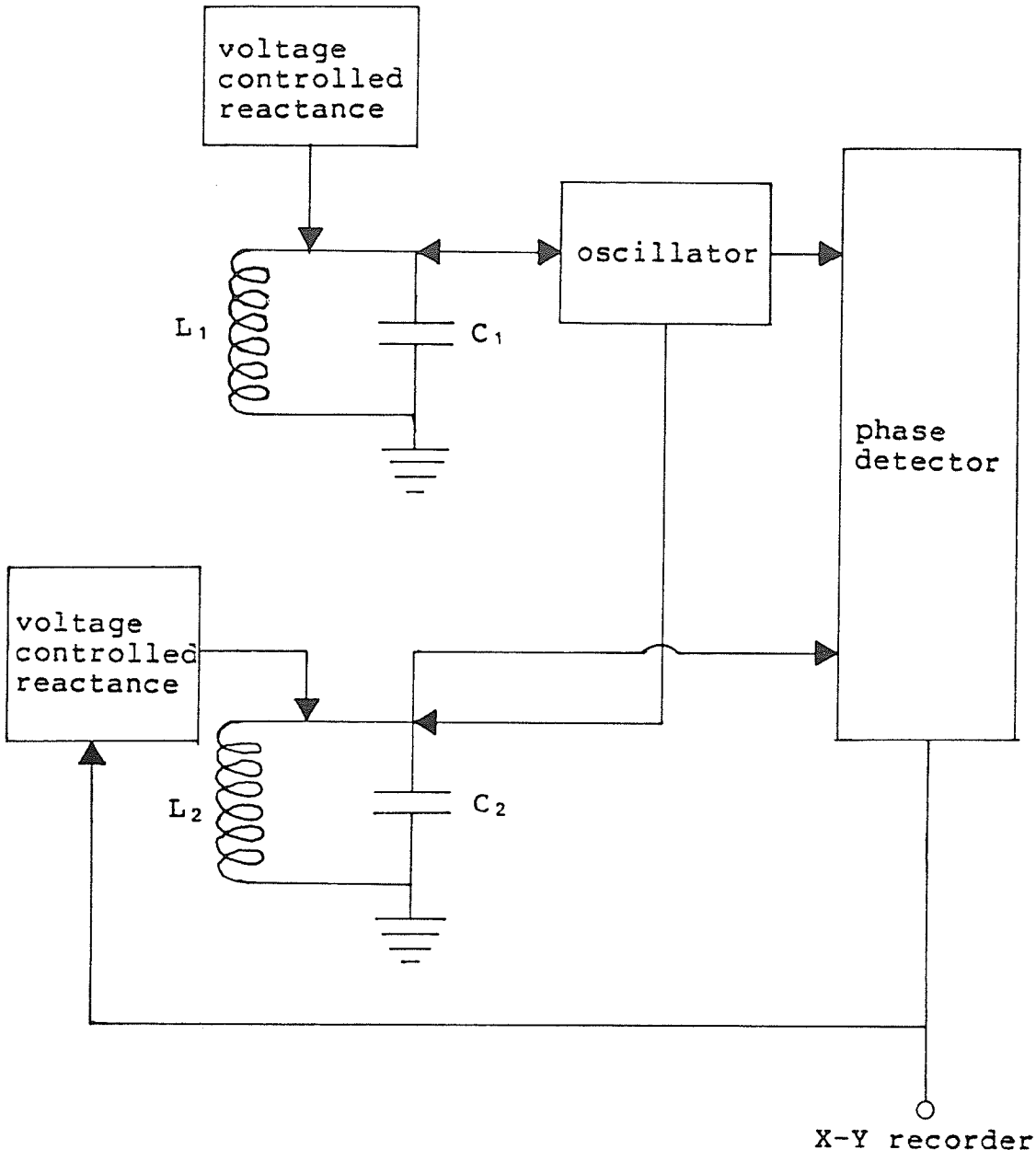

Fig.(4.3): Block diagram of Phase-locked magnetometer.

equalise the frequencies ω_2 and ω_1 is a measure of the magnetic susceptibility. The output of the phase detector circuit is connected to the Y-channel of an X-Y recorder in order to obtain a continuous record of susceptibility with changing sample temperature (the latter driving the X-channel of the recorder). The signal height in volts can be converted to susceptibility values provided a calibration factor is known. The calibration of the susceptibility has been described previously by Ho [66]. Gd_2O_3 is a paramagnet at 77 K. At any given temperature it's susceptibility is given by the Curie law. A comparision of the output signal from the phase detector circuit and the calculated susceptibility at a given temperature gives the calibration factor: 8.58×10^{-4} emu/V-Oe. It is expected to be good to within 10 %. This rather large uncertainty in absolute value is a result of varying filling factors for different samples in the sensing coil L_2 and of changing demagnetising fields for samples with different shapes. However, relative susceptibility for a given sample is probably accurate to 1 part in 10^4.

4.3 ELECTRICAL RESISTIVITY

Both the d.c. and a.c. resistivities of the PdGd samples were measured. While the former was measured at a fixed temperature (boiling point of Helium) the latter was measured as a function of temperature in the range 1.4 K to 10 K. The effect of an applied magnetic field (70 kG) on

the a.c. resistivity was also studied. The d.c. measurements employed the usual four-probe potentiometric method to obtain accurate resistivity values at 4.2 K. The low-frequency a.c. resistivity measurements, on the other hand, provided more accurate values for the changes in resistivity with changing temperature because they are not subject to the effects of thermal emf's. In conjunction therefore, accurate values of the electrical resistivity at all temperatures of interest could be obtained.

4.3.1 The Cryostat Assembly

The Helium dewar contains a 5 in. long, high-conductivity Copper sample chamber attached at the lower end of a much longer (41 inches) stainless steel tube which is suspended from a brass plate on the cryostat head assembly [fig.(4.4)]. Surrounding the sample chamber is the gas-thermometer bulb used for monitoring the temperature of the sample space. The two are in good thermal contact through the thin, high-conductivity Copper walls. Another coaxial cylinder outside the sample space separates it from the surrounding Helium bath. The enclosed region contains an exchange gas, usually Helium, whose pressure can be varied in order to regulate the degree of thermal linkage between the sample space and the surrounding Helium bath. Hence it may be referred to as the vacuum space or the isolation chamber. A very long tube connected to the interior of this chamber emerges at the top of the cryostat head and

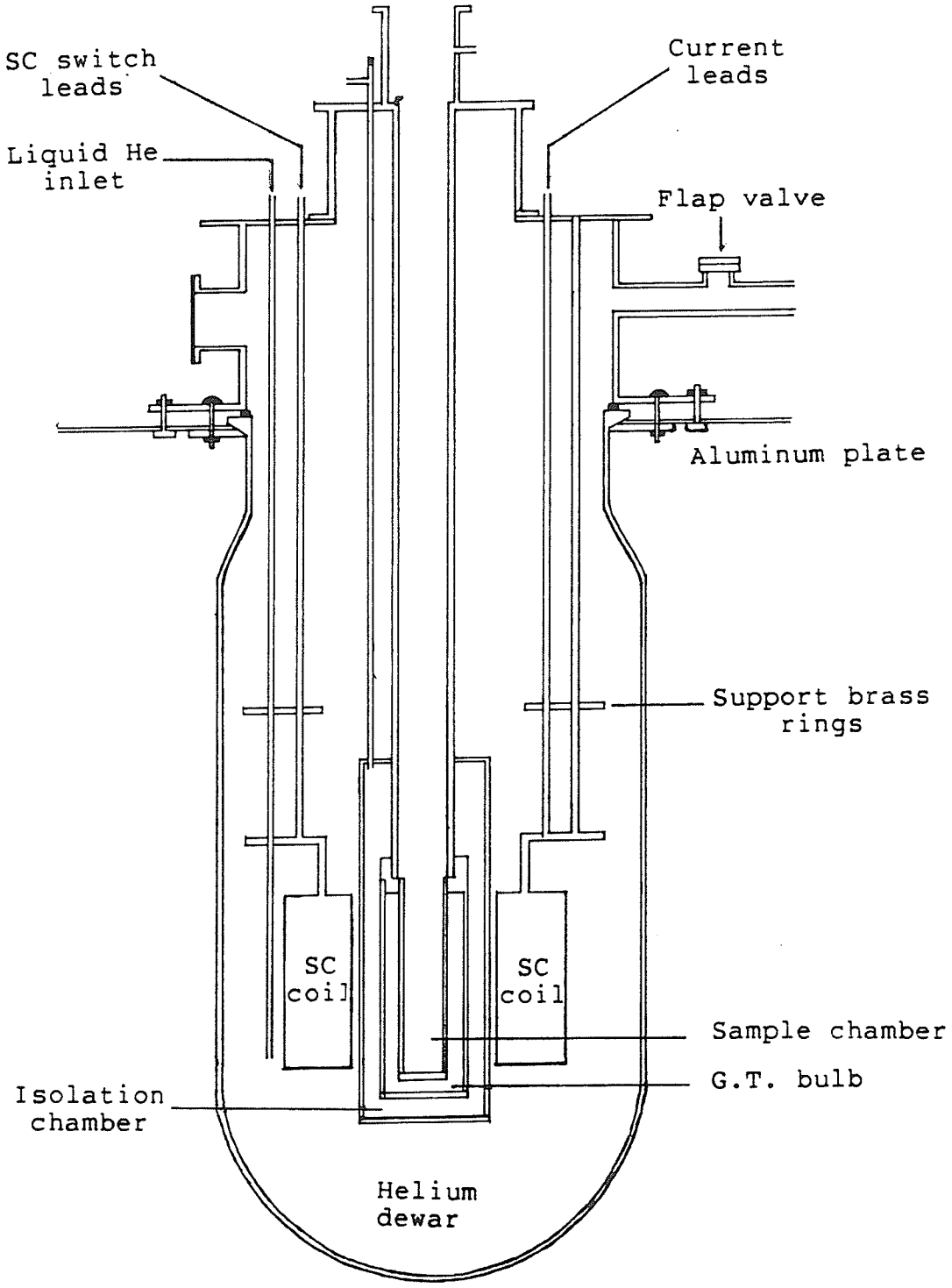

Fig.(4.4): Cryostat for resistivity measurements.

(Not drawn to scale.)

facilitates pressure control. A stainless steel needle tube runs down the length of this tube going via the vacuum-chamber into the gas-thermometer bulb. This tube conveys the pressure changes in the gas-thermometer to an external pressure gauge. The whole assembly of vacuum-chamber, sample space and bulb is placed inside a superconducting solenoid (SHE Manufacturing Co., U.S.A.). While in operation, the dewar housing this assembly contains liquid Helium. A thermal jacket is provided for the Helium dewar by liquid N_2 contained in a surrounding dewar [not shown in fig.(4.4)]. As stated above, the cryostat head is designed as an anchor for various inserts. Additionally, as shown in fig.(4.5), it also has the necessary attachments for liquid He transfer, magnet current supply, and for the control and measurement of pressure in the sample space, the vacuum space and the Helium space. A large Copper tube attached to the cryostat head, as shown, is connected to a 500 l/min. rotary pump for pumping the interior He-space in order to cool the system below the boiling point of liquid Helium. When this is not desired, the flap valve on the Copper tube serves as an emergency release for gaseous Helium, in case the superconducting magnet accidentally goes normal. The current supply to the magnet is carried down the length of two lead-coated brass tubes. A superconducting heater switch is located close to the magnet and its leads are anchored into a plug at the bottom plate of the cryostat head.

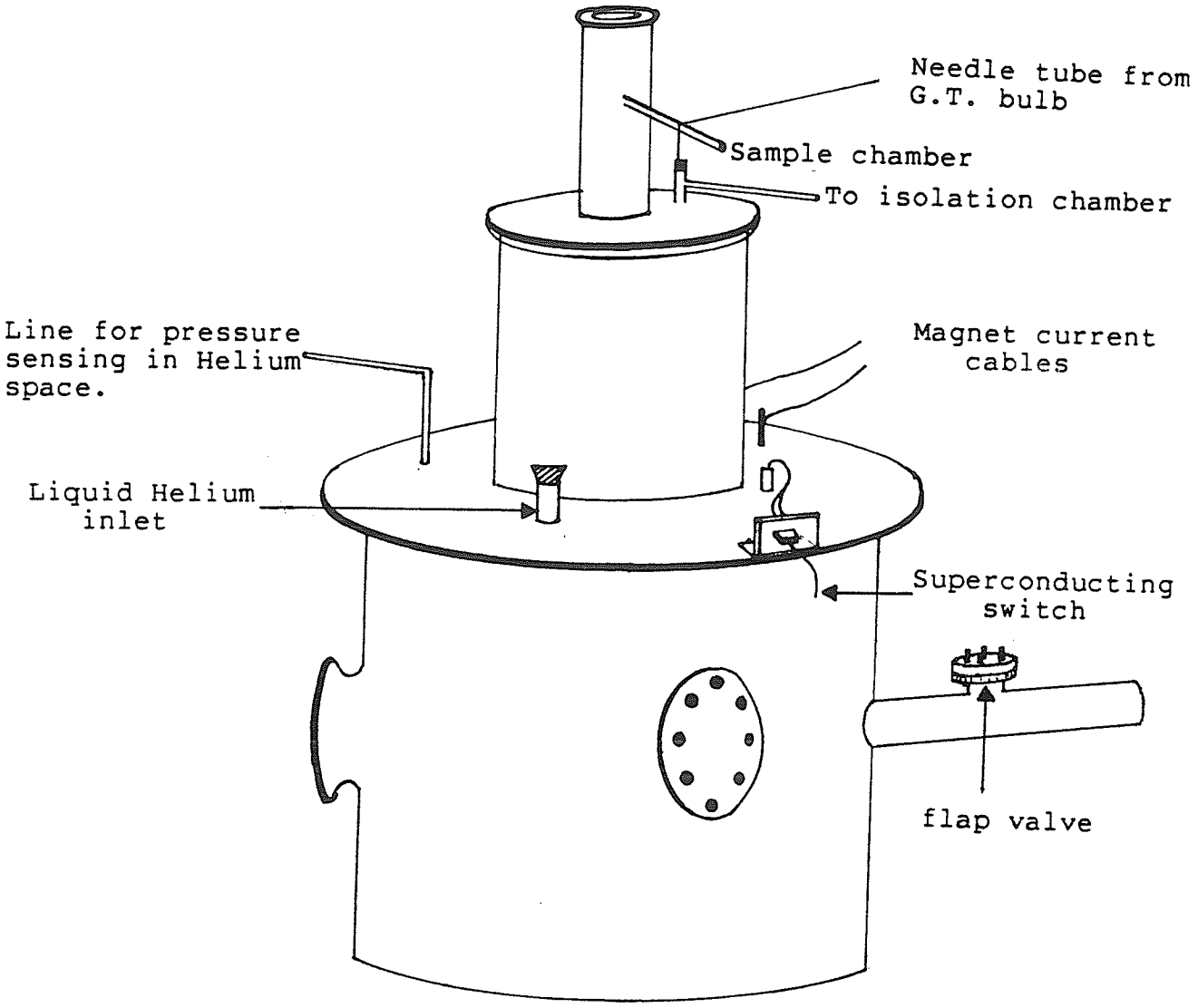

Fig.(4.5): Full perspective of cryostat head.

Both the cryostat head and the cryostat are supported by a thick Aluminum plate which is the top of a cage [not shown in fig.(4.4)] enclosed on four sides by plexiglass and plywood to ensure protection of the dewars and the magnet.

4.3.2 The Vacuum System

The flow-chart in fig.(4.6) shows the associated vaccum system. Three different pumping systems are contained in the chart. The first relates to the Helium space but its details are not indicated in the diagram because it is an isolated, mechanical pump-based system (pump 3) with a provision for control of the pumping speeds through three different-sized valves arranged "in parallel". The second has a mechanical pump (pumping capacity 100 l/min.) connected to the sample space. The pressure inside the sample space can be monitored through any of the two sets of manometers or gas-thermometer pressure gauges connected to it. For this purpose set 2 of the manometers was frequently used. Finally, the third system uses mechanical pump 2 and diffusion pump 2 with access to the vacuum-chamber. The pressure in this segment of the system can be monitored by the manometer set 2. The reference side of the gas-thermometer is accessible to both pump sets 1 and 2. The various pumping systems are inter-connected to provide greater versatility for the system.

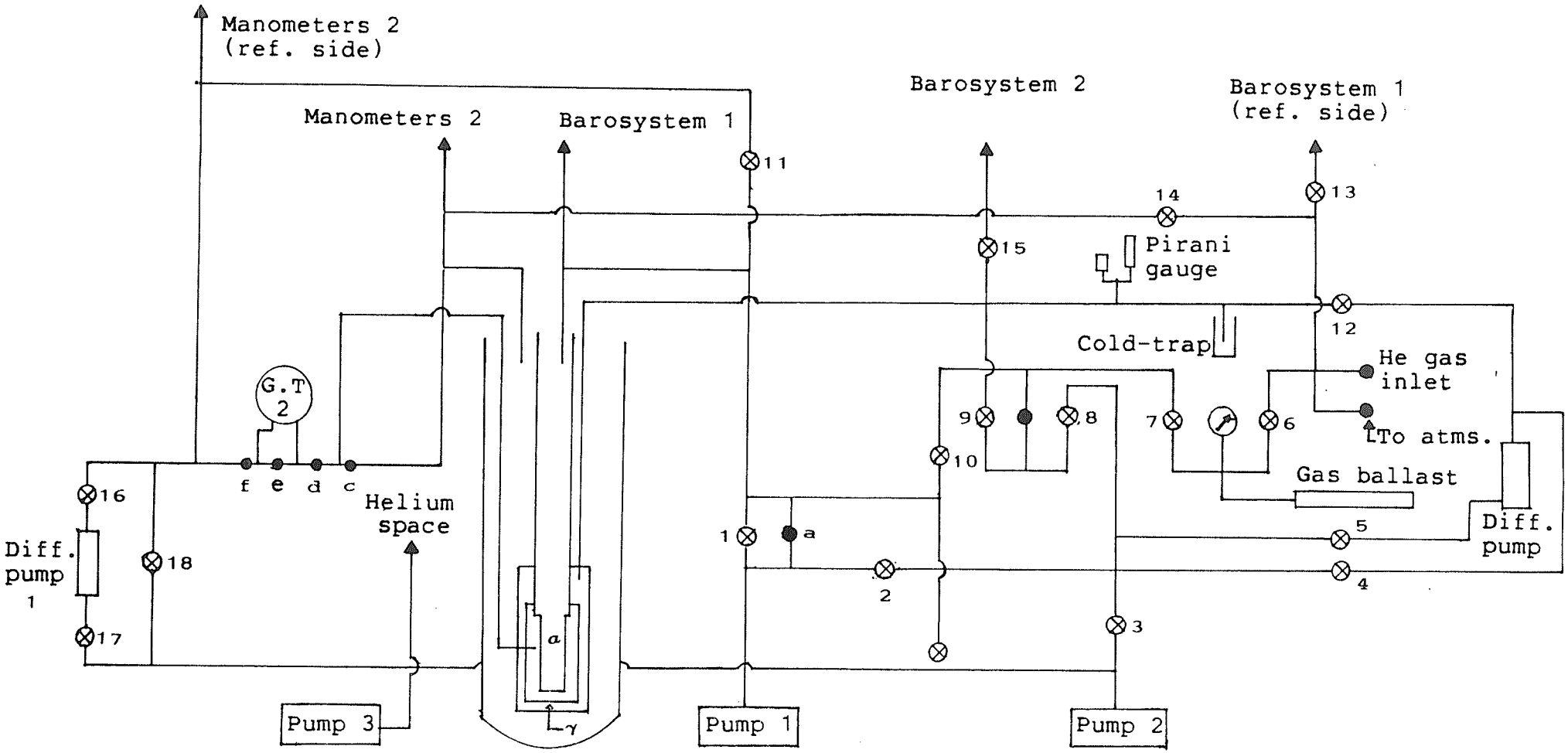

Fig.(4.6): Flow-chart of the pumping system used for temperature control and measurement. α: Sample chamber; β: G.T. bulb; γ: Isolation chamber.

This system allows temperatures above and below 4.2 K to be stabilised and measured, as described below.

To cool the sample chamber below 4.2 K a small amount of Helium gas is introduced into the vacuum-chamber with the help of the gas ballast shown in fig.(4.6). The valves 7 and 9 must be opened to the ballast, along with the intervening regulator needle valve b. To avoid damage to the manometers the valve 15 must be kept closed initially and then carefully opened once the exchange gas has been transferred to the vacuum-chamber. A very small pressure, typically 10 cms Hg, is sufficient to provide a good thermal link between the external He-bath and the sample chamber. Then, the pressurised Helium gas from the supply cylinder is admitted into the sample space by opening valves 7 and 10 to the gas ballast. Pressurised He gas starts to condense. As it condenses, the crude pressure gauge attached to the gas ballast drops continuously. The Helium input is continued until no rapid reduction in the pressure of He gas is registered on shutting off the supply cylinder. The condensation in the sample chamber is then complete. The exchange gas from the surrounding vacuum-chamber is then evacuated using pump set 2. The valves 3, 5, and 12 must be open to achieve a good isolation vacuum. Once evacuation is complete the temperature in the sample space can be lowered by pumping on it with mechanical pump 1. The pumping capacity of the rotary pump and transport of liquid Helium

through thin-film creep limit the lowest achievable temperature to approximately 1.5 K. The sample space pressure is measured using manometer set 1 (which was later replaced by an electronic Datametrics Barocell Pressure Sensor, capable of measuring up to 1000 Torr). Vapour pressure tables are used to calculate the sample temperature from the measured pressure, following correction for room temperature and local gravity.

The operation of the vacuum system for attaining temperatures above 4.2 K involved a complete evacuation of the isolation chamber. A Pirani gauge attached to the pumping line provides a measure of the pressure inside. The sample temperature may be raised above that of the He-bath by using a heater on the sample insert in conjunction with a feedback control circuit. In this case the sample temperature is measured by gas-thermometer 2.

4.3.3 Sample Insert

The insert, shown in fig.(4.7), is a rectangular Copper plate 10.5 cms x 2 cms in dimensions, soldered to the end of a long, narrow stainless steel tube which carries various current and voltage leads for the four samples mounted on the insert. The stainless steel tube also carries, around its lower end, a thin Cu-wire heater element. The same winding runs down the Copper insert and is held in place by G.E. Varnish which is a good thermal conductor and a good electrical insulator. On each side of the sample insert are

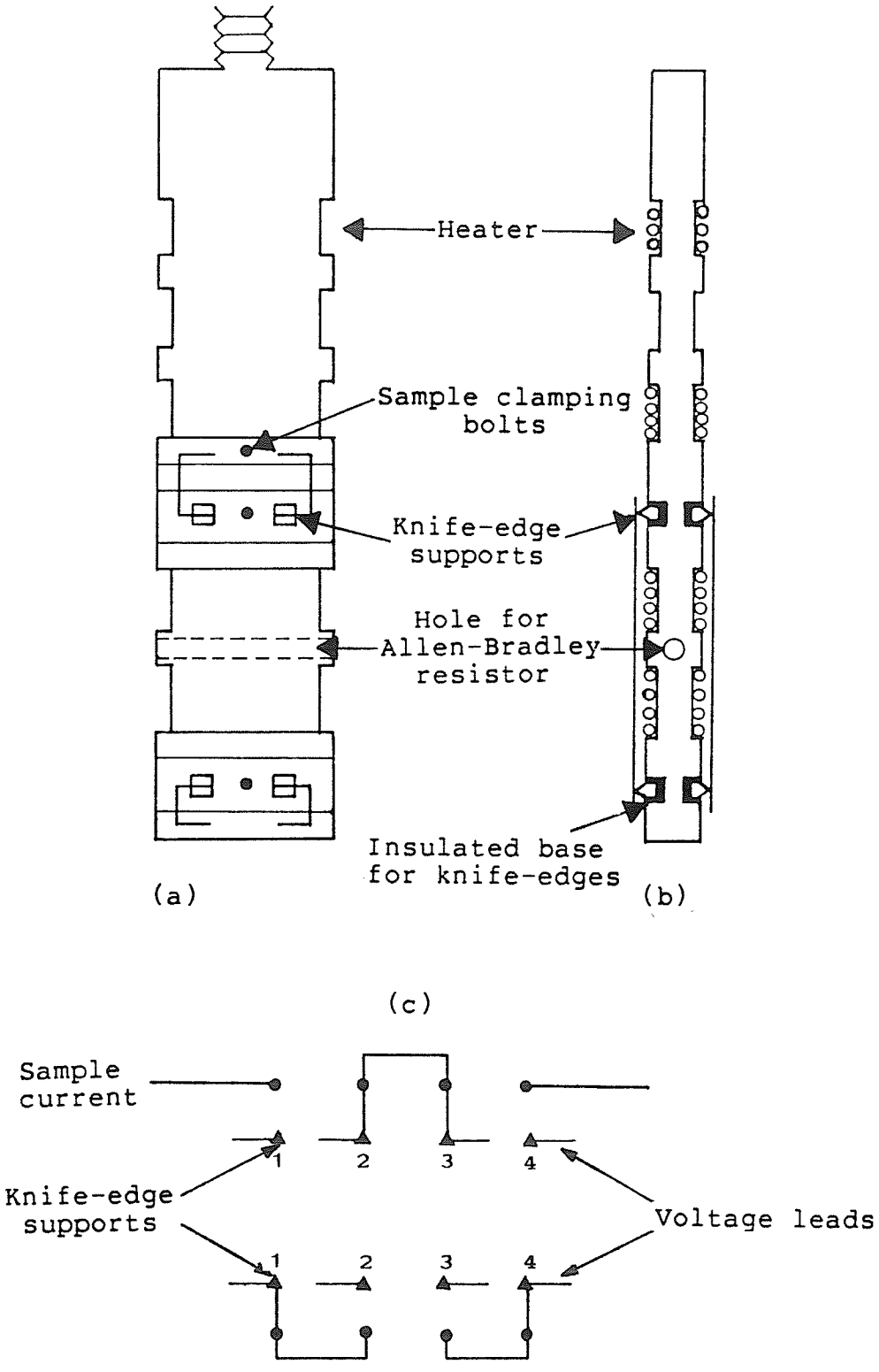

Fig.(4.7): Front- and edge-views of the sample insert (a,b); Current and voltage lead connections (c).

mounted two sets of brass wedges which are electrically insulated from the insert base. They are used to clamp down the thin, long sample strips lengthwise with the help of screws and nylon washers. Connections to the current leads are made on the samples once they are in place. All the voltage and current leads are connected to a "switch-board" box from where the connecting leads run to the appropriate external circuits.

4.3.4 Temperature Stabilisation and Measurement

Temperature stability below 4.2 K is achieved by the use of a manostat (not shown in the flow-diagram) in the pumping line connected to the sample space, while the temperature is measured by monitoring the vapour pressure above the Helium liquid contained in the sample chamber using Mercury and oil manometers (or by the Datametrics electronic pressure sensor). Above 4.2 K an a.c. bridge circuit containing a temperature sensitive carbon resistor is used for temperature stabilisation and a gas-thermometer for its measurement. Each of these four components of the stabilisation and measurement system is discussed below in more detail.

(i) Manostat:- This device works by either making or breaking contact between the evacuating pump and the sample chamber depending upon whether the pressure inside the sample chamber is higher or lower than a variable reference

pressure locked into it. The design of the manostat is shown in fig.(4.8).

It consists of a 0.01 inch thick latex rubber sheet stretched between two perforated brass retaining plates. One of the plates, which has 177 regularly spaced holes of 1/16 inch diameter each, forms the top of a gas reservoir. The other plate is connected to a mechanical pump and the sample chamber through two perforated ports, respectively. A small valve provides a facility for connecting the manostat reservoir to the line leading into the sample chamber and hence for changing the reference pressure.

Initially the reservoir is opened to the sample chamber while the latter is being pumped down. The pressure in the reservoir thus reflects the vapour pressure inside the sample chamber. To stabilise a certain vapour pressure (and hence the sample-space temperature) the small valve referred to above is closed to the manostat thus breaking the connection to the sample chamber. If subsequently, the reference pressure exceeds the He vapour pressure in the sample space, the two-port plate inlet is sealed. It remains sealed until the vapour pressure has risen just enough to force it back against the reservoir pressure. Some gas is allowed to be evacuated thus until, once again, the reservoir pressure just exceeds the vapour pressure. The presence of 177 holes on the reservoir plate is intended to permit fast response and to protect against membrane rupture in case of sudden, large pressure changes.

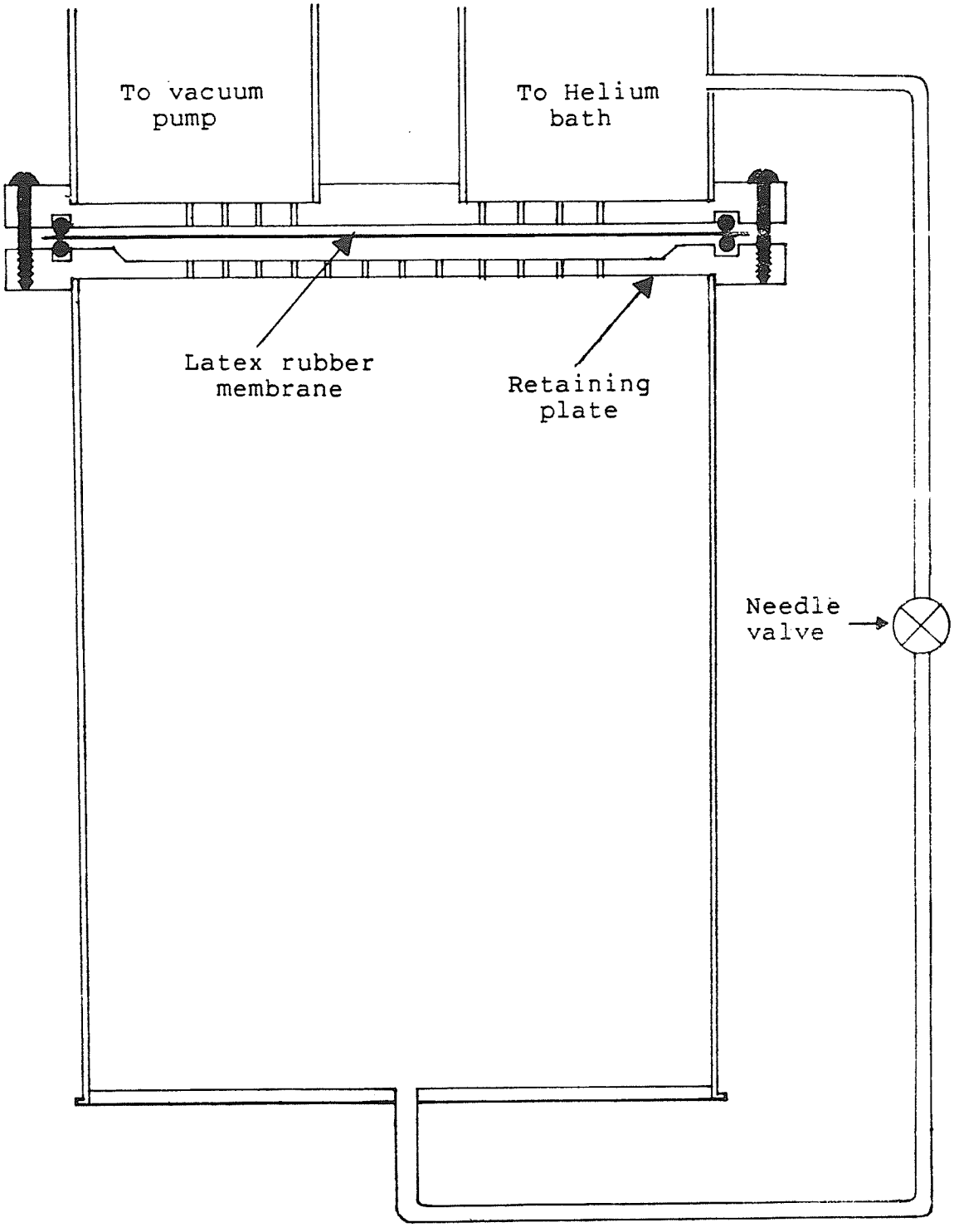

Fig.(4.8): The manostat (drawn to scale)

(ii) Manometer System and the Barocell:- For the first of the two sets of resistivity measurements performed during the course of this project, the vapour pressure of liquid Helium in the sample chamber was measured using a combination of Mercury and Apiezon B low-vapour pressure oil manometers. The former was used from the atmospheric pressure down to about 2 cms of Mercury; the pressure in the range of 4 cms to 2 cms of Hg was monitored on both manometers and an average conversion ratio was obtained to convert the oil manometer pressures directly to equivalent Hg manometer readings. Lower pressures were measured on the oil manometers alone. The manometer meniscus levels were read to ±0.001 cm using a Griffin and George Ltd. cathetometer. The barometric heights measuring the vapour pressures were corrected to standard gravity (local value of g is 980.99 cm/sec^2). Further, their measured values at room temperature were reduced to those at 0^oC. From the published Helium vapour pressure tables [91], the temperatures corresponding to these corrected vapour pressures at various settings were calculated.

In the repeat set of measurements the manometer system was replaced by an electronic pressure sensor, as mentioned earlier. The device [89] is based on the variable capacitance principle. The pressure sensing element in the barocell is a high-precision, stable, capacitative potentiometer the variable element of which is a thin,

highly pre-stressed metal diaphragm stretched between two fixed capacitor plates. It separates two gas-tight chambers which are connected to the external pressure ports. Any pressure differential across the diaphragm deflects it, thereby changing the relative capacitance of the diaphragm and the fixed capacitor plates. The Barocell is arranged in an electrical bridge circuit, which is balanced when the pressures on each side of the diaphragm are equal. Hence when evacuated on the measuring side (the reference side is evacuated and sealed), the imbalance signal is zero. Any imbalance in the circuit produces an output voltage (±10 VDC) proportional to the applied pressure. Pressure changes as small as 1×10^{-4} Torr can be detected with appropriate voltage measuring devices. In the present experiments, pressures were measured only to about 0.1 Torr. The proportionality factor for conversion of the barocell output reading to the pressure reading is 100 Torr/volt.

(iii) A.C. Bridge Circuit:- The circuit used for temperature control above 4.2 K contains two standard 1 kΩ resistors, one in each of the upper two arms of the bridge. The third arm has a variable resistor R. The fourth arm carries a temperature-sensitive Allen-Bradley resistor, in thermal contact with the sample insert inside the cryostat [fig.(4.9)]. The fact that the resistance of the AB resistor decreases very rapidly (roughly logarithmically, as shown in fig.(4.10)) as the temperature is increased, is exploited to

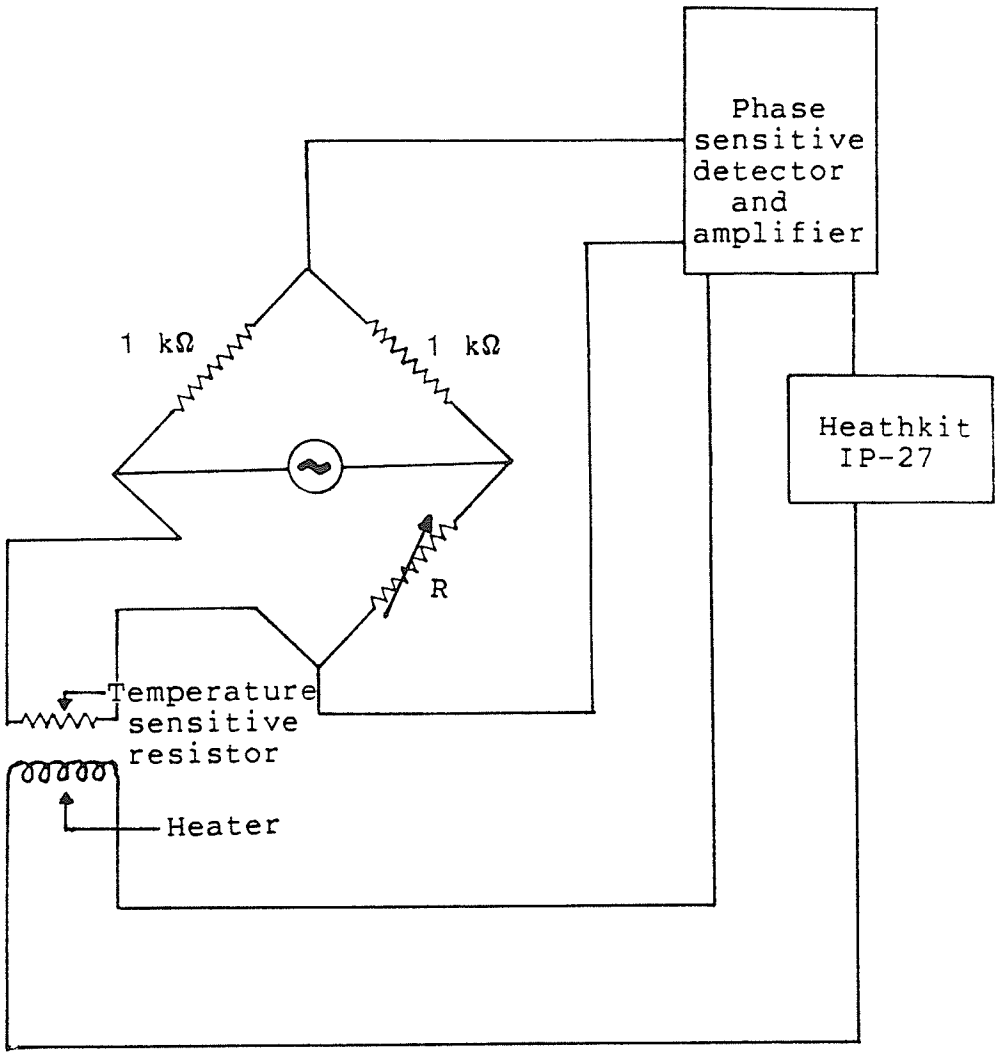

Fig.(4.9): A.C. bridge for temperature stabilisation

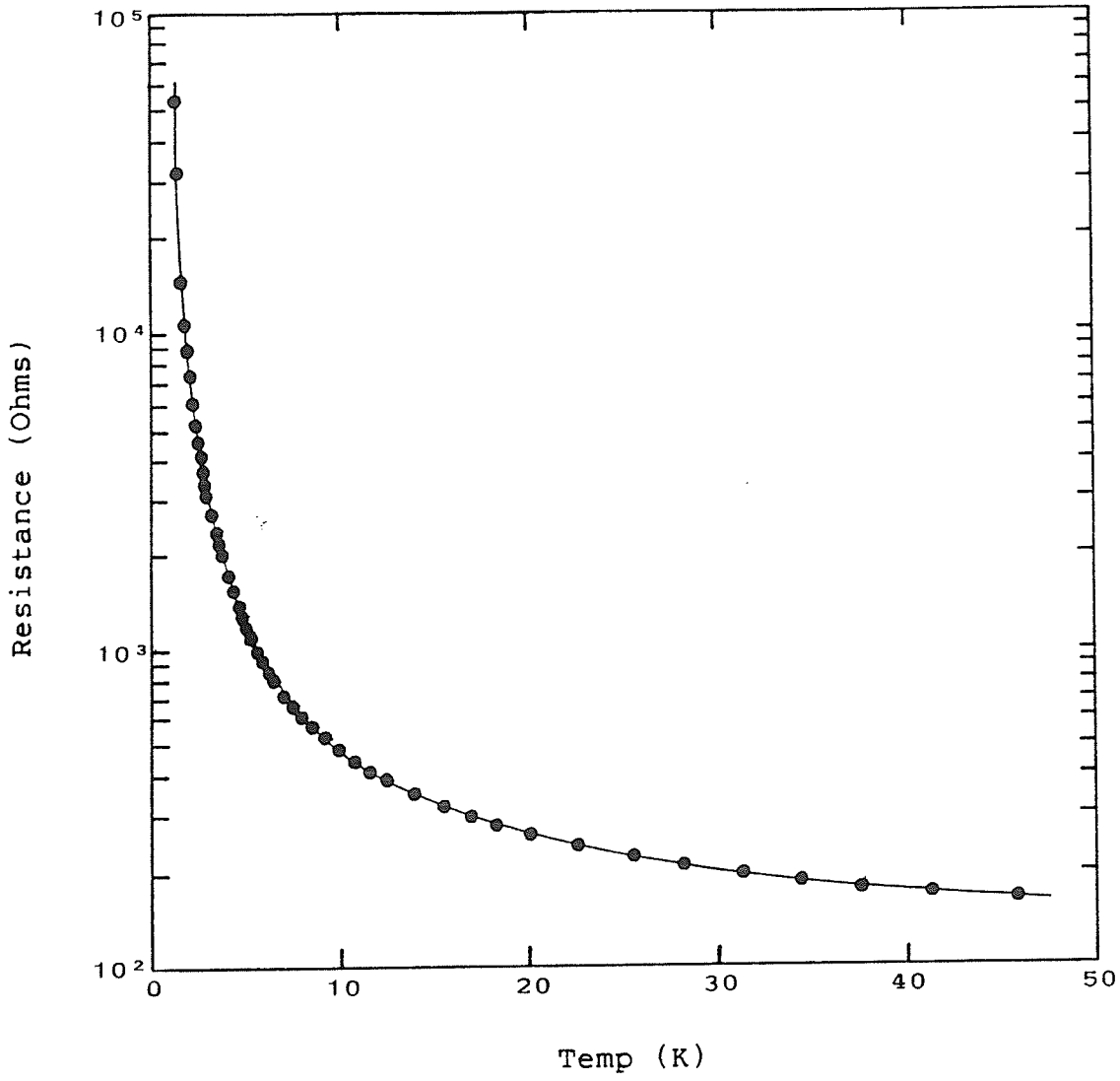

Fig.(4.10): Resistance-vs-Temperature characterstic of the Allen-Bradley resistor.

control the temperature. In the balanced condition of the bridge, the AB resistor is equal in resistance to the variable resistor R. A new lower value for the resistor R, chosen from the resistance-vs-temperature characterstic for the AB resistor to correspond to a required higher temperature, can be "dialled". The bridge responds through the generation of an imbalance signal which is fed into a phase sensitive detector and amplifier. The amplified output is used to drive a current proportional to the positive difference between the resistance of the AB resistor and the set resistance R through the heater coil wound on the sample insert. The temperature in the sample chamber is raised. The value of the AB resistor falls towards the dialled value of R with rising temperature, and thus reduces the difference signal from the bridge. Were it not for the cooling effect of the He-bath, the heater current would simultaneously drop until it was reduced to zero. However, in order to maintain a given temperature above that of the Helium bath, the heater current stabilises at an appropriate value. At this point the AB resistor has achieved the lower desired value fixed by the resistance R. The bridge circuit acts to nullify any deviations from this state by either supplying or stopping an additional feedback current to the heater. The sample chamber temperatures are stabilised thus. Upto 25 K the bridge output is sufficient to supply the requisite heating power. An auxiliary Heathkit (IP-27) power supply connected in series with the output of the

phase detector extends the heating capacity up to room temperature. In the present study, it wasn't needed.

(iv) The Gas Thermometer:- Temperature measurements above 4.2 K were performed using a non-linear gas thermometer. The latter used a Wallace and Tiernan (62A-4c-0125) pressure gauge capable of measuring pressures up to 125 inches of water and connected to the gas thermometer bulb surrounding the sample chamber through a 0.024" inner diameter, stainless steel tube. Helium gas was used to fill the thermometer bulb because its behaviour is very nearly "ideal". However, deviations from linearity are caused by the presence of dead spaces in the measuring devices and the connecting tubes. The volume of the dead space in the pressure gauge depends linearly on pressure. Corrections to the ideal gas law are made in order to compute the correct temperatures from the measured gas pressure readings. A virial expansion of PV to first order in P is utilised [90].

$$PV = AT + B'(T).P \qquad (4.2)$$

where

$$A = A_0/273.15$$

For Helium gas the constant A_0 has a value 0.999488 N-m/^{0}K The values for the constant B'(T) are tabulated in the above reference. The expansion accounts for the deviations from

the ideal behaviour. For simplicity of analysis the gas themometer is divided into three interconnected compartments [fig.(4.11)].

(a) the gas thermometer bulb with a volume V and a temperature T.

(b) the pressure gauge dead space volume V' + dead space volume V_1 of the portion of the connecting tube that lies outside the cryostat; both dead spaces are at room temperature T'.

(c) the dead space volume V_2 of that portion of the connecting tube which runs down the cryostat into the bulb; a temperature gradient from T' to T exists along the length.

The modified gas law [eqn.(4.2)] for such an interconnected assembly can be approximately (neglecting temperature discontinuities at the boundaries of the conceived compartments) written as

$$\sum_i PV_i/(T_i + BP) = \text{const.} \qquad (4.3)$$

where

$$B(T) = B'(T)/A$$

The pressure P of the gas is identical in all compartments due to inter-connectedness. The three terms in eqn.(4.3) are

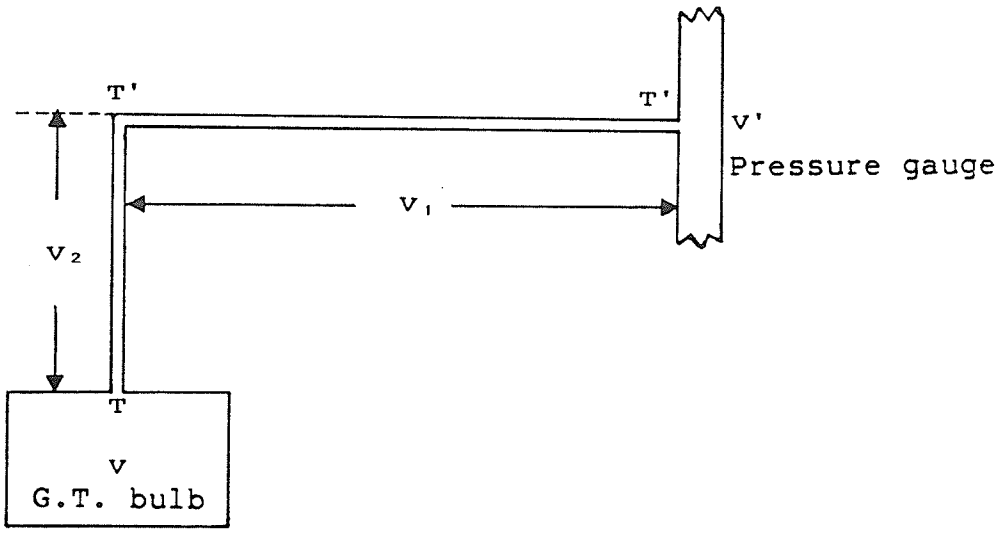

Fig.(4.11): Simplified picture of the Gas-thermometer for analysis.

Term 1 : $PV / [RT + B(T)P]$

Term 2 : $P(V' + V_1) / [RT' + B(T')P]$

Term 3 must be separately calculated as it involves a temperature gradient along the tube length:

$$dT(l)/dl = -\gamma \qquad (4.4)$$

Contributions to term 3 come from the elemental volumes dv, each at a temperature T(l) depending upon its location relative to the top end of the tube length L_1. The form of the contributions is

$$Pdv / [RT(l) + B\{T(l)\}.P]$$

A summation over all such elemental contributions, with B{T(l)} replaced by its value B{(T'+T)/2} at an average temperature (T'+T)/2, gives the third term. The volume integral can first be transformed to an integration over the tube length through

$$dv = \pi r^2 dl$$

and then over temperature with the use of eqn.(4.4). The result of integration between appropriate temperature limits is

$$\text{Term 3} = PV_2/R(T'-T) \; . \; \ln \{(T'+C)/(T'-C)\}$$

where,

$$C = P/R \; . \; B\{(T'+T)/2\}$$

The sum of terms 1, 2 and 3, assuming that the pressure gauge volume V' is directly proportional to the pressure (i.e. $V' = V_0 + aP$), must be a constant according to the modified gas law. Thus

$$V/[RT + B(T)P] + P(V_1 + V_0 + aP)/[RT' + B(T')P]$$

$$PV_2/R(T'-T) . \ln \{(T'+C)/(T'-C)\} = \text{const.} \qquad (4.5)$$

The gas thermometer bulb volume V can be measured at room temperature. The constructed volume of the bulb used in this study is 2.992 cu inches. At any other temperature its volume can be calculated using the coefficient of expansion of Copper. The only two unknown coefficients above are V_0 and a. To calculate these the gas thermometer is calibrated at the boiling point of Helium (4.213 K) and the triple point of water (273.16 K) with a fixed amount of Helium gas. Eqn.(4.5) evaluated at both temperatures must give identical constants. Hence this calibration generates one equation relating V_0 and a. Another relation is obtained by reducing the Helium gas pressure in the bulb and re-calibrating at the same two temperatures. A simultaneous solution of the two equations yields values for V_0 and a [66]. The results of this procedure in the present case are

$$V_0 = 1.027 \text{ cu inch} \quad , \quad a = 1.0557 \text{ cu inch/atm.}$$

For high-field resistivity measurements above 4.2 K another gas thermometer with different constants was used. The constant in eqn.(4.5) can subsequently be determined by measuring a known temperature T_0 and substituting in that equation. Then eqn.(4.5) is ready to be used for temperature calculation at any given pressure. An iterative procedure is used for its solution. For the first calculation two assumptions are made:

$V(T) \simeq V(T_0)$

$B(T) \simeq 0$

Term 3 $\sim 1/T'$

The temperature so estimated corresponds roughly to an ideal-gas estimate. The neglect of the logarithmic term in eqn.(4.5) is accounted for next. The first estimate of temperature is substituted on the left side of eqn.(4.5) while retaining the first two assumptions above. This yields a second estimate of temperature. Next, the thermal contraction of the gas thermometer bulb and the non-zero value of the virial coefficient B are allowed for. Hence the final estimate of the sample temperature! The calculated temperatures are estimated to be good to within ±0.5 %.

4.4 D.C. RESISTIVITY MEASUREMENT

In the four-probe technique for d.c. resistivity measurement a known current, i, is sent through the sample and the voltage drop V across the wedge-mounts is applied in opposition to a precisely measurable variable voltage in a potentiometer. At the null-point the unknown sample voltage V exactly equals the standard potentiometer voltage. The resistance of the length of the sample between the wedge-mounts is given by the Ohm's law, $R = V/i$.

A block diagram of the requisite arrangement for the measurement of sample resistivities is shown in fig.(4.12). The sample current, i, is provided by a highly stable (1 part in 10^6) Guildline 9770 B constant current source, referenced by a standard-cell which is one of six housed in a thermally regulated Guildline 9152T6 standard-cell enclosure. A Tinsley 3589 R Auto Diesselhorst potentiometer was calibrated to give the value of the sample voltage directly in terms of the highly stable emf of another of the six cells mentioned above. The voltage source for the potentiometer is a Guildline 9781 supply. The calibration cell and the voltage source are both connected to the potentiometer through a Tinsley 4092 reversing switch. The unknown sample voltages to be measured, chosen one at a time by a Guildline low-thermal selector switch (9145 A10) are also applied to the potentiometer through the reversing switch. The latter enables a thermal emf-free measurement

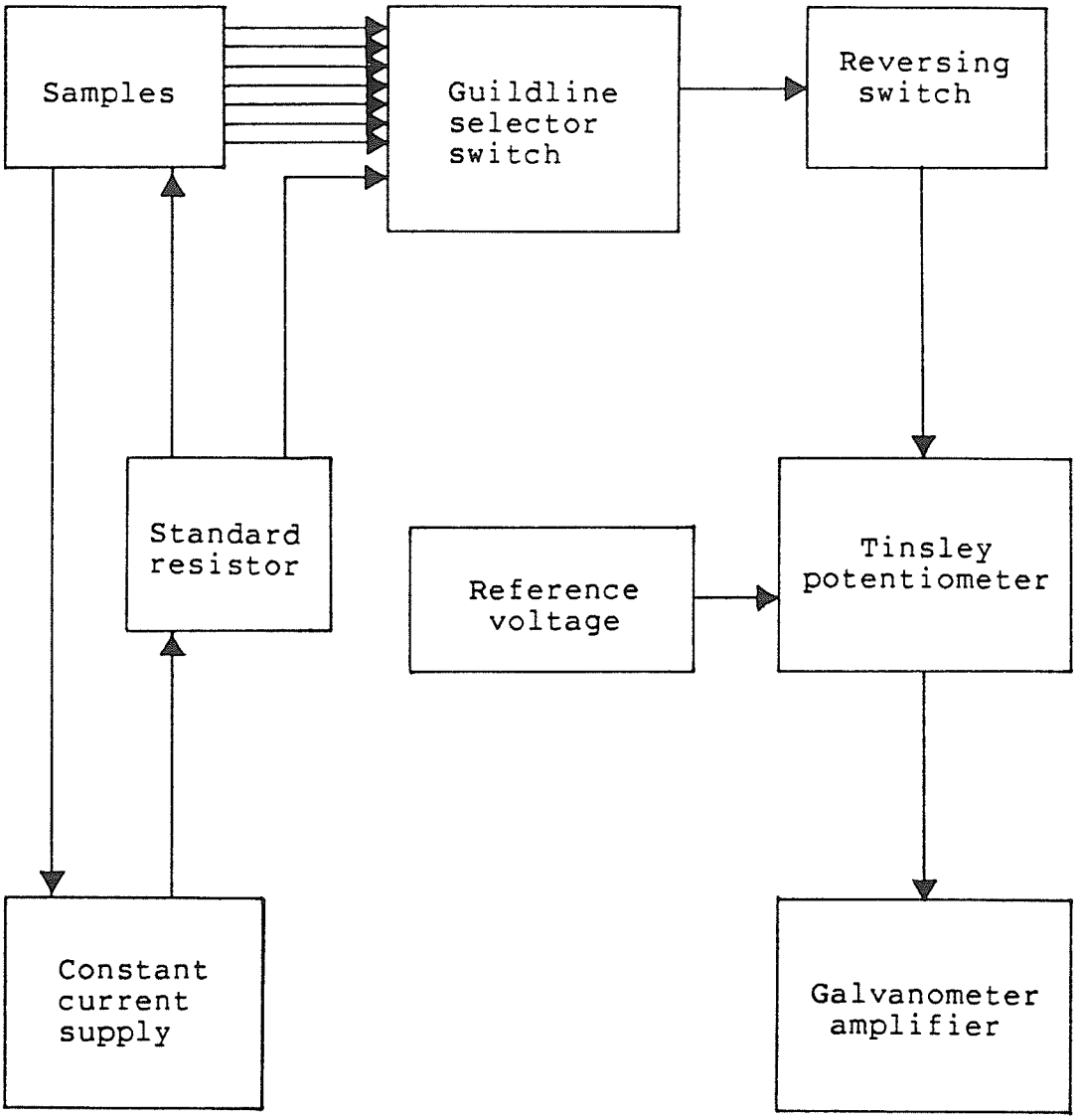

Fig.(4.12): Block diagram of the arrangement for measuring d.c. resistivity.

of sample voltages. This is accomplished by two successive measurements of the sample voltage V, one direct and the other with all relevant voltages reversed. The average of the two results may be taken as an accurate measure of the true sample voltage. A similar measurement of potential across a series standard resistor (Guildline, 0.1 Ω), accessible through the selector switch, gives the sample current.

4.5 A.C. RESISTIVITY MEASUREMENT

To measure accurately the small changes introduced in the sample resistivity by controlled changes in temperature a back-off voltage signal, directly proportional to the sample current, is subtracted from the sample voltage. The difference signal is thus rendered free from the effects of sample current fluctuations to the first order. This difference is measured accurately with the use of a Princeton Applied Research HR8 precision lock-in amplifier. The latter is essentially a detection system which obtains large signal-to-noise ratios by converting a selected spectrum of frequencies in the input signal to an equivalent bandwidth about d.c. and then filtering out all but an extremely narrow band of frequencies around the d.c. component.

The circuit used for measuring the a.c. resistivity is shown in fig.(4.13). A low-frequency (37 Hz) signal

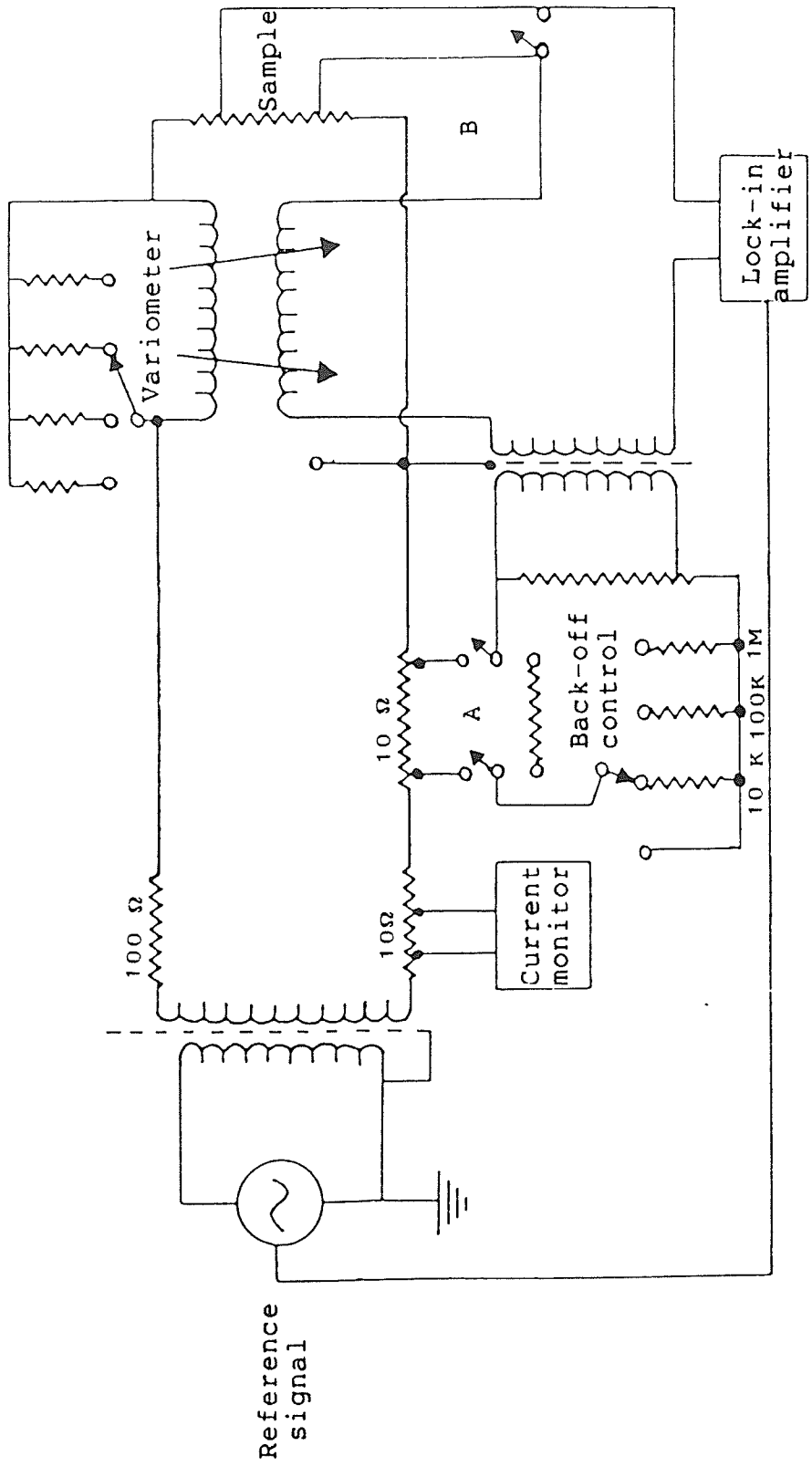

Fig.(4.13): Circuit used for a.c. resistivity measurements.

obtained from a General Radio 1311-A audio oscillator is applied to the sample under observation and also to a series-connected, variable Kelvin-Varley type resistor. This choice of operating frequency avoids the problem of interference from the line frequency components and from the high-frequency skin-effect. The difference between the sample voltage and the adjustable series resistor voltages is fed to the input of the PAR, which is tuned to the driving frequency of the a.c signal. For high differential sensitivity in the resistivity measurements interference from stray quadrature components in the signal across the sample must be eliminated. This is achieved by the use of a variometer, consisting of a stationary coil of 150 turns of no. 30 Copper wire with two rotatable secondary coils having 250 and 10 turns respectively of the same wire, in the input circuit. With the back-off circuit connected, the quadrature signal is nullified at the input to the lock-in amplifier by using the variometer to provide a compensating quadrature signal. The device also provides an accurate quadrature signal for setting the phase of the lock-in amplifier. The quadrature-free input signal is converted to an equivalent noise-free d.c. component inside the lock-in amplifier and subsequently amplified by a d.c. amplifier. The output is measured on a Keithley DVM. Once the resistivity is known accurately from d.c. measurements at 4.2 K it can be calculated at all other temperatures from the small signal changes measured using the a.c. equipment.

Chapter V

DATA ANALYSIS AND DISCUSSION

5.1 A.C. SUSCEPTIBILITY

5.1.1 Correction of the Data

The measured susceptibilities of the various PdGd alloys need two corrections. The first is a simple background correction. In the absence of a sample in the sample-insert the bundle of Copper wires at its lower extremity should fill both sensing coils equally and hence no net signal should result. In practice, however, the background signal is non-zero and negative (i.e. diamagnetic). The reasons lie in small differences in the construction of the two sensing coils, non-uniformities in the bundle of Copper wires and, perhaps, also in the proximity of temperature-sensing elements like the Germanium resistor and the thermocouple wires (both of which are embedded in the bundle of wires) to the field region. The background correction was determined by measuring the difference signal at a typical high value of magnetic field (usually 400 Oe, because at high fields, the zero-correction is significant in relation to the strongly suppressed susceptibility signals from the samples) in the temperature range of interest. Temperature-independent signals of typical

magnitudes about -0.025 V were obtained. These were added to the measured susceptibilities (in volts).

The second correction is due to the sample geometry. A magnetic field applied to the sample produces a demagnetising field within it and the net field inside the sample is given by

$$H_i = H_a - NM \tag{5.1}$$

where M is the magnetisation induced in the sample and N is the demagnetisation factor. The purely geometrical factor N is extremely difficult to estimate for all but the simplest of sample shapes.

Eqn.(5.1) leads to an expression

$$\chi_{tr.} = \chi_m/(1 - N\chi_m) \tag{5.2}$$

This equation suggests that the maximum values of the measured susceptibilities (corrected for background) are limited by the requirement that

$$1 - N\chi_m \geq 0 \tag{5.3}$$

The demagnetisation factors of the samples were estimated by regarding them as ellipsoids with principal axes equal to the sample dimensions [92] and evaluating the appropriate

elliptic integrals. Next, the magnetisation M in eqn.(5.1) was estimated by "integrating" the susceptibility as a function of field using the trapezoidal rule.

$$M(T_0) = \sum_i \chi_i(T_0).\Delta H_i \qquad (5.4)$$

Since the lengths of the intervals ΔH_i were rather large and their numbers statistically very small, such an integration procedure is rather crude. Nevertheless, in view of the uncertainty in the values of the demagnetisation factors, arising due to an idealised ellipsoid calculation, these estimates for M are not unreasonable. The values obtained for N and M as above were finally used to obtain the internal fields corresponding to the applied external fields using eqn.(5.1). The "true" values of the sample susceptibilities were calculated using eqn.(5.2).

Corrections to the temperature-readings of the Germanium-sensor were found to be necessary for all temperatures above the boiling point of liquid Helium (4.2 K approximately) because of the relative placement of the Ge-resistor with respect to the sample in the sample-insert. The former is located higher than the latter. Temperatures above 4.2 K are achieved in the present equipment by simply allowing the liquid Helium surrounding the sample and the Ge-sensor to boil away, and controlling the rate of heat-leak into the system. Since the Ge-sensor lies higher in the sample-

holder, liquid Helium falls below its level first. The resistor consequently starts to warm-up whereas the sample, being still immersed, stays at the Helium-bath temperature. Thus, the temperature-readings by the Ge-sensor do not, any longer, reflect the true sample temperatures. This build-up of a temperature-differential between the Ge-resistor and the sample continues slowly until enough Helium is lost through boiling that its level falls below that of the sample. At that point the latter also begins to warm-up out-of-step with the Ge-resistor. As more heat leaks into the system, the initial temperature differential begins to decline and, at higher temperatures, the thermal equilibrium between the thermal-sensor and the sample is restored. Once again, then, the Ge-readings begin to measure the sample temperatures directly.

The range of Ge-sensor temperature-readings (just above the boiling point of liquid Helium) where the sample response is frozen at its 4.2 K value while the Ge-resistor drifts upwards in temperature slowly is hereafter referred to as the "dead range". Samples of such a region actually observed during the experiments are presented in fig.(5.1).

One way of obtaining the "true" sample temperatures is to shift the temperature-scale above 4.2 K using a height-and-slope matching technique as illustrated. However, this method assumes inherently that the maximum initial temperature-differential $\Delta T^0 = (T^0_{Ge} - T^0_S)$ between the Ge

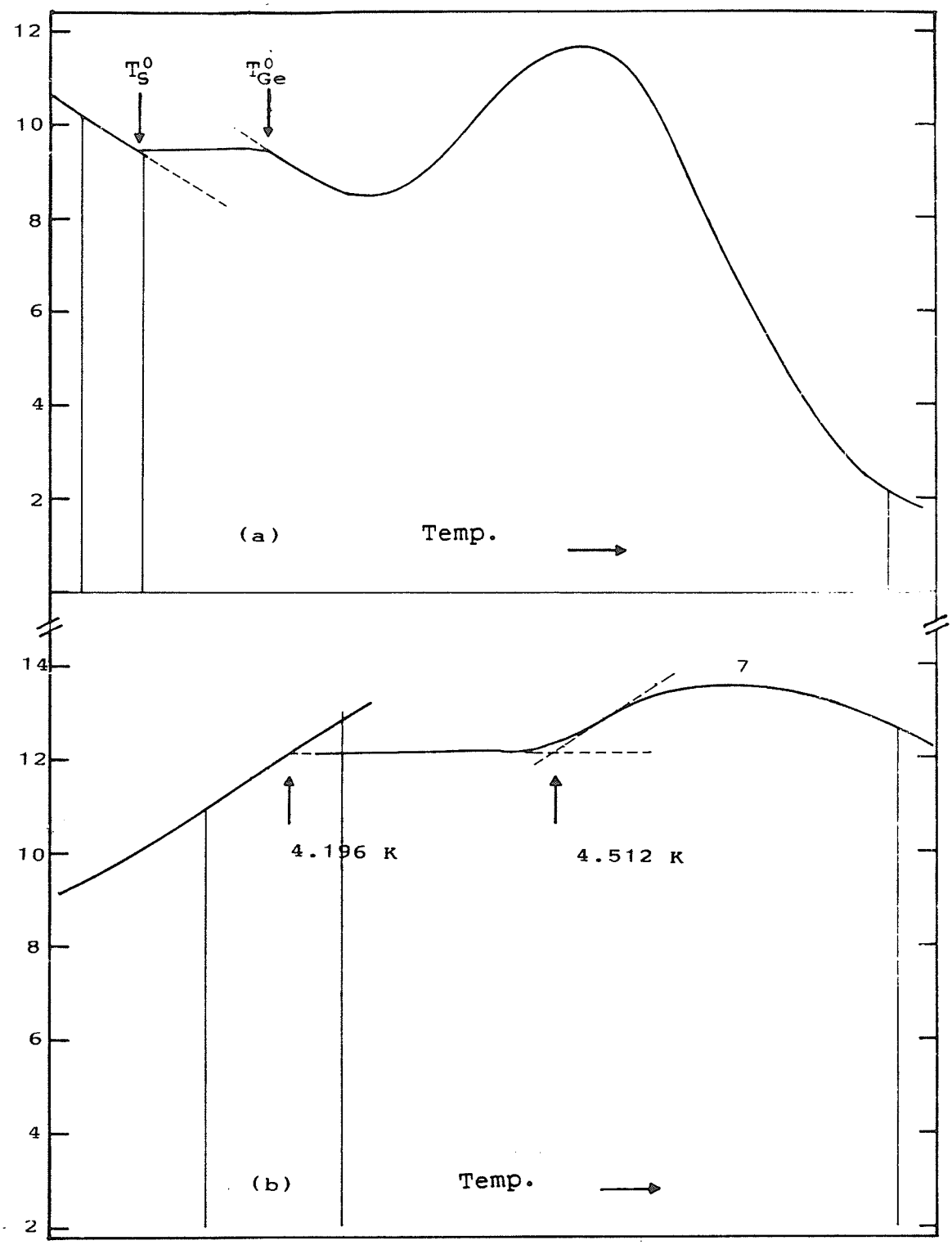

Fig.(5.1): "Dead range" around 4.2 K (arbitrary y-scale)

(a) 8 at.% : 150 Oe

(b) 7 at.% : 200 Oe

-sensor and the sample is maintained at all temperatures above 4.2 K. An improved approximation allows the former to decrease with increasing temperature. Hence, at any temperature, T_{Ge}, of the Ge-sensor the differential is

$$(T_{Ge} - T_s) = \Delta T = \Delta T^0_{Ge} x\ T^0\ /T_{Ge} \qquad (5.5)$$

In some cases, it was difficult to locate T^0_{Ge} because of a very weak temperature-dependence of the sample response just above and below the "dead range". In such cases a calibration graph called TRUECAL was drawn [fig.(5.2)] to find the true sample temperatures, given a Ge-sensor reading. Previous "good" temperature assignments for cases where the dead range is sharply defined were used to obtain the calibration graph. For most cases plotted on the graph, the "true" sample temperatures calculated as above agree closely with one another. An "average" calibration line was used. If the heating conditions in the dead range are similar the spread in sample temperature estimates is of the order of 0.1 K. While the temperatures above 4.2 K for the 7 and 8 at.% alloys could be dealt with simply by the decreasing temperature-differential method outlined above, some of the high-field measurements for the 9 and 10 at.% alloys required the use of TRUECAL graph. The rather large temperature inaccuracies associated with this procedure translate into large error bars on the T -vs-$H^{0.56}$ graphs.

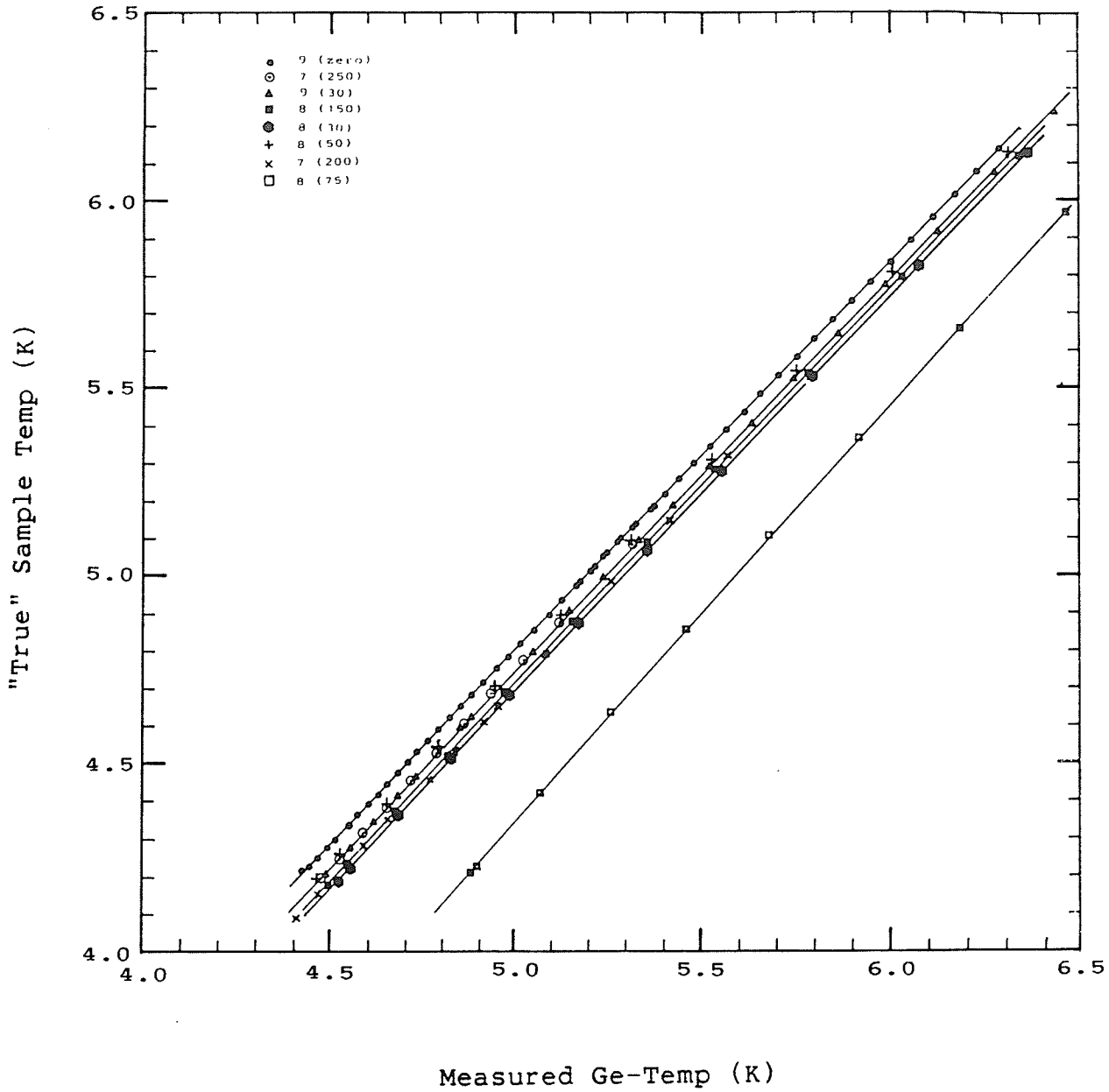

Fig.(5.2): TRUECAL calibration graph.

The various symbols represent the different cases of temperature estimation for three of the high-concentration alloys in different fields.

5.1.2 Results

The zero-field susceptibility, $\chi(0,T)$ of the 2 at.% sample shows a monotonic decline above 1.6 K. A Curie-Weiss plot, shown in fig.(5.3) has a linear section (extending from 1.825 K upto the vicinity of the Helium λ-point) which extrapolates to a paramagnetic Curie temperature of about 1.65 K. A value of (1.7 ± 0.2) K has previously been reported by Cannella et al [72]. However, a rather large value for the effective Gd-moment is obtained from the measured slope. This, perhaps, is a direct consequence of not being in the true paramagnetic regime.

The temperature-dependent, zero-field susceptibilities of the other ($3 \leq c \leq 10$ at.% Gd) samples have, at least, one feature in common. In the vicinity of the ordering temperature, $\chi(0,T)$ increases rapidly with decreasing temperature, passes through a maximum (the Hopkinson peak) and then decreases slowly at the temperatures beyond [fig.(5.4)]. These maximum values for $\chi(0,T)$ lie in the range 0.5-1 emu/g-Oe and represent from 50-15 % of the limit set by the demagnetisation factors estimated using the elliptic integral method. The appearance of the Hopkinson peak is a bulk effect related not to critical ordering effects but to the domain-wall dynamics. In addition to this peak, the 5 to 10 at.% alloys exhibit a second, broader peak at a lower temperature in their zero-field susceptibilities. A typical example of the double-peak

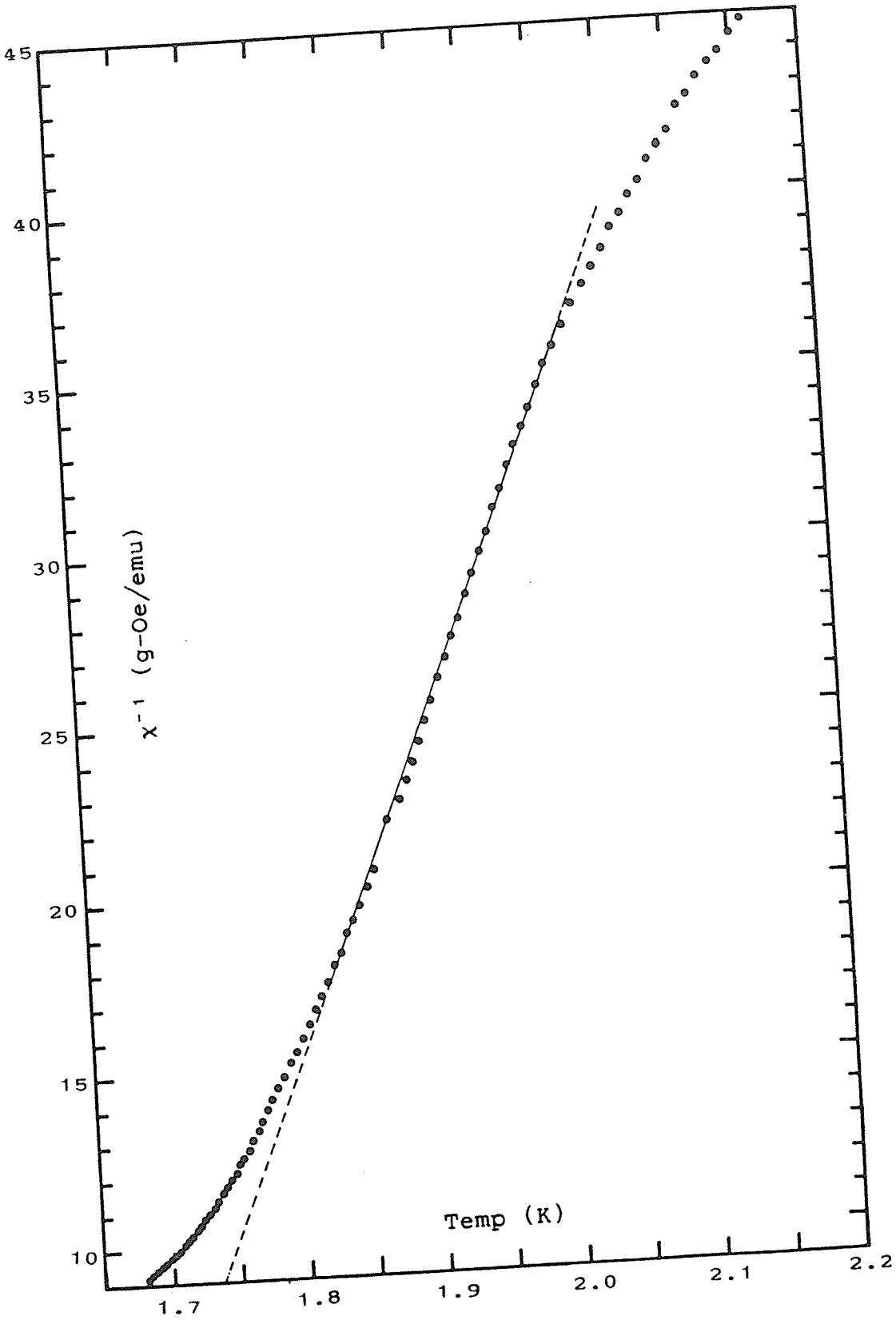

Fig.(5.3): Curie-Weiss plot for Pd + 2 at.% Gd.

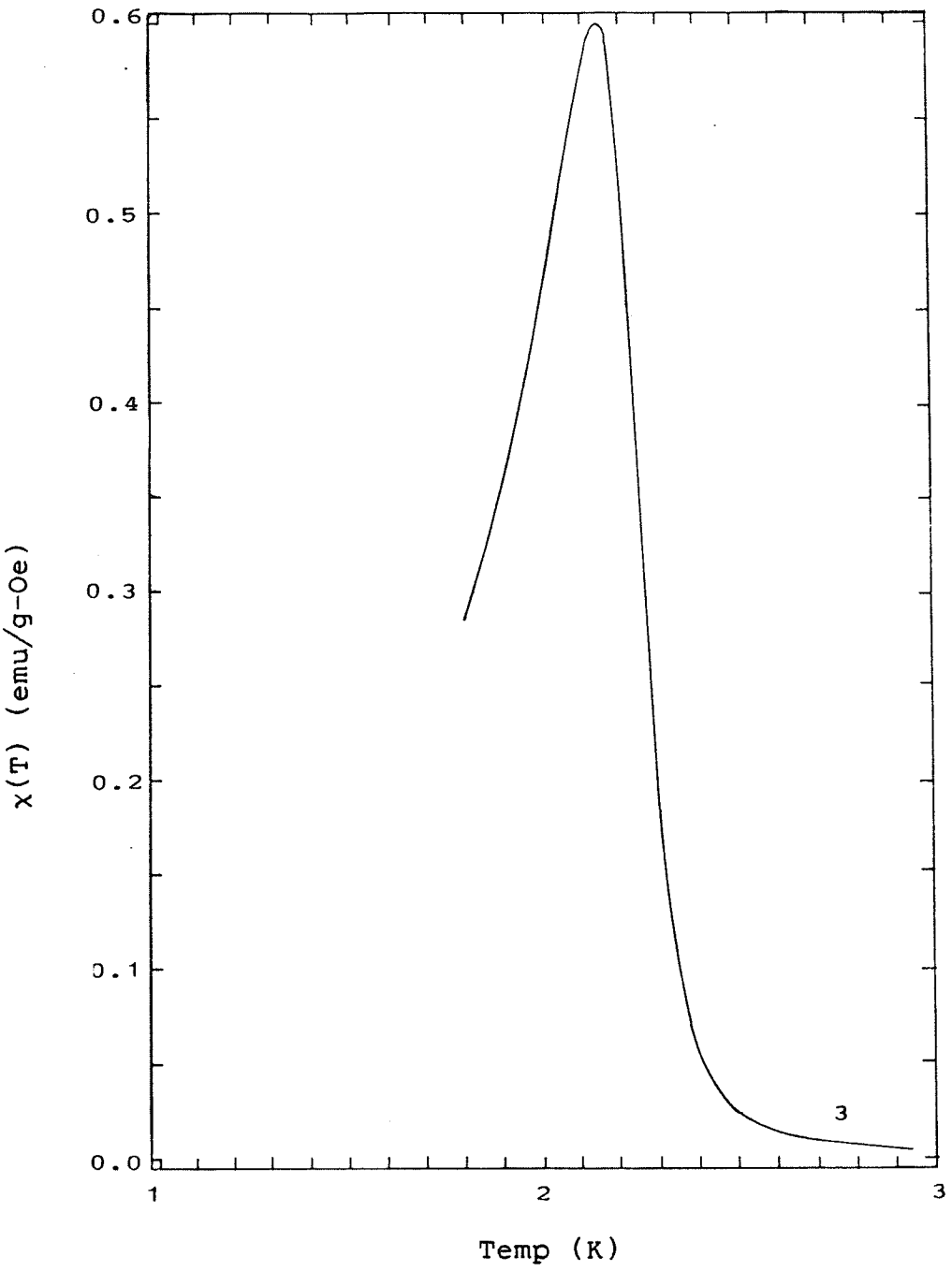

Fig.(5.4): The Hopkinson susceptibility peak;
a typical example -- Pd + 3 at.% Gd.

structure is presented in fig.(5.5) for the 5 at.% alloy. (The zero-field susceptibility data for other high concentration samples is compiled in appendix A.)

When a large part of the Hopkinson susceptibility is removed by applying small external fields (10-30 Oe), the data on all of the above alloys reveals secondary peaks at temperatures above those of the respective Hopkinson's peaks. The qualitative dependence of these secondary peaks on field is very similar in all cases. As shown in figs.(5.6) and (5.7) for a typical case of 3 at.% alloy, while the principal maximum is strongly suppressed and quickly pushed downward in temperature, the height of the secondary maximum is reduced to a smaller extent and its position is pushed up on the temperature scale. A progressive rounding of the peaks also occurs with increasing fields. As mentioned in Chapter II, such a behaviour is seen in PdMn alloys undergoing a paramagnetic to ferromagnetic transition. The scaling law [eqns.(2.36) and (2.37)] correctly reproduces the systematics of their critical peaks. A more detailed comparison between PdMn and PdGd reveals some interesting facts.

Specifically, the additional peaks in the zero-field susceptibility of PdGd alloys with $c \geq 6$ at.% have no counterparts in the PdMn system in any of the three distinct concentration regimes. In PdGd system, these peaks may very well be associated with bulk magnetisation effects.

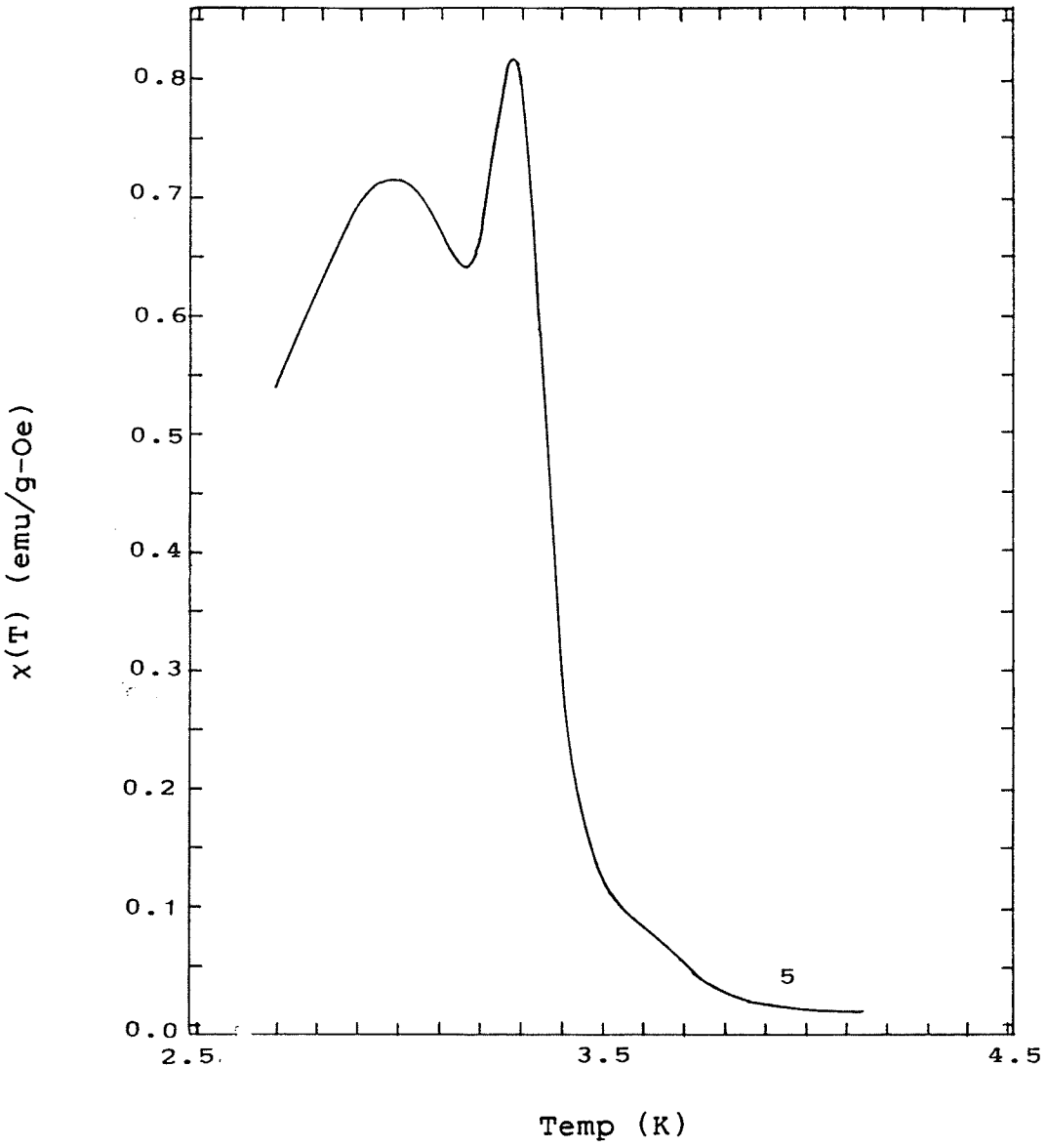

Fig.(5.5): Double-peaked structure in the zero-field susceptibility of a typical high concentration alloy (5 at.% Gd).

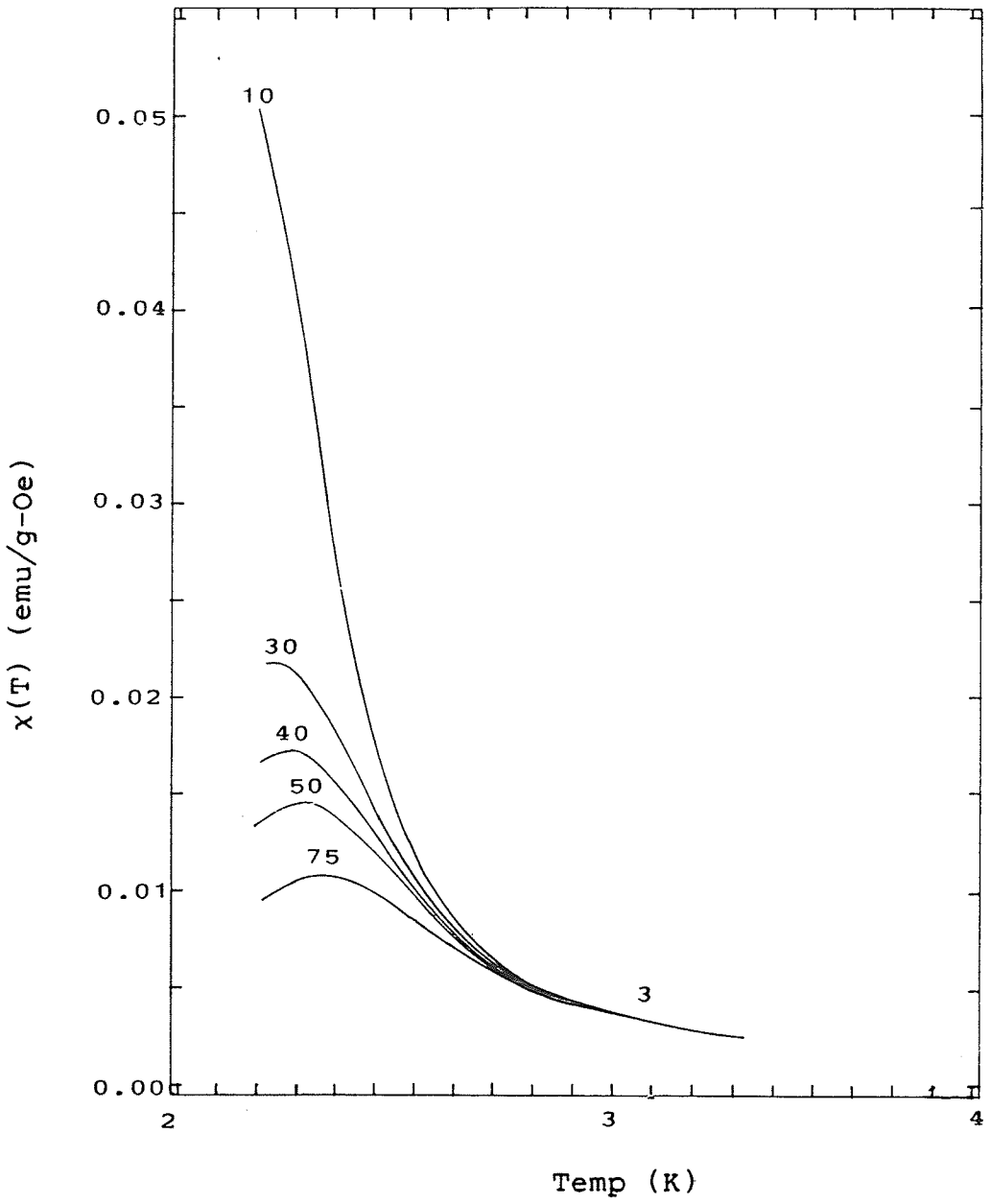

Fig.(5.6): A typical example of field-dependence of secondary peaks in a.c. suceptibility (Pd + 3 at.% Gd). Field strengths are marked on the respective curves.

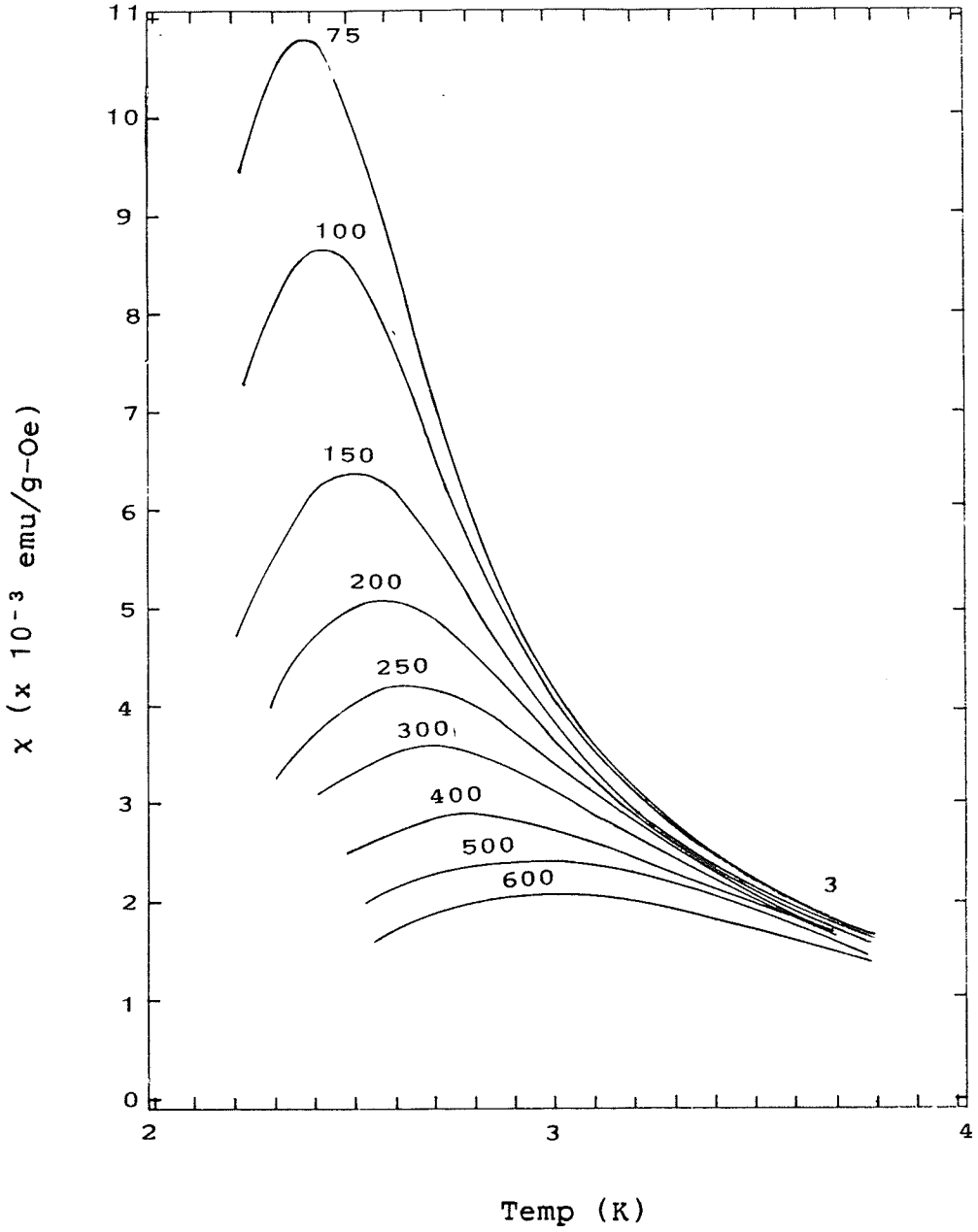

Fig.(5.7): A typical example of field-dependence of secondary peaks in a.c. suceptibility (Pd + 3 at.% Gd). Field strengths are marked on the respective curves.

However, anticipating the data on magnetic resistivity of these alloys (section 5.2.2), it is of interest to note that the position (in temperature) of the additional susceptibility peak for a given alloy corresponds rather closely with that of an interesting feature noted in the corresponding magnetic resistivity; it falls close to the higher temperature edge of the peak noted in magnetic resistivity [see figs.(B.9)-(B.13)].

Next, though in comparably concentrated specimens of PdMn and PdGd the susceptibilities at the respective principal maxima are comparable their suppression in the former is more rapid than in the latter. Consequently, the secondary peaks emerge at somewhat lower fields (2-5 Oe) in PdMn. Once established, however, the critical peaks have heights twice as large in PdGd as in PdMn.

Further, in PdMn the concentration-dependent susceptibility at the critical peaks (for a fixed biasing field) follows its phase diagram (i.e. T_c^*-vs-c diagram). It increases slowly with rising concentration in the ferromagnetic regime ($c \leq 2.5$ at.%) and decreases sharply in the spin-glass regime ($5.5 \leq c \leq 10$) [66]. In the intermediate range, it remains essentially independent of concentration or, at best, only very weakly dependent on it. However, in the PdGd system an unambiguous, continuous rise in the peak suscpetibility follows a rise in concentration, at least up to 9 at.% Gd, as demonstrated by Table (5.1).

TABLE (5.1)

Concentration dependence of susceptibility peak heights

H (Oe)	χ (emu/g-Oe) for alloys with conc. (in at.% Gd)							
	3	4	5	6	7	8	9	10
10	> 0.05	0.064	0.087	0.11	0.136	0.165	0.18	0.125
30	0.022	0.028	0.039	0.044	0.058	0.078	0.085	0.064
50	0.014	0.018	0.024	0.028	0.036	0.048	0.053	0.044
75	0.011	0.014	0.017	0.02	0.023	0.028	0.035	0.03
100	0.009	0.011	0.014	0.016	0.018	0.019	0.024	–

As will be discussed below, a quantitative analysis of the critical susceptibility peaks in the context of scaling hypothesis leads to values for the critical indices, especially for the index δ, which are difficult to explain on the basis of a simple competing-interactions picture.

The Index δ:

This index not only charaterises the field-dependence of magnetisation

$$M(H) \; a \; H^{1/\delta} \qquad \text{at } T = T_c$$

but, as the scaling law shows, also describes that of the susceptibility at the critical peaks,

$$\chi(H,t_p) \; a \; H^{1/\delta - 1} \qquad t_p = (T_p - T_c)/T_c > 0$$

Provided that the critical fluctuations are the dominant source of susceptibility at these peaks, a double-logarithmic plot of the peak susceptibility against the internal field provides a direct estimate of δ through its slope $(1/\delta - 1)$. Moreover, the value so determined is independent of the choice of the ordering temperature for the alloy.

A unique value of δ adequately describes the data for the lower concentration samples ($3 \leq c \leq 6$ at.% Gd) over the nearly two decades of the experimental field-range [fig.(5.8)]. The value of δ for the 3 and 4 at.% samples,

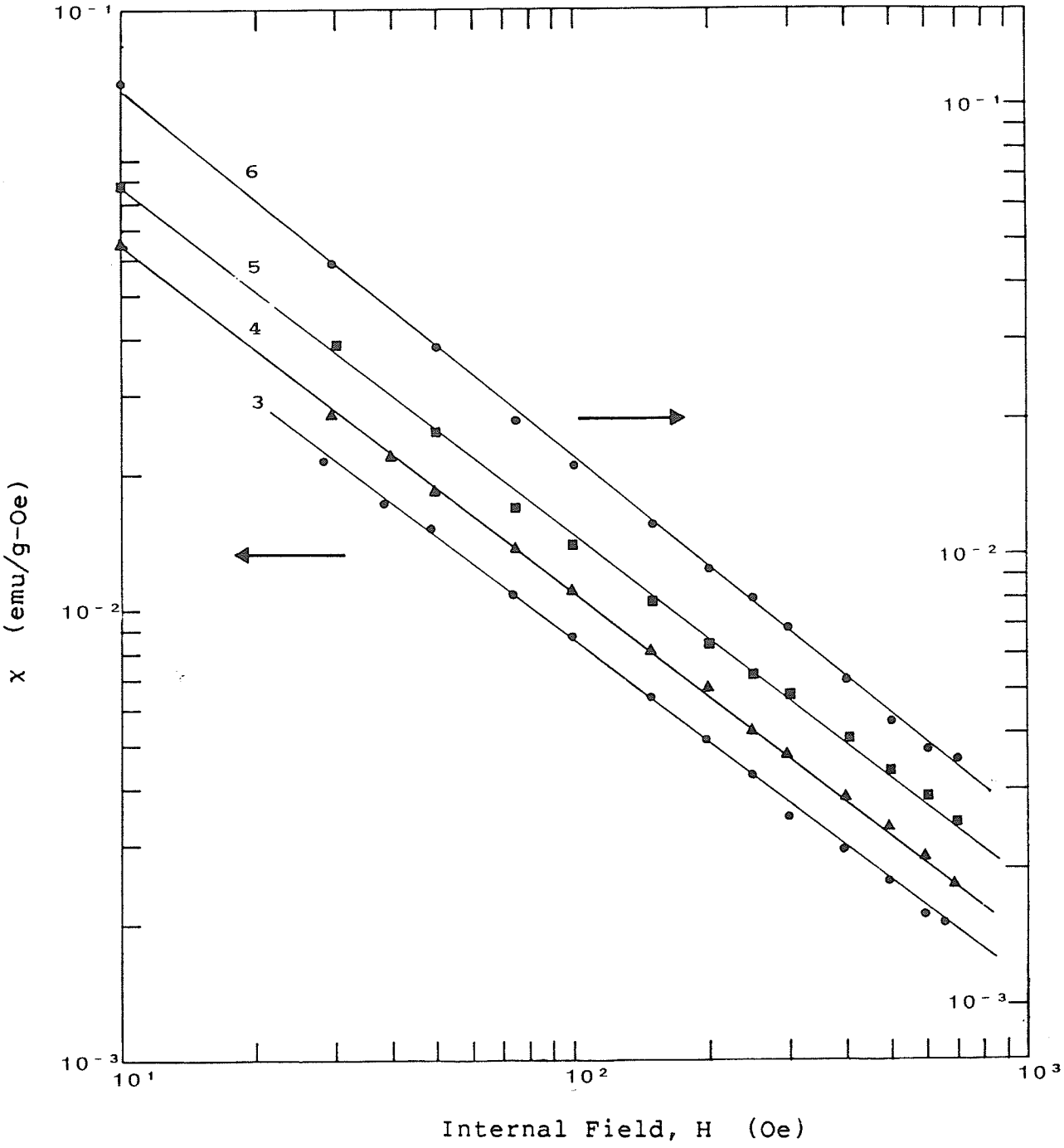

Fig.(5.8): Critical peak plots for alloys with $c \leq 6$ at.% Gd. Concentrations are marked against each straight-line fit. Plot for 6 at.% Gd refers to the scale on the right, as indicated.

as Table (5.2) shows, are close to those reported in ferromagnetic alloys such as PdMn [50] and amorphous ferromagnets [51,93]. For the 5 and 6 at.% alloys the δ values increase. A similar behaviour is reported in some amorphous systems [94] with concentrations approaching the critical value for the disappearance of the local moments. The ferromagnetic δ values observed in alloys up to 4 at.% Gd are consistent with the picture of well-localised Gd-moments interacting with one another through the long-range polarisations induced in the d-band of Palladium. Furthermore, the s-f exchange is too weak [72] to threaten the stability of Gd-moments in Palladium through mixing with non-localised conduction states.

The rise in δ values with increased concentration of Gadolinium (from 3 to 6 at.%) contrasts with the behaviour noted in the PdMn system. In the latter, the broadening of the internal field distribution caused by competing ferro-antiferromagnetic interactions leads to a decrease in δ values, not to an increase. Indeed, model calculations by Roshko and Williams [46], based on a Gaussian distribution of internal fields whose width increases with concentration, reproduce the experimentally observed critical peak behaviour in PdMn. If a similar broadening of the internal field distribution follows an increase in Gd-concentration in the PdGd system, the direction of change in the δ-values with rising concentration is quite surprising.

TABLE (5.2)

Summary of critical parameters

c	δ_{LF}	δ_{HF}	Range (Oe)	slope K/Oe^m	$T_c^{(1)}$ (K)	$\gamma^{(1)}$	$T_c^{(2)}$ (K)	$\gamma^{(2)}$
3	4.15	4.15	> 28	0.027	2.1+0.1	2.9	2.25	1.55
4	4.17	4.17	> 10	0.027	2.8 "	2.9	3.0	1.65
5	4.38	4.38	> 10	0.029	3.3 "	2.55	3.5	1.55
6	5.5	5.5	> 10	0.037	3.6 "	2.21	3.75	1.60
7	>10	3.2	10:150-700	0.035	3.7(5) "			
8	>10	3.8	" "	0.045	4.4 "			
9	>10	4.5	10:200-700	0.035	4.5 "			
10	>10	4.8	" "	0.037	4.6 "			

An increase in Gd-concentration above 6 at.% causes the critical peak plots [figs.(5.9) and (5.10)] for such alloys to exhibit a rather abrupt decrease of slope (in magnitude) in the vicinity of 150 Oe, yielding apparently smaller δ-values for the high-field regime than those for the lower fields. A similar qualitative trend observed in PdMn alloys with concentrations between 3 and 5 at.% Mn could be reproduced by the model calculations mentioned above. Yet again, however, the quantitative details of the critical peak plots for PdGd and PdMn alloys differ significantly. Whereas in the latter the low-field values increase towards that noted in "good" ferromagnets (approx. 4.2) and, the high-field values decrease progressively with rising Mn-concentration, the reverse is noted for the not-so-dilute (7 at.% and above) PdGd samples. The high-field values increase from 3.2 for the 7 at.% alloy to 4.8 for the 10 at.% alloy [see Table (5.2)]. Because the low-field slopes of the critical peak plots are close to -1, the associated δ-values are quite high (> 10) and are also subject to large errors resulting from the smallest of uncertainties in the slopes.

The origin of the above-mentioned effects is unclear. However, it may be stated with confidence that a competing-interactions approach of the type used to explain the behaviour of PdMn alloys is inadequate in the case of PdGd alloys. The magnetic behaviour of the latter system may be more complex than that of the former.

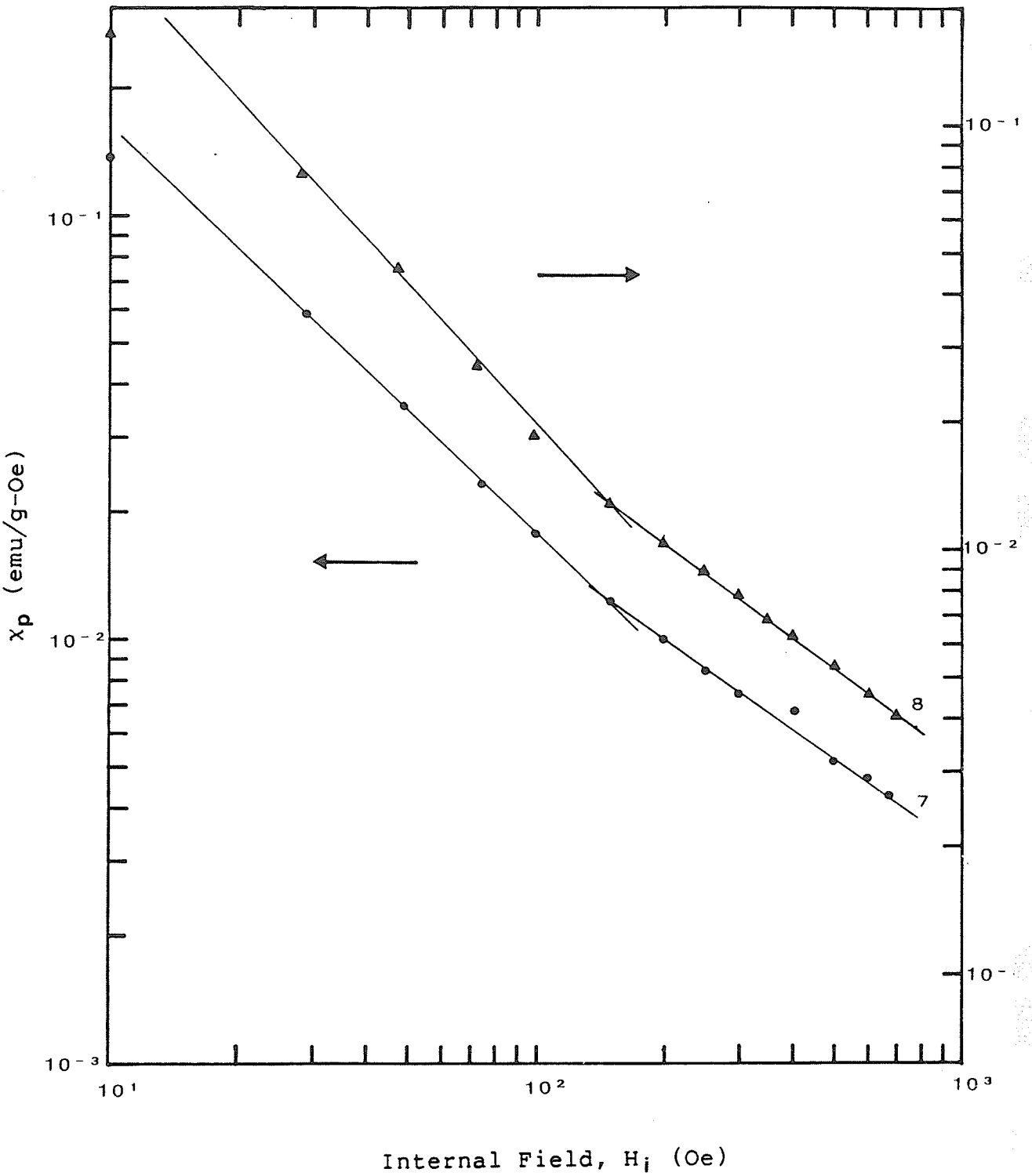

Fig.(5.9): Critical peak plots for 7 and 8 at.% Gd alloys.

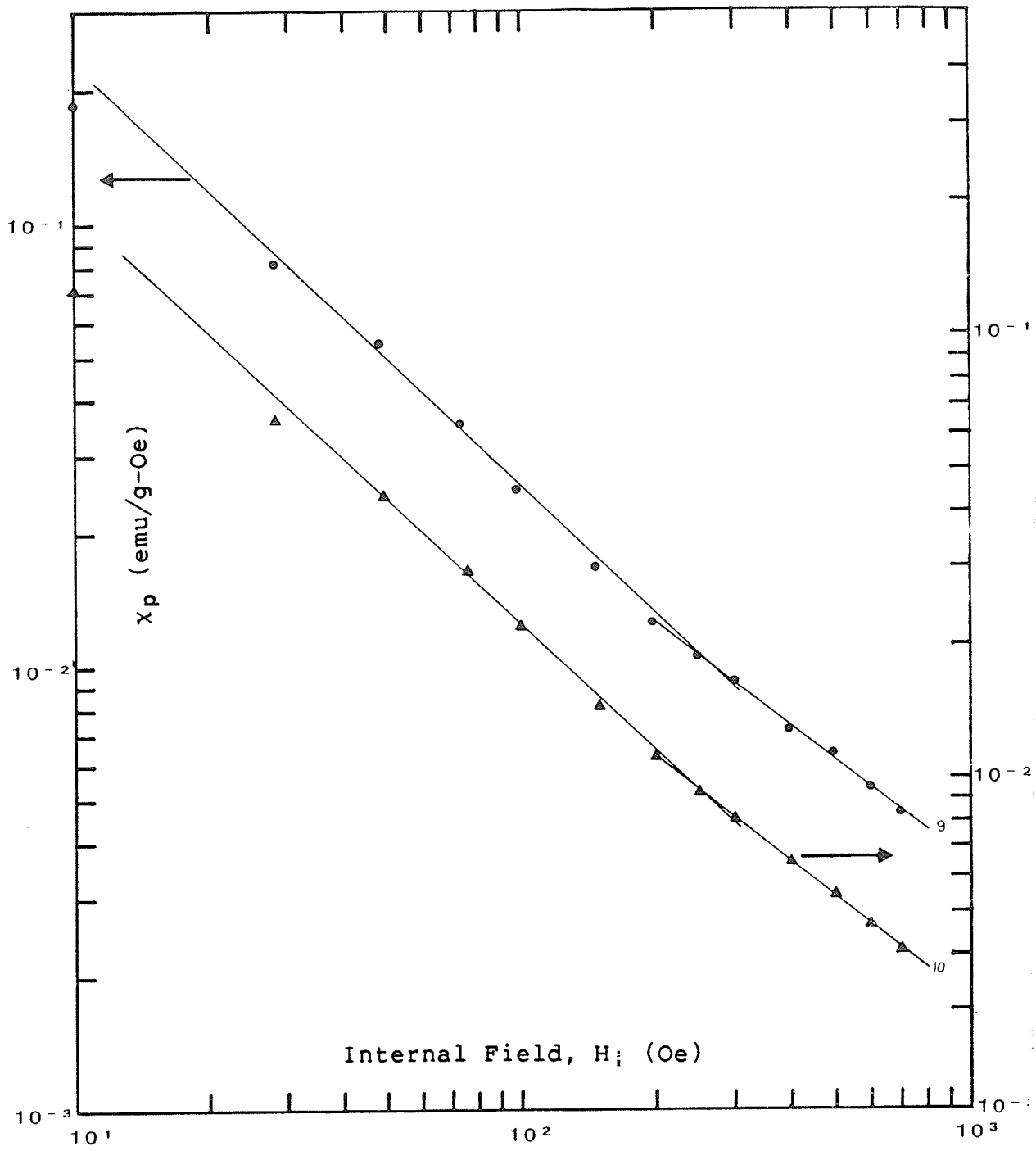

Fig.(5.10): Critical peak plots for 9 and 10 at.% Gd alloys.

The Index γ:

Unlike the parameter δ, which could be estimated without reference to the ordering temperature of the alloy under consideration, the index γ needs an apriori estimate of T_c for its evaluation since it is defined through the power law

$$\chi(0,t) \propto t^{-\gamma} \qquad T > T_c$$

The scaling equation

$$(T_p - T_c)/T_c \propto H_i^{1/\gamma+\beta}$$

furnishes a first estimate of T_c as the y-intercept of the straight line obtained by plotting the critical peak temperatures T_p against a reasonable power (approximately 0.56) of H_i. The data for all the alloys studied is summarised in figs.(5.11), (5.12) and (5.13). Within experimental uncertainty, the scaling law equation written above is satisfied. The slopes of the straight line fits and the estimated ordering temperatures, $T_c^{(1)}$, are listed in Table (5.2). In general, the scaling estimates fall below the susceptibility inflection points and close to the principal maxima. Similar situation exists for PdMn alloys which exhibit mixed ordering [50]. However, the slopes of the straight-line fits are comparable to those reported for ferromagnetic PdMn alloys [50]. The initial estimates for the ordering temperatures lead to rather large values for γ when, in accordance with the scaling equation, a double-

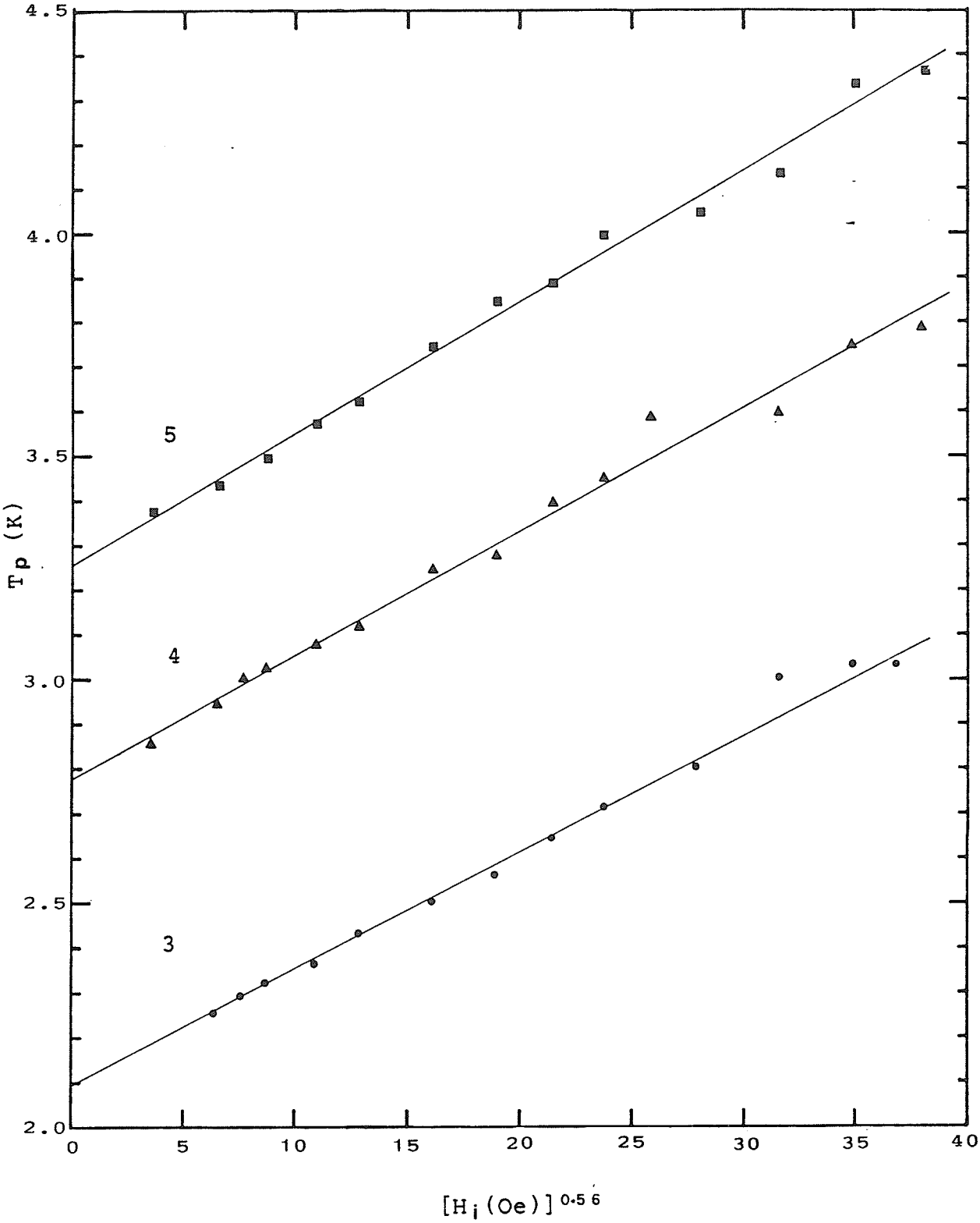

Fig.(5.11): Scaling law plots; field-dependence of critical peak temperatures. Concentrations are marked on the plots.

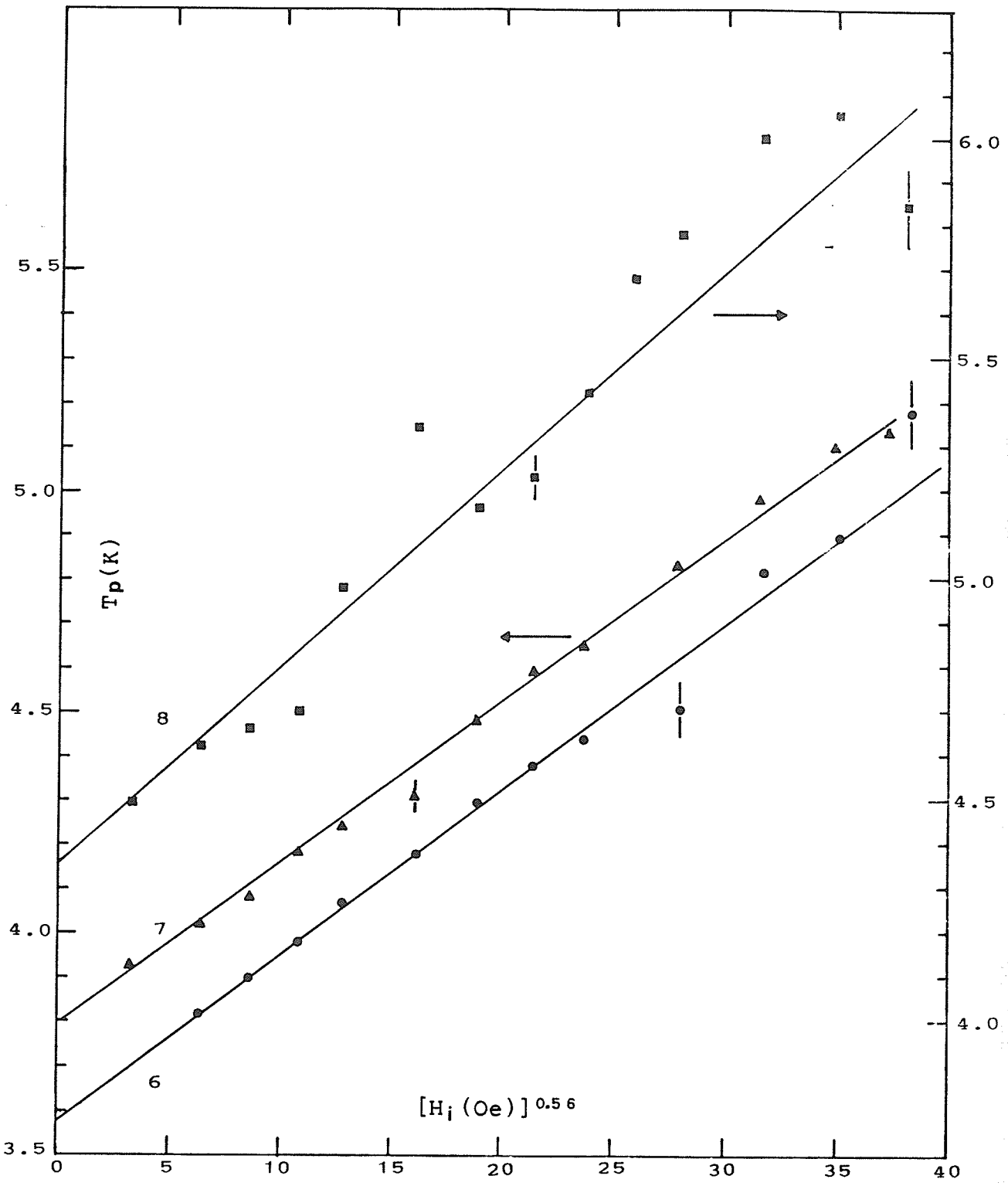

Fig.(5.12): Scaling law plots; field-dependence of critical peak temperatures. Concentrations are marked on the plots.

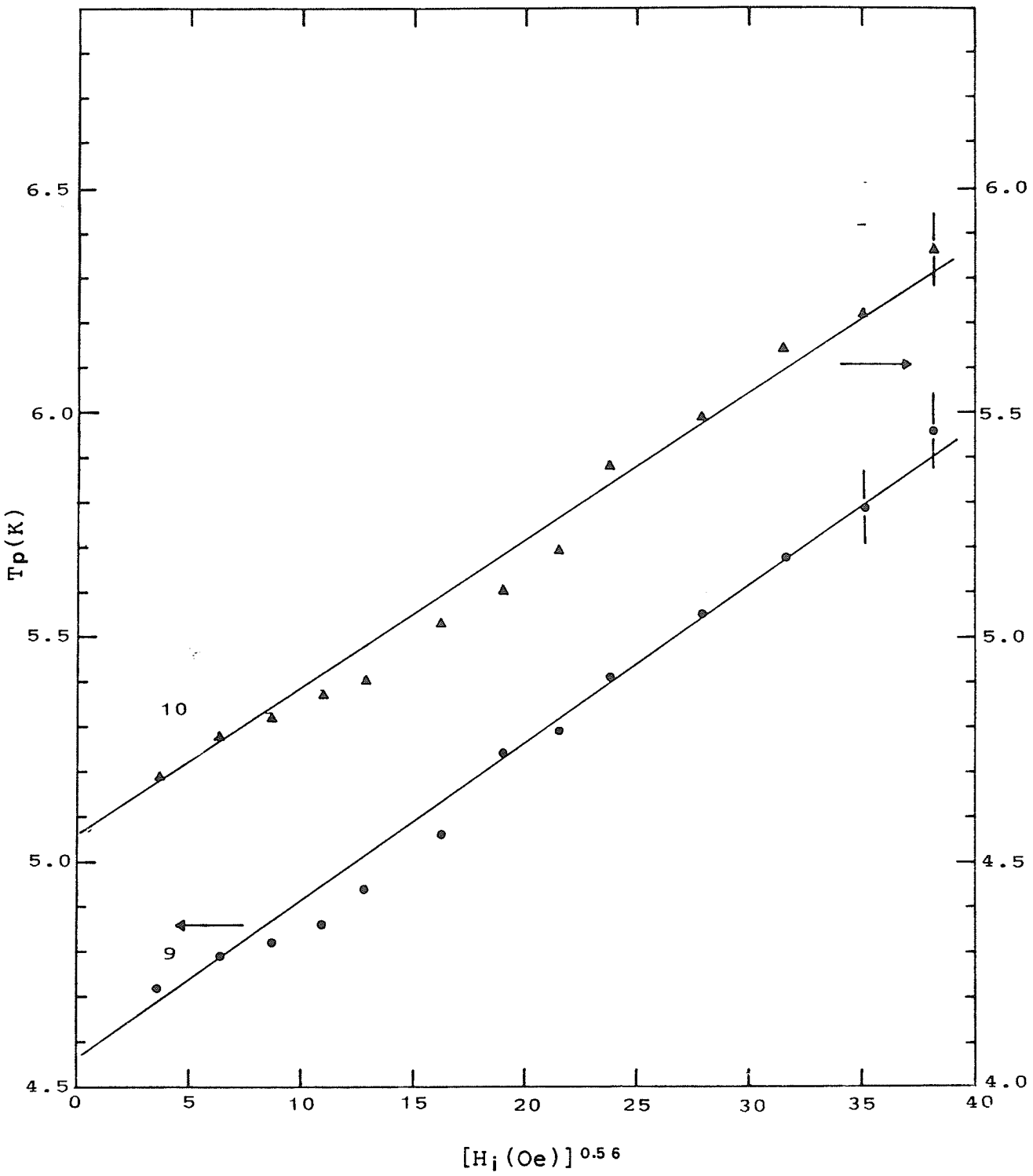

Fig.(5.13): Scaling law plots; field-dependence of critical peak temperatures. Concentrations are marked on the plots.

logarithmic plot of $\chi(0,t)$ against t is made. If the scaling equality of Widom [38]

$$\gamma = \beta(\delta - 1)$$

remains valid, enhanced β-values are predicted. Furthermore, the exponents $(\gamma+\beta)$ in the scaling equation are also enhanced above the value assumed in the scaling plots of T_p against $H_i^{0.56}$. This is in contrast with the trend deduced from a double-logarithmic plot of $(T_p - T_c)$ against H_i (not reproduced) which, though not sufficiently precise to enable an independent estimate of $(\gamma+\beta)$, nevertheless favours values of $(\gamma+\beta)$ less than, not greater than 2. The alternative to this inconsistency was to re-adjust the initial estimates of T_c in order to achieve values of γ (roughly about 1.5 to 1.6) which are consistent both with Widom's equality and with the assumed exponent $(\gamma+\beta)^{-1} = 0.56$, when a conventional value of β (roughly between 0.35 and 0.40) is used. Shifts between 0.15 to 0.2 K were required to achieve this consistency. The re-adjusted estimates, $T_c^{(2)}$ and the corresponding γ-values, $\gamma^{(2)}$, obtained are also listed in Table (5.2). The γ-values have been derived from fits spanning a range $4 \times 10^{-2} \leq t \leq 2 \times 10^{-1}$, as shown in figs.(5.14) and (5.15). Such an analysis has been carried out only for concentrations below 7 at.% Gd. For higher concentrations the data show structure and preclude any meaningful straight-line fits through them. No γ-estimates for them are thus available.

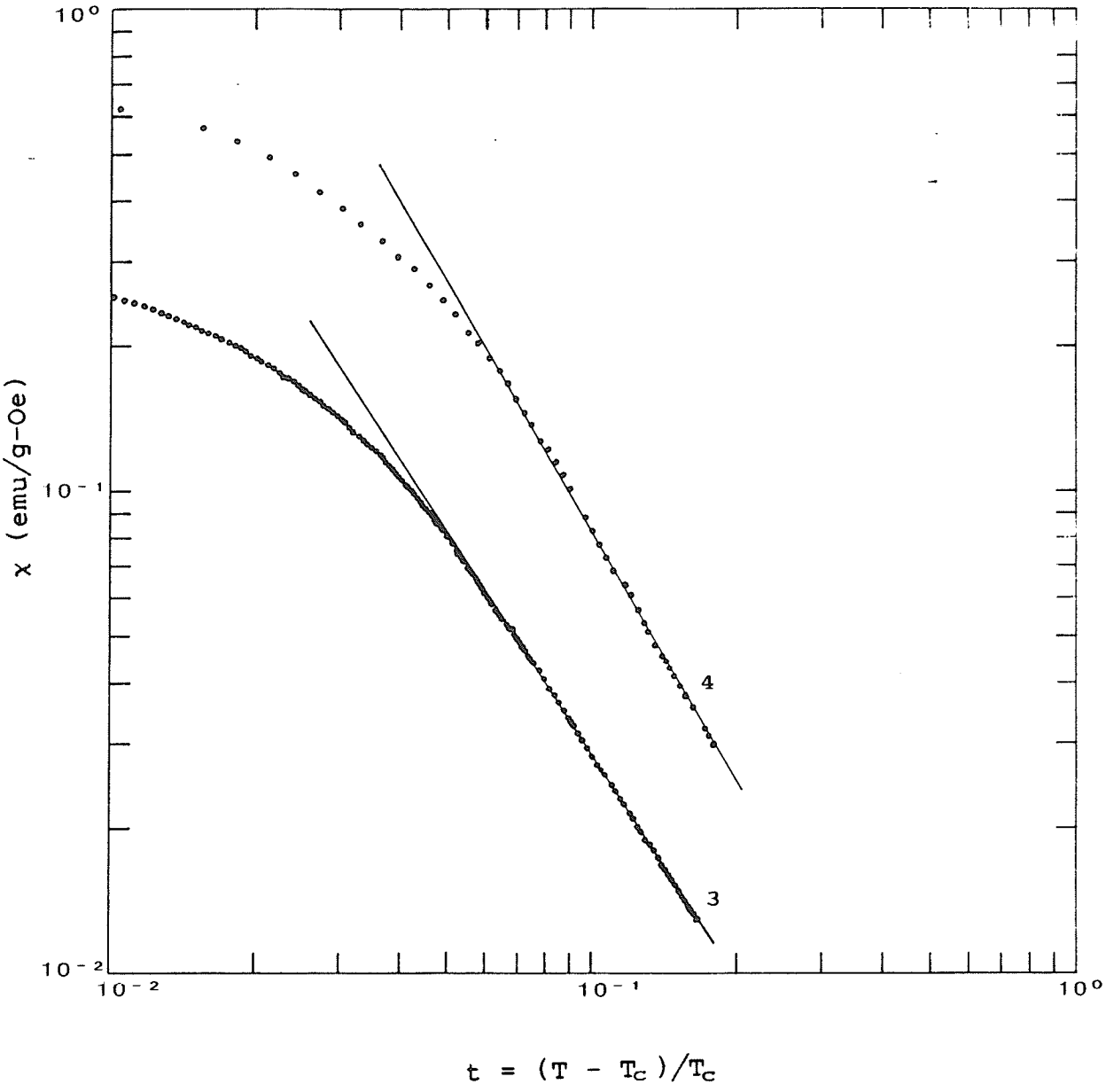

Fig.(5.14): Susceptibility-vs-reduced temperature (γ-plots). Concentrations are marked on the plots.

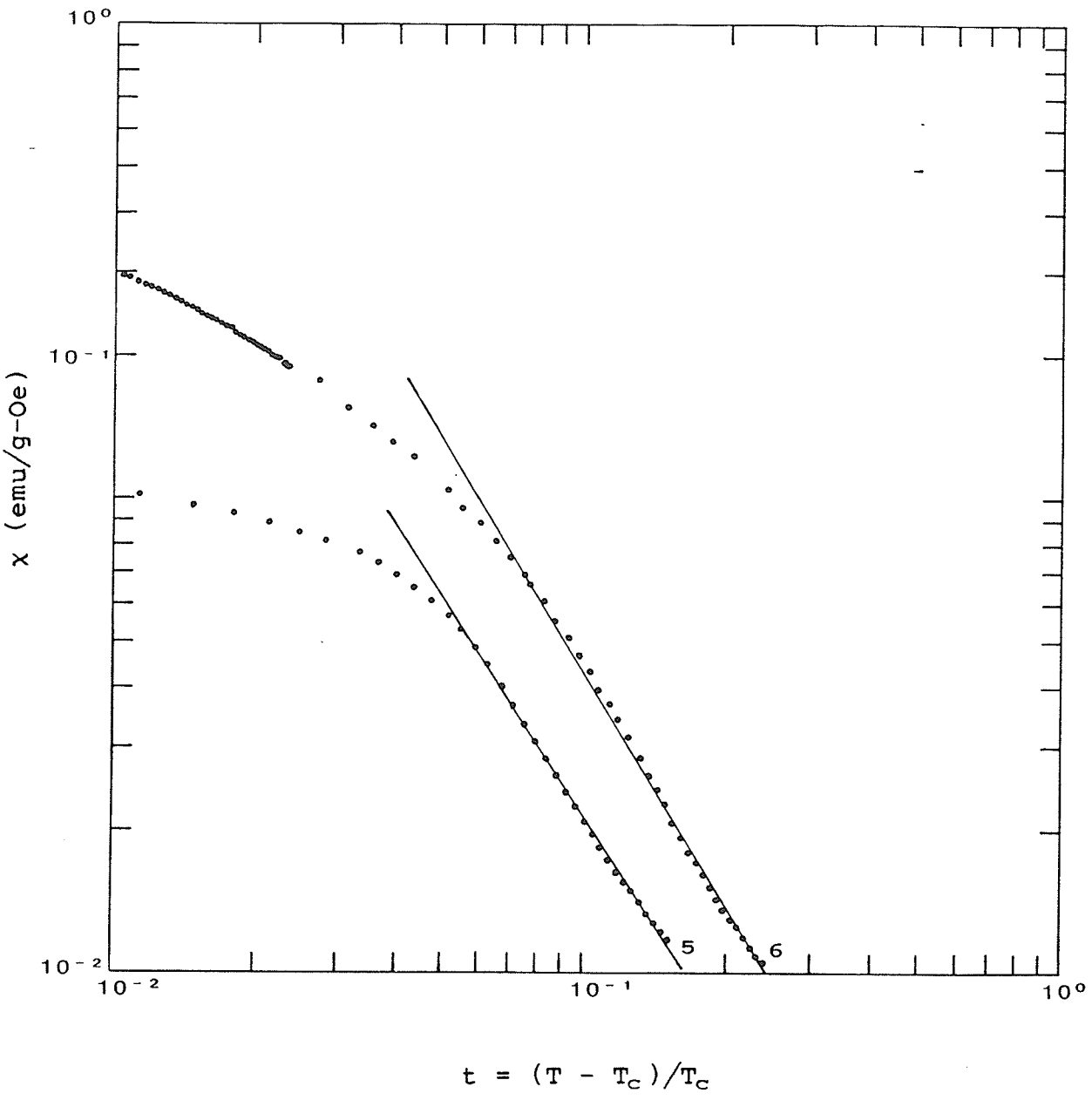

Fig.(5.15): Susceptibility-vs-reduced temperature (γ-plots). Concentrations are marked on the plots.

Following Ho et al [50], estimation of the critical amplitudes and hence the effective Gd-moments was attempted using the γ-plots and the mean-field approximation.

$$\chi(H=0,\ T>T_c) = N\mu_{eff}^2/3k(T-\theta) \qquad (5.6)$$

Within the mean-field approximation θ is identical to the Curie temperature and, $\gamma = 1$. The above expression may be re-written as

$$\chi(H=0,\ T>T_c) = At^{-\gamma} \qquad (5.7)$$

where t is the reduced temperature and A is the critical amplitude which is related to the effective moment by

$$A = N\mu_{eff}^2/3kT_c \qquad (5.8)$$

in the mean-field approximation.

Hence if the γ-plots are extrapolated to t=1 (i.e. $T=2T_c$) the above equation can furnish estimates for the effective moment. A meaningful result (7.4 μ_B) is obtained only for the 3 at.% alloy. A rather tentative choice of γ (hence of T_c) and, perhaps, non-validity of the mean-field approximation in the higher concentration samples prevent reasonable estimates for the effective moments to be obtained for them.

5.2 ELECTRICAL RESISTIVITY

The low-temperature resistivity of dilute PdGd alloys has two essential temperature-dependent contributions. The first -- pure host resistivity -- is controlled by the specific electronic structure of Palladium. The second, called the impurity resistivity, results from the presence of imperfections and impurities (including Gd) in the host lattice. Hence, it is convenient to write the total resistivity as

$$\rho(T) = \rho_h(T) + \rho_i(T) \tag{5.9}$$

The scattering of electrons from the randomly distributed Gd-moments causes the impurity resistivity $\rho_i(T)$ to be temperature-dependent. The presence of static imperfections and non-magnetic impurities in the host lattice is responsible for a temperature-independent component, ρ_0, of the impurity resistivity. Hence, $\rho_i(T)$ may be written as

$$\rho_i(T) = \rho_0 + \Delta\rho(T) \tag{5.10}$$

where $\Delta\rho(T)$ is sometimes referred to as the magnetic contribution to resistivity because it arises as a result of magnetic interactions between the conduction electron spins and the dissolved Gd-moments. Equations (5.9) and (5.10) lead to

$$\rho(T) = \{\rho_0 + \rho_h(T)\} + \Delta\rho(T) \qquad (5.11)$$

The separation of the alloy resistivity into these apparently independent components is a useful first approximation, and an example of what is known as the Matthiessen's rule. In its generalised form the rule asserts that the various resistive scattering mechanisms present in a solid produce a net resistivity which may be obtained as a sum of the resistivities due to each mechanism acting independently. In the present work, the magnetic component $\Delta\rho(T)$ is isolated from the total measured resistivity of the alloy through a simple subtraction of the Gadolinium-free host resistivity {i.e. $\rho_0 + \rho_h(T)$}, assuming that Matthiessen's rule remains valid.

The validity of the above assumption depends upon the extent to which the various mechanisms normally believed to be responsible for causing deviations from the Matthiessen's rule can either be neglected or ruled out. First, the thermal effects can be neglected because the temperature range examined is extremely small and lies below 10 K; both the geometrical form factor and the atomic volume are essentially temperature-independent in that range. Secondly, at low temperatures the modification of the host phonon spectrum due to the presence of a small number of impurities in the lattice is not important for two reasons:

one, the phonon resisitivity is almost completely extinguished at the working temperatures (between 1.5 K and 10 K) and second, at such low temperatures the spectrum, if at all, is dominated by long wave-length phonons which are insensitive to the presence of a few alien atoms in the lattice. The above two mechanisms, therefore, may not be expected to cause significant breakdown of Matthiessen's rule. In all metals generally, the difference in relaxation time anisotropies due to the various scattering mechanisms is expected to cause deviations from Matthiessen's rule [95]. However if the solute resistivity dominates, the deviations from the rule are proportional to the weaker, pure-host resistivity and independent of the solute concentration [95].

The resistivity of the pure sample of Palladium (resistivity ratio $\rho(300\ K)/\rho(4.2\ K) = 100$) used in this investigation is shown in fig.(5.16). The data were fitted to a T^2-curve in the range $1.5\ K \leq T \leq 4.5\ K$, as shown in fig.(5.17). Schindler and Coles [55] have previously reported a T^2-dependence up to 7 K for a sample of pure Palladium with a resistivity ratio in excess of 1000. Such a dependence may result from two types of processes -- a non-magnetic process involving scattering from charge-density fluctuations, or a magnetic one involving scattering from spin-density fluctuations in the d-band of the incipient ferromagnet, Pd. There is disagreement on the

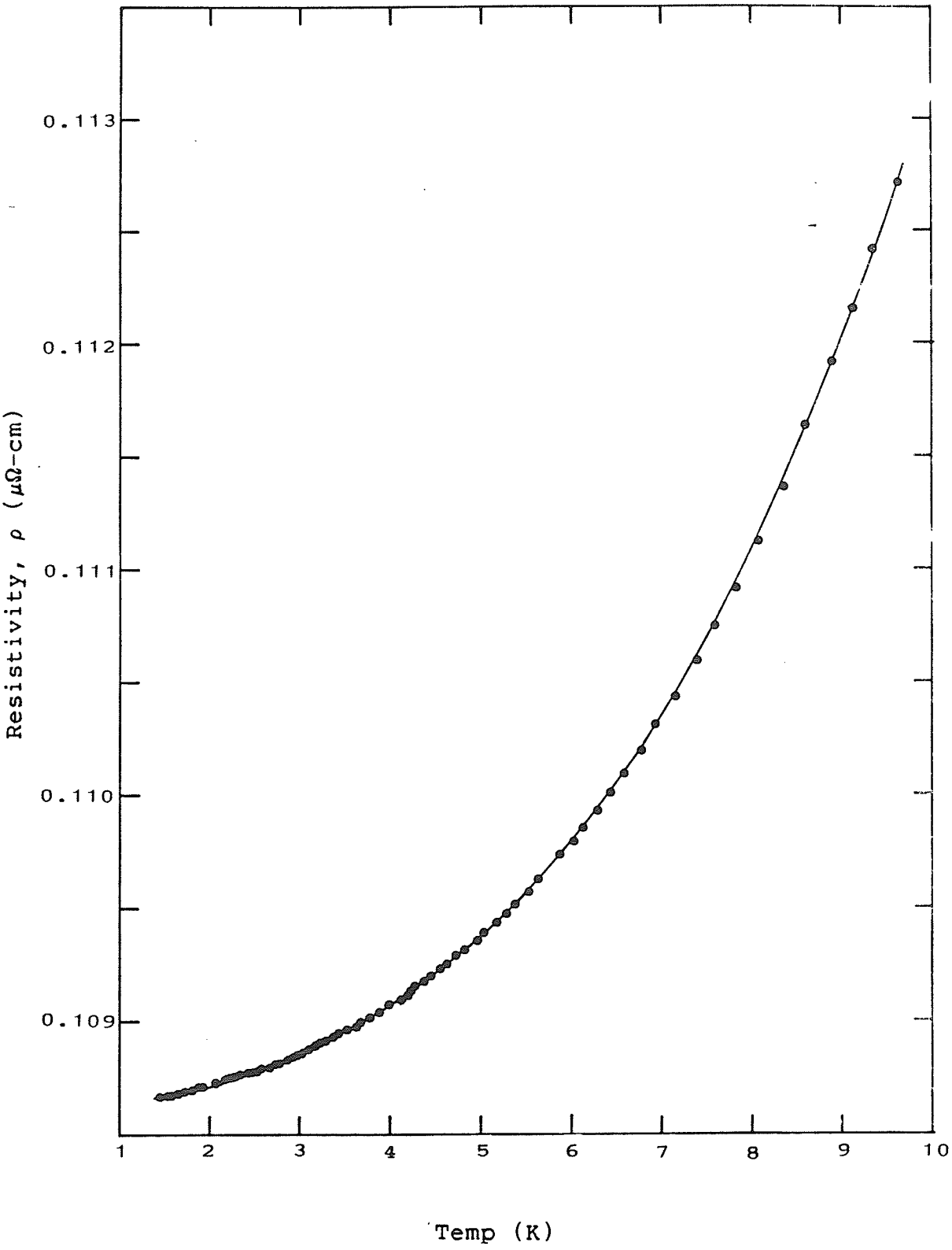

Fig.(5.16): Resistivity-vs-temperature characterstic for pure Palladium.

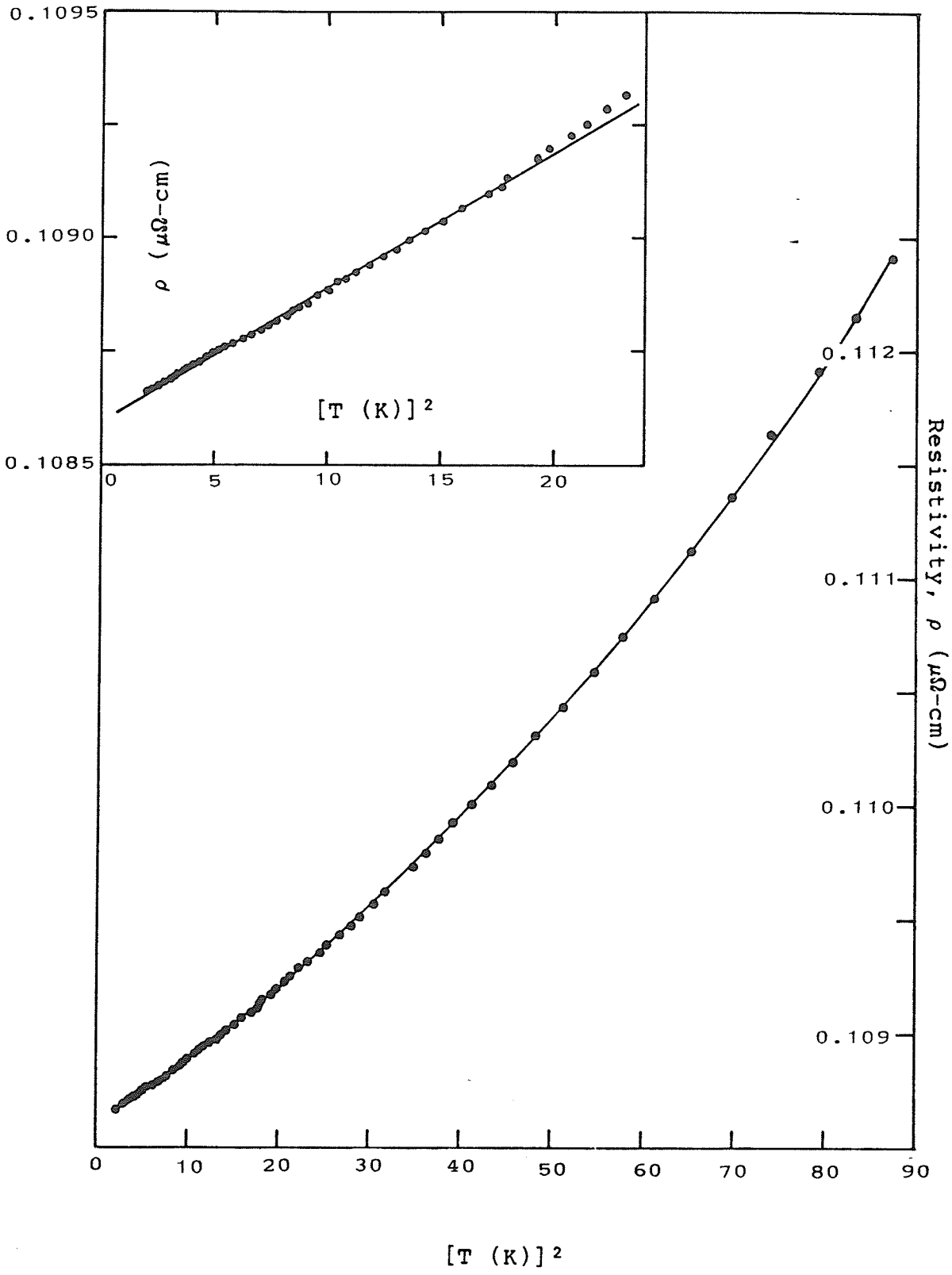

Fig(5.17): Resistivity-vs-T^2 for pure Palladium. The inset shows the low-temperature region on an expanded scale.

question of the dominant mechanism. Nevertheless, as an experimental result, the Pd resistivity may be expressed as

$$\rho_{Pd} = \rho_0' + AT^2 \qquad (5.12)$$

with ρ_0' = 0.108601 $\mu\Omega$-cm and A= 2.92 x 10^{-5} $\mu\Omega$-cm/$^0K^2$. The value of A obtained here agrees to within 8 % with that quoted previously by Purwins et al [96] and others.

The solute resistivity dominates the pure-host resistivity (represented in eqn.(5.12) as AT^2) for even the least concentrated of PdGd alloys studied, as can be seen from the total magnitudes of the alloy resistivities (which are greater than 5.5 $\mu\Omega$-cm at 4.2 K). Consequently, deviations from Matthiessen's rule should remain very weak, provided that the perturbations to the host band-structure due to the presence of Gd-impurities stay insignificant.

Hence the question: Up to what concentrations do the Gd-impurities not modify the Pd band-structure appreciably? A plot of residual resistivities (extrapolated for T = 0) against Gd-concentration was fitted to a straight line passing through the origin. As discussed later, such a procedure indicates that Gd concentrations as high as 7 at.% may allow the use of Mattheissen's rule.

5.2.1 Correction of the Data

Assuming, therefore, that the Mattheissen's rule remains valid for $c \leq 7$, the pure-host resistivities at various temperatures were simply interpolated from the experimental data and subsequently subtracted from the measured zero-field alloy resistivities at corresponding temperatures. In the absence of an alternative, the same procedure was used for concentrations above 7 at.%.

To treat the resistivity data in high-fields (70 kG), an alternative approach was adopted because no independent measurements of the high-field pure-Pd resistivity were made. The T^2-dependence noted in the zero-field data on pure Pd in the temperature range $1.5K \leq T \leq 4.5K$ was also assumed to hold in the presence of an applied magnetic field. The coefficient A in eqn.(5.12) was assumed to carry the field-dependence and the latter was approximately estimated from a paper by Schindler and Laroy [97].

$$A(H) = A - 2.8 \times 10^{-10} H$$

Within the range of applicability of the T^2-behaviour, an applied field of 70 kG modifies the host resistivity by up to 0.3 % . In the high-field case, the T^2-behaviour was assumed to be valid up to temperatures about 6 K because in this temperature interval, the deviations of the zero-field, pure-Pd resistivity from a T^2-curve are only about 0.1 % of its value at the lowest measured temperature. Since the

field-dependent correction of 0.3 % (or larger at temperatures above 4.5 K) exceeds this error, it was considered worth applying to the data. The corrected host resistivities were subtracted from the alloy resistivities measured in 70 kG to obtain the magnetic component in accordance with Mattheissen's rule.

5.2.2 Results

Two sets of zero-field resistivity measurements on PdGd alloys, separated in time by about 2.5 yrs were performed, the first set being immediately after the samples were prepared and homogenised. For the most part, the gross features, such as a sharp linear decline below an ordering temperature followed by a non-linear decay at still lower temperatures, are reproduced. The differences are seen in the position of the various characterstic features on the temperature axis and in the different magnitudes of resistivity changes between similar temperature zones. The differences are larger for larger concentration alloys. The 3 at.% Gd sample shows almost no change in the quantities of interest. The 4 at.% Gd sample, shows approximately 9% smaller decline in resistivity between 4.2 K and 1.5 K. The "kink" in the resistivity is broader compared to the first measurments. Both these facts point to the existence of greater amount of disorder in the material and may be ascribed to aging of the samples. The resistivity of the rest of the alloys shows larger decreases between 4.2 K and

1.5 K. The total resistivity in all these cases at 4.2 K is higher in the second set of measurements than in the first. Again, this has an easy explanation as an aging effect. In view of this interpretation, the following discussion will be based exclusively on the first set of resistivity measurements.

The first sample in the series, Pd + 2 at.% Gd, shows a negative temperature coefficient of resistivity between 1.5 K and 4.5 K [fig.(5.18)]. The total fractional decline of resistivity (compared to its value at 4.5 K) in this temperature range is well above the limits of resolution of the equipment; therefore, this result merits consideration.

The data between 2.20 K and 4.43 K could be fitted to a Kondo-type logarithmic expression [98] {see inset in fig.(5.18)}

$$\rho = A + B \ln T \qquad (5.13)$$

with

$A = 5.7748\ \mu\Omega$-cm

$B = 1.17 \times 10^{-3}\ \mu\Omega$-cm

If Gd impurities are assumed to be responsible for this logarithmic behaviour, the effective s-f exchange constant J can be estimated since the constants A and B are both related to it.

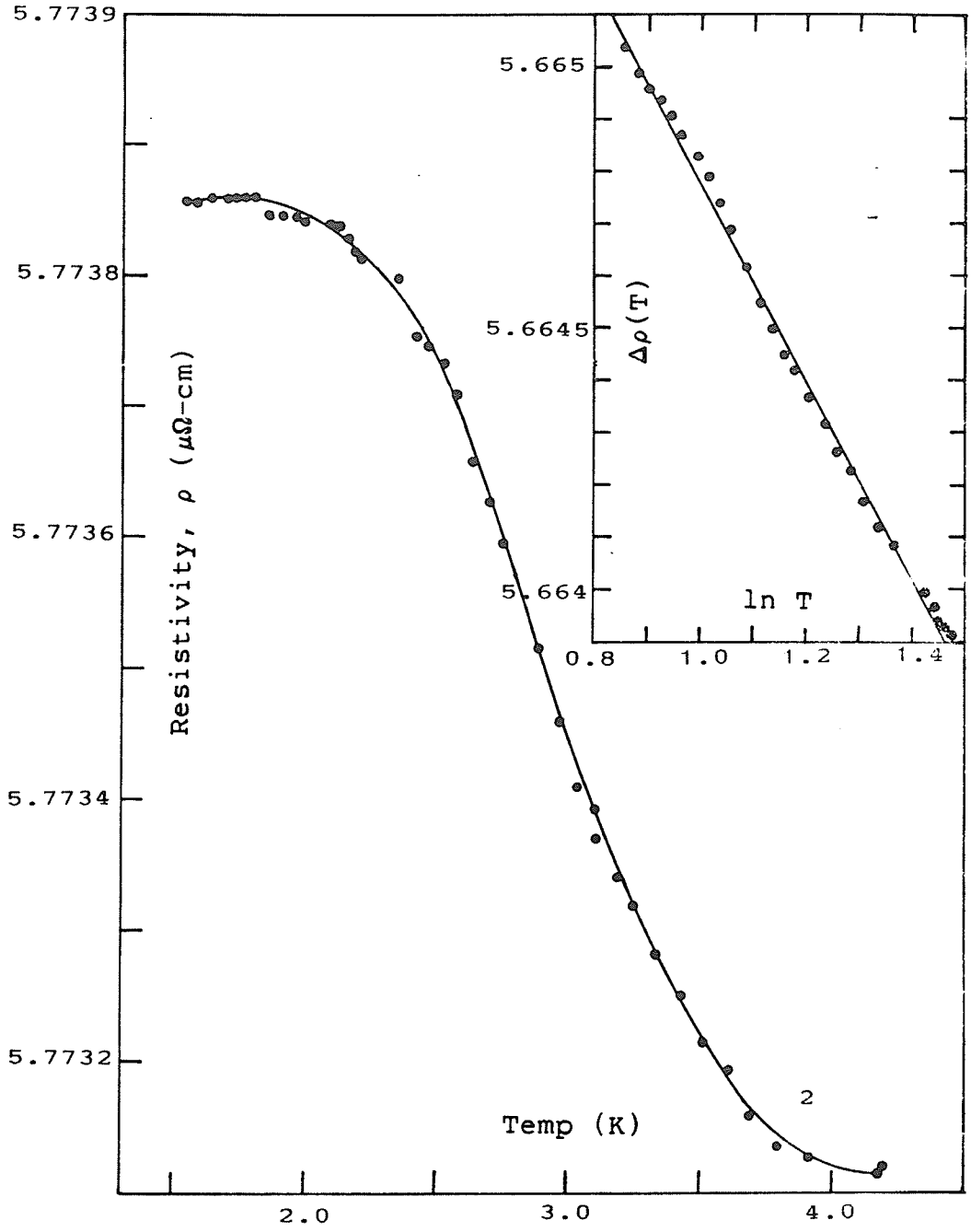

Fig.(5.18): Resistivity-vs-temperature and, incremental resistivity-vs-ln T for 2 at.% Gd alloy.

$$A = \rho_{sd}^{(1)} [1 + JN(\epsilon_f).\ln(k/D)]$$

$$B = \rho_{sd}^{(1)} JN(\epsilon_f)$$

where

$$\rho_{sd}^{(1)} = \alpha c J^2 S(S + 1)$$

is the paramagnetic resistivity. Here α is a parameter related to the band properties of Pd having a value 5.88 $\mu\Omega$-cm/at.%-(eV)^2 and c is the concentration in atomic percent. Interestingly, the estimate thus obtained for J, -0.014 eV, agrees with the value reported previously [99] from EPR g-shift measurements on alloys of much lower concentrations. A fairly concentrated sample such as Pd + 2 at.% Gd is not likely to show a single-impurity behaviour due to strong polarisability of the Pd-matrix. An early study by Sarachik and Shaltiel of the resistivity of PdGd alloys with Gd concentrations as low as 0.1 at.% did not reveal any Kondo behaviour. Further, a subsequent study by Cannella et al [72] on a 2 at.% sample simply suggested a cooperative transition to a ferromagnetic ground state below 1.5 K, a value which falls well below the 'Kondo temperature' of 3.1 K estimated for the alloy in the present case. The behaviour becomes even more difficult to comprehend when it is noted that the estimates of J obtained from the measurements on higher concentration samples are concentration-independent and considerably smaller

(0.003 eV), in close agreement with the values reported by Cannella et al [72]. It is possible that this unexpected Kondo behaviour is a result of other rare-earth impurities, possibly Europium, in this alloy.

The resistivity data for PdGd alloys with concentrations between 3 and 5 at.% Gd are presented in fig.(5.19). A weak temperature-dependence of resistivity changes into a much stronger one as the temperature falls through a narrow range of values about a critical point for each of the alloys considered. The behaviour reflects the characteristics of a Long and Turner model system [29] which has been cooled through its ferromagnetic ordering temperature. The resistivity declines linearly below the ordering temperature in all three cases. However, the ordering temperature itself is sharply defined only for the 3 at.% alloy. In other alloys, the discontinuity in the first temperature-derivative occurs through a range of temperatures; the range widens as the concentration increases from 4 to 5 at.% Gd. Further, the ordering temperature increases with concentration.

As mentioned above, the Long and Turner model [p.48] provides a good qualitative description of the resistivity behaviour in these alloys. Just above the ordering temperatures, the well localised Gd-moments are disordered; the resistivity contribution due to this source is thus saturated and consequently, temperature-independent. Below

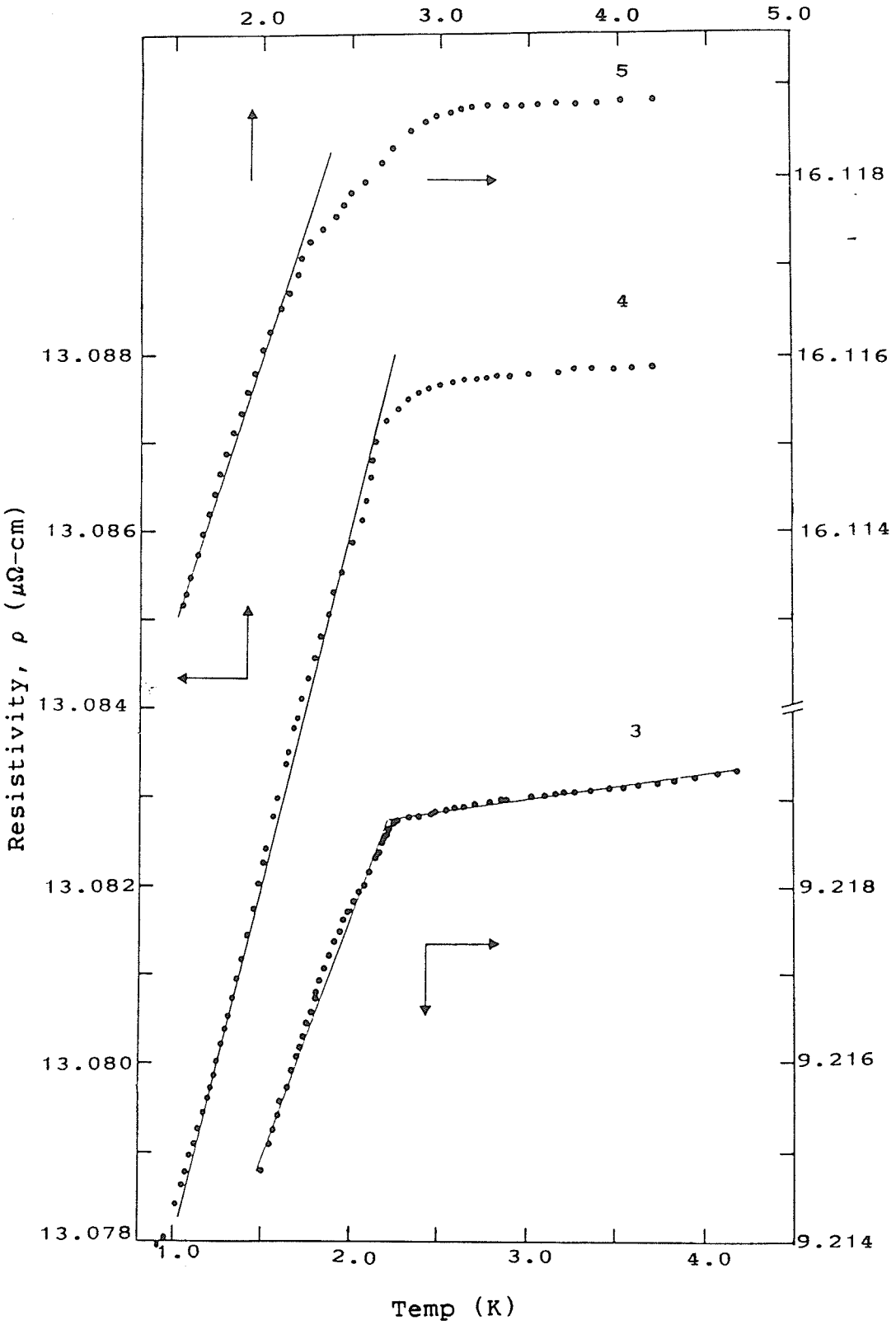

Fig.(5.19): Resistivity-vs-temperature data. Concentrations are marked against the plots.

the ordering point the moments begin to order co-operatively. Some of the inelastic spin-flip scattering channels start to freeze out. As the temperature falls further below the ordering point, more and more inelastic channels are removed leading to a sharp reduction in the resistivity. The Long and Turner model predicts an additional feature in the resistivity, arising due scattering from spin-waves in the coupled d-band - impurity spin system at very low temperatures. The predicted $T^{3/2}$-dependence is not observed down to about 1.5 K in any of the above three alloys. Perhaps, the lowest achieved temperature in this study is still an appreciable fraction of the ordering temperatures of the alloys. Spin-waves are not significantly excited at such temperatures.

If indeed, the above explanation is correct, it can be said that the alloys with $3 \leq c \leq 5$ at.% Gd undergo a transition from a paramagnetic to a predominantly ferro-magnetic state as the temperature falls below the ordering temperature. While in the 3 at.% alloy, a sharp transition must indicate a correspondingly sharp distribution of internal fields at impurity sites, the gradual smearing of this transition with rising concentration must result from the increasing probability of direct impurity-impurity interactions. As inferred from the susceptibility data these interactions, which are expected to be antiferromagnetic, do not seem to compete with the long-

range RKKY exchange in the same manner as observed in moderately concentrated PdMn alloys. Further, an increasingly stronger magnetic response (as evidenced by the a.c. susceptibility) with increasing Gadolinium concentrations also signals an increase of the ferromagnetic component in the ordered state.

In the resistivity of PdGd alloys with c > 5 at.% , peaks emerge below the respective ordering temperatures. An example is presented in fig.(5.20) for the case of 6 at.% alloy (other data is in appendix B). For ferromagnetic alloys based on exchange enhanced hosts such as Palladium, no such peaks are predicted by the Long and Turner model. However, the other predicted features are observed in the experimental data. The resistivity still exhibits a very weak temperature-dependence at higher temperatures. As the temperature is lowered, initially it declines but within an interval of a few-tenths of a degree it begins to rise, attains a maximum value above the saturated spin-disorder resistivity and then resumes its decline which remains linear until very low temperatures (compared to the respective ordering temperatures) are attained. At these low temperatures the resistivity shows a $T^{3/2}$-decline, as expected for disordered ferromagnetic systems with significant electron-magnon scattering. The behaviour in the vicinity of the peaks is similar to that observed in some YGd alloys [23] which were predicted to show helical

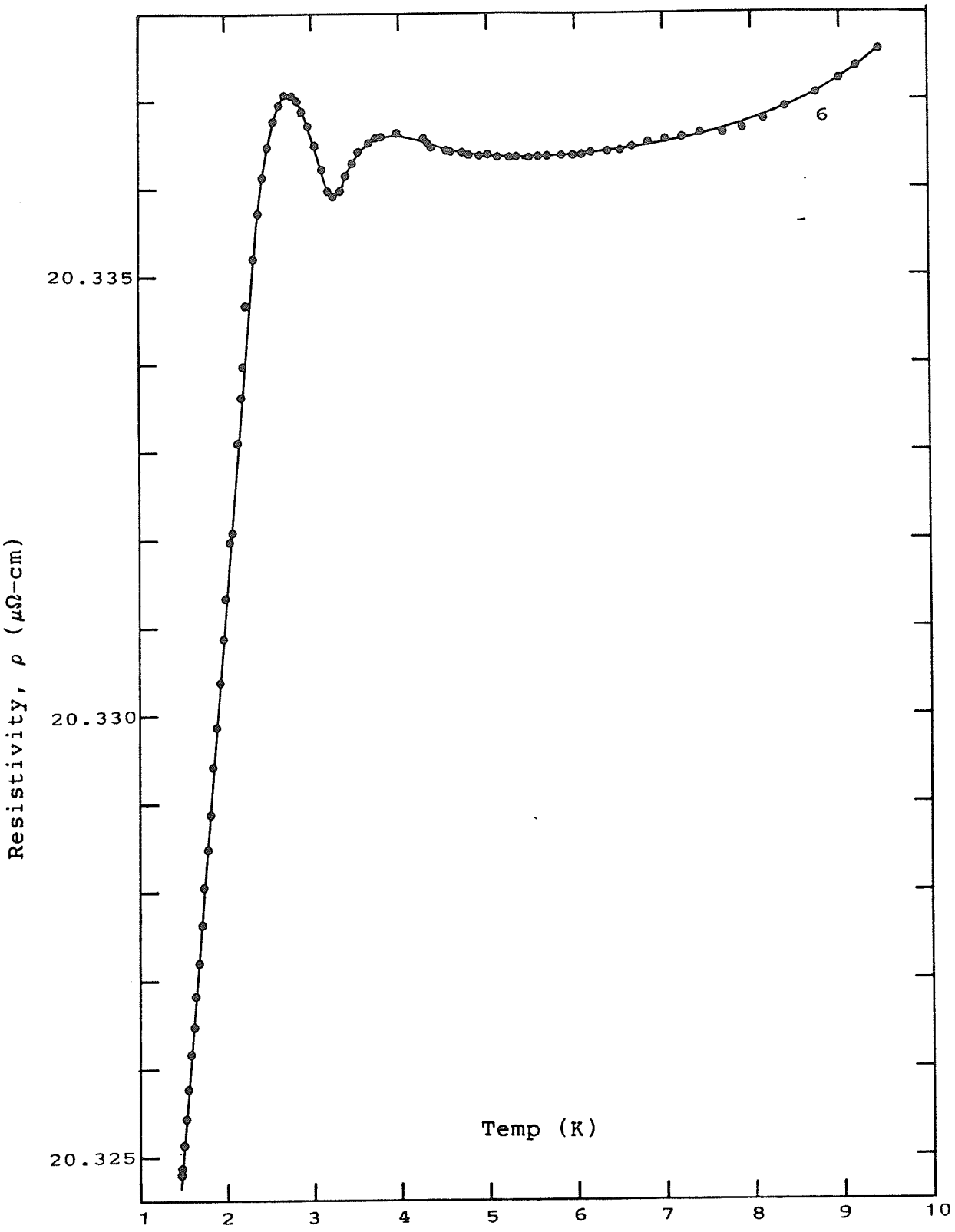

Fig.(5.20): A typical example of peaks in resistivity below the ordering temperatures. (Pd + 6 at.% Gd).

ordering above 2.6 at.% Gd by Southern and Sherrington [24]. An Overhauser stabilisation [22] of a spin-density wave (SDW) in the conduction electron gas of the host by interactions with the impurity moments is believed to cause a spiral magnetic structure in YGd alloys. On the other hand, a peak in the resistivity of a 9 at.% PdGd alloy noted by Schiffrin [100] was ascribed to the presence of undesirable Pd_3Gd phases in his sample by Guertin et al [79].

While none of the samples was examined microscopically at the time of the first resistivity measurements, a disc-shaped specimen of the 8 at.% Gd alloy, cut from the resistivity sample strip was studied under a transmission electron microscope after completion of all measurements on it to check for the presence of the above-mentioned inter-metallic phases. Diffraction patterns taken from several areas of the sample did not reveal any super-structure spots upon indexing with an f.c.c. lattice parameter of 3.956 Å (for 8 at.% alloy) [101]. One tiny area (less than 0.26 μ x 0.33 μ) did, however, show mixed even and odd, along with the regular unmixed f.c.c. indices on the pattern. A second examination of the sample after re-annealing at 1030 ^{0}C for 42 hours under vacuum (3 x 10^{-6} torr at room temperature) showed no signs of an ordered cubic structure despite a thorough scan through the "transparent" areas of the sample. Since this repeated heat treatment was similar to that given

initially it can be said with reasonable certainty that ordered phases did not consititute a significant fraction of the random PdGd alloys; that resistivity peaks are, indeed, intrinsic to them.

An Overhauser-type of mechanism, similar to that proposed in YGd alloys may cause the appearance of resistivity peaks. The exchange between the Pd d-band electrons (which are more strongly polarisable than the s-electrons) and the impurity might lead to the stabilisation of a periodic spin-density wave in the former. The introduction of a magnetic periodicity uncorrelated with the lattice structure could cause new Brillouin zone boundaries; the associated energy gaps in the spectrum of conduction states could be established in the vicinity of the Fermi surface. Depending upon the exact situation of the Fermi energy in relation to the new boundaries, the Fermi surface may be sliced or distorted. The attendant depletion of the scattering states for the Fermi electrons would cause the resistivity to rise above the spin-disorder limit. As the temperature drops, the thermal energy gets progressively insufficient to excite electrons across the energy gap into the new conduction band. The resistivity, therefore, continues to rise until the thermal excitation energy is wholly inadequate to raise electrons to the new conduction band. Further lowering of temperature below that of ordering only serves to suppress the fluctuations in the collective magnetic order and hence,

to decrease the resistivity in the same manner as in the lower concentration PdGd alloys where the increasingly more stable ferromagnetic order leads to a decline in spin-disorder resistivity.

Estimation of Exchange Constants:

Assuming that complete disorder exists above the ordering temperature, the spin-disorder resistivity can furnish an estimate of J, through

$$[\Delta\rho(T_c) - \Delta\rho(0)] = \alpha c J^2 S(1 + 4S) \qquad (5.14)$$

In high concentration alloys for which the ordering temperatures are comparatively higher, a $T^{3/2}$-behaviour is noted in the resistivity at the lowest temperatures examined. Plots of incremental resistivity vs $T^{3/2}$ for alloys from 7 to 10 at.% Gd are shown in figs.(5.21) and (5.22). Estimates for the residual resistivities, $\Delta\rho(0)$, for use in eqn.(5.14) may be obtained by a linear extrapolation of the above plots to T = 0. For samples between 3 and 6 at.% Gd, which do not exhibit such a $T^{3/2}$-dependence within the experimental temperature range, an estimate for $\Delta\rho(0)$ is difficult. However, the values of $\Delta\rho(T)$ at the lowest achievable temperatures (roughly 1.5 K) provide a lower bound on the value of J. An upper bound on its value is obtained by linear extrapolation of the $\Delta\rho$-vs-T curve to T=0. A plot of the incremental resistivities of

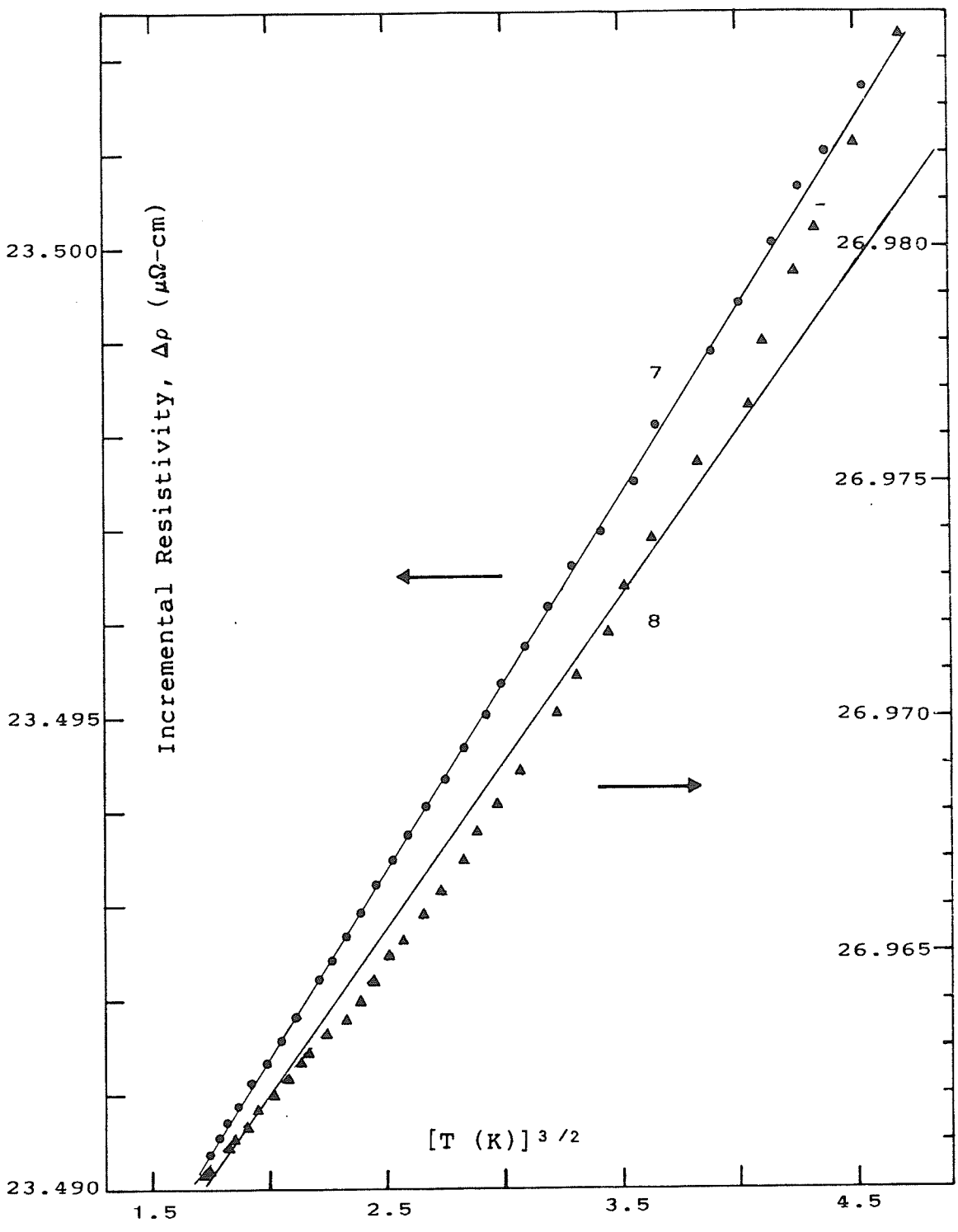

Fig.(5.21): Incremental resistivity-vs-$T^{3/2}$ plots.
Concentrations are marked against the plots.

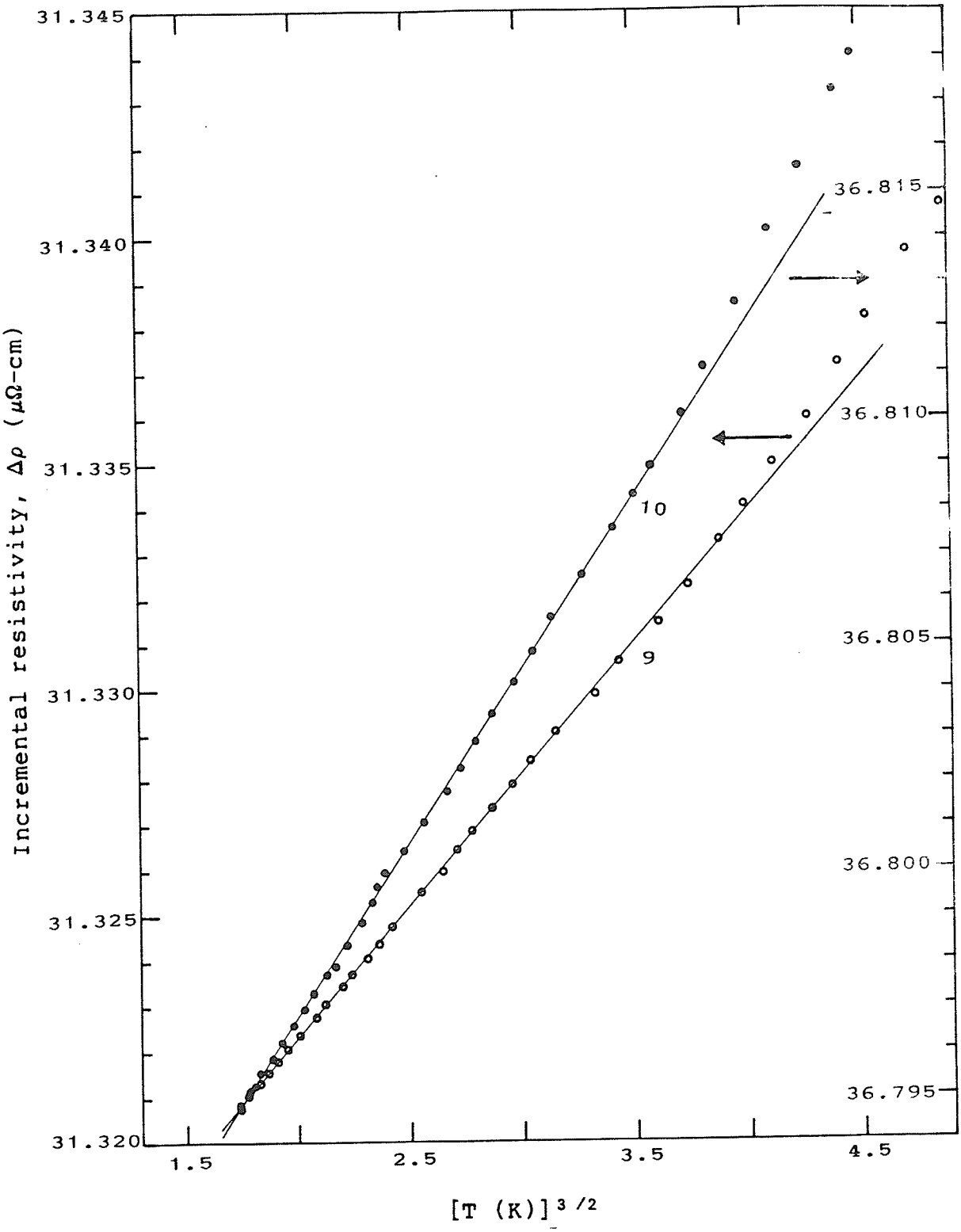

Fig.(5.22): Incremental resistivity-vs-$T^{3/2}$ plots.
Concentrations are marked against the plots.

the 3, 4 and 5 at.% alloys is presented in fig.(5.23). Similar plots for all other samples examined are compiled in appendix B.

J could also be estimated from the slope of the linear part of the $\Delta\rho$-vs-T curves. The expression relating J to the slope is

$$J^2 = \{(2S^2+ 2S+ 1)/acS(S+1)[40/3S(S+1) - 5]\}.T_c[d(\Delta\rho)/dT]_{T_c}$$

$$\simeq 1.712 \times 10^{-3} [d(\Delta\rho)/dT]_{T_c}.T_c/c \qquad (5.15)$$

A free-atom value for Gd-spin, equal to 7/2, has been used to calculate the constant in accordance with the values obtained from magnetisation measurements by Praddaude et al [80] and by Guertin et al [79]. Approximate values of T_c, as obtained from the resistivity measurements themselves, were used. The positions of the 'kink' in the resistivity of the lower concentration alloys are taken as the respective estimates of their ordering temperatures. For samples exhibiting peaked structures in their resistivities ($c \geq 6$) temperatures above the peak where the resistivity starts to rise just before saturating have been taken as their ordering temperatures. For c, nominal concentration values were assumed.

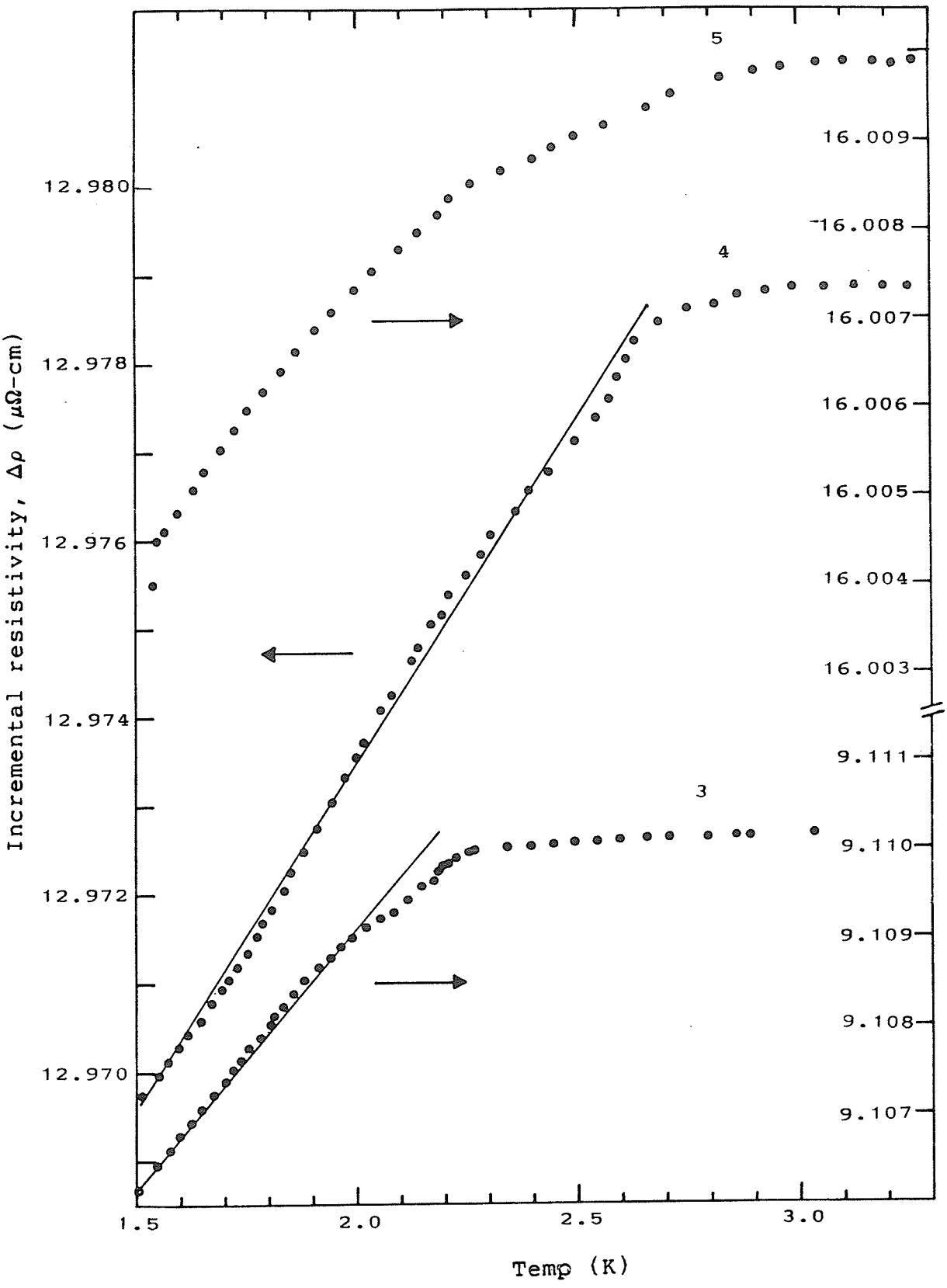

Fig.(5.23): Incremental resistivity-vs-temperature. Concentrations are marked against the plots.

The values of J_{ls} derived by the two methods mentioned above are listed in Table (5.3) and agree within the limits of evaluation. In fact, the slope measurements give a very nearly constant value for J up to c = 7 at.% . The spin - disorder resistivity method then yields almost constant values, within experimental errors, for all but the 10 at.% Gd alloy. The value 0.003 eV may be taken as the concentration-independent estimate for the conduction electron-local spin exchange coupling, J. This is in agreement with the value 0.003 eV obtained by Cannella et al [72] through resistivity measurements on PdGd alloys with $c \leq 5$ at.% and, with the value (0.003 + 0.0005) eV obtained earlier by the EPR line-width measurements performed on Gd in single crystals of Pd by Devine et al [99]. Also listed in Table (5.3) are the values for the effective exchange constant between the localised Gd moment and the d-holes of Pd, which are calculated using the Long and Turner model formula [29]

$$kT = |J_{ld}|^2 \, cSN(0)/24 \, K_0^4 (z/2)^{2/3} \qquad (5.16)$$

where $N(0)K_0^2$ is the enhanced d-state density and z = 0.36 electrons/atom. They are consistently lower than the effective Gd moment-conduction electron exchange J. Finally listed in Table (5.3) are the residual resistivities of the various alloys as determined from the resistivity measurements and the values for the lattice periodicity-

TABLE (5.3)

Exchange parameters from resistivity measurements (set I)

c	T (K)	slope $\mu\Omega$-cm/K	$\Delta\rho(0)$ ($\mu\Omega$-cm)	J_{ls}(eV) calculated from		J_{ld} (eV)	V (eV)
				spin disorder resistivity	slope		
3	2.28	0.006	9.097-9.106	0.002-0.004	0.003	0.001	0.72
4	2.70	0.008	12.958-12.969	0.003-0.004	0.003	0.001	0.74
5	3.17	0.007	- -	0.002-0.003	0.003	0.001	-
6	3.28	0.013	20.197-20.216	0.002-0.004	0.003	0.001	0.76
7	3.62	0.010	23.474-23.490	0.003	0.003	0.001	0.76
8	4.30	0.029	26.902-26.960	0.004	0.005	0.001	0.76
9	4.54	0.026	31.266-31.321	0.004	0.005	0.001	0.77
10	4.63	0.034	36.726-36.795	0.005	0.005	0.001	0.79

breaking potential V calculated on the basis of Long and Turner model. The estimated values of the former are plotted in fig.(5.24) as a function of alloy concentration. In the previous discussion it was suggested that a linear-relationship between the two quantities is indicative of applicability of Mattheissen's rule. While the concentrations are uncertain, the linear plot passing through the origin suggests that the deviations start to appear at concentrations about 7-8 at.% Gd. They grow as the concentration rises. The incremental resistivities for alloys with concentrations as high as 7 at.% may be interpreted as magnetic impurity contributions to the alloy resistivity. As a corollary therefore, it follows that the estimates of J_{ls} from spin disorder resistivity $[\Delta\rho(T_c) - \Delta\rho(0)]$ are likely to be reasonably good. By the same token, the Long and Turner model estimates for the non-magnetic potential V are fairly good. While the exchange constants J_{ls} and J_{ld} show almost no concentration dependence, the symmetry-breaking potential does, as must be expected.

It is interesting to note that in Table (5.4) the second set of resistivity measurements on apparently aged samples give values for the local-moment-conduction electron exchange constants (as estimated from the slopes), for alloys with $c \leq 6$ at.% Gd which very nearly equal those obtained by first set of resistivity measurements. In general, the slopes are reduced but the ordering temperatures are increased for these alloys.

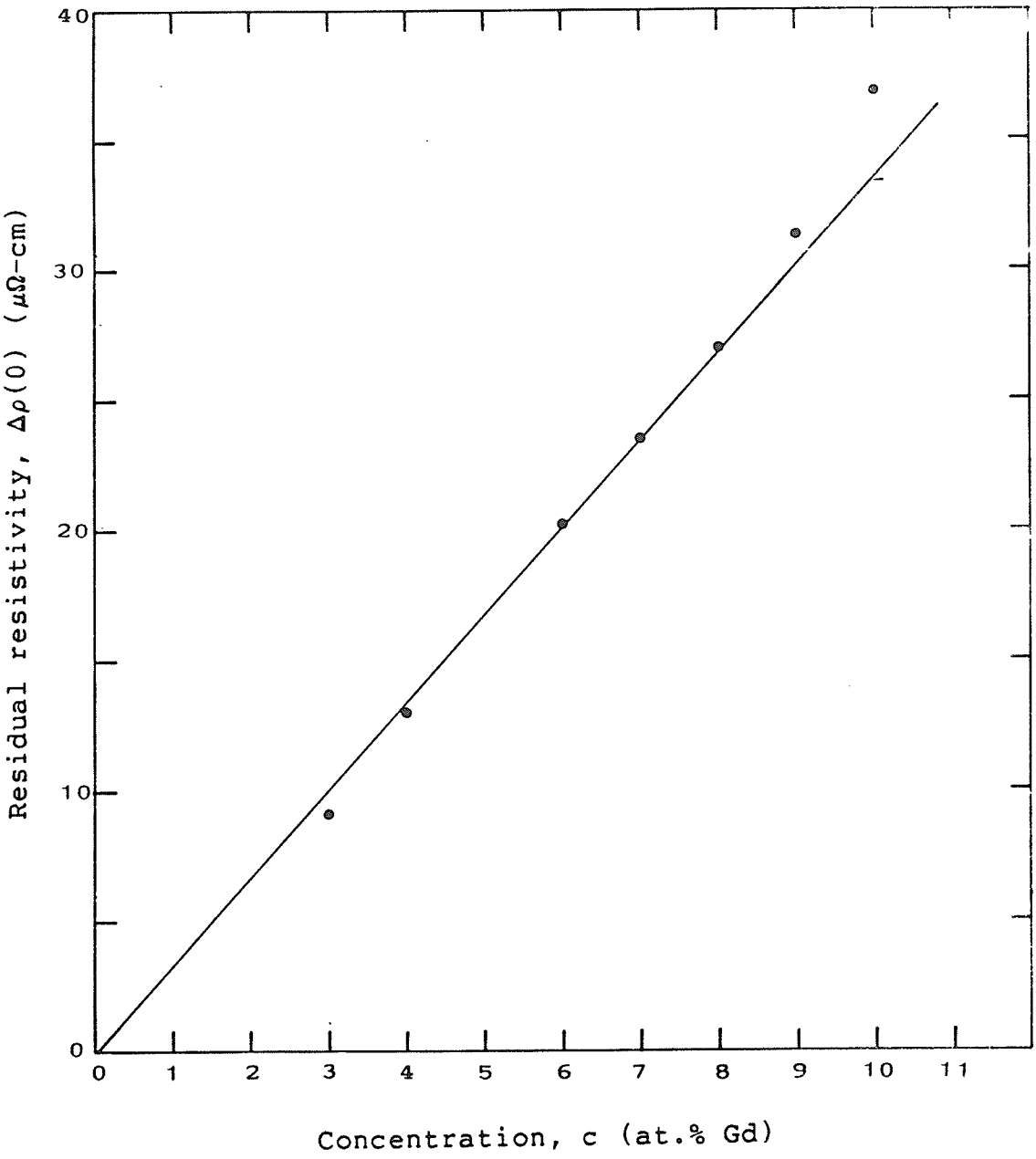

Fig.(5.24): Residual resistivity-vs-concentration.

TABLE (5.4)

Exchange parameters from resistivity measurements (set II)

c	T_c (K)	slope $\mu\Omega$-cm/K	$\Delta\rho(0)$ $\mu\Omega$-cm	J_{ls} (eV) calculated from		J_{ld} (eV)	V (eV)
				spin disorder resistivity	slope		
3	2.4	0.004	9.07	0.002-0.003	0.0024	0.001	0.72
4	2.9	0.006	12.90	0.003-0.004	0.003	0.001	0.74
5	4.2	0.006	16.00	0.003	0.003	0.001	0.74
6	4.0	0.009	20.20	-	0.003	0.001	0.76
7	3.9	0.017	23.48	0.004	0.004	0.001	0.76
8	4.2	0.087	26.90	0.006	0.009	0.001	0.76
9	>4.5	0.015	31.32	-	>0.004	0.001	0.77
10	4.5	0.038	36.78	0.005	0.005	0.001	0.79

5.3 MAGNETORESISTANCE

In order to clarify the nature of the ordered ground state in PdGd alloys, the field- and temperature-dependence of resistivities of these alloys were studied.

The resistivities, at three different fixed temperatures, were measured as a function of field up to 85 kOe. In general, all alloys showed a negative magneto-resistance at low fields. This is consistent with the gradual removal of spin-disorder in these alloys by the external applied fields which act to re-orient the disordered, local Gd-moments.

The lowest fixed temperature investigated, 1.5 K, lies below the ordering temperatures for all alloys (except, possibly, for the 2 at.% sample, where it is comparable to T_c) while the second, 4.2 K, is higher than the ordering temperatures for most alloys (except for 8, 9 and 10 at.%) and the third, 10 K, is well into paramagnetic range for all alloys considered.

At 1.5 K, in zero-field, all alloys are ordered. If this ordered state is considered to be simply ferromagnetic, the proximity to saturation (or complete spin alignment) would depend upon the reduced temperature T/T_c and hence on the concentration, being larger for larger concentration alloys at the above temperature. Thus the residual spin-disorder resistivity should be smaller for larger Gd-concentrations and at 1.5 K the more concentrated samples should exhibit a

weaker negative magnetoresistance. The data presented in fig.(5.25) does not conclusively support this contention. For the 2, 3, and 4 at.% alloys the magnitudes of the negative magnetoresistance are very nearly the same. For concentrations beyond while no definite trend is discernible, these magnitudes are larger than those for the above three alloys.

Fig.(5.25) also shows a rise in the magnetoresistance at high fields. This rise is, most probably, caused by the Koehler term, i.e. the curvature of the conduction electron orbits in an applied field. Indeed, the general shape of the resistivity-vs-field curves can be qualitatively understood as a combination of two effects:

(a) decline in spin-disorder resistivity (spin-wave or single-particle) with rising fields and,

(b) increase in the Koehler term, $\Delta\rho_k$.

Since the residual resistivities of the alloys are much larger than that of pure Palladium, an estimate of the Koehler resistivity in the alloys (at 1.5 K, in 70 kOe field) was made from the data on a typical ferromagnetic sample with 3 at.% Gd. The approach followed is described below.

Even for free-spins, the magnetisation (i.e. the Brillouin function) approaches 97 % of its saturation value in an applied field of about 40 kOe at a temperature of approximately 2 K (i.e. H/T = 20). In the present case, in

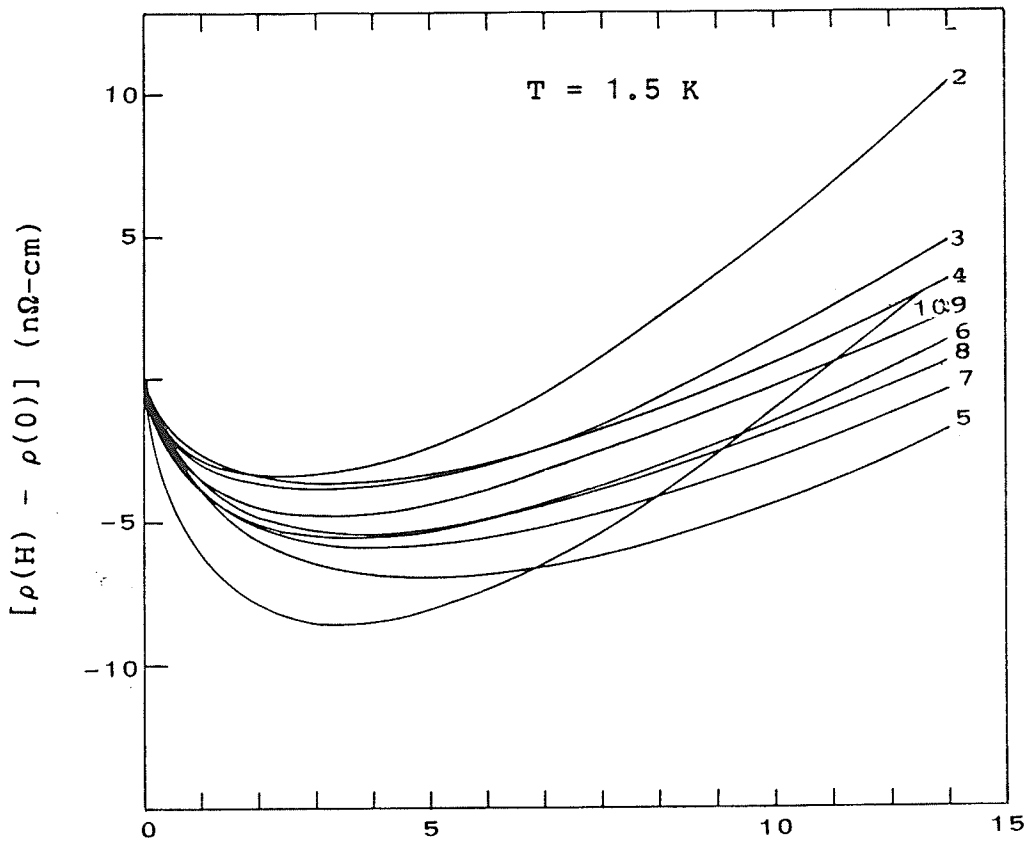

Fig.(5.25): Field-induced resistivity changes at 1.5 K. Concentrations are marked against the curves.

70 kOe at 1.5 K (i.e. with a ratio H/T = 47), the spin-disorder resistivity may be expected to be completely removed. The remaining resistivity must then be a sum of the residual resistivity (due to lattice perturbations and defects) and the Koehler resistivity. The magnitude of the latter can thus be estimated by subtracting the zero-field residual resistivity at 1.5 K (assumed field-independent) from that measured in 70 kOe at the same temperature. Such an approach yields an estimate of about 3×10^{-3} $\mu\Omega$-cm (at 1.5 K in 70 kOe) for the Koehler term. At smaller fields, the latter will obviously be smaller than this estimate. As the external field is reduced to zero the magnitude of the Koehler term will be governed by the strength of the internal molecular field alone.

The field-dependence of resistivity, shown in figs.(5.26) and (5.27), at the other two fixed temperatures does not yield further information about the detailed nature of either the ordered ground state or the various interactions possibly present in the PdGd alloys because these temperatures fall in the paramagnetic regime, in general. The qualitative features of the data data are explainable, once again, in terms of the two effects mentioned above.

The generally larger magnitudes of the negative magnetoresistance at 4.2 K and 10 K compared to those at 1.5 K are consistent with an increased presence of thermal disorder which the applied external fields must now

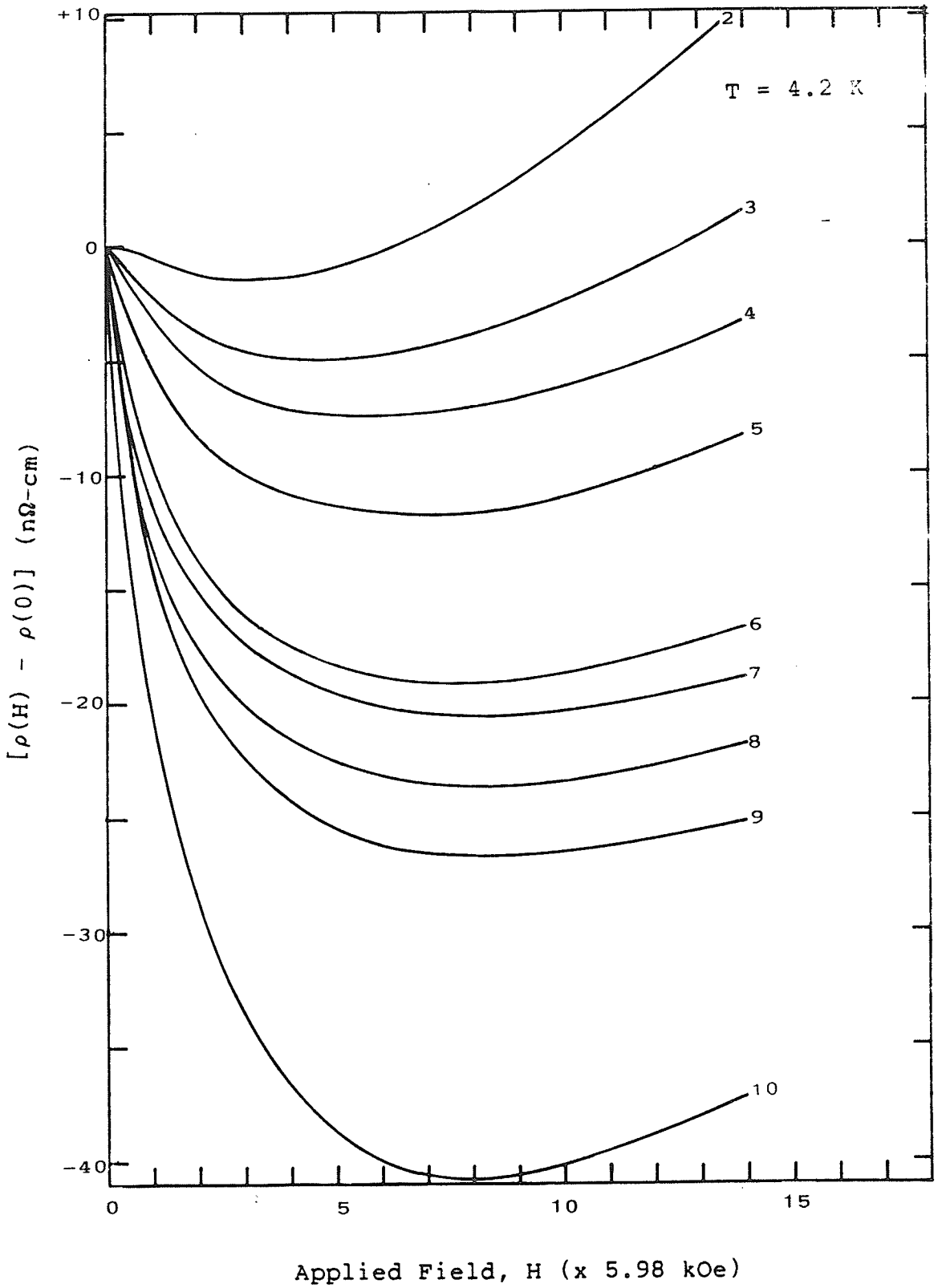

Fig.(5.26): Field-induced resistivity changes at 4.2 K. Concentrations are marked against the curves.

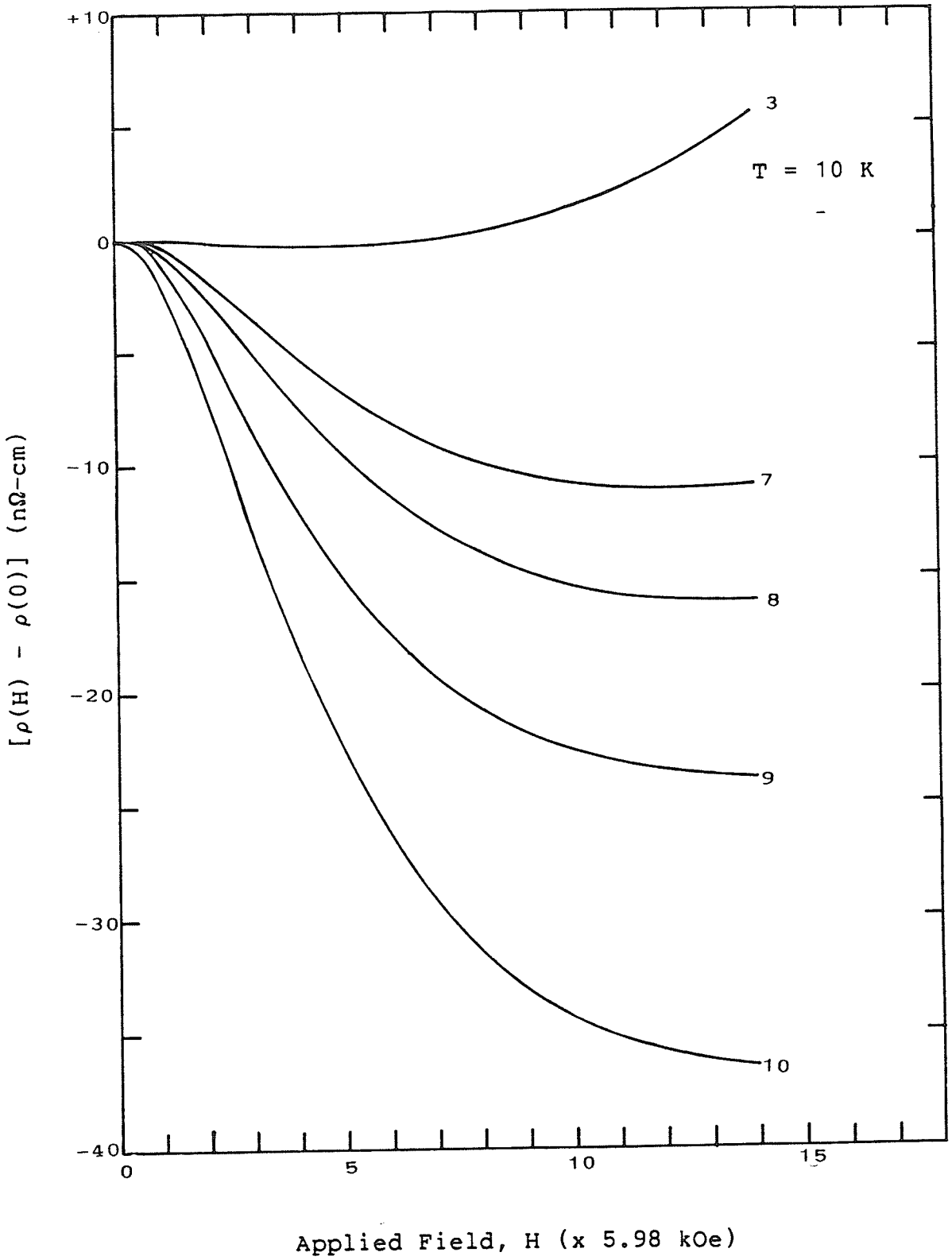

Fig.(5.27): Field-induced resistivity changes at 10 K. Concentrations are marked against the curves.

overcome. The increased disorder would require higher magnetic fields for its suppression. The observed shift of the position of the resistivity minimum for a given alloy towards higher fields is consistent with the above expectation.

The temperature-dependent resistivity of PdGd alloys in fixed external field (70 kOe) also shows some interesting features. The s-d model calculations of Long and Turner [29] predict a $T^{3/2}$ dependence of zero field resistivity in ferromagnetic alloys well below T_c which arises due to electron-magnon scattering in the disordered alloy system. As mentioned previously, such a dependence is, indeed, observed in alloys with a Gd-concentration above 6 at.%. When modified to include the effect of an applied magnetic field [102], a strong suppression of the $T^{3/2}$-resistivity, resulting from the introduction of a gap in the magnon spectrum, is predicted. If the PdGd alloys are considered as simple ferromagnets, the effect of the applied fields must be to simply suppress the resistivity which must, nevertheless, continue to rise with rising temperatures. While this is observed for the 3 and 4 at.% alloys [fig.(5.28)], the temperature-dependent resistivity of some higher concentration alloys [figs.(5.29) and (5.30)] shows a negative temperature-coefficient in a fixed applied field of 70 kOe. Since the Koehler term, given by

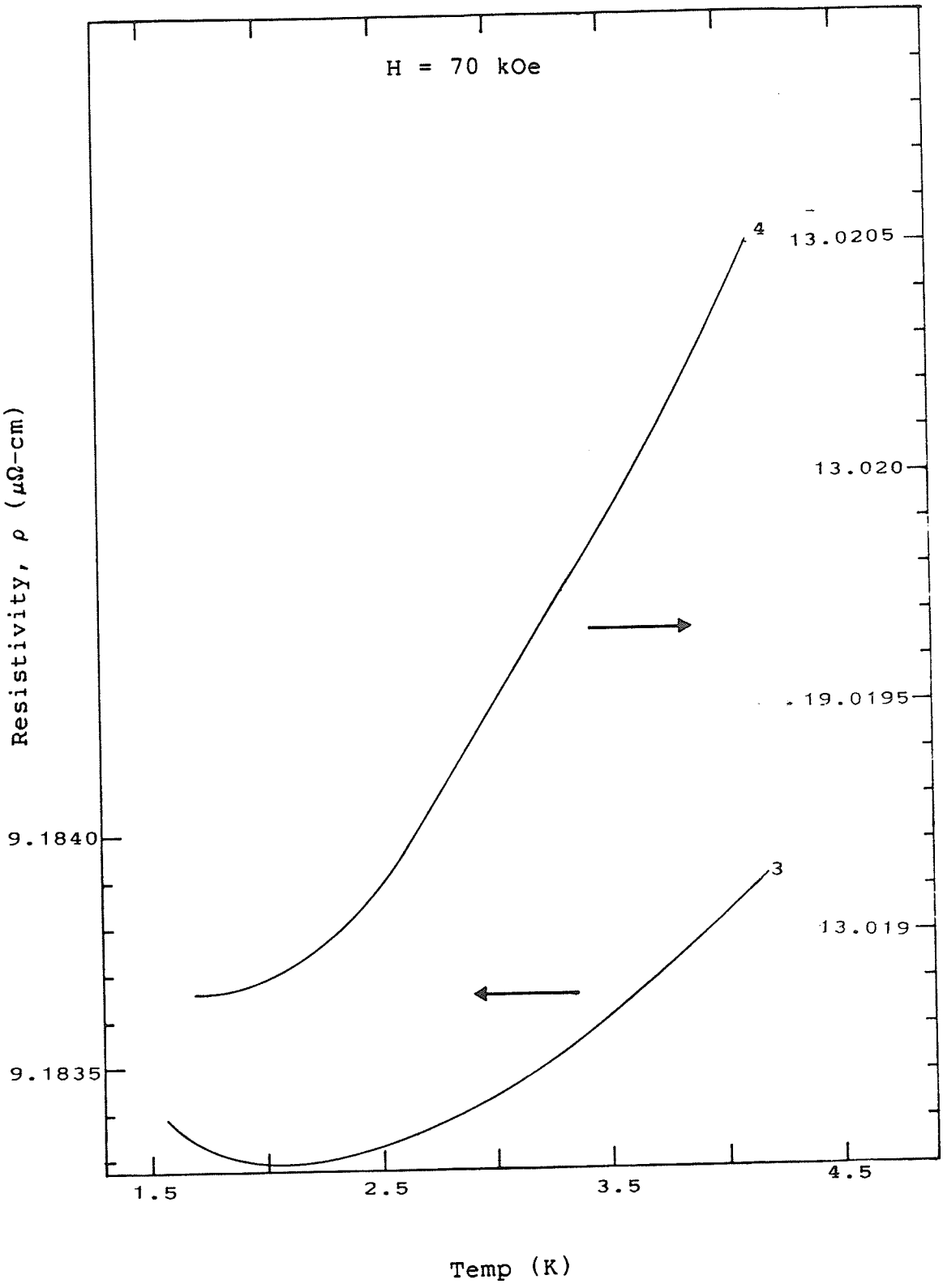

Fig.(5.28): Temperature-dependence of resistivity in 70 kOe. Concentrations are marked against the curves.

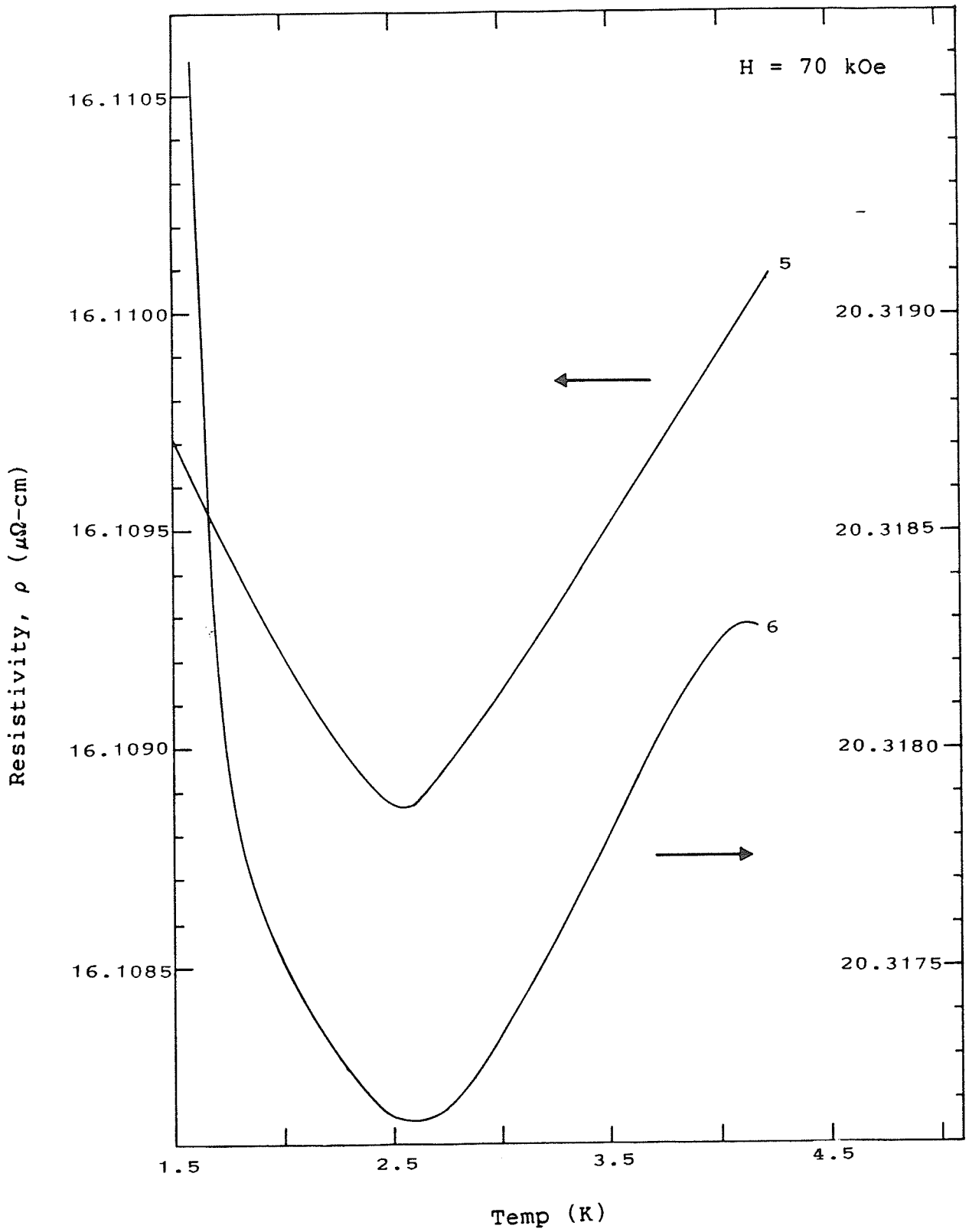

Fig.(5.29): Temperature-dependence of resistivity in 70 kOe. Concentrations are marked against the curves.

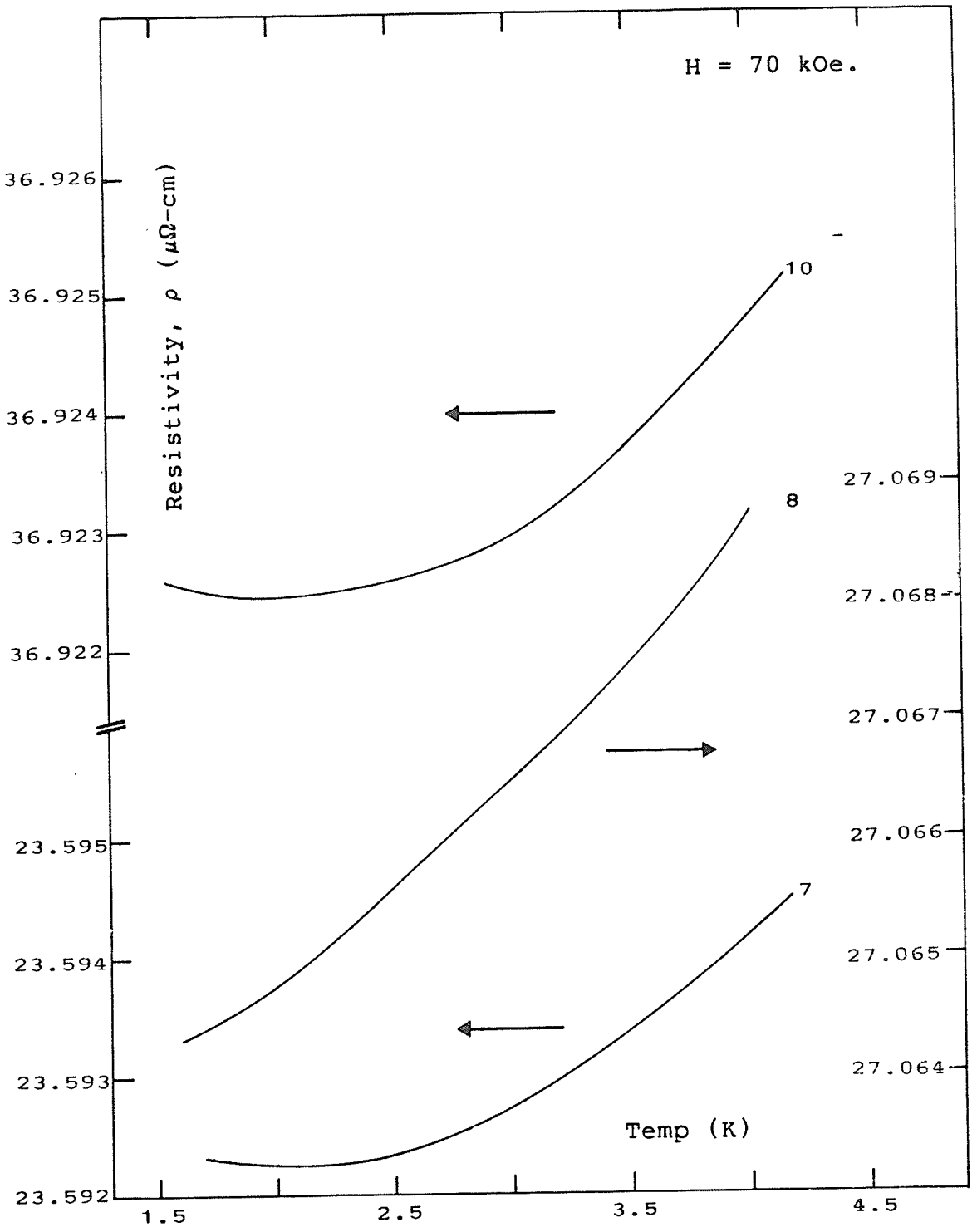

Fig.(5.30): Temperature-dependence of resistivity in 70 kOe. Concentrations are marked against the curves.

$$\Delta\rho/\rho(0) = F\ [H/\rho(0)] \qquad (5.17)$$

involves the zero-field resistivity which is very weakly dependent on temperature, it may be assumed to be independent of temperature within the narrow experimental range of temperatures. Hence, the observed negative temperature-coefficient will not be affected to any significant extent even if the Koehler correction is accounted for.

Again, while the situation remains somewhat ambiguous, the negative temperature-coefficient of resistivity may imply a weak anisotropy which is overcome in the presence of an applied field and a small thermal energy. A helical arrangement of impurity spins (with a non-trivial ferromagnetic component) which collapses to a ferromagnetic order in the presence of a strong magnetic field can give rise to the observed effect.

5.4 SUMMARY AND CONCLUSIONS

We present the first systematic study of the low-field a.c. susceptibility and the low-frequency a.c. resistivity of the PdGd system over an extended concentration range.

The EPR data on small amounts of Gadolinium dissolved in Palladium had revealed that the former retains an ionic-like

S-state, just as Manganese does in the same host. Previous measurements of some of the above properties of PdGd alloys over a limited concentration range ($c \leq 5$ at.%) by Cannella et al [72] were interpreted as indicating a purely ferro-magnetic ground state below the respective, measured Curie temperatures. Extensive studies of the related PdMn system have established that while the indirect long-range RKKY interactions between distant Mn-impurities (through a polarisation of the d-band) are always present, direct 3d-overlap interactions can occur when the average inter-impurity separation roughly equals the third-neighbour distance. Furthermore, such direct interactions are antiferromagnetic. Indeed, any direct overlap interactions between ions with exactly half-filled shells are expected to be antiferromagnetic [17]. The effects of such interactions are clearly visible in PdMn alloys with concentrations above 2.5 at.% Mn. At a concentration of about 5 at.%, these interactions are strong enough to compete effectively with the ferromagnetic ones of the RKKY type and modify the ground state from predominantly ferromagnetic to spin-glass. In view of the more localised nature of the Gadolinium 4f-wavefunctions the near-neighbour interactions are expected to become important only at concentrations higher than 2.5 at.% Gd. However, given the fact that Gd-impurities retain their half-filled shell structure, such interactions are expected to be antiferromagnetic and, hence, to produce a phase diagram with features similar to that for PdMn.

Measurements of resistivity and a.c. susceptibility were made as a fuction of temperature (range 1.5 K to 10 K) and as a function of applied field (range 0 to 700 Oe). They confirm that the 3 and 4 at.% alloys undergo a transition-to a predominantly ferromagnetic state below their respective Curie points. A relatively straightforward analysis of the systematic behaviour of the secondary susceptibility peaks with changes in temperature and field in the light of the scaling hypothesis furnishes estimates for the various critical indices γ, β, and δ which are in good agreement with those reported for other ferromagnetic systems, both crystalline and amorphous. The negative magnetoresistance observed in these alloys is consistent with local-moment behaviour and, the zero-field resistivity shows the effects of interactions between these randomly distributed, localised moments. The Long and Turner model (described in Chapter II) for ferromagnetic alloys based on an exchange-enhanced host, such as Palladium, correctly predicts the various features observed in the zero-field magnetic resistivities of these alloys. The magnetic resistivity above the Curie temperature is saturated. Below it, the predicted linear decline with decreasing temperatures is observed. However, the $T^{3/2}$-behaviour, predicted by the Long and Turner model to occur at temperatures well below the Curie point is not observed in any of the two alloys, probably because the lowest achieved temperatures in the susceptibility study remain a substantial fraction of the

respective ordering temperatures. Nevertheless, the above evidence for a ferromagnetic ground state is quite strong. The sharp discontinuity in the first temperature-derivative of resistivity when the local-moments order indicates that the distribution of internal fields is sharply peaked in the 3 at.% alloy. A broadening tendency becomes apparent as the concentration rises up to 5 at.% Gd. This effect is perhaps a result of increased probability of near-neighbour Gd-Gd interactions. A reduction in slope of the ordering temperature-vs-concentration plot [fig.(5.31)] is consistent with the statistical increase in the direct exchange which, if antiferromagnetic as anticipated, would compete with the long-range, ferromagnetic, indirect RKKY exchange and possibly cause frustration in the ground state similar to that observed in the more concentrated PdMn alloys.

Here, the present study raises some questions about the true nature of the ground state in more concentrated specimens of PdGd. Contrary to the above expectations, the ground state in the higher concentration alloys does not appear to be frustrated in the same manner as in the more concentrated PdMn alloys. The strong magnetic response (high susceptibilities at the critical peaks) which persists up to concentrations as high as 10 at.% Gd, unlike that observed in PdMn system where it is suppressed above a concentration of 2.5 at.% Mn as a result of increasing competition between opposing interactions, provides evidence

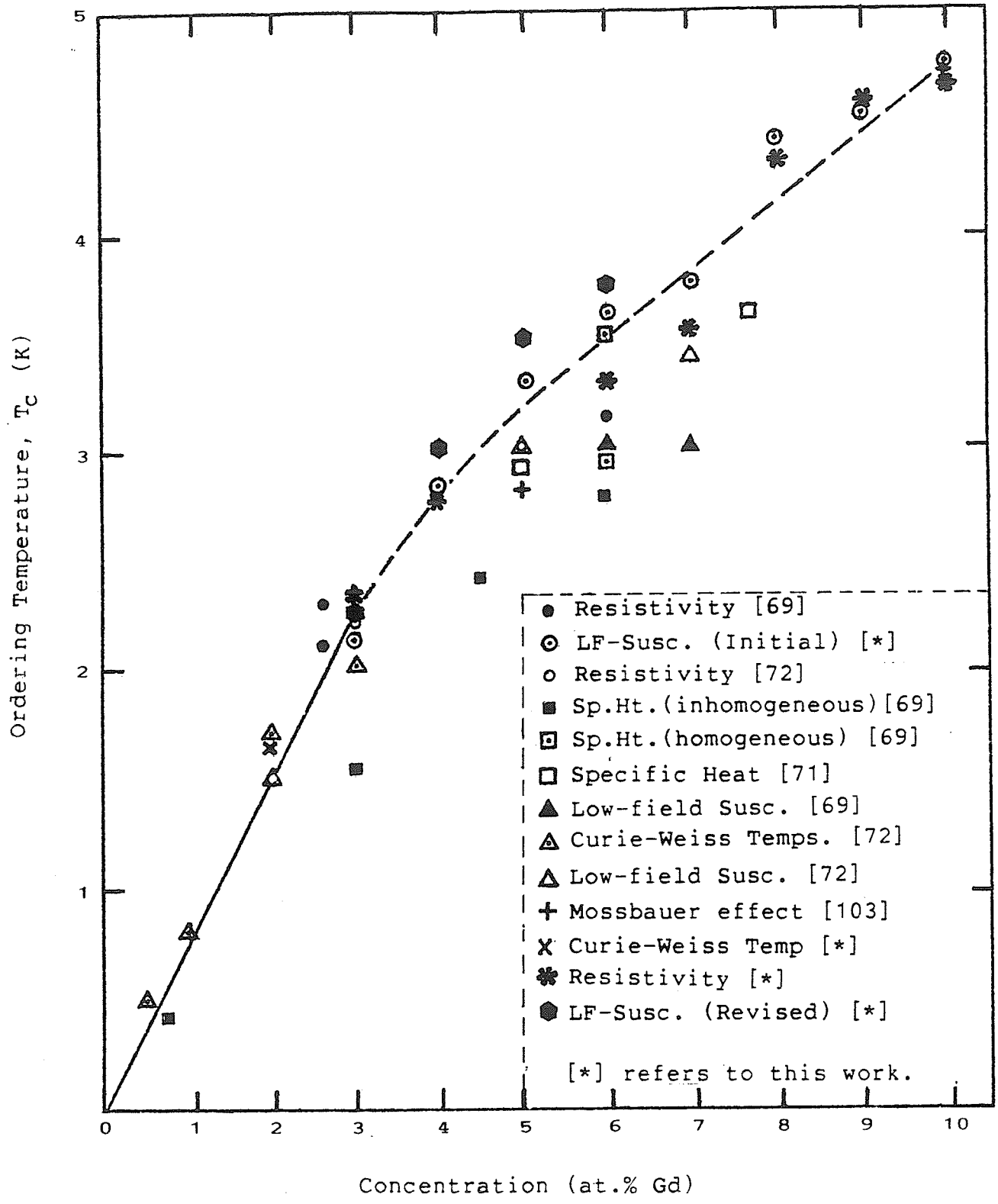

Fig.(5.31): Ordering temperatures vs Gd-concentration.

against a substantial presence of similar opposing interactions in the PdGd system. The surprising rise of δ-values with increased concentration is opposite to that observed in PdMn alloys having significant competition between opposing interactions. As the calculations by Roshko and Williams [46] demonstrate, the broadening of internal field distribution resulting from the above competition cannot lead to a concentration-related increase in the δ values. Therefore, it appears that the ground state in higher concentration PdGd alloys may be fundamentally different from that observed in the more concentrated PdMn alloys. Although increasing δ-values have been previously reported for amorphous systems with concentrations reaching the critical value for the disappearance of magnetism in them, in the present case, localised-moment behaviour is expected to persist at all concentrations of interest. The reason for the rise in δ-values is not clear.

The resistivity and the susceptibility data indicate together that it might be possible to catagorise the PdGd alloys with $c \leq 4$ at.% Gd as predominantly ferromagnetic. For concentrations beyond, classification may be possible only when the magnetic structure of the ground state is further clarified. The present data do not rule out the possibility that in more concentrated PdGd alloys ($c > 6$ or 7 at.%) stabilisation of a spiral structure (presumably with

a non-vanishing moment) having features similar to those predicted to occur in YGd alloys by Southern and Sherrington [24] and observed by other researchers [23,82] may be energetically favourable. The observed peaks in the resistivity of the more concentrated PdGd alloys are similar to those observed in helically ordered YGd alloys. Interference from the presence of other intermetallic phases, in particular, from Pd_3Gd which is antiferromagnetic below 7 K, is not expected to be the cause of these resistivity peaks. In addition to the negative results obtained through the TEM studies in search for other intermetallic phases of Palladium and Gadolinium in the present alloy samples, the consistently higher ordering temperatures (compared with those obtained by previous studies) above 5 at.% Gd, according to Zweers [74], are consistent with less inhomogeneous samples.

The present study offers only tentative answers to the question of the true nature of the ground state in alloys with $c \geq 6$ at.% Gd. The ground state in 3 and 4 at.% alloys appears to be predominantly ferromagnetic. Above these concentrations the situation becomes more complex. A study of the a.c. susceptibility and the a.c. resistivity on a series of alloys with more closely spaced Gd-concentrations at and around the ferromagnetic limit (approximately 4 at.% Gd) may reveal the details of change in the nature of the ordered state. In particular, the strange rise in the δ-

values with rising concentration needs corroboration. Once corroborated, it would require a satisfactory theoretical explanation. Another related question is whether an increase in Gd-concentration above 10 at.% Gd would ultimately lead to a frustrated ground state of the type noted in the PdMn system. As Table (5.1) shows, the susceptibilities of the 10 at.% alloy at the critical peaks in small, non-zero fields are suppressed below those for the 9 at.% alloy. Additionally, the ordering temperatures seem to approach a plateau at a concentration of about 10 at.% Gd suggesting that increasing competition between opposing interactions may be gaining importance. Again, studies furnishing good estimates of the ordering temperatures are required on samples with closely spaced concentrations around 10 at.% Gd. Special attention would be required for the preparation of such high concentration alloys in view of the low solubility of Gadolinium in Palladium (12 at.% at 1000 ^{o}C). A study of the a.c. susceptibility may again prove useful. However, in this respect, it must be pointed out that problems in temperature measurement above the boiling point of liquid Helium limit the ability to conclusively decipher any trends in the concentration-dependence of ordering temperatures at higher concentrations. Hence, the suggested study will first need to address the more technical problem of accurate temperature measurement in a rather difficult range of temperatures.

Appendix A

SUSCEPTIBILITY DATA

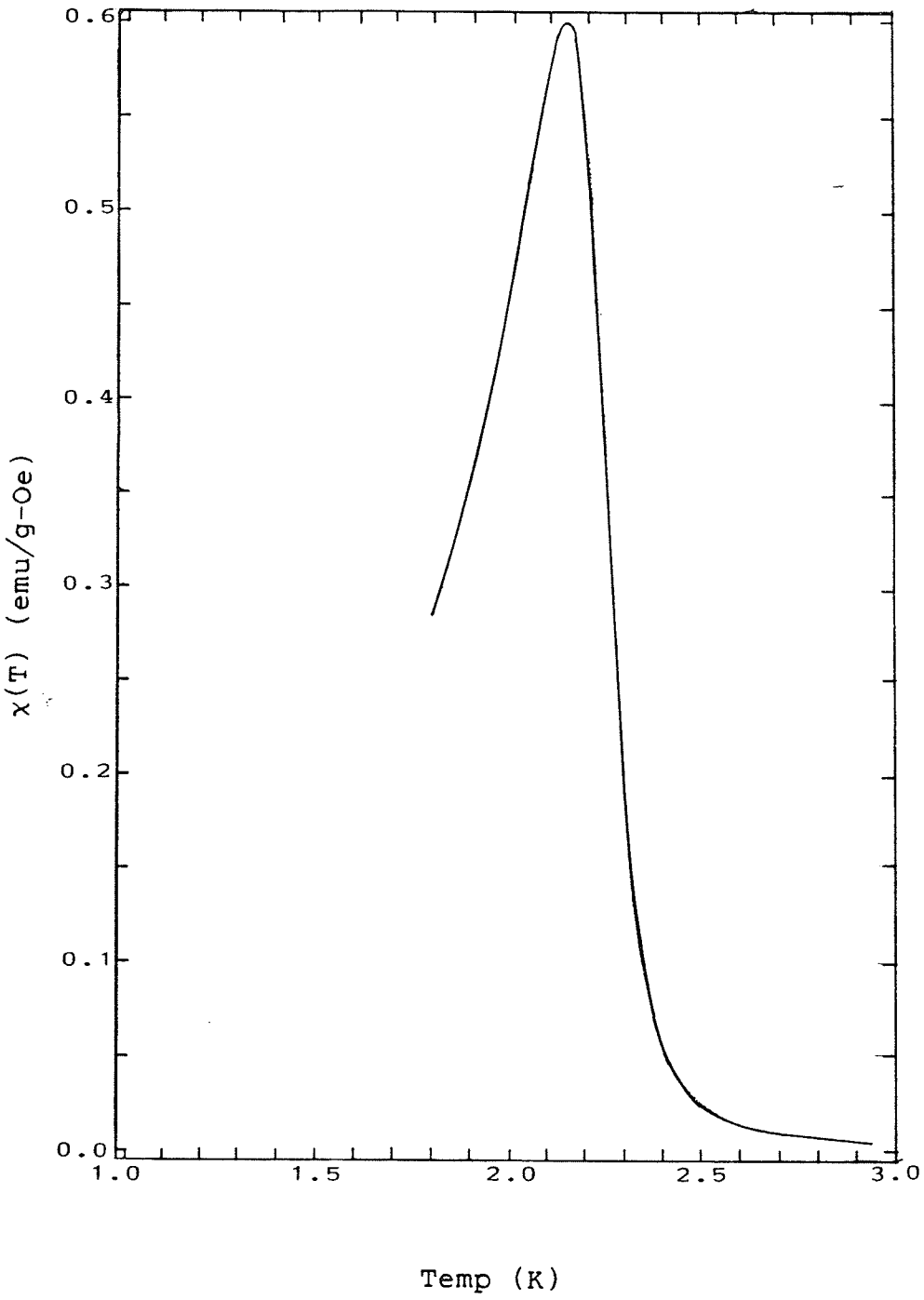

Fig.(A 1): Zero-field a.c. susceptibility of Pd + 3 at.% Gd.

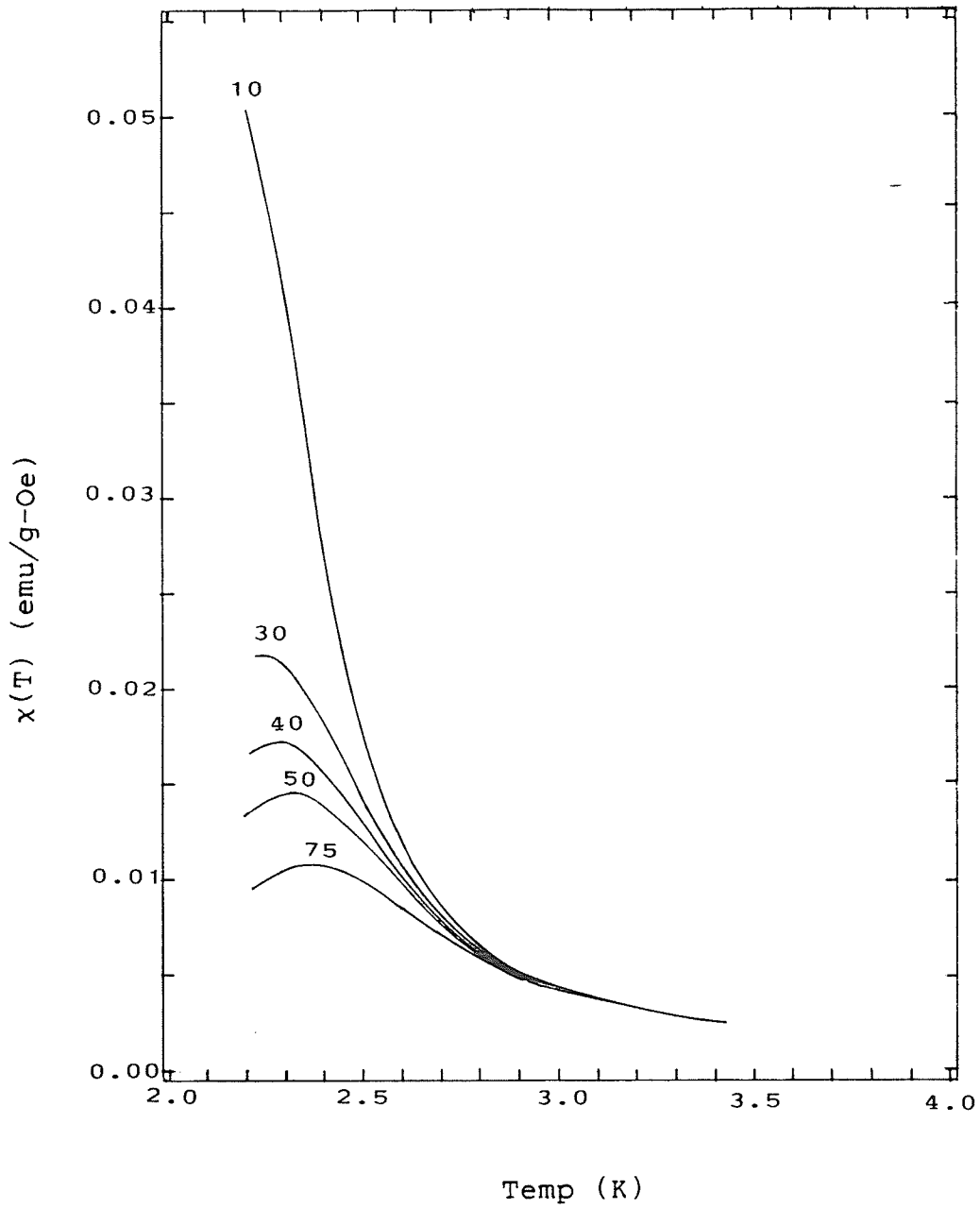

Fig.(A 2): Susceptibility of Pd + 3 at.% Gd in various biasing fields.

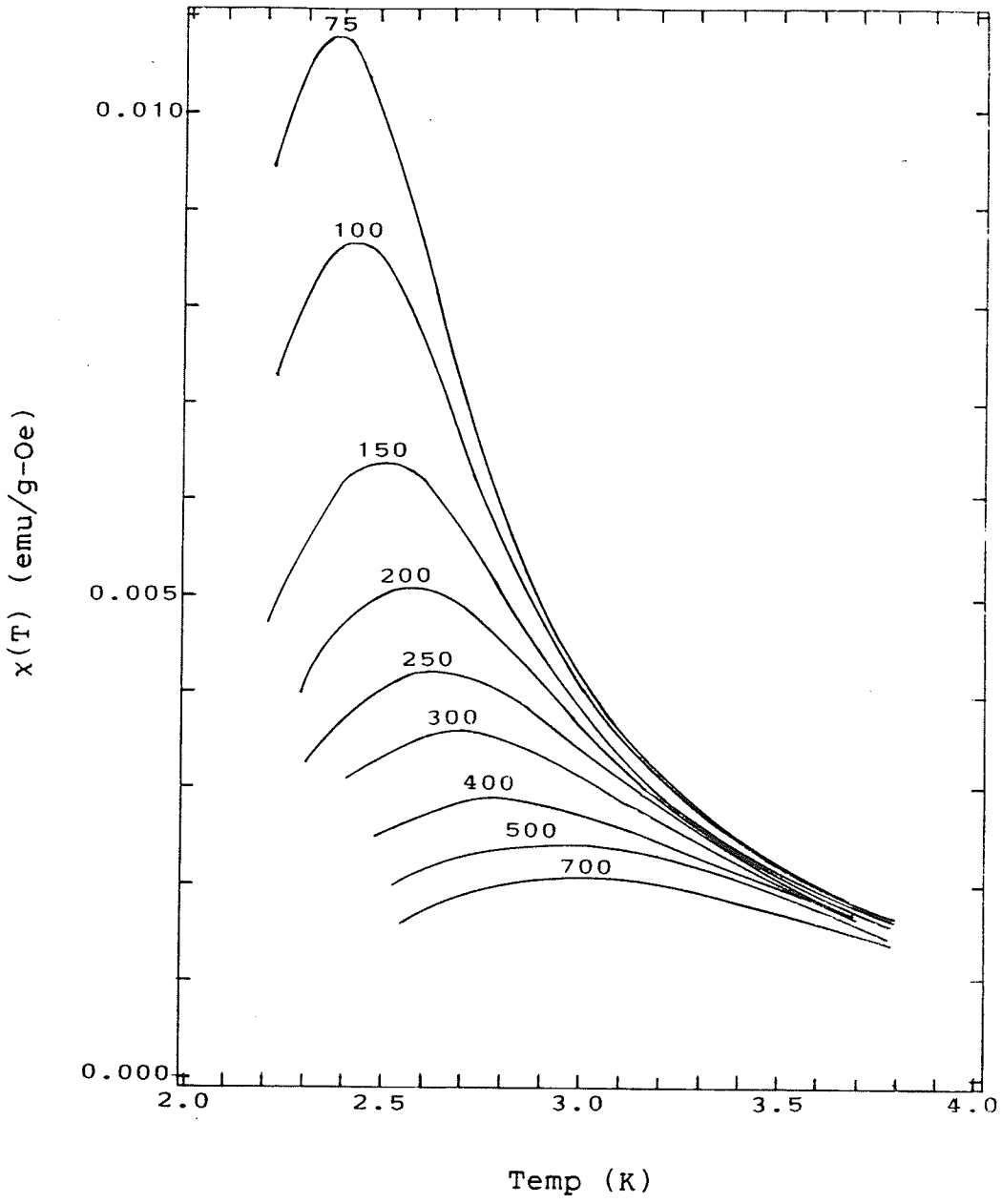

Fig.(A 3): Susceptibility of Pd + 3 at.% Gd in various biasing fields.

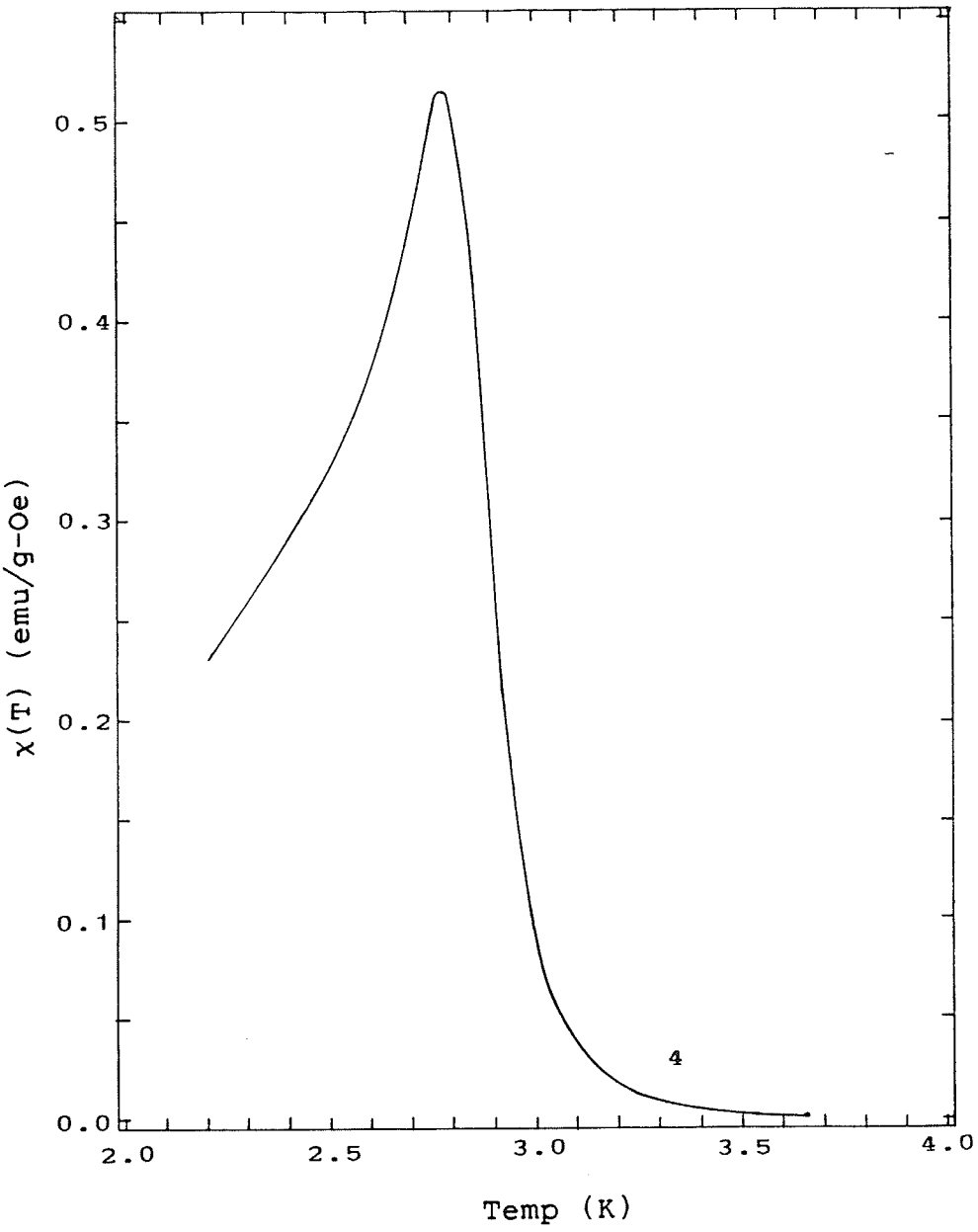

Fig.(A 4): Zero-field a.c. susceptibility of Pd + 4 at.% Gd.

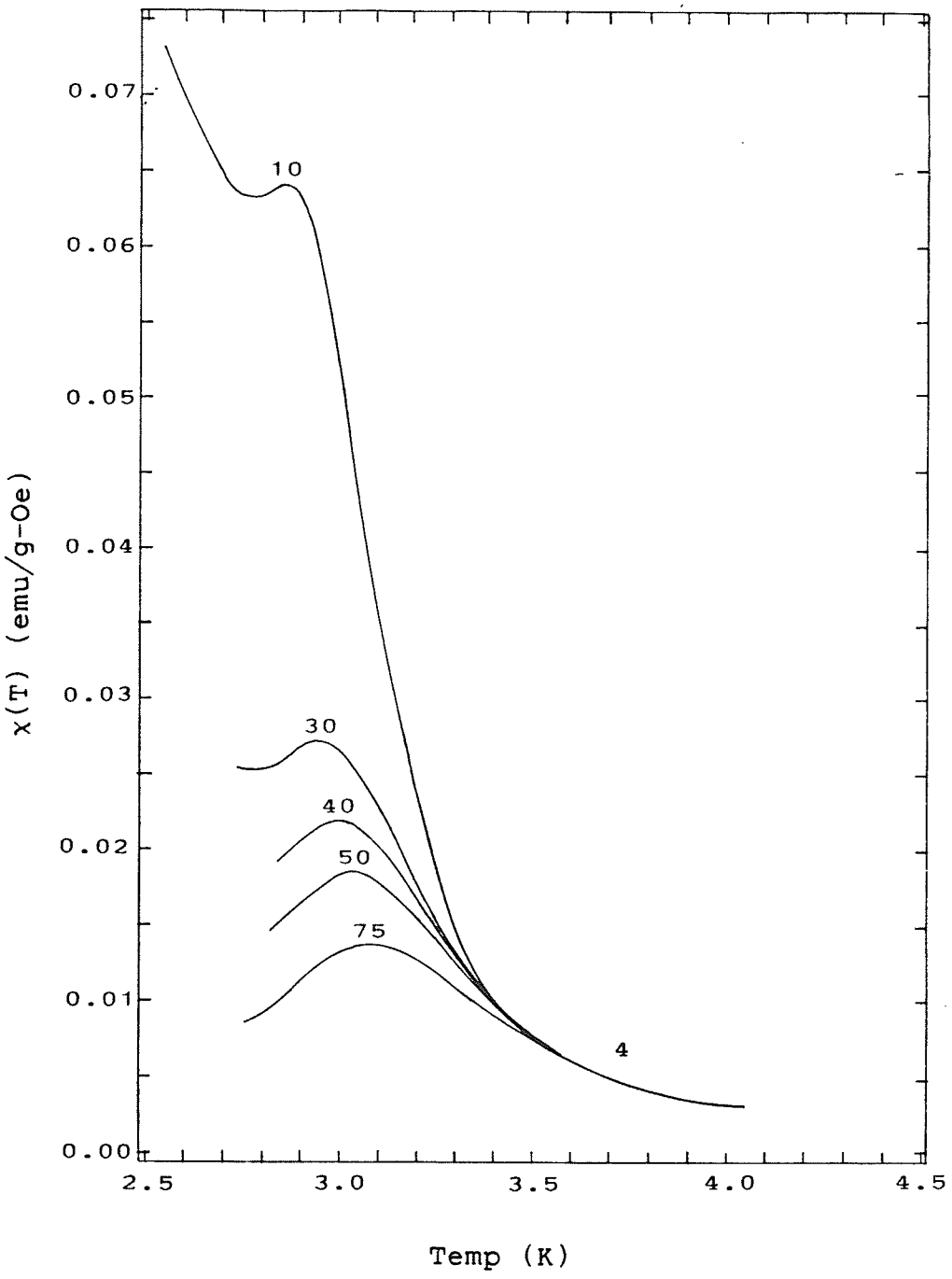

Fig.(A 5): Susceptibility of Pd + 4 at.% Gd in various biasing fields.

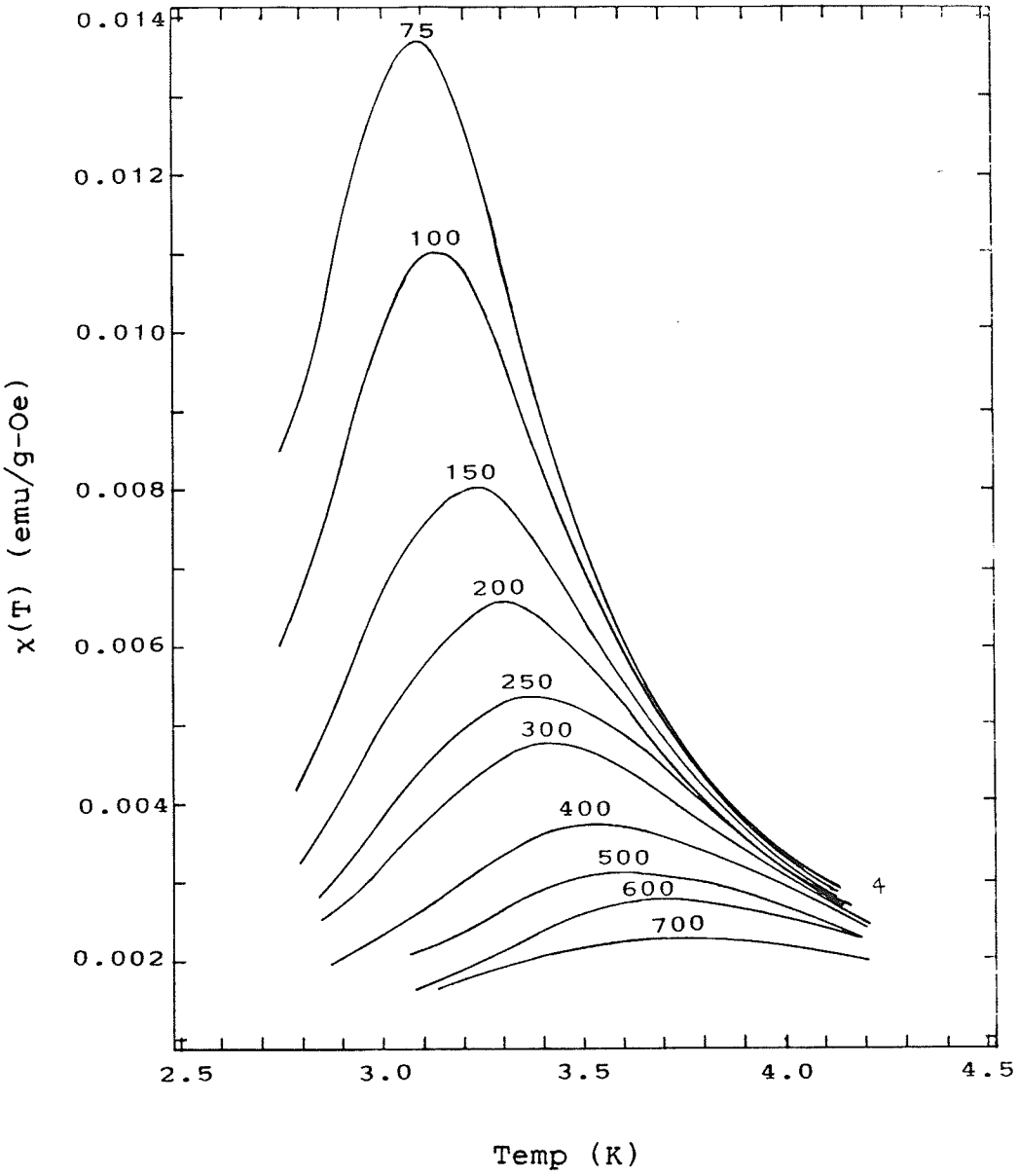

Fig.(A 6): Susceptibility of Pd + 4 at.% Gd in various biasing fields.

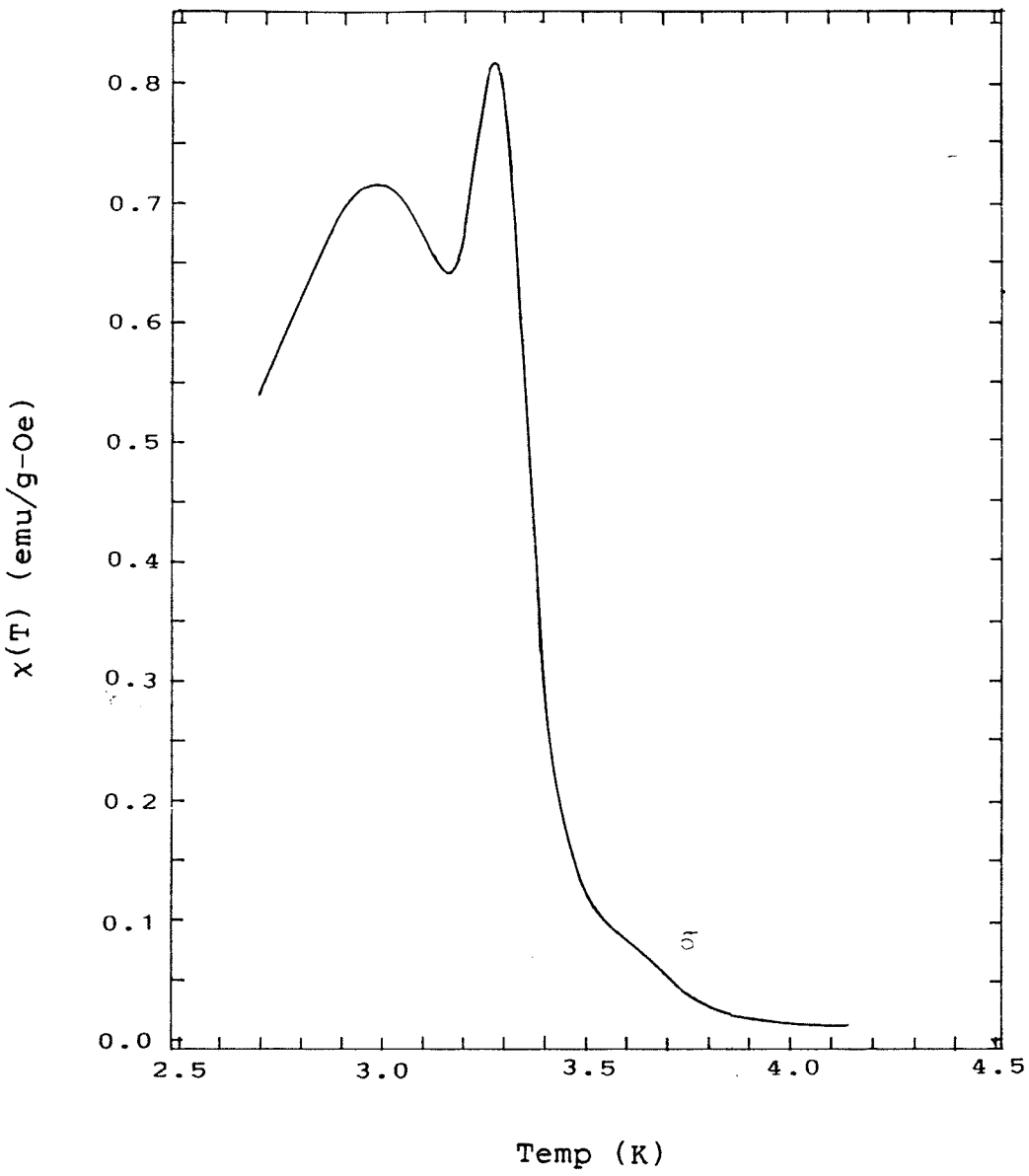

Fig.(A 7): Zero-field a.c. susceptibility of Pd + 5 at.% Gd.

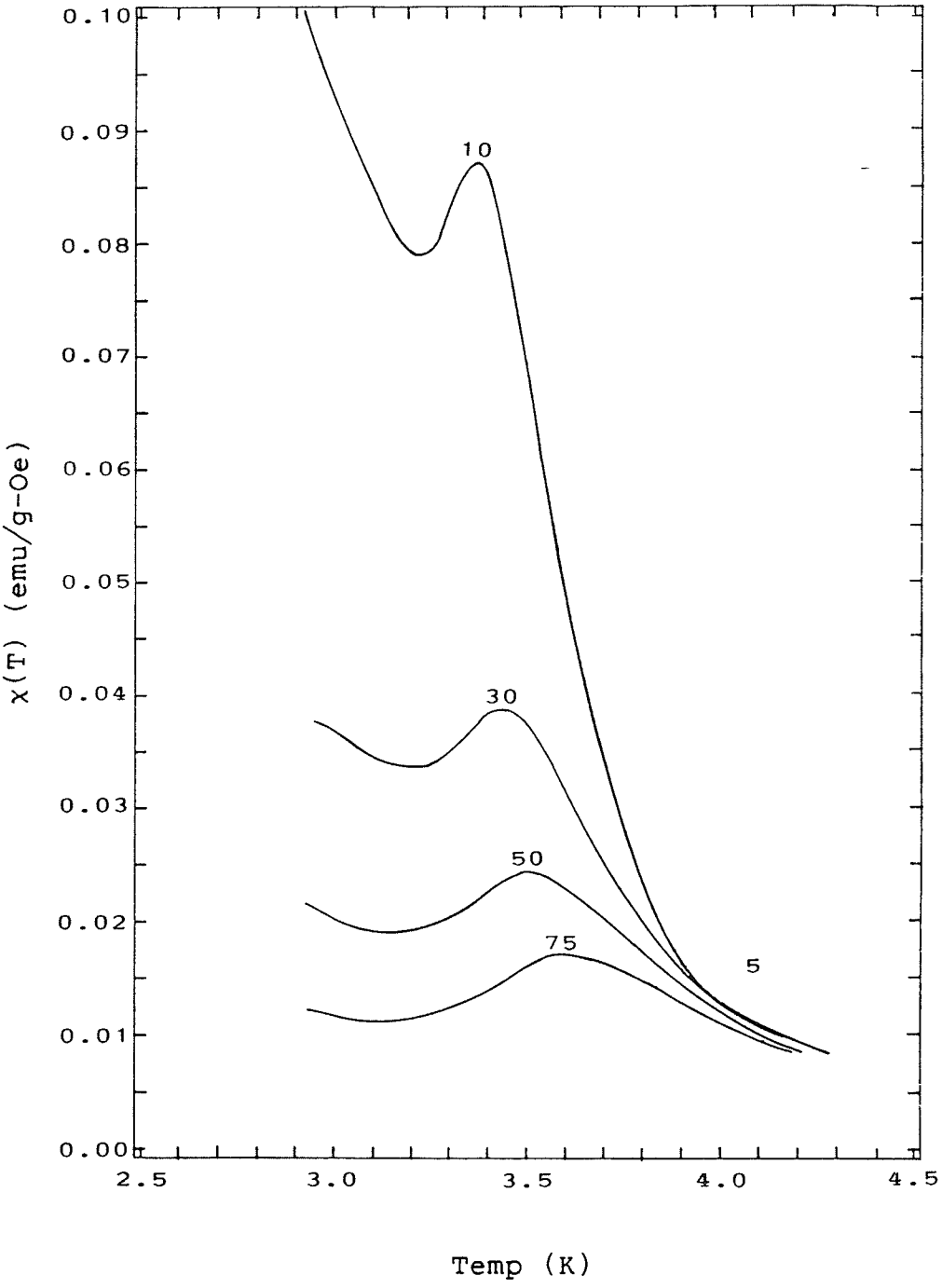

Fig.(A 8): Susceptibility of Pd + 5 at.% Gd in various biasing fields.

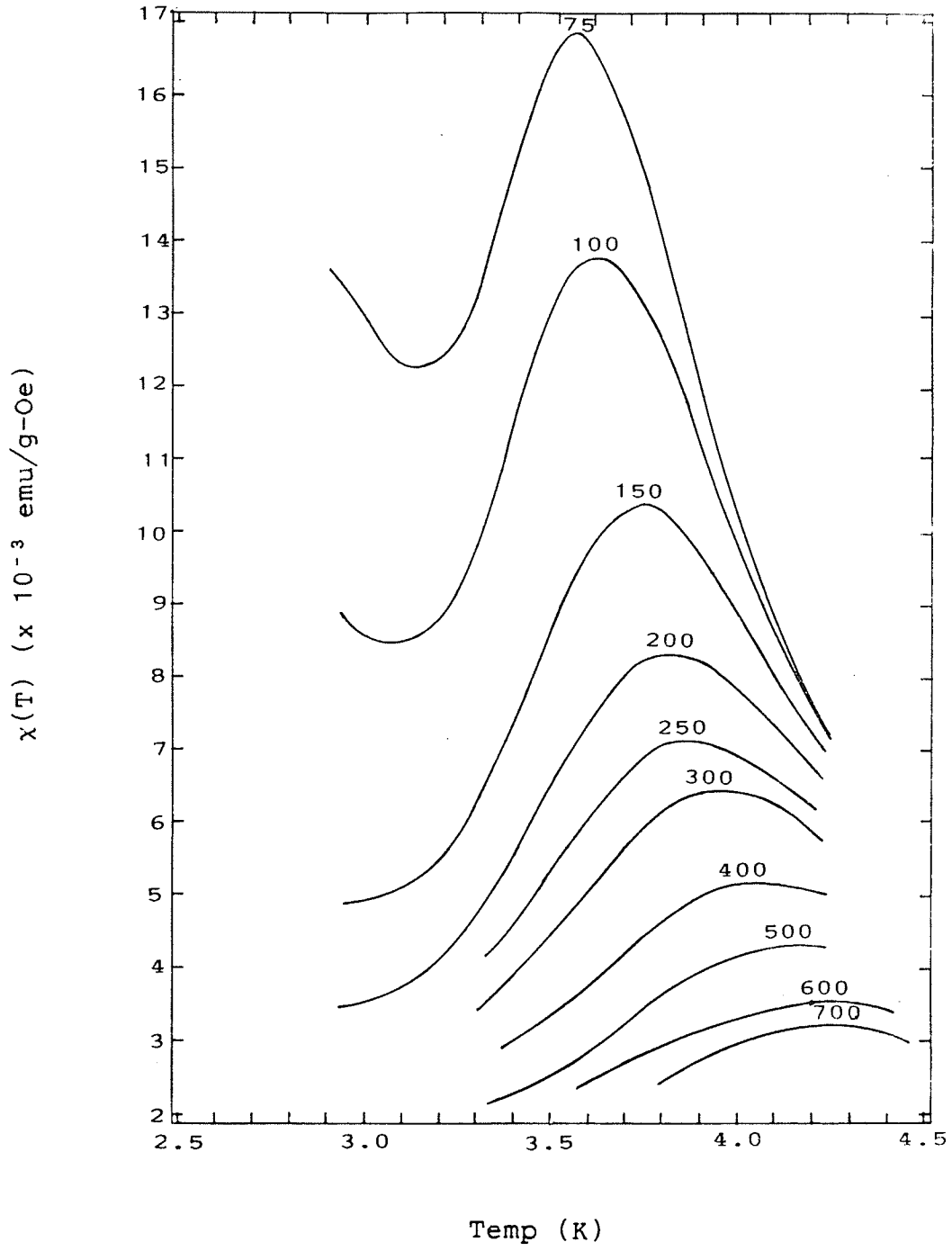

Fig.(A 9): Susceptibility of Pd + 5 at.% Gd in various biasing fields.

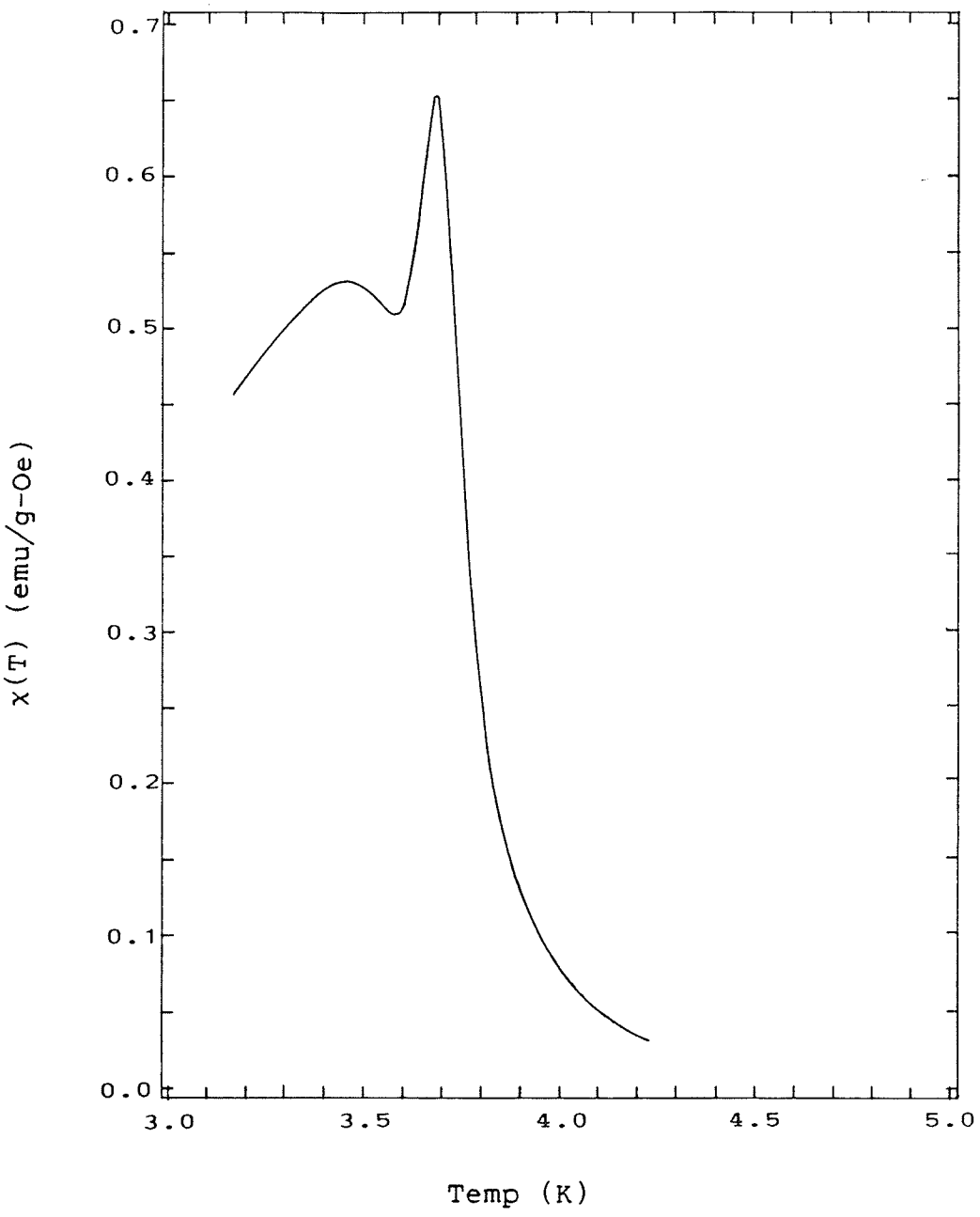

Fig.(A 10): Zero-field a.c. susceptibility of Pd + 6 at.% Gd.

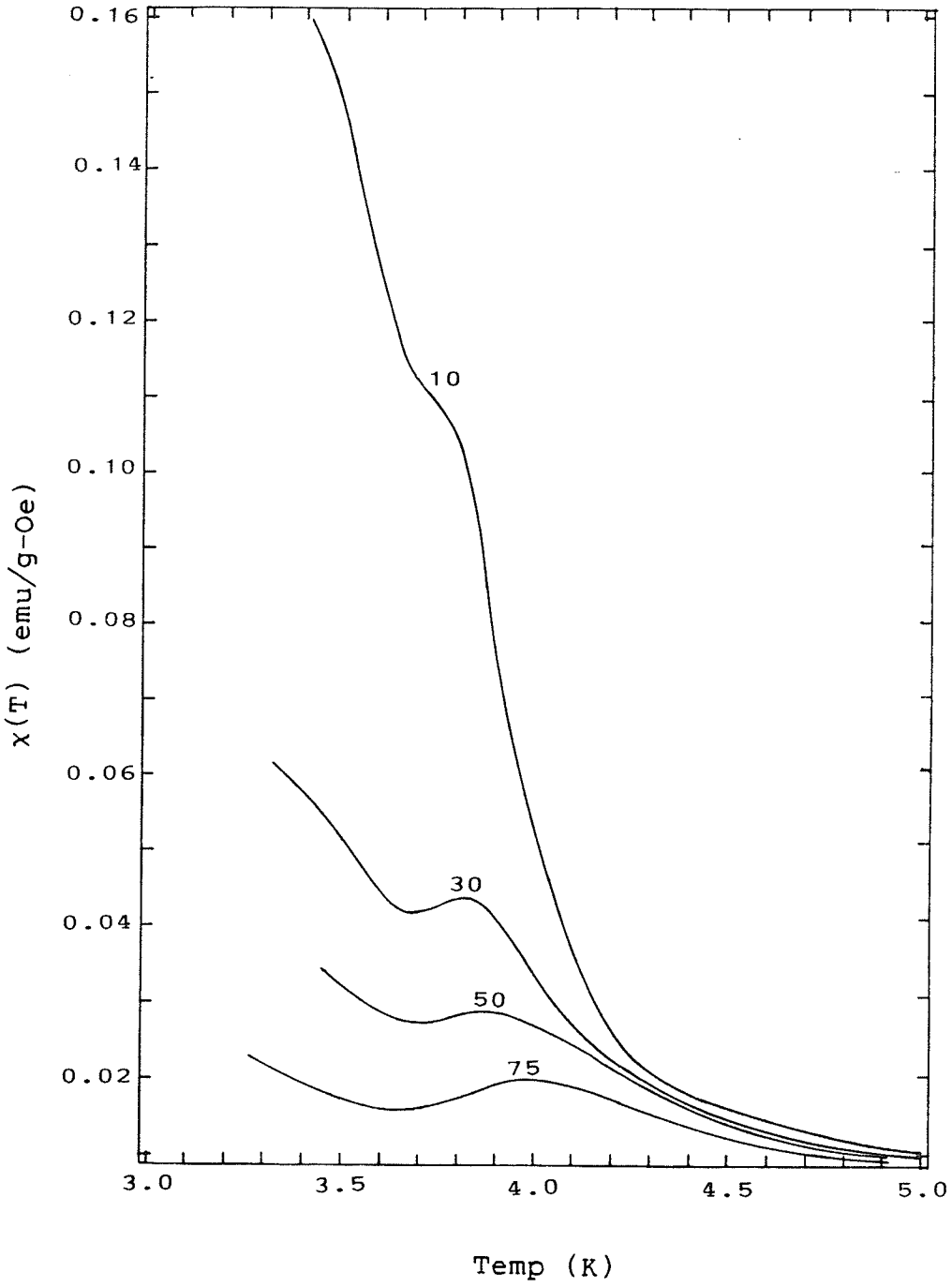

Fig.(A 11): Susceptibility of Pd + 6 at.% Gd in various biasing fields.

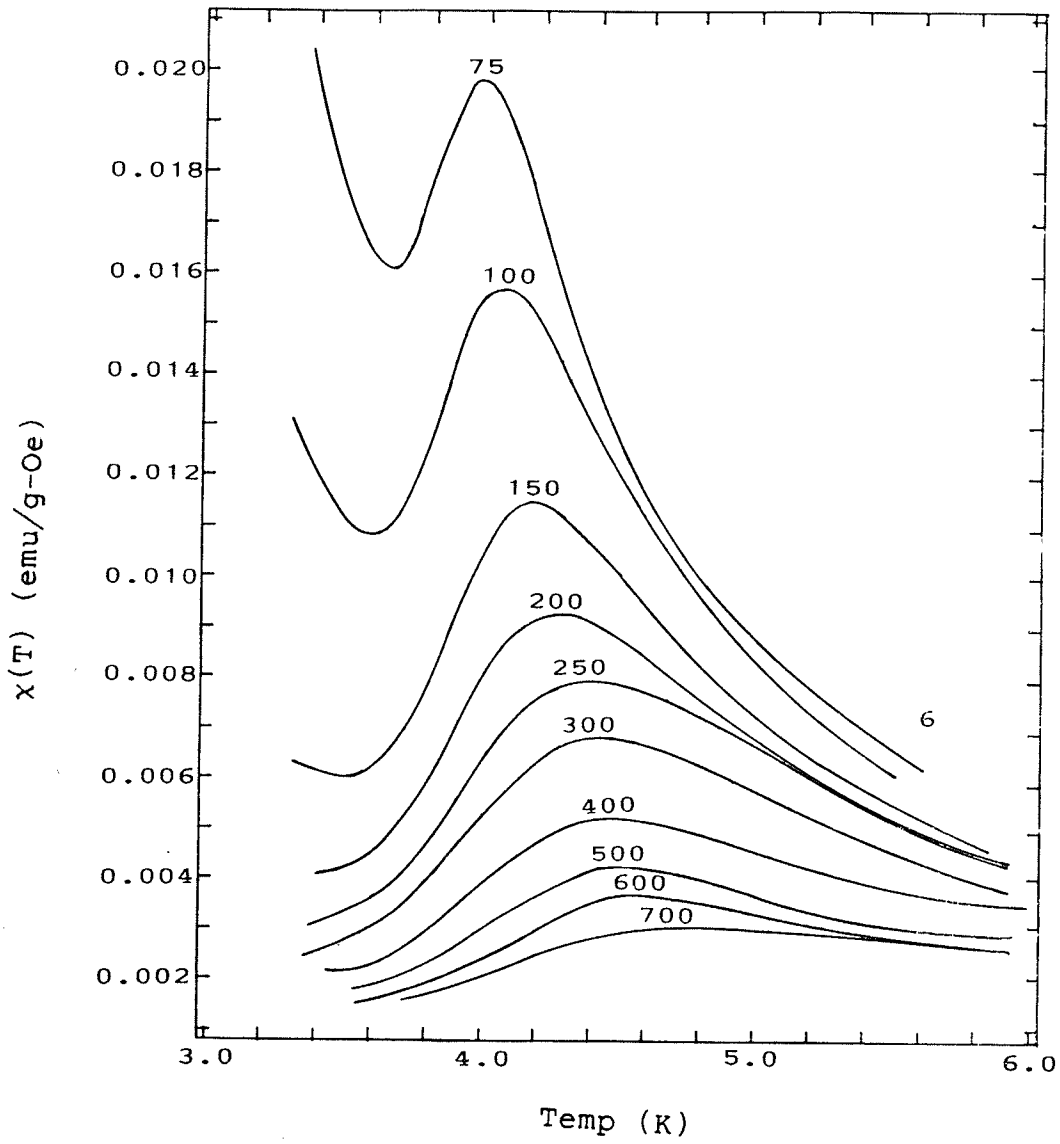

Fig.(A 12): Susceptibility of Pd + 6 at.% Gd in various biasing fields.

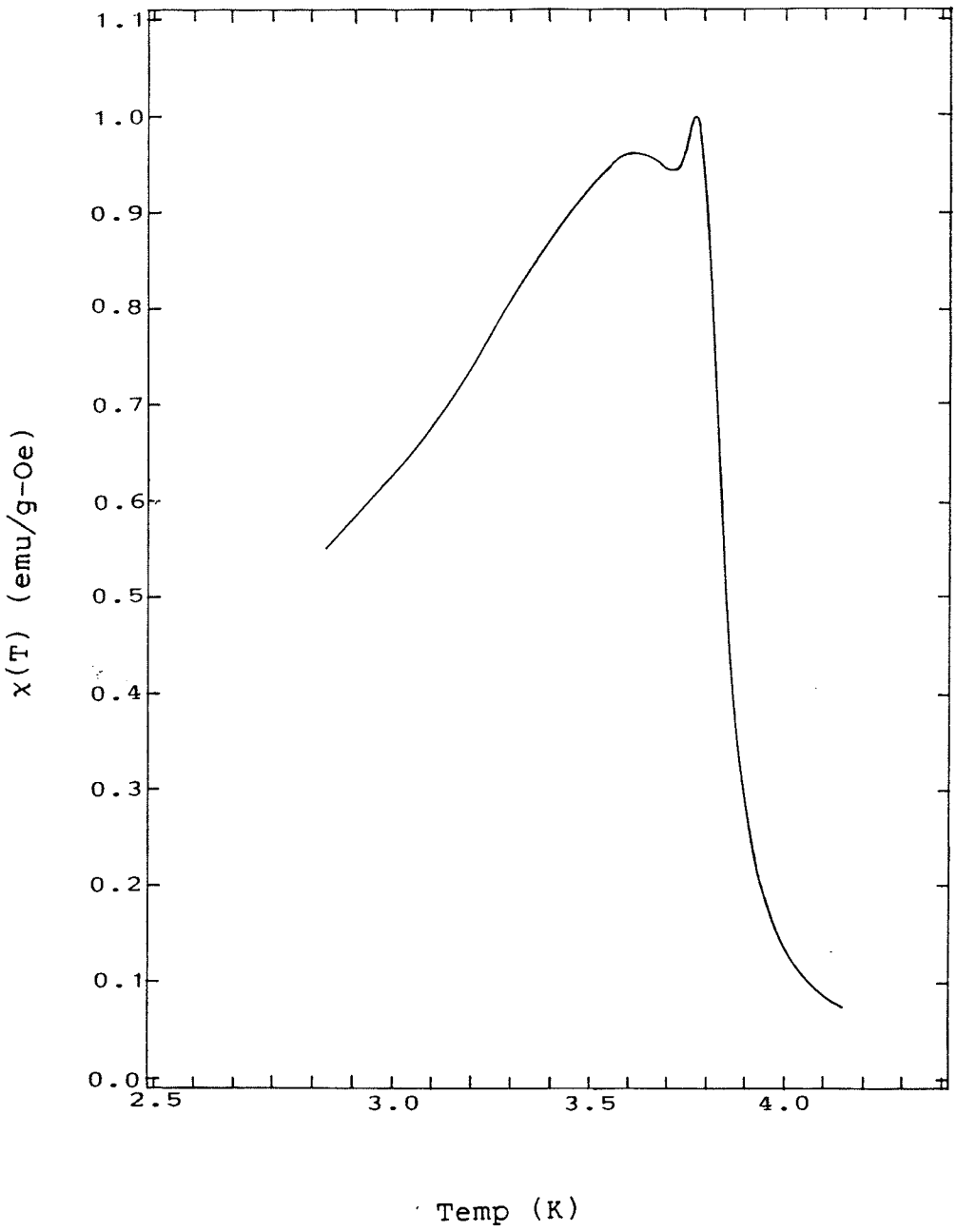

Fig.(A 13): Zero-field a.c. susceptibility of Pd + 7 at.% Gd.

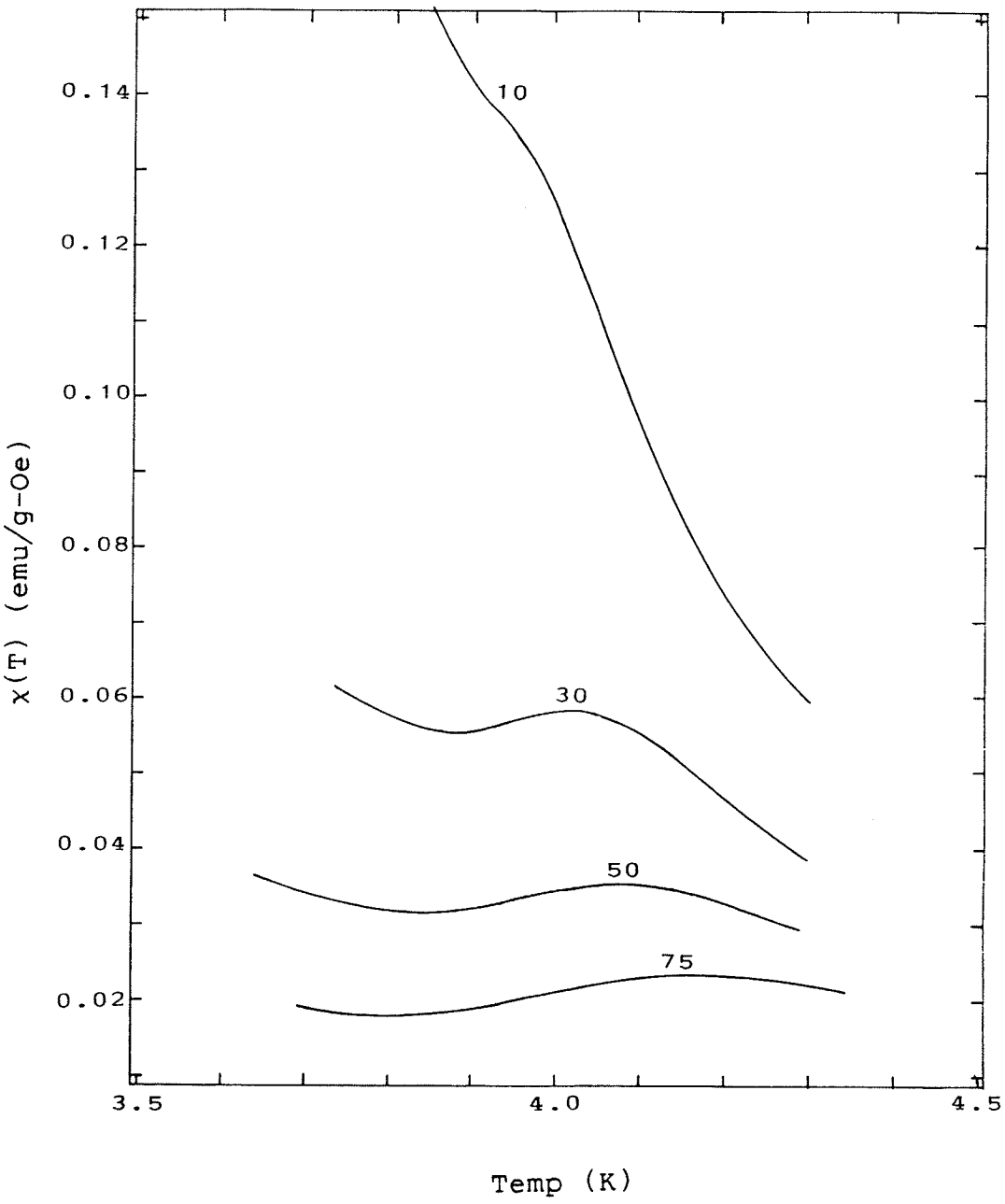

Fig.(A 14): Susceptibility of Pd + 7 at.% Gd in various biasing fields.

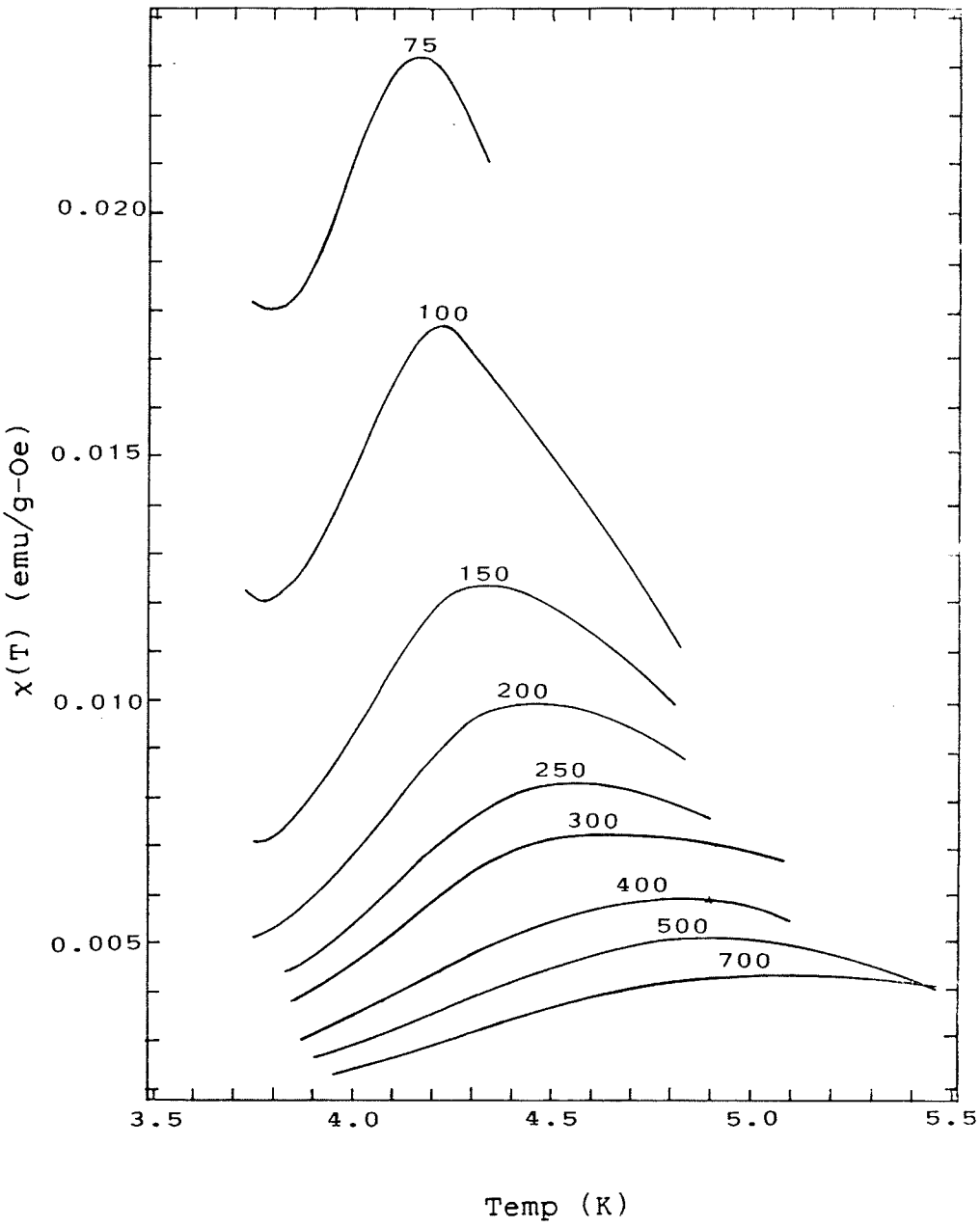

Fig.(A 15): Susceptibility of Pd + 7 at.% Gd in various biasing fields.

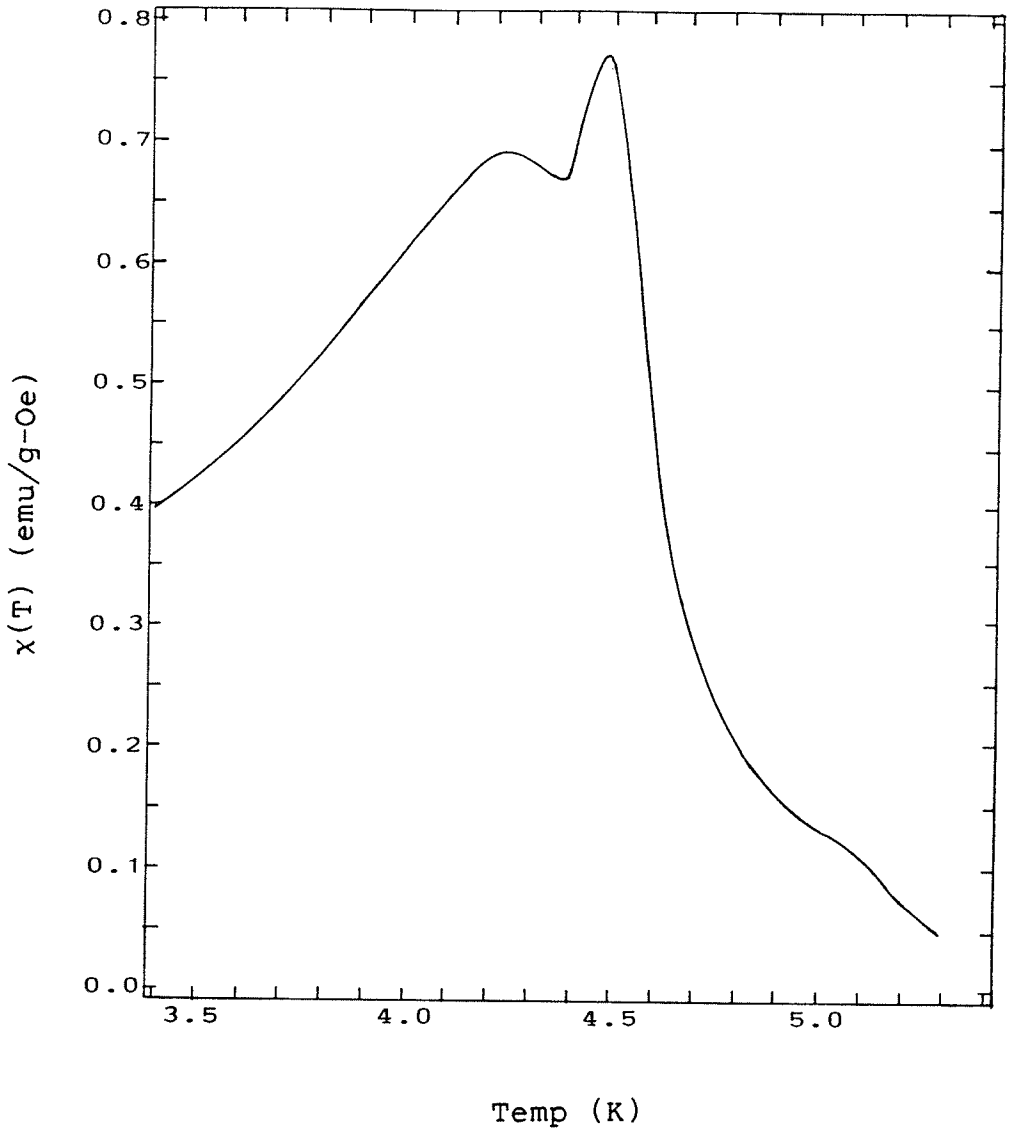

Fig.(A 16): Zero-field susceptibility of Pd + 8 at.% Gd.

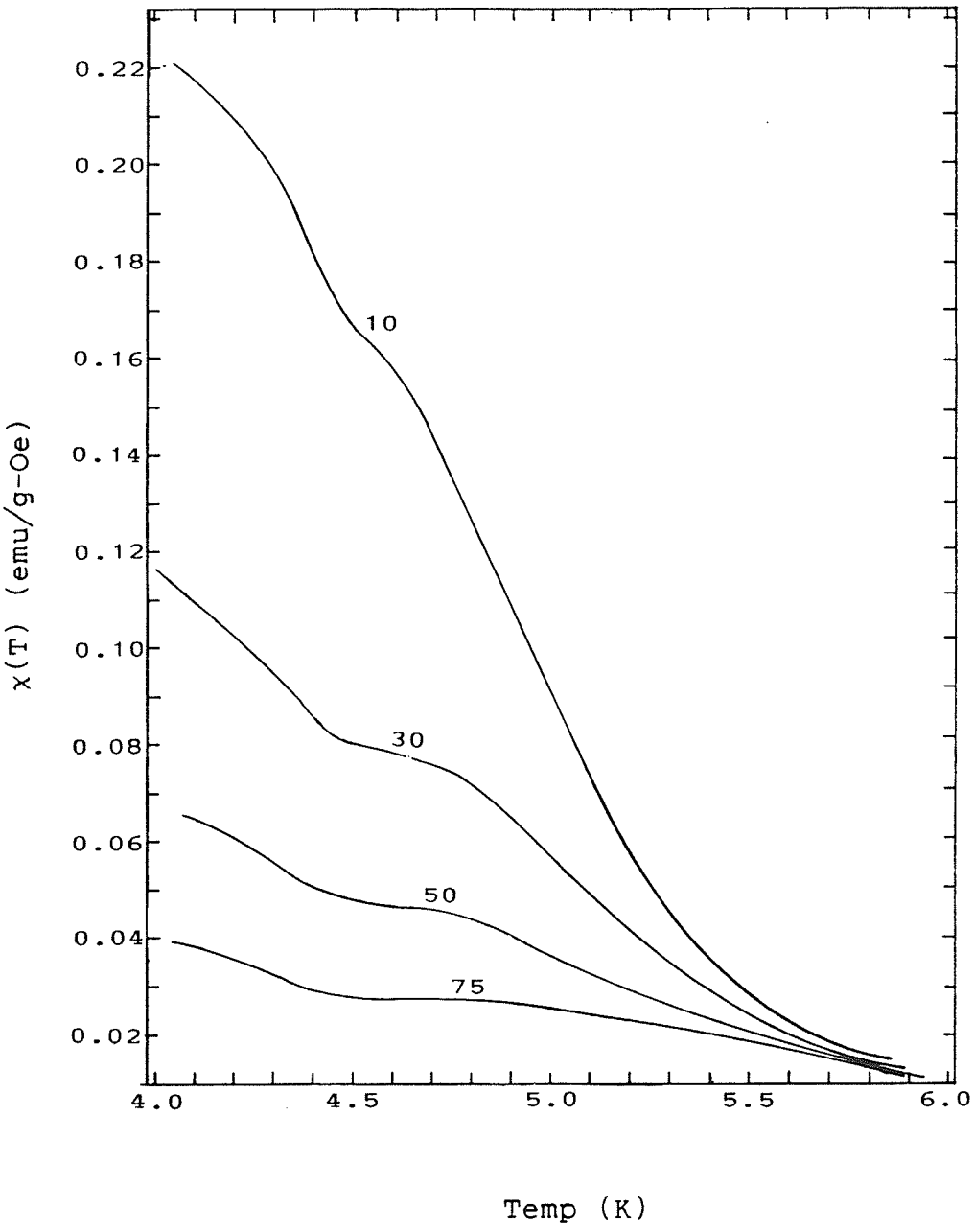

Fig.(A 17): Susceptibility of Pd + 8 at.% Gd in various biasing fields.

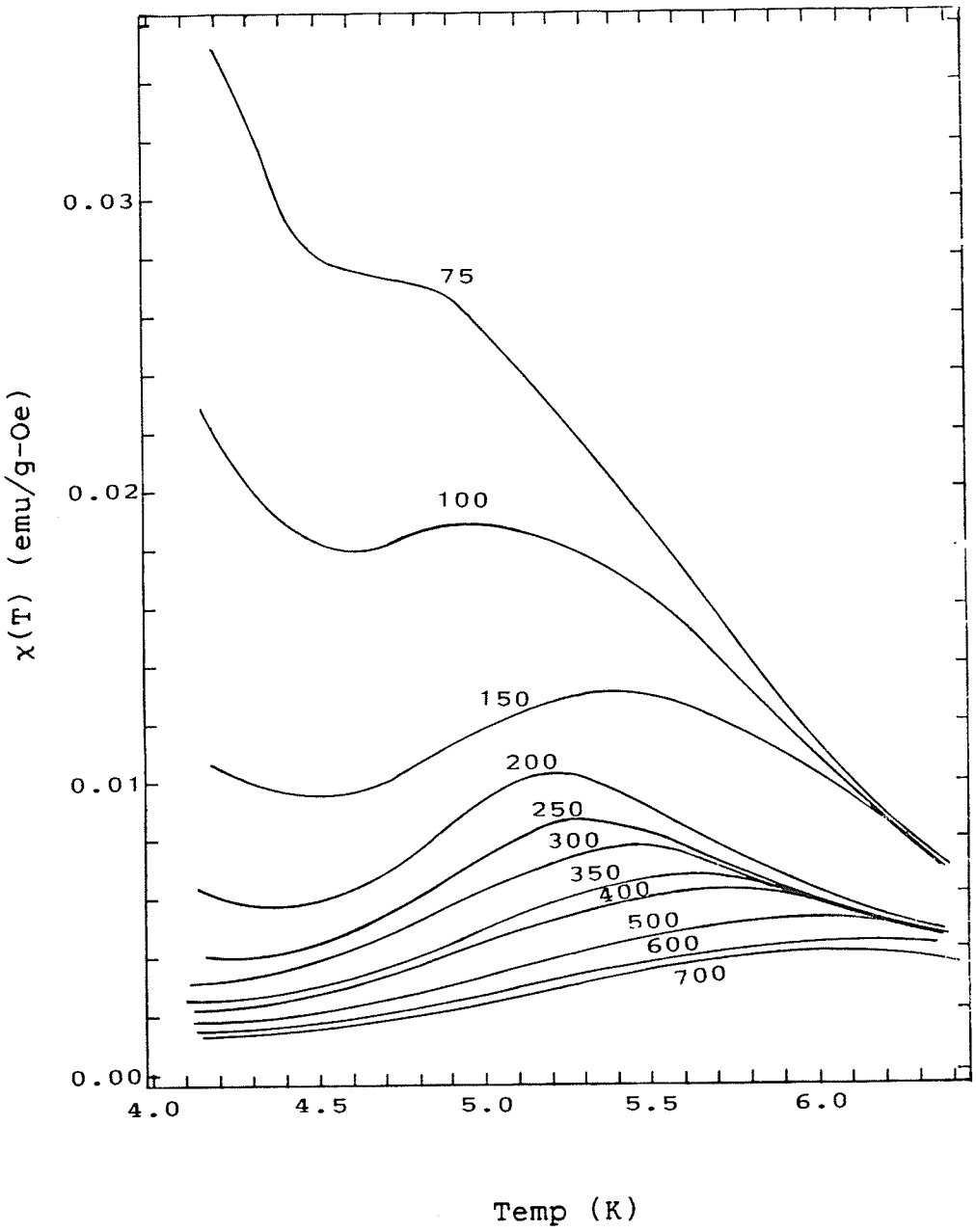

Fig.(A 18): susceptiility of Pd + 8 at.% Gd in various biasing fields.

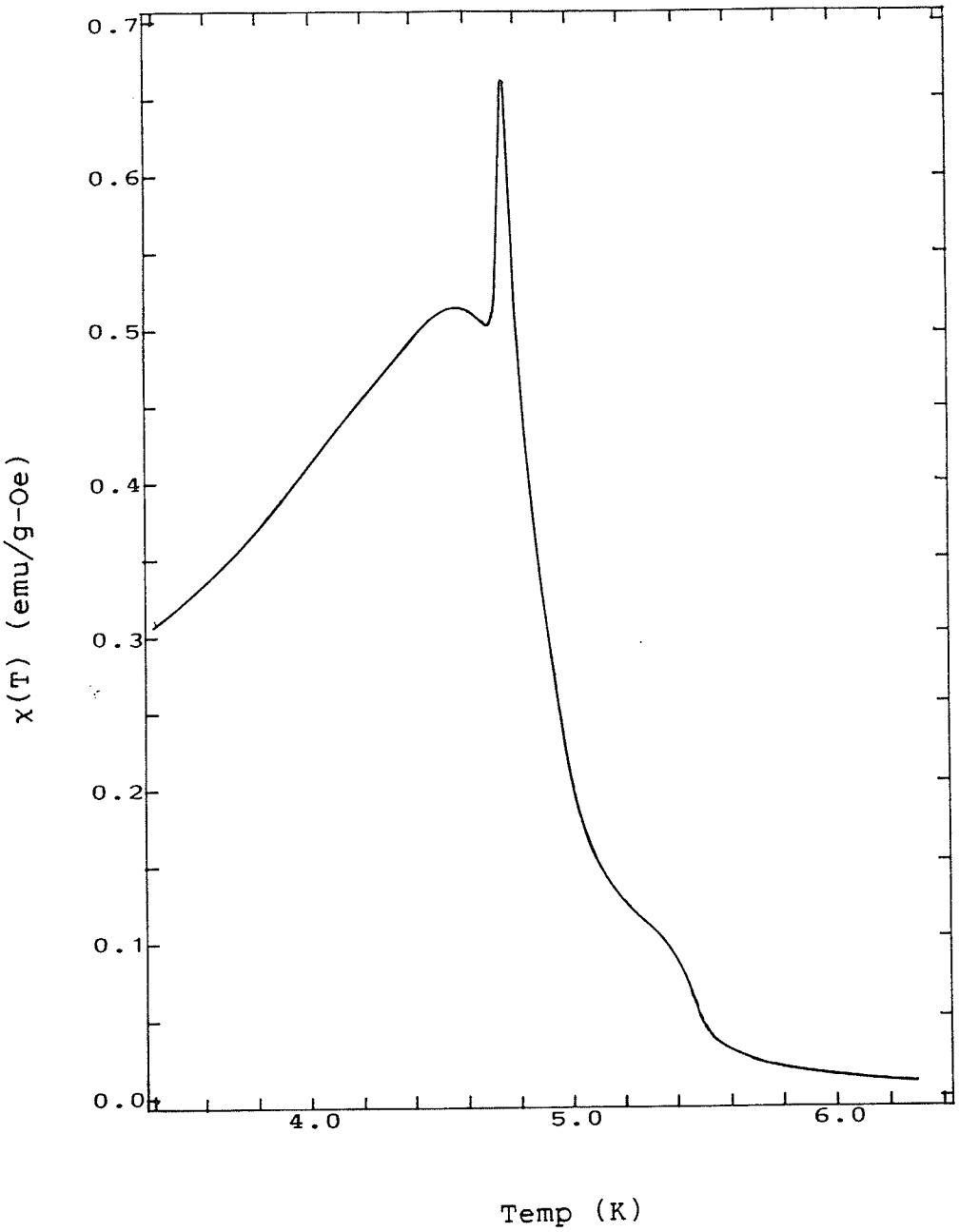

Fig.(A 19): Zero-field a.c susceptibility

Pd + 9 at.% Gd.

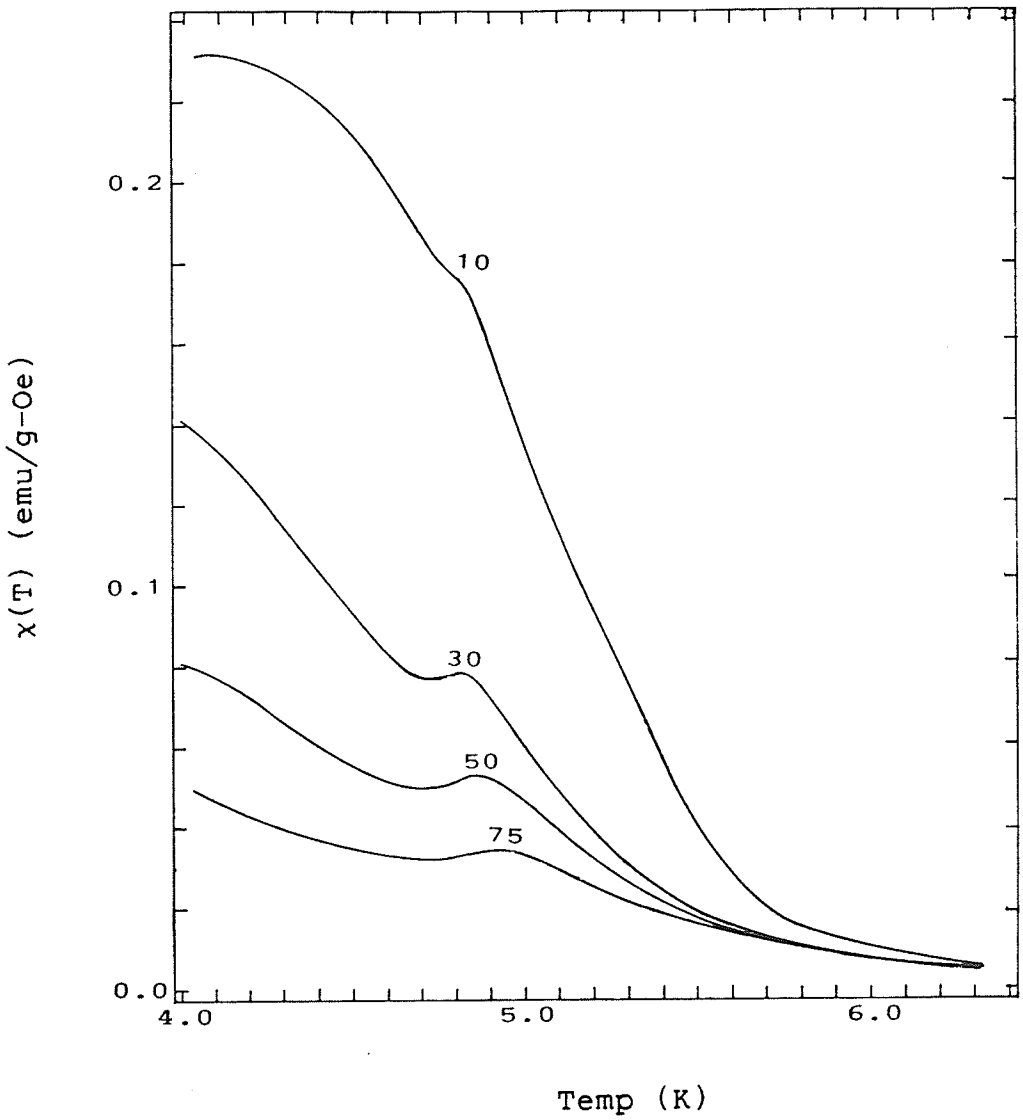

Fig.(A 20): Susceptibility of Pd + 9 at.% Gd in various biasing fields.

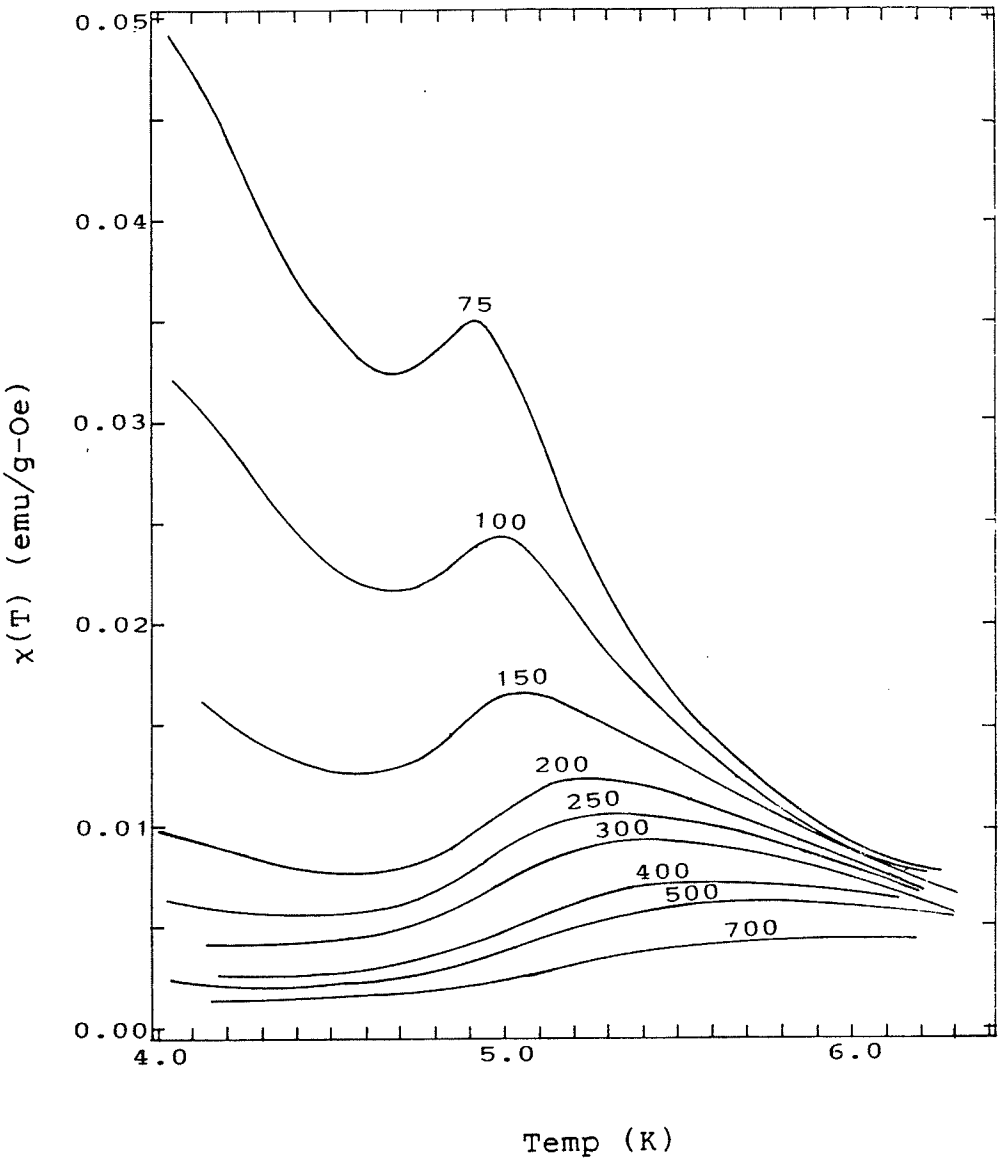

Fig.(A 21): Susceptibility of Pd + 9 at.% Gd in various biasing fields.

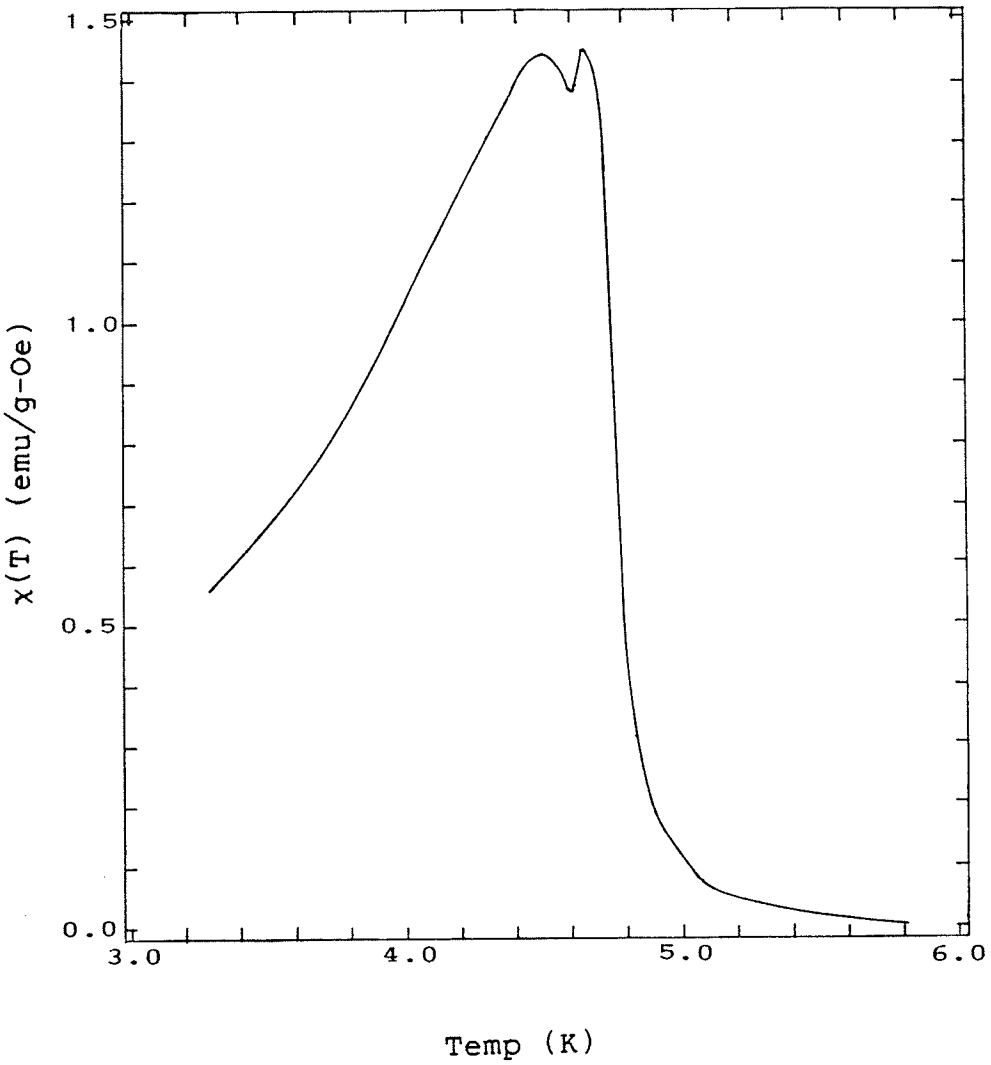

Fig.(A 22): Zero-field a.c. susceptibility of Pd + 10 at.% Gd.

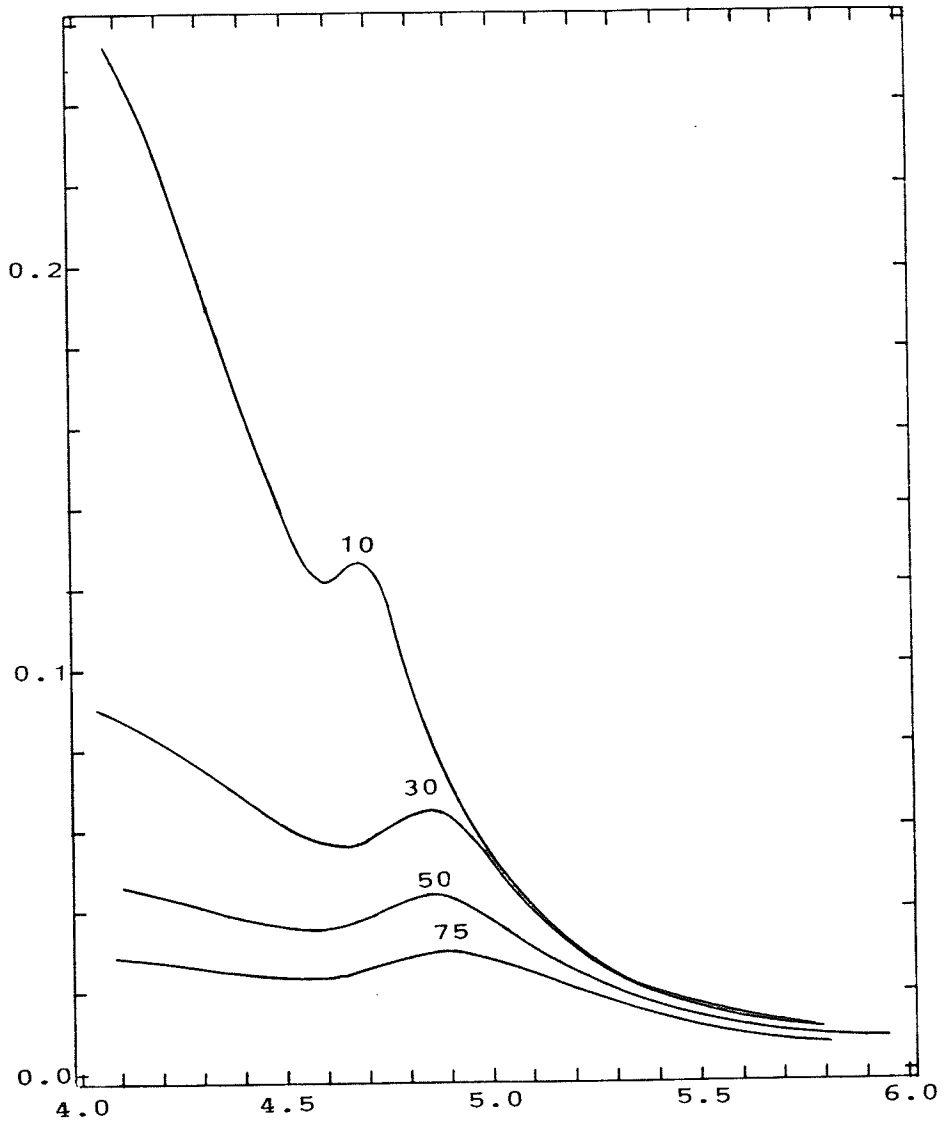

Fig.(A 23): Susceptibility of Pd + 10 at.% Gd in various biasing fields.

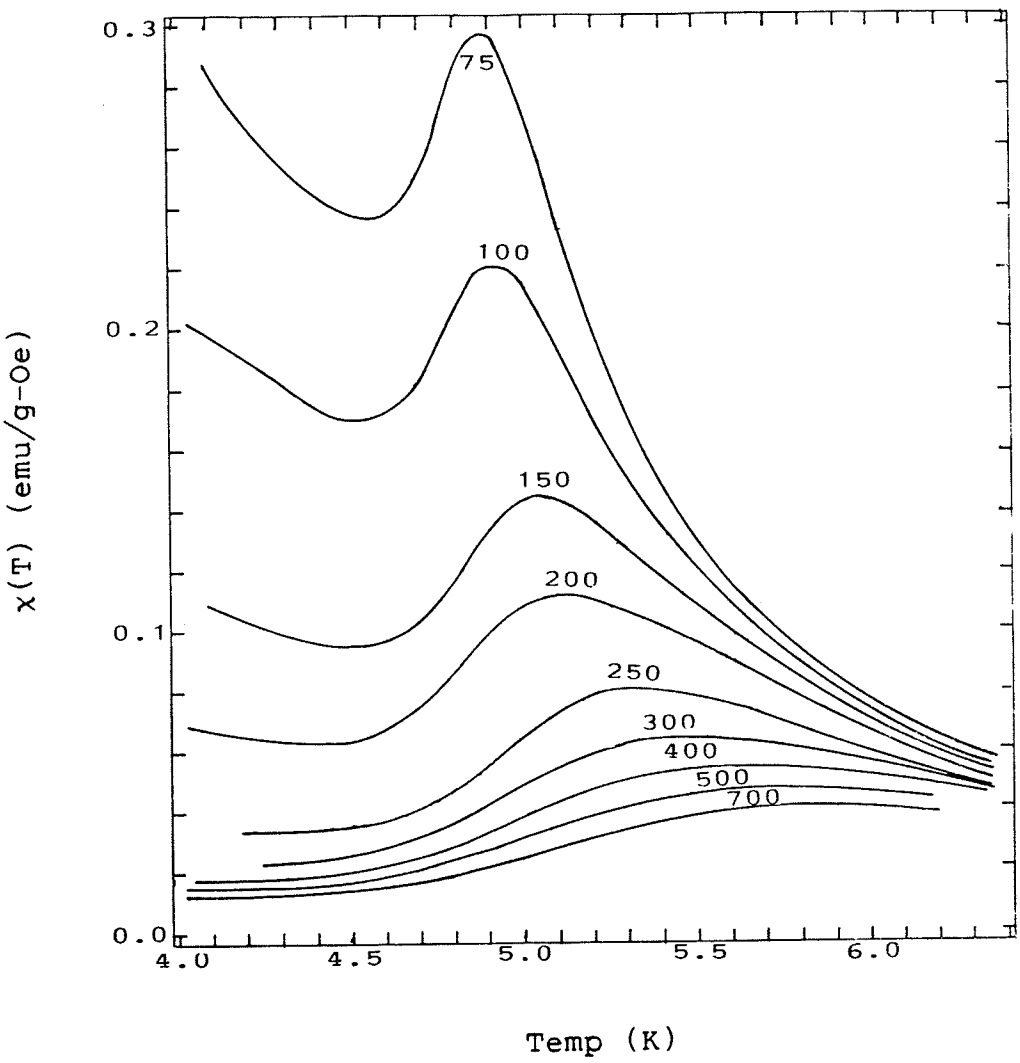

Fig.(A 24): Susceptibility of Pd + 10 at.% Gd in various biasing fields.

Appendix B

RESISTIVITY DATA

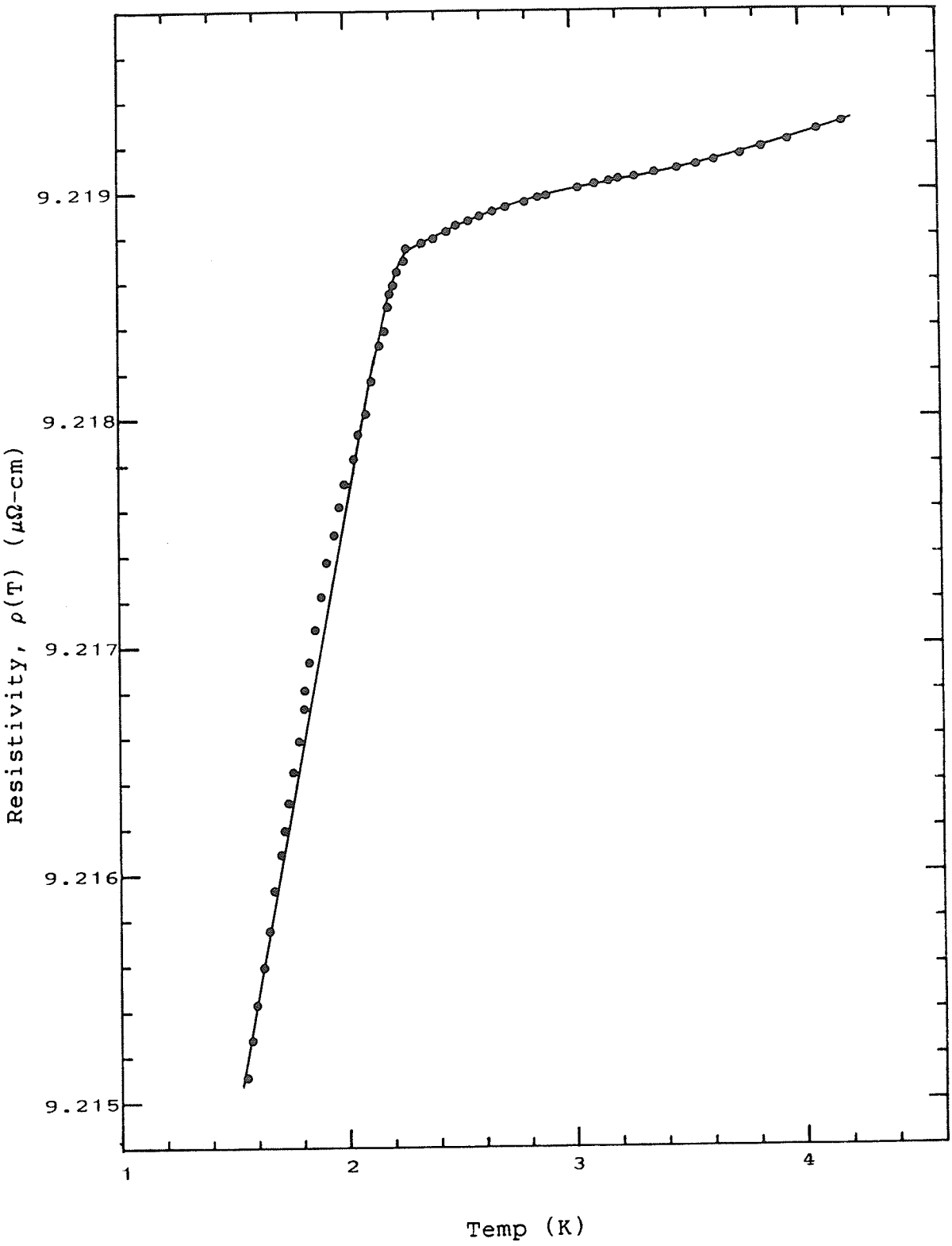

Fig.(B 1): Temperature-dependent resistivity of Pd + 3 at.% Gd.

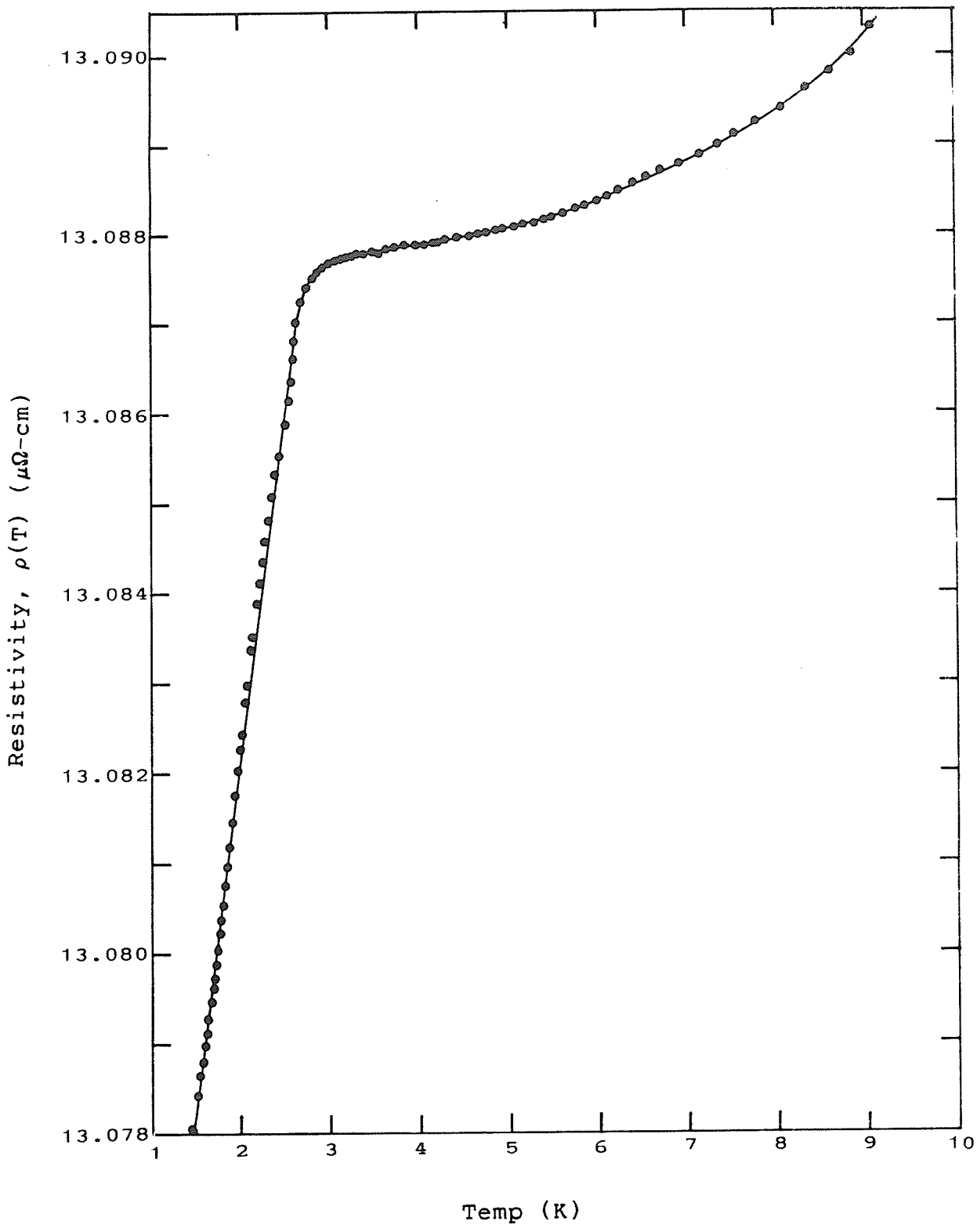

Fig.(B 2): Temperature-dependent resistivity of Pd + 4 at.% Gd.

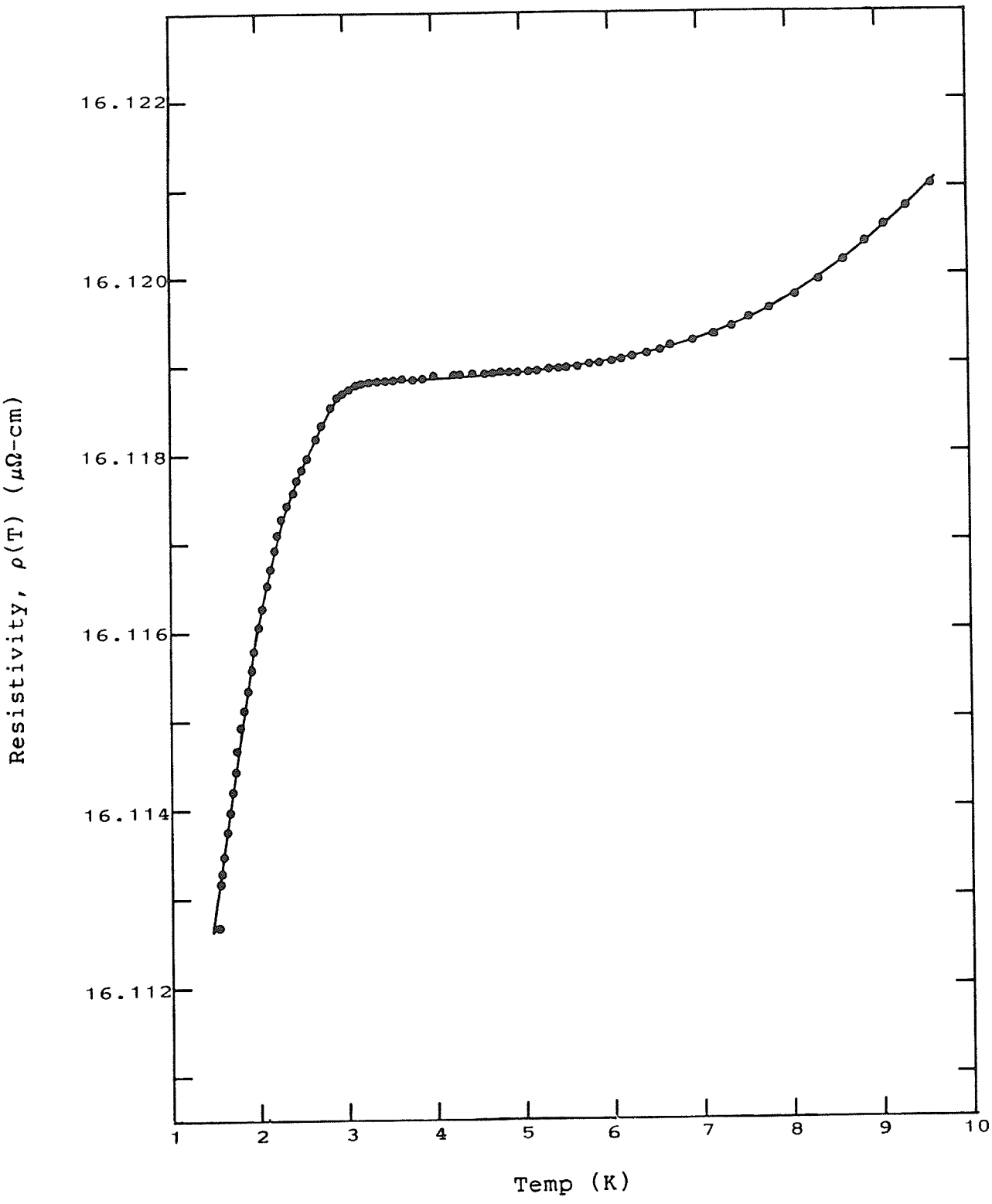

Fig.(B 3): Temperature-dependent resistivity of Pd + 5 at.% Gd.

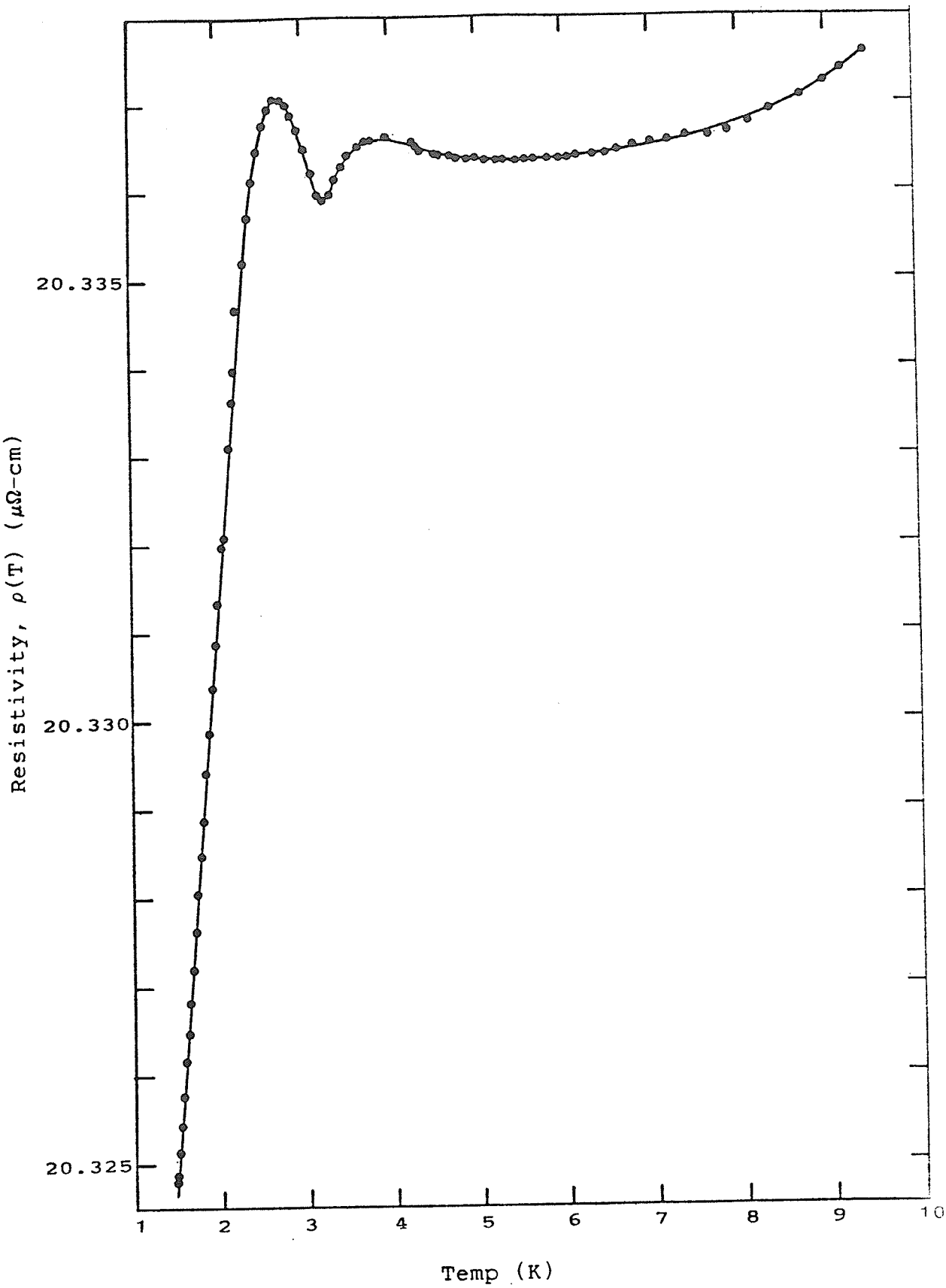

Fig.(B 4): Temperature-dependent resistivity of Pd + 6 at.% Gd.

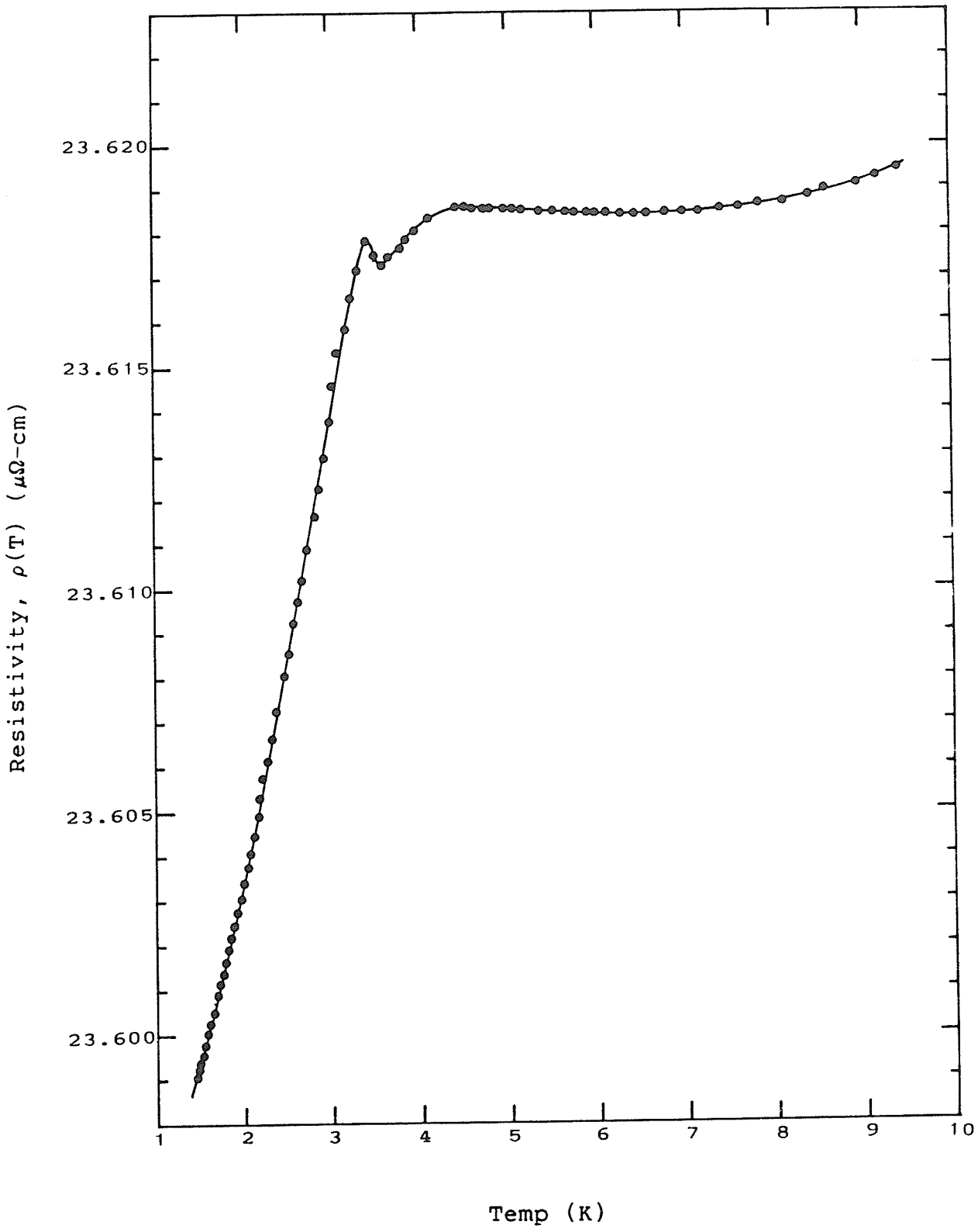

Fig.(B 5): Temperature-dependent resistivity of Pd + 7 at.% Gd.

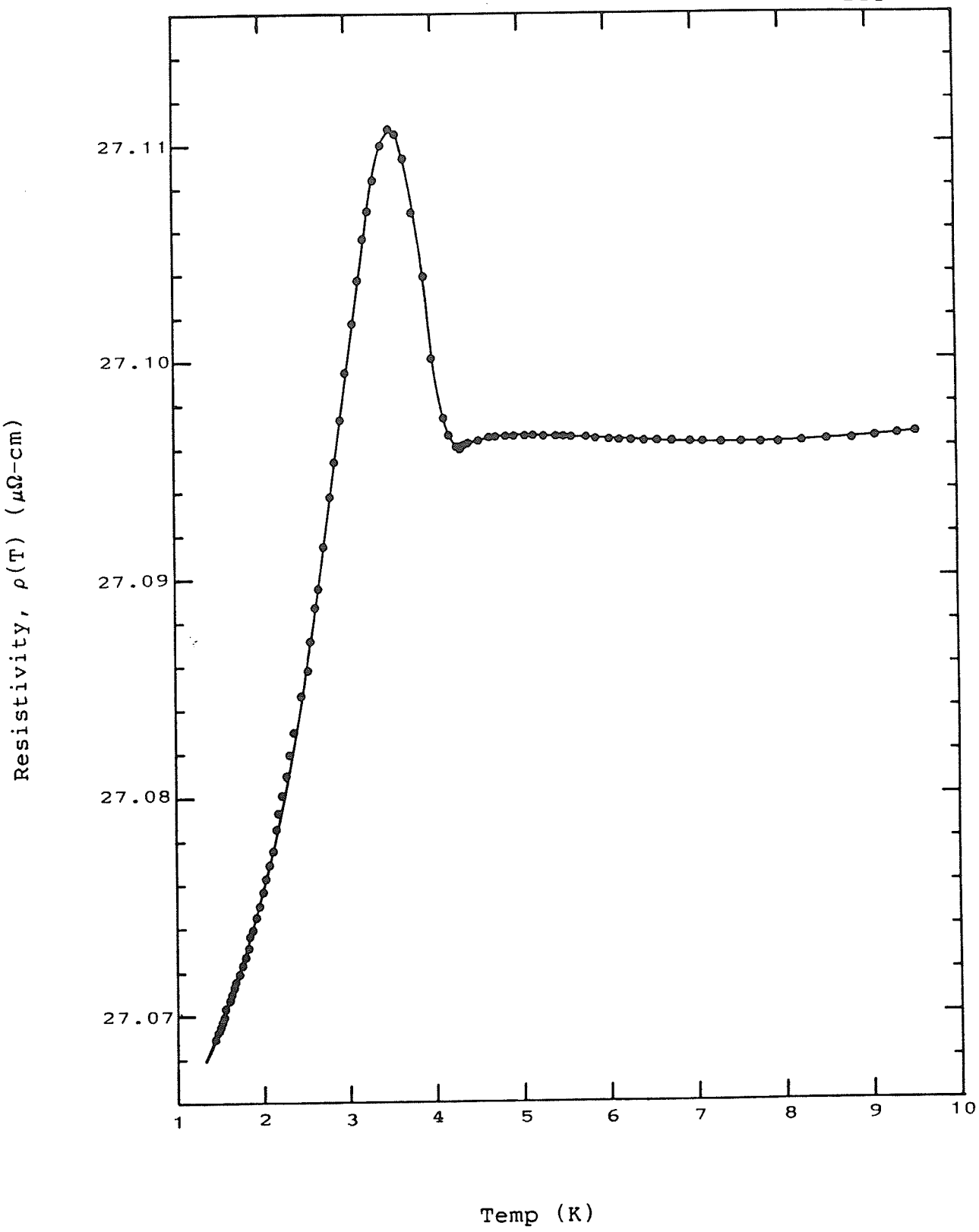

Fig.(B 6): Temperature-dependent resistivity of Pd + 8 at.% Gd.

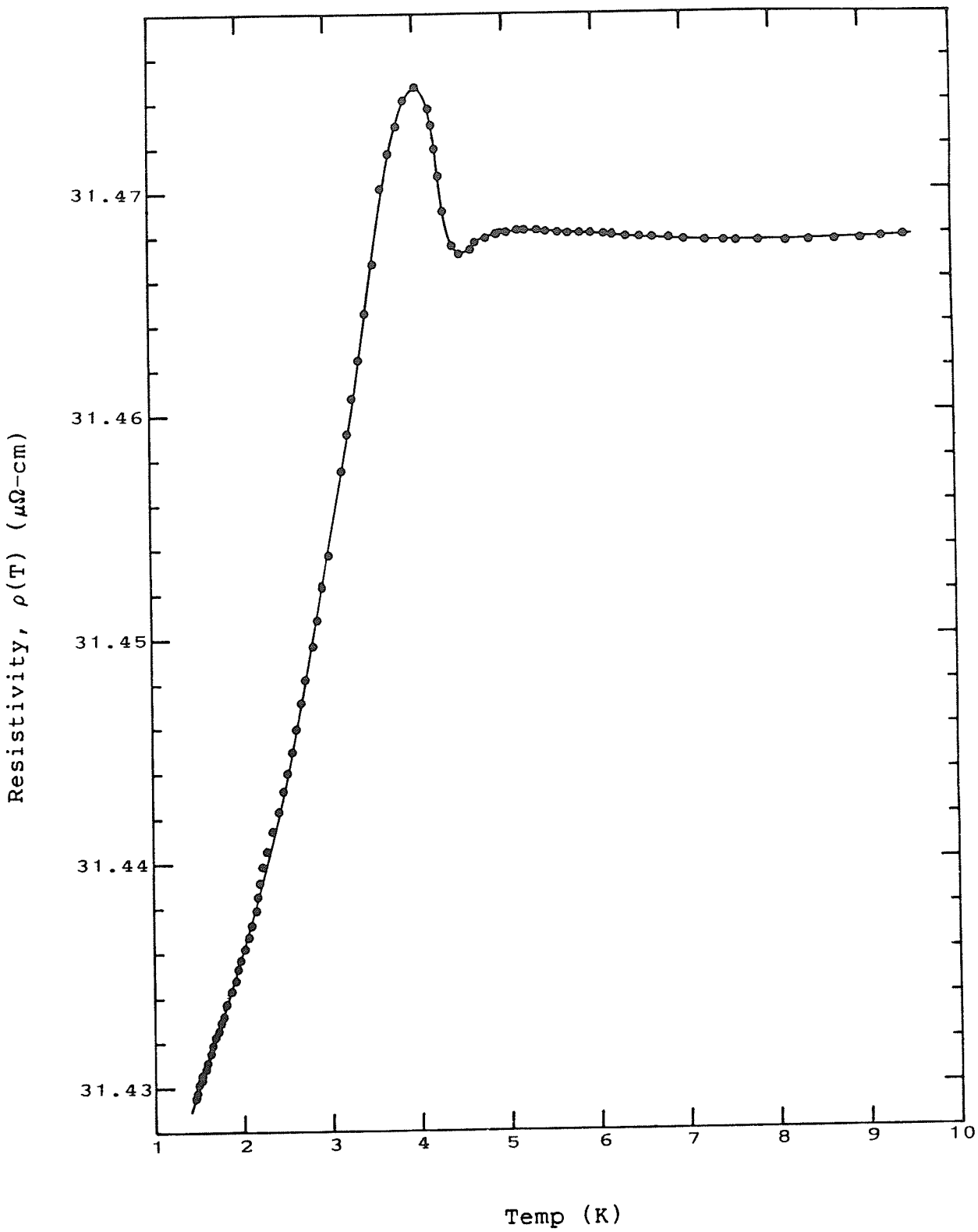

Fig.(B 7): Temperature-dependent resistivity of Pd + 9 at.% Gd.

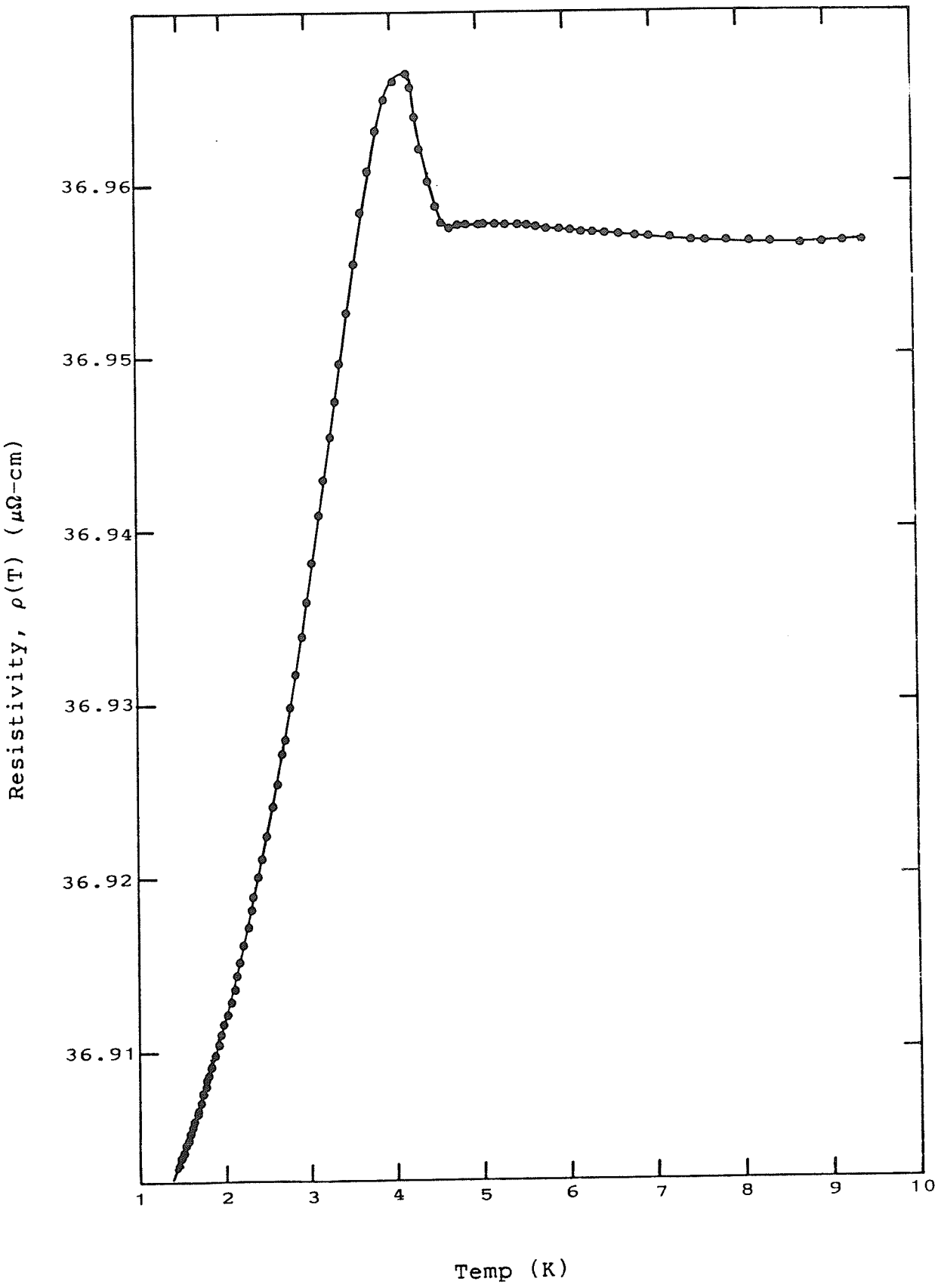

Fig.(B 8): Temperature-dependent resistivity of Pd + 10 at.% Gd.

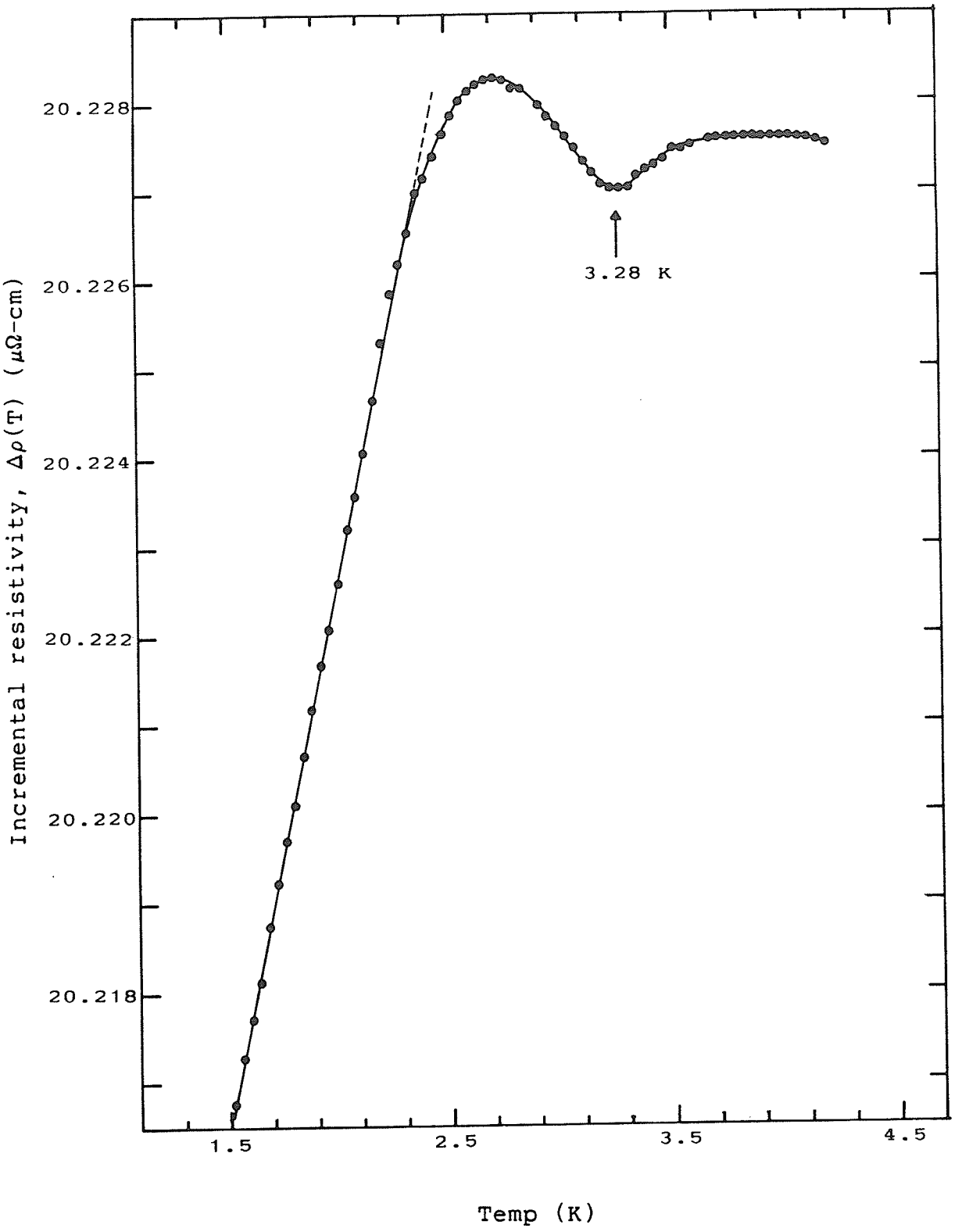

Fig.(B 9): Incremental resistivity-vs-Temperature plot for Pd + 6 at.% Gd.

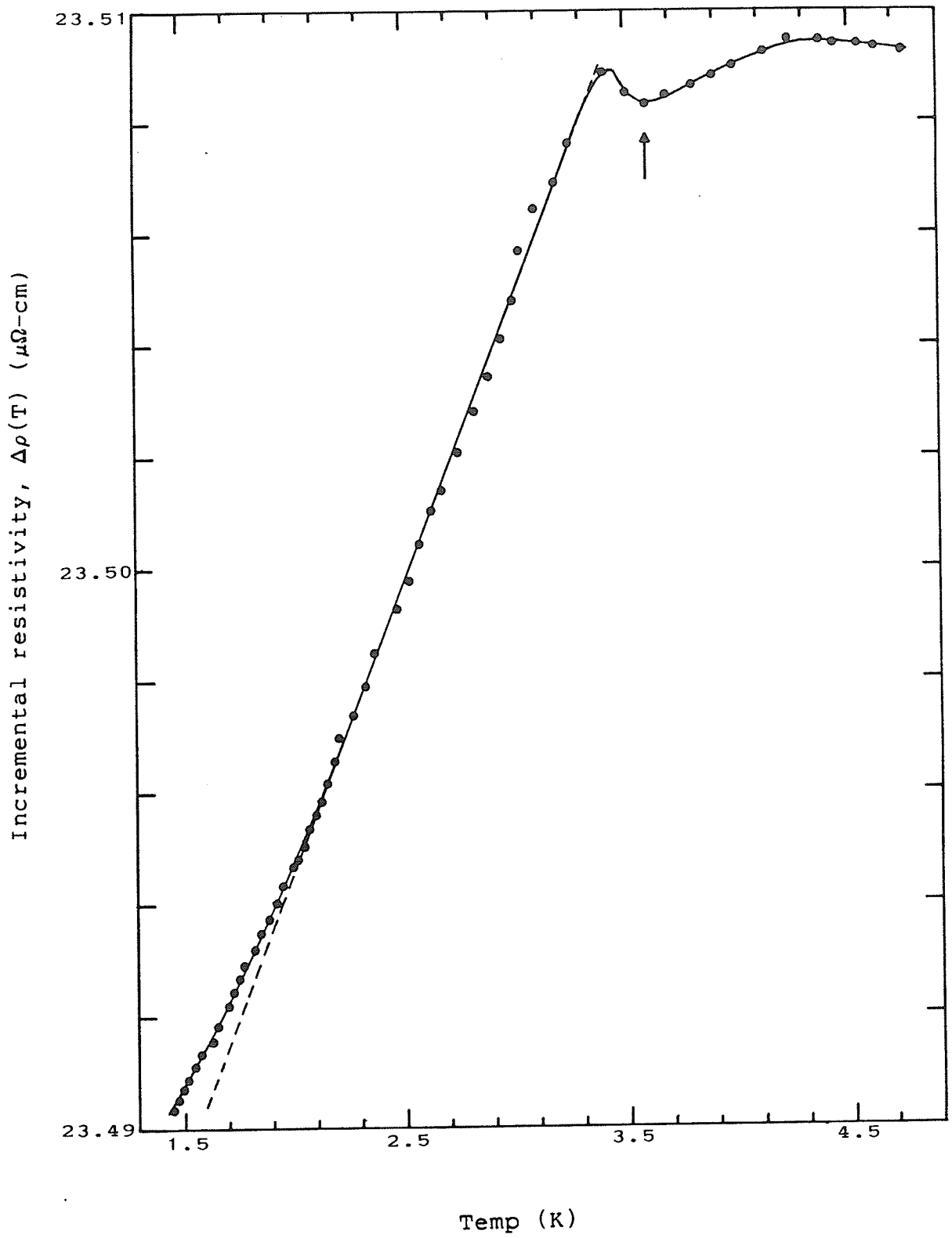

Fig.(B 10): Incremental resistivity-vs-Temperature plot for Pd + 7 at.% Gd.

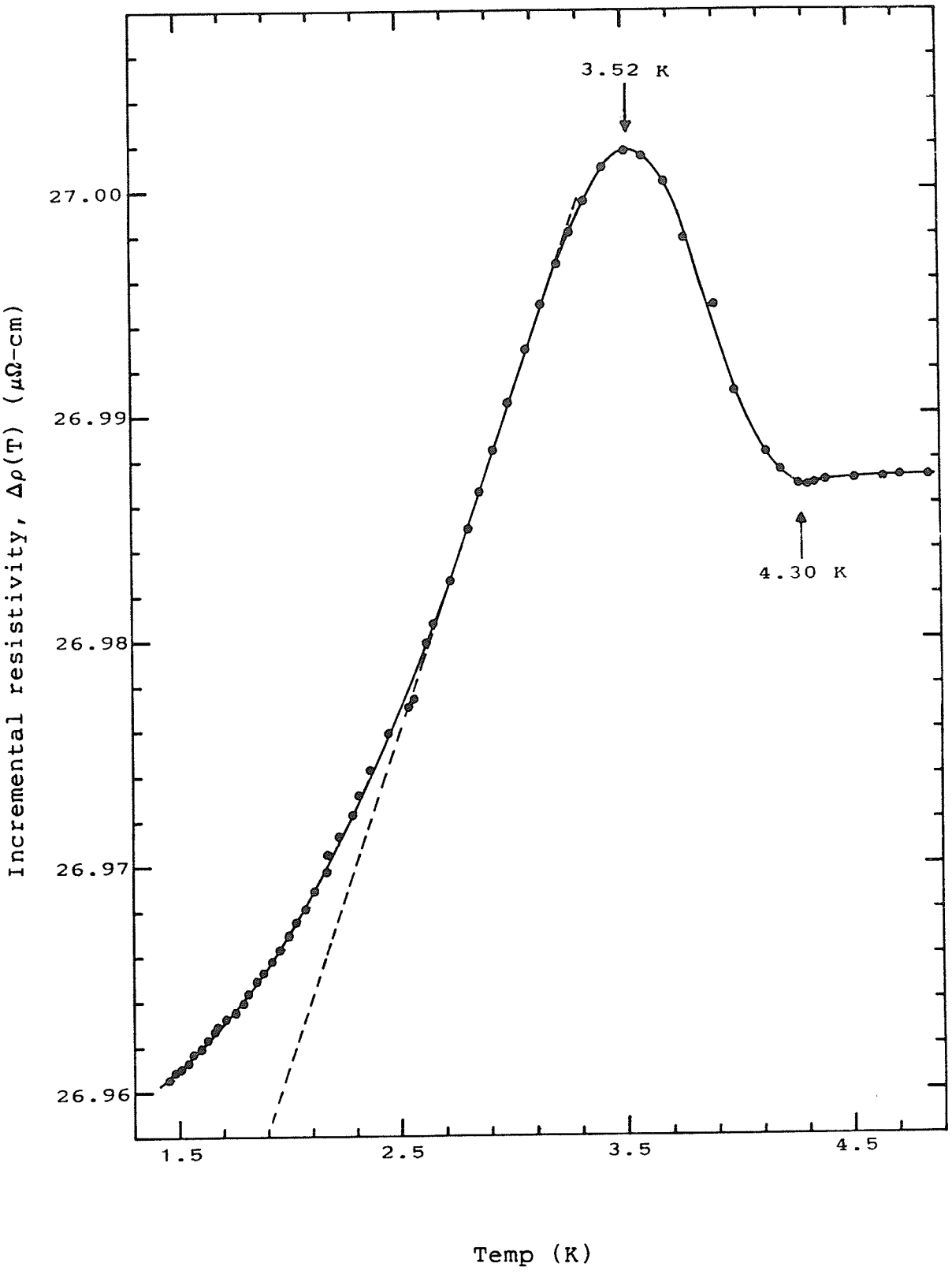

Fig.(B 11): Incremental resistivity-vs-Temperature plot for Pd + 8 at.% Gd.

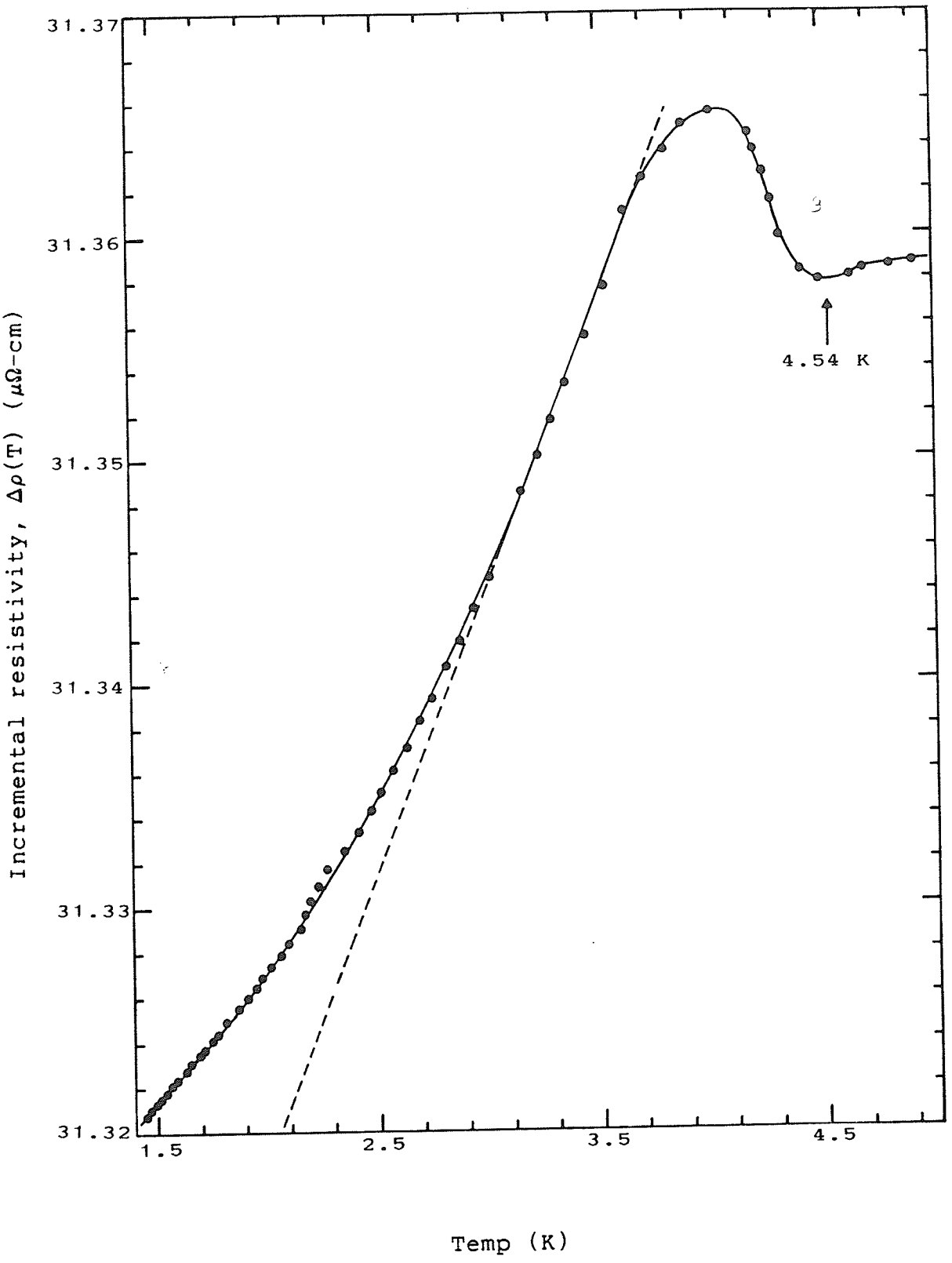

Fig.(B 12): Incremental resistivity-vs-Temperature plot for Pd + 9 at.% Gd.

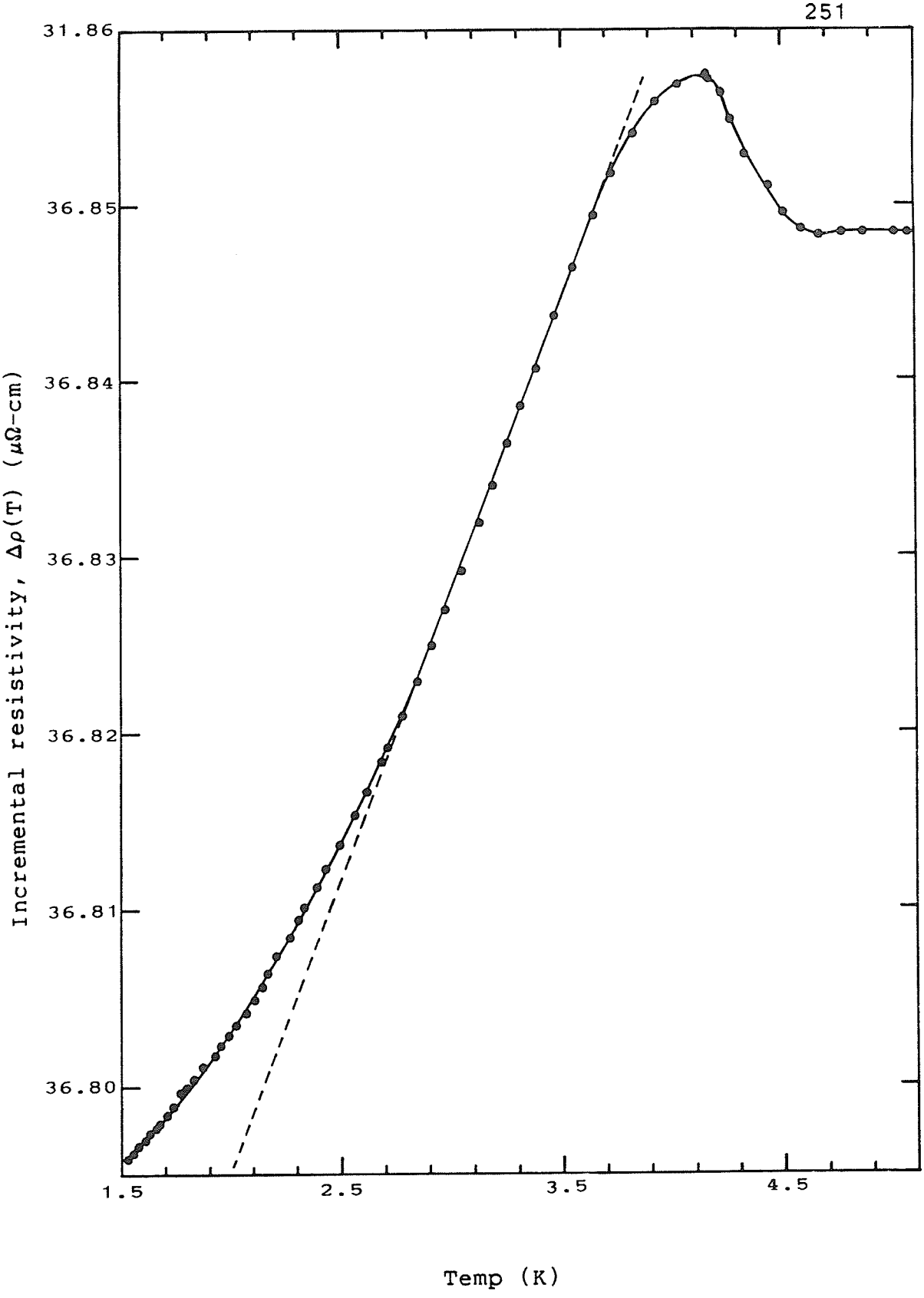

Fig.(B 13): Incremental resistivity-vs-Temperature plot for Pd + 10 at.% Gd.

REFERENCES:

1. Friedel J.
(a) Can. J. Phys. 34 (1956) 1190.
(b) Nuovo Cimento Suppl.7 (1958) 287.

2. Blandin A. and Friedel J.
J. Phys. Radium 20 (1959) 160.

3. Anderson P.W.
Phys.Rev. 124 (1961) 41-53.

4. Hirst L.L.
AIP Conf. Proc. 24 (1975) 11-15.

5. Zener C.
Phys. Rev. 81 (1951) 440.

6. Schrieffer J.R. and Wolff P.A.
Phys. Rev.149 (1966) 491.

7. Rudermann M.A. and Kittel C.
Phys. Rev. 96 (1954) 99.

8. Frohlich F. and Nabarro F.R.N.
Proc. Roy. Soc. London A175 (1940) 382.

9. Kasuya T.
Progr. Theor. Phys. 16 (1956) 45.
Progr. Theor. Phys. 16 (1956) 58.

10. Yosida Kei.
(a) Phys. Rev. 106 (1957) 893.
(b) Phys. Rev. 107 (1957) 396-403.

11. Wolff P.A.
Phys. Rev. 120 (1960) 814-19.

12. Mueller F.M. Freeman A.J. Dimmock J.O. and Furdyna A.M.
Phys. Rev. B 1 (1970) 4617-31.

13. Anderson O.K.
Phys. Rev. B 2 (1970) 883-905.

14. Roth L.M. Zeiger H.J. and Kaplan T.A.
Phys. Rev. 149 (1966) 519.

15. Caroli B.
(a) Phys. de la Mat. Cond. 1 (1963) 346.
(b) J. Phys. Chem. Solids 28 (1967) 1427-1440.

16. Blandin A.
Proc. Int. School of Phys. "Enrico Fermi" Course 37
(New York, Academic 1967) 393.

17. Moriya T.
Proc. Int. School of Phys. "Enrico Fermi" Course 37
(New York, Academic 1967) 206.

18. Alexander S. and Anderson P.W.
Phys. Rev. 133 (1964) A1594-1603.

19. Turov E.A.
'Elements of Theoretical Magnetism' (1968)

20. Yosida K. and Watabe A.
Progr. Theor. Phys. 28 (1962) 361.

21. Vonsovskii S.V.
Magnetism (English translation) (New York,
John Wiley & Sons 1974).

22. Overhauser A.W.
(a) J. Phys. Chem. Solids 13 (1959) 71-80.
(b) Phys. Rev. Letts. 3 (1959) 414-6.

23. Sarkissian B.V.B. and Coles B.R.
Comm. on Phys. 1 (1976) 17-23.

24. Southern B.W. and Sherrington D.
J. Phys. C: Sol. St. Phys. 8 (1975) 2111-23.

25. Gerritsen A.N. and Linde J.O.
Physica 17 (1951) 573-584.

26. Owen J. Browne M. Knight W.D. and Kittel C.
Phys. Rev. 102 (1956) 1501.

27. Owen J. Browne M. Arp V. Kip A.F.
Phys. Chem. Solids 2 (1957) 85.

28. Yosida K.
Phys. Rev. 107 (1957) 396-403.

29. Long P.D. and Turner R.E.
J. Phys. C: Met. Phys. suppl. 2 (1970) S127.

30. Ashcroft N.W. and Mermin N.D.
Solid State Physics (Holt, Rinehart and
Winston 1976).

31. Williams Gwyn and Loram J.W.
(a) J. Phys. Chem. Solids 30 (1969) 1827-33;
(b) Solid St. Commun. 7 (1969) 1261-65.

32. Vuillemin J.J.
Phys. Rev. 144 (1966) 396.

33. Kleiman R.N. and Williams Gwyn.
J. Phys. F: Met. Phys. 12 (1982) 169-76.

34. Ma S.K.
Modern Theory of Critical Phenomena (New York, Benjamin 1976)

35. Sobotta G.
J. Magn. Magn. Mater. 28 (1982) 1.

36. Sobotta G. and Wagner D.
DPG Fruhjahrstagung (Munster) 1984.

37. Stanley H.E.
Phase Transitions and Critical Phenomena (London, Oxford 1971).

38. Widom B.
J. Chem. Phys. 43 (1965) 3898-905.

39. Kadanoff L.P. Gotze W. Hamblen D. Hecht R. Lewis E.A.S. Palciauskas V.V. Rayl M. Swift J. Aspnes D. and Kane J.
Rev. Mod. Phys. 39 (1967) 395.

40. Marshall W.
Phys. Rev. 118 (1960) 1519.

41. Klein M.W. and Brout R.
Phys. Rev. 132 (1963) 2412.

42. Klein M.W.
(a) Phys. Rev. 136 (1964) A1156.
(b) Phys. Rev. 173 (1968) 522.
(c) Phys. Rev. 188 (1969) 933.

43. Cannella V. and Mydosh J.A.
Phys. Rev. B 6 (1972) 4220.

44. Edwards S.F. and Anderson P.W.
J. Phys. F: Met. Phys. 5 (1975) 965.

45. Sherrington D. and Kirkpatrick S.
Phys. Rev. Letts. 35 (1975) 1792-96.

46. Roshko R.M. and Williams Gwyn.
J. Phys. F: Met. Phys. 14 (1984) 703-709.

47. Blandin A. Gabay M. and Garel T.
J. Phys. C: 13 (1980) 403.

48. Parisi G.
J. Phys. A 13 (1970) L115.

49. Southern B.W.
J. Phys. C: Sol. St. Phys. 9 (1976) 4011-19.

50. Ho S.C. Maartense I. and Williams G.
(a) J. Phys. F: Met. Phys. 11 (1981) 699-710.
(b) J. Phys. F: Met. Phys. 11 (1981) 1107-17.
(c) J. Appl. Phys. 52 (1981) 1670-72.

51. Gaunt P. Ho S.C. Williams G. and Cochrane R.W.
Phys. Rev. B 23 (1981) 251-5.

52. Dugdale J.S.
The Electrical Properties of Metals and Alloys
(London, Edwards Arnold 1977) 240.

53. Baber W.G.
Proc. Roy. Soc. London A 158 (1937) 383.

54. Schindler A.I. and Rice M.J.
Phys. Rev. 164 (1967) 759.

55. Schindler A.I. and Coles B.R.
J. Appl. Phys. 39 (1968) 956-7.

56. Rice M.J.
J. Appl. Phys. 39 (1968) 958-9.

57. Windmiller L.R. Ketterson J.B. and Hornfeldt S.
Phys. Rev. B 3 (1971) 4213.

58. Abrahams S.C.
J. Phys. Chem. Solids 24 (1963) 589.

59. Cable J.W. and Wollan E.O.
Phys. Rev. 140 (1965) A2003.

60. Hoare F.E. and Matthews J.C.
Proc. Roy. Soc. A212 (1952) 137.

61. Bozorth R.M. Wolff P.W. Davis D.D. Compton V.B. and Wernick J.H.
Phys. Rev. 122 (1961) 1157.

62. Crangle J. and Scott W.R.
J. Appl. Phys. 36 (1965) 921.

63. Boerstoel B.M. Zwart J.J. and Hansen J.
Physica 57 (1972) 397-420.

64. Nieuwenhuys G.J. Boerstoel B.M. Zwart J.J. Doktor H.H. and Van den Berg G.J.
Physica 62 (1972) 278-96.

65. Sarachik M.P. and Shaltiel D.
J. Appl. Phys. 38 (1967) 1155-56.

66. Ho S.C.
Thesis, University of Manitoba (1982).

67. Star W.M. Foner S. and McNiff Jr. E.J.
Phys. Rev. B 12 (1975) 2690-709.

68. Smit J.J. Nieuwenhuys G.J. and de Jongh L.J.
Sol. St. Commun. 30 (1979) 243-7.

69. Zweers H.A.
Thesis, University of Leiden (1976).

70. Rault J. and Burger J.P.
C.R. Acad. Sci. (Paris) B 269 (1969) 1085.

71. Bellarby P.W. and Crangle J.
J. Phys. C: Met. Phys. Suppl. 3 (1970) S362.

72. Cannella V. Burch T.J. and Budnick J.I.
AIP Conf. Proc. 24 (1975) 464-5.

73. Crangle J.
Phys. Rev. Letts. 13 (1964) 569-70.

74. Zweers H.A. van der Linden H.W.M. and Nieuwenhuys G.J.
Physica B 79 (1975) 83.

75. Peter M. Shaltiel D. Wernick J.H. Williams H.J. Mock J.B. and Sherwood R.C.
Phys. Rev. 126 (1962) 1395-1402.

76. Shaltiel D. Wernick J.H. and Williams H.J.
Phys. Rev. 135 (1964) A1346-62.

77. Coles B. Griffiths D. Lowin R.J. and Taylor R.H.
J. Phys. C. 3 (1970) L121.

78. Guertin R.P. Foner S. McNiff Jr. E.J. and Praddaude H.C.
J. Appl. Phys. 42 (1971) 1550-51.

79. Guertin R.P. Praddaude H.C. Foner S. McNiff Jr. E.J. and Barsoumian B.
Phys. Rev. B 7 (1973) 274-86.

80. Praddaude H.C. Foner S. McNiff Jr. E.J. and Guertin R.P.
Phys. Rev. B 13 (1976) 441-6.

81. Sousa J.B. Moreira J.M. Braga M.E. Palmer S.B. Bates S. and Beaudry B.J.
J. Phys. F: Met. Phys. 15 (1985) 1171-77.

82. Pureur P. Fert A. Wendler R. and Baberschke K.
J. Appl. Phys. 57 (1985) 3230-31.

83. Nigh H.E. Legvold S. Spedding F.H. and Beaudry B.J.
J. Chem. Phys. 41 (1964) 3799-3801.

84. Child H.R. and Cable J.W.
J. Appl. Phys. 40 (1969) 1003-5.

85. Bates S. Palmer S. McIntyre G. Sousa J.B. and Beaudry B.J.
To be Published (1985).

86. Elliott R.J. and Wedgewood F.A.
Proc. Roy. Soc. 81 (1963) 846.

87. Loebisch Jr. O. and Raub E.
J. of Less Common Met. 30 (1973) 47.

88. Maartense I.
Rev. Sci. Inst. 41 (1970) 657.

89. Datametrics Instruction Manual, Type 590 Barocell Pressure Sensor.

90. Keesom W.H.
Helium (Amsterdam: Elsevier 1942).

91. White G.K.
Experimental Techniques in Low-Temperature Physics (Oxford, Clarendon 1979).

92. Osborn J.A.
Phys. Rev. 67 (1945) 351-56.

93. Kaul S.N.
J. Magn. Magn. Mater. 53 (1985) 5-53.

94. Olivier M. Strom-Olsen J.O. Altounian Z. and Williams Gwyn.
J. Appl. Phys. 53 (1982) 7696-98.

95. Schwerer F.C. Conroy J.W. and Arajs S.
J. Phys. Chem. Solids 30 (1969) 1513-25.

96. Purwins H.G. Schulz H. and Sierro J.
Int. J. Magn. 2 (1972) 153-9.

97. Schindler A.I. and LaRoy B.C.
Sol. St. Commun. 9 (1971) 1817-20.

98. Kondo J.
Progr. Theor. Phys. 32 (1964) 37-49.

99. Devine R.A. Shaltiel D. Moret J.M. Ortelli J. Zingg W. and Peter M.
Sol. St. Commun. 11 (1972) 525-9.

100. Schiffrin A.M.
Phys. Stat. Sol. 39 (1970) K81.

101. Schaller H.J. Craig R.S. and Wallace W.E.
J. Sol. St. Chem. 5 (1972) 338-41.

102. Williams G.
Sol. St. Commun. 8 (1970) 1451-54.

103. Prowse D.B. and Cashion J.D.
Phy. Stat. Sol.(a) 22 (1974) 631.